Advances in Experimental Medicine and Biology 1267

Guillaume Duménil
Sven van Teeffelen *Editors*

Physical Microbiology

Springer

Advances in Experimental Medicine and Biology

Volume 1267

Advances in Experimental Medicine and Biology provides a platform for scientific contributions in the main disciplines of the biomedicine and the life sciences. This series publishes thematic volumes on contemporary research in the areas of microbiology, immunology, neurosciences, biochemistry, biomedical engineering, genetics, physiology, and cancer research. Covering emerging topics and techniques in basic and clinical science, it brings together clinicians and researchers from various fields.

Advances in Experimental Medicine and Biology has been publishing exceptional works in the field for over 40 years, and is indexed in SCOPUS, Medline (PubMed), Journal Citation Reports/Science Edition, Science Citation Index Expanded (SciSearch, Web of Science), EMBASE, BIOSIS, Reaxys, EMBiology, the Chemical Abstracts Service (CAS), and Pathway Studio.

2019 Impact Factor: 2.450 5 Year Impact Factor: 2.324

More information about this series at http://www.springer.com/series/5584

Guillaume Duménil • Sven van Teeffelen
Editors

Physical Microbiology

Springer

Editors
Guillaume Duménil
Pathogenesis of Vascular Infections
Institut Pasteur
Paris, France

Sven van Teeffelen
Microbial Morphogenesis and Growth
Institut Pasteur
Paris, France

ISSN 0065-2598 ISSN 2214-8019 (electronic)
Advances in Experimental Medicine and Biology
ISBN 978-3-030-46885-9 ISBN 978-3-030-46886-6 (eBook)
https://doi.org/10.1007/978-3-030-46886-6

This Springer imprint is published by the registered company Springer Nature Switzerland AG.
The registered company address is: Gewerbestrasse 11, 6330 Cham, Switzerland

Preface

Macroscopic phenomena in biology are the result of the complex interplay of many stochastically interacting microscopic proteins and molecules. To understand how macroscopic behavior comes about from microscopic interactions, we have to build quantitative physical models. While this concept has been understood in developmental and also in eukaryotic cell biology, bacteria have long been regarded as "bags of enzymes" that do not provide complex multi-scale self-organization. However, with increasing technical possibilities to observe and quantify bacterial behavior and bacterial cell biology, this point of view has slowly changed. Today, there are multiple bacterial subsystems that have profited from physical approaches, notably the flagellar motor, the cell envelope, the chromosome, and osmotic pressure. Other, more complex systems or sets of systems, such as bacterial virulence, are also under investigation with approaches from physics.

The contents of the book intend to illustrate this trend of approaching questions of self-organization in bacterial microbiology with approaches from physics, which we refer to as *Physical microbiology*. This book attempts to present recent concepts and tools in this emerging field. Chapters are written to be of interest to biologists, who wish to add concepts and tools from physics to their research and for physicists who wish to explore biological processes.

A set of technical developments shed a new light on all aspects of microbiology, basic bacterial physiology, and division but also on issues related to infection, through antibiotics resistance, virulence factors, and host response to infection. Video microscopy is of particular interest here as it allows to follow specifically labelled proteins in space and time. Microscopes and cameras of video microscopes now allow to reach resolutions compatible with observations of specific components inside bacteria and determine their position relative to major bacterial components such as membrane, nucleoid, or bacterial poles. Microfluidics-based approaches to confine or constrain bacteria provide a powerful tool in combination with video-microscopy. Super-resolution microscopy takes these observations an extra step further in resolution. Finally, cryo-electron microscopy combined with single-particle averaging brings a molecular-level view.

A key feature of the techniques described above is the ability to extract quantitative information. Biological objects of interest can be counted, their size measured, and their speed determined in the case of video microscopy. This quantitative aspect is critical as it allows confrontation with physical laws

and testing of specific physical models leading to validation or invalidation. In most instances there is a necessity to revisit physics to address these specific questions. Together, physics and quantitative observation provide a novel vision of microbiology.

The book starts with a chapter by Enrique Rojas that explores and describes the mechanical properties of bacteria. This chapter highlights the role of different cell-envelope components, the bacterial cytoskeleton, and of the nucleoid. The main mode of transport in bacteria is diffusion. The chapter by Christopher H. Bohrer and Jie Xiao is devoted to characterizing diffusion of proteins in bacteria, and to the different tools to measure diffusion, with a focus on single-molecule tracking. One of the main tasks of bacteria during every generation of growth is the faithful replication and segregation of their DNA. Antoine Le Gall and Marcelo Nollmann describe the physical mechanism underlying chromosome and plasmid segregation through the ParABS system. Le Gall and Nollmann demonstrate that the system displays complex dynamics, and its understanding requires physical modeling. Ines Baptista and colleagues give an overview of the spatial distribution of different cellular components, and they provide evidence that the nucleoid has a major organizing function in bacteria. Bacteria contain remarkably complex multi-component machines such as secretion systems and flagellar motors. Ashley Nord and Francesco Pedaci describe the complexity of the bacterial flagellar motor and its implications for physical function. During infection, bacterial pathogens interact with their host in a variety of ways including through the secretion of toxins. David Gonzalez-Rodriguez and colleagues explore the physical principles that allow certain toxins to form large openings through host cells. Finally, Tory Doolin and colleagues review current knowledge on a mechanism of bacterial killing by histones from eukaryotic cells.

The contents of these chapters are intended to provide a state-of-the-art view of the emerging field of physical microbiology for biologists and physicists. We are convinced of the huge potential of this field both in terms of basic and applied sciences and we hope this book will be a source of inspiration for students and researchers.

Paris, France — Guillaume Duménil
Paris, France — Sven van Teeffelen

Contents

The Mechanical Properties of Bacteria and Why they Matter

1

Enrique R. Rojas

"It behooves us always to remember that in physics it has taken great scientists to discover simple things. They are very great names indeed which we couple with the explanation of the path of a stone, the droop of a chain, the tints of a bubble, the shadows in a cup. It is but the slightest adumbration of a dynamical morphology [of biological systems] that we can hope to have until the physicist and the mathematician shall have made these problems of ours their own."

– D'arcy Thompson, On Growth and Form.

Abstract

I review recent techniques to measure the mechanical properties of bacterial cells and their subcellular components, and then discuss what these techniques have revealed about the constitutive mechanical properties of whole bacterial cells and subcellular material, as well as the molecular basis for these properties.

Keywords

Mechanobiology · Cell growth · Cellular morphogenesis

E. R. Rojas (✉)
Department of Biology, New York University, New York, NY, USA
e-mail: rojas@nyu.edu

1.1 Introduction

Bacteria are the smallest, simplest, and most successful (that is, most numerous) class of living organisms on Earth. It is reasonable to assume that these three traits are intimately connected with each other, and with bacteria's foundational role in our understanding of molecular biology. However, these traits have historically been "selected against" by those interested in biomechanics: their small size renders bacterial cells intractable to many biophysical assays used on eukaryotic cells or tissues, and their relative simplicity (for example, their lack of a true cytoskeleton) along with a historical focus on their genetics and molecular biology have perhaps caused scientists to underestimate the richness of their mechanics and the value of studying them.

Over the last 10 years there has been a realization of the importance of mechanical sensing and signaling in bacteria (reviewed elsewhere in this

G. Duménil, S. van Teeffelen (eds.), *Physical Microbiology*, Advances in Experimental Medicine and Biology 1267, https://doi.org/10.1007/978-3-030-46886-6_1

volume; also see Persat et al. 2015). In parallel, several fundamental measurements have begun to elucidate the intriguing mechanical properties of bacterial cells. Due to the size of bacteria, these measurements have typically required Herculean efforts in assay development to make what are relatively crude mechanical measurements compared to what can be measured for eukaryotic cells or non-living materials. Yet these seminal measurements have already demonstrated that bacteria possess many novel materials from a mechanics perspective, and underscore the importance of endeavoring to characterize these materials.

While the field of bacterial cell mechanics is still in its infancy, in certain cases it is clear how the mechanical properties of subcellular material are adaptive with respect to subcellular physiological processes or survival of the cell in complex environments. Here, I will review what we have learned about the mechanical properties of bacteria, beginning with measurements of whole-cell mechanical properties and proceeding to those of each subcellular material. Instead of simply listing the absolute quantitative values of mechanical properties (stiffness, viscosity, etc.), I will focus on discussing the **constitutive properties** (Box 1.1) of the cell and its subcellular materials, that is, the functional form of the quantitative dependence of the deformation of a material on the forces applied to it. Along the way, I will highlight the current methods available for assaying bacterial mechanics. Finally, in each case, I will discuss the relevance of the mechanical properties to cellular physiology.

Box 1.1: A Brief Glossary of Mechanics

Mechanical Stress (σ): A force distributed over an area. Stress has dimensions of pressure.

Mechanical Strain (ε): The degree to which a material is stretched. Strain has no dimensions – it is a fractional change in length, area or volume.

Constitutive property: The specific, quantitative relationship between the magnitude of deformation of a material and the magnitude of mechanical stresses applied to it.

Elastic: Possesses the simplest constitutive relationship for a solid material in which strain is proportional to stress, $\sigma = E\varepsilon$, and deformation is reversible when the force is removed. E is the "Young's Modulus" and has dimensions of pressure.

Nonlinear elastic: Possesses a constitutive relationship in which deformation increases with applied stress but not proportionally.

Strain-stiffening: A specific type of nonlinear elasticity in which the amount of additional force required to stretch a material a given amount increases as the material is stretched.

Viscoelastic: Has properties of both a solid and a liquid. A viscoelastic material behaves as a solid immediately after a stress is applied, but flows like a liquid after longer periods.

Plastic: Deforms irreversibly if the applied stress exceeds a certain threshold or is applied for long enough. A plastic material is a solid.

Glass: A material that behaves as a viscous liquid or rubbery material above a certain critical temperature and a brittle solid below it.

Anisotropic: Possesses different structural and mechanical properties in different directions.

Flexural Rigidity (κ): The degree to which a material (like a cell) resists bending when a deflection force is applied to it. Flexural rigidity has dimensions of force times area.

1.2 Mechanical Elements of the Bacterial Cell

Most readers of this chapter will be familiar with the structural components of the bacterial cell. I will briefly outline the bacterial cell features relevant to the topic of mechanics.

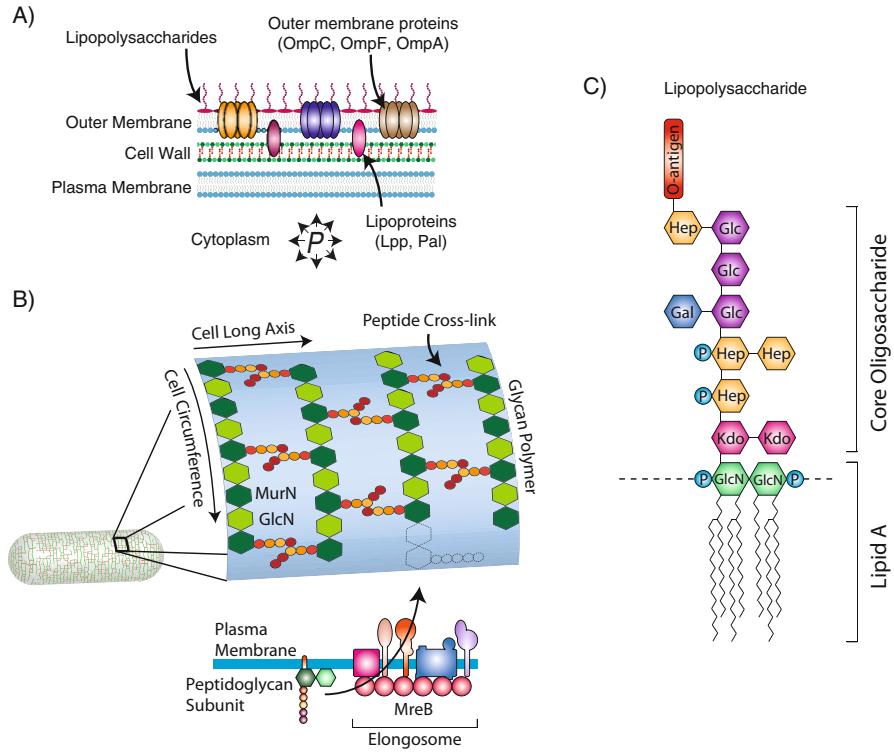

Fig. 1.1 The bacterial cell envelope. (**a**) Layers of the Gram-negative bacterial cell envelope, including proteins that bind the outer membrane. *P* turgor pressure. (**b**) Peptidoglycan and the peptidoglycan biosynthetic machinery, i.e., the "elongosome." *GlcN* N-acetyl glucosamine, *MurN* N-acetyl muramic acid. Adapted from Cho et al. 2014. (**c**) *E. coli* K12 lipopolysaccharide. *P* phosphate, *Kdo* 3-deoxy-D-*manno*-oct-2- ulosonic acid, *Hep* L-*glycero*-D-*manno*-heptose, *Glc* glucose, *Gal* galactose

Bacteria are small and, as mentioned above, it is likely that their small size is selected for by nature. As a result, bacterial cells must concentrate all the biomolecules required for life into a very small volume, resulting in a large concentration differential between the inside and the outside of the cell. This differential results in a hydrostatic, osmotic pressure, called the turgor pressure (Fig. 1.1), which is between about 1 atm (for Gram-negative bacteria; Deng et al. 2011) and 10 atm (for Gram-positive bacteria; Whatmore and Reed 1990) above atmospheric pressure. The highly concentrated nature of the cytoplasm, and the resulting turgor pressure, has important consequences for both the mechanical properties of the cytoplasm and those of the cell envelope.

For the sake of this review, the cell envelope (Fig. 1.1) will be defined as all the layers of the cell surface *outside* the plasma membrane. The cell wall is superficial to the plasma membrane, and is primarily composed of peptidoglycan, a covalently cross-linked network of polysaccharides and short peptides (Fig. 1.1b). Depending on the species, other components of the cell envelope may also be present. For example, Gram-positive bacteria covalently attach teichoic acids – anionic polymers of alternating phosphate and sugar-alcohol residues – to their cell walls. Besides the cell wall, Gram-negative bacteria additionally possess an outer membrane (Fig. 1.1a, c); the inner leaflet of the outer membrane is composed of phospholipids but the outer leaflet is composed of lipopolysaccharides, which are themselves complex molecules that possess acyl chains, phosphate, and several sugar moieties (Fig. 1.1c). Largely due to the phosphate groups, the outer membrane is highly anionic and thus binds cations such as magnesium, which stabilize the membrane by preventing repulsive in-

teractions between the lipopolysaccharides. Like the plasma membrane, the outer membrane is rich in proteins, especially β-barrel porins, and several abundant proteins such as Lpp, OmpA, and Pal also link the cell wall and the outer membrane (Fig. 1.1; Sonntag et al. 1978; Mizuno 1979). Other Gram-indeterminate bacteria, such as the *Mycobacteria* also have outer membrane-like structures, but with different chemical composition.

Many bacteria have still other envelope layers, such as S-layer and capsule, but very little is known about the mechanical contributions of these structures and so I will not treat them in this review.

1.3 Whole-Cell Measurements

1.3.1 Cell Bending

Galileo Galilei became the first quantitative biophysicist when he astutely applied his new theory of bending beams to animal bones (Galilei 1914). It then seems appropriate to begin our discussion of the new bacterial biomechanics with similar bending experiments at the microscale performed almost 400 years later. These experiments were enabled by inventive applications of optical tweezers (Wang et al. 2010) and microfluidics (Amir et al. 2014). In the optical tweezers assay, a positively charged polysterene microsphere was suspended with a laser, and was then used to apply and measure bending forces to filamentous *E. coli* cells that were adhered to a cover glass at one end (Fig. 1.2a). This was performed on an inverted microscope, which allowed simultaneous measurement of the deflection of the cell. In the microfluidic assay, filamentous *E. coli* cells (created by genetically inhibiting cell division) were grown in long dead-end channels (Fig. 1.2b). When one end emerged from the open end of the channel, they were subjected to an orthogonal fluid flow; displacement was measured and force was calculated using the theory of viscous drag. Both studies observed **elastic** (Box 1.1) deformation in response to short periods of deformation. By treating the cell as an elastic rod, the **flexural rigidity** (Box 1.1) of the cell could then be calculated, and the two measurements agreed well with each other (3×10^{-20} and 5×10^{-20} Nm^2, respectively). The molecular basis for this bending rigidity will be discussed later (see *Cytoskeletal proteins* and *Outer membrane*).

The microfluidics-based assay was also used to question whether the cell as a whole had **plastic** properties (Box 1.1): if you bent a cell for long enough, or applied large enough forces, would the cell stay bent? It was found that *E. coli* cells were indeed plastic, but that this plasticity required deformation on the time scale of the cell cycle and that cell growth had to be taking place during this period for plasticity to occur. That is, growth seemed to "fix" deformation in place. Conversely, growth also was able to straighten cells on similar time scales once the force was released. These data agreed with qualitative and quantitative studies observing the growth of *E. coli* cells trapped and released in micron-scale wells (Takeuchi et al. 2005).

Because the shape of the bacterial cell is conferred by the peptidoglycan cell wall, the connection between plastic deformation and active cell growth points to an intimate connection between the mechanical properties of the bacterial cell (its plasticity) and the physiology of cell-shape maintenance via peptidoglycan synthesis. To sum, cell shape, an adaptive feature of bacteria (Young 2006), is robust to mechanical forces that act over time scales that are less than the time scale of cell growth (approximately the doubling time), yet if forces are applied for longer cell shape will conform to the mechanical environment. This is likely adaptive as well, allowing bacteria to grow in highly constrained environments (Takeuchi et al. 2005; Männik et al. 2009).

1.3.2 Cell "Squeezing"

Another microfluidic device was developed to assay whole-cell mechanics by measuring how far cells could be driven into wedge-shaped traps as a function of applied pressure (Fig. 1.2c; Sun 2014a). This assay could distinguish between the

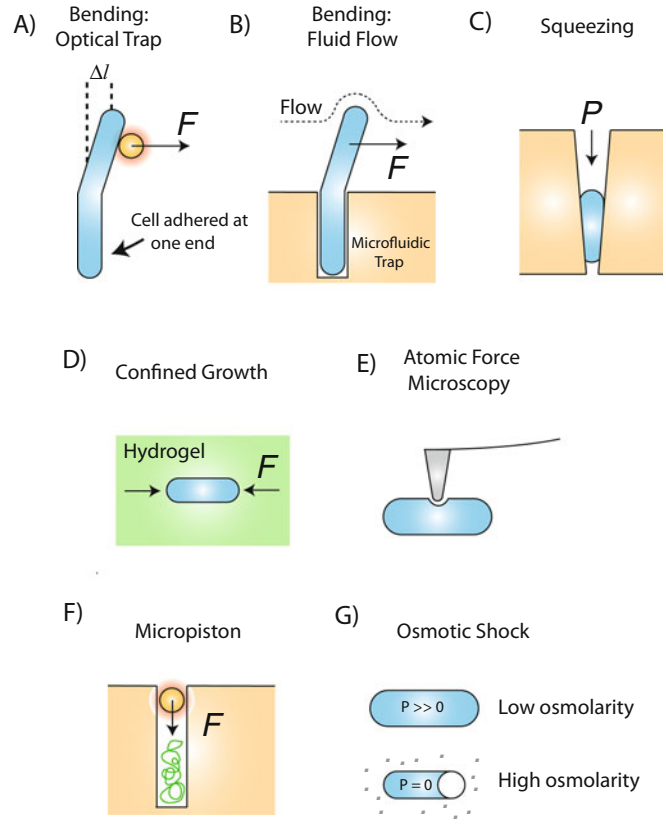

Fig. 1.2 Methods for measuring the mechanical properties of bacterial cells

model Gram-negative and Gram-positive bacteria, *E. coli* and *B. subtilis*, with *E. coli* cells moving ≈20–50% further into the wedges, depending on pressure. That is, *E. coli* cells are "softer" than *B. subtilis* cells. While many factors could be mediating cell softness viz-à-viz this assay, this result is consistent with *E. coli* cells having less stiff cell envelopes and lower turgor pressures than *B. subtilis* cells. Thus, while more sophisticated modeling would be required to assess the material properties of the cell quantitatively from this assay and compare them with those obtained by other assays, the "squeezing" assay does provide a relative measurement of whole-cell mechanical compliance. Physiologically, this compliance is surely related to the ability of *E. coli* cells to grow through constrictions well below their typical cell diameter in search of nutrients (Männik et al. 2009), which could provide an adaptive value in natural niches with similar spatial constraints, such as microvilli in the gut.

1.3.3 Growing Cells in Agarose Hydrogels

Whole-cell mechanics were also assayed indirectly by embedding growing cells in an agarose gel and measuring the effect of the gel on single-cell growth (Fig. 1.2d; Tuson et al. 2012). The gel reduces growth rate to a degree that increases with increasing gel stiffness; analytical and finite-element based models were used to quantitatively calculate the stiffness of the whole cell. As for the "squeezing" assay, *B. subtilis* had a modestly higher stiffness (about twofold) than *E. coli*; interestingly, though, the stiffness of *P. aeruginosa*, a Gram-negative bacterium, was similar to that of *B. subtilis*.

While the meaning of whole-cell stiffness is unclear physiologically, the key advantage of the hydrogel assay is that it was easily adaptable to a high-throughput format, allowing cell mechanics to be measured across a non-essential gene

deletion library, thereby connecting genetics and mechanics in bacteria for the first time (Auer et al. 2016). What genes contributed significantly to cell stiffness? As expected, deletion of genes involved in cell envelope synthesis often resulted in less stiff cells. These included the top hit, *mrcB*, a gene that encodes PBP1b, a protein that plays a key role in the incorporation of peptidoglycan subunits into the cell wall (Fig. 1.1b). However, cell-envelope related genes accounted for only a fifth (9/46) of the hits in the screen. Other highly represented categories of genes included genes involved in energy production and DNA replication. How genes from these latter categories affect stiffness is an open question. It is possible that they do so through an effect on turgor pressure; lower turgor would lower the force that the cell could exert on the hydrogel, potentially resulting in a slower growth and therefore a lower effective value of cell stiffness. However, a surprising finding in this study was that de-energizing cells using the uncoupler CCCP made cells stiffer. The mechanistic basis for this was not explored.

1.3.4 Atomic Force Microscopy

Atomic force microscopy (Fig. 1.2e) has been used extensively to measure the mechanical properties of whole bacterial cells. In this method, a microscopic cantilever is used to locally indent the cell, and force-displacement relationships are calculated by measuring the degree to which the cantilever bends as a function of indentation distance. The effective "stiffness" of the cell assayed using AFM is dependent on many factors, including the turgor pressure and the mechanical properties of all of the envelope components. Thus, while it is difficult to dissect the molecular basis for whole-cell AFM measurements, this method has been useful for making phenomenological measurements of whole-cell mechanics. Both **viscoelastic** and **plastic** (Box 1.1) properties have been reported (Vadillo-Rodriguez and Dutcher 2009; Gaboriaud et al. 2008). Furthermore, AFM has been used to measure the effects of various antimicrobial agents on global cell mechanics. For example, it has been observed that bacteriophage, EDTA, chitosans, and antibiotics each have a softening effect on bacteria (Chen et al. 2009; Eaton et al. 2008; Perry et al. 2009; Francius et al. 2008).

1.4 The Cytoplasm

I will now discuss what is understood about the mechanical properties specific to each subcellular component of the bacterial cell, beginning with the cytoplasm and ending with the outer membrane.

The cytoplasm of bacteria is composed of about ≈70% water, 15% proteins, and 7% nucleic acids by mass (Todar 2006), with the remaining content composed of sugars, ions and other small molecules. Thus, it stands to reason that any deviation of the mechanical properties of the cytoplasm from the incompressibility of water is due largely to proteins, with potential lesser contributions from DNA and RNA. Few studies have addressed the mechanics of the bacterial cytoplasm directly, and the wealth of data concerning the mechanics of the eukaryotic cytoplasm is irrelevant since it is clearly dominated by the properties of the cytoskeleton (Janmey 1991), which is absent in bacteria despite the presence of homologues of the eukaryotic cytoskeleton proteins.

1.4.1 Gross Mechanical Properties of the Cytoplasm

The bacterial cytoplasm is largely composed of water and, as such, has fluid properties: the shape of the cell is determined by the geometry of the cell wall, which is adopted by the cytoplasm. However, more complex mechanical properties have been inferred from detailed experiments in which the motion of fluorescent molecules in the cytoplasm was tracked. Several such experiments found that many molecules move "subdiffusively" through the cytoplasm: whereas a molecule exhibiting a Brownian random walk in a fluid would diffuse away from its initial position with the mean squared displacement proportional

to time, MSD $\sim t$, molecules undergoing sub-diffusive motion move randomly with MSD $\sim t^{\alpha}$, where $\alpha < 1$ (Metzler et al. 2014).

Sub-diffusive motion can result from a number of causes, including obstruction by the cytoskeleton (in eukaryotic cells; Saxton 1994) and "molecular crowding," that is, when macromolecular concentration is approximately equal to that of free water. However, in one case sub-diffusion pointed directly to the mechanical properties of the bacterial cytoplasm. In this study, chromosomal loci were observed to move sub-diffusively, with MSD $\sim t^{0.4}$ (Weber et al. 2010). This could not be explained by obstruction by the cytoskeleton, nor could the constraint imposed on the locus by the chromosome itself account for all of the effect. The key result that elucidated the basis of the sub-diffusive motion was that the direction of locus motion was anti-correlated with the direction of motion less than one second in the past. This suggested that the loci were "rebounding" from the cytoplasm, that is, the cytoplasm is **elastic** (Box 1.1) at time-scales less than a second and therefore the cytoplasm has **viscoelastic** properties (Box 1.1) as a whole. Similar results were obtained with RNA-protein complexes. While this study clearly demonstrated viscoelasticity, technical limitations prevented the calculation of the elastic or loss moduli from these data, preventing quantitative comparison to that of other cellular components or to the eukaryotic cytoplasm.

It is unlikely that there is a specific adaptive value (or cost) of sub-diffusive motion in bacteria. Rather, given their small size, sub-diffusive motion is almost certainly not selected against strongly since diffusing species explore the entire cell within milliseconds (Milo and Phillips 2015). However, if bacteria are selected to be small, and viscoelasticity results from crowding effects, then viscoelasticity is an inherent byproduct of selection. While viscoelasticity inhibits molecular transport via diffusion, this inhibition is acceptable evolutionarily so long as there are not great distances over which transport needs to occur.

Observation of sub-diffusive motion revealed that whether or not the cytoplasm behaved as a solid or a fluid depended on the time-scale at which its mechanics are assayed (Weber et al. 2010). A separate study demonstrated that cytoplasmic mechanical properties also depend on the length-scale at which they are assayed by tracking the cytoplasmic motion of particles of a range of sizes. "Anomalous diffusion," in which the distribution of random step sizes was not Gaussian, as would be expected from Brownian diffusive motion, was observed for particles larger than 30 nm (Parry et al. 2014). The distribution of random motion was also heterogeneous within the same cell, that is, different particles obeyed different distributions of random motion. These properties suggested that the cytoplasm has **glass-like** properties (Box 1.1), whereby even though it is a fluid, that it is "close to" a fluid-to-solid phase transition. What does "close to" mean? Remarkably, de-energizing cells with metabolic uncouplers resulted in highly constrained diffusion of large particles, characteristic of a solid. This is consistent with earlier results demonstrating that metabolism increased the mobility of chromosomal loci (Weber et al. 2012). That is, metabolism "fluidizes" the cytoplasm, allowing large particles to explore the entire volume of the cell.

Because the random motion of particles underlies biochemical reactions, it is very likely that the specific characteristics of the glassy cytoplasm, such as the degree to which metabolism can fluidize it, is highly adaptive. Biomolecules that undergo biochemistry must be able to move randomly in the cytoplasm and thus the cytoplasm must stay in the fluid phase with respect to the size scale of these molecules. It was suggested that this may set an upper limit to the size of biomolecules in the cell. Since the glassy nature of the cytoplasm is a direct result of molecular crowding, there may also be an evolutionary trade-off between cell size and how glassy (how close to the solid phase) the cytoplasm is.

1.4.2 Cytoskeletal Proteins

While bacteria do not have cytoskeletons, that is, cytoplasmic polymeric networks that can bear load and actuate forces, they do have homologs of

the three main eukaryotic cytoskeleton proteins: actin, microtubules, and intermediate filaments, that perform other functions (Shih and Rothfield 2006). It was natural, then, to question whether these proteins contribute to the mechanical properties of the cell. This was done in the case of MreB, the actin homolog found in most rod-shaped bacteria (Margolin 2009). MreB forms short (<200 nm) polymers (Billaudeau et al. 2019) that bind to the plasma membrane and orchestrate peptidoglycan synthesis, likely by acting as a scaffold for various biosynthetic enzymes (Fig. 1.1b; Shi et al. 2018). Depolymerization of MreB using a chemical inhibitor, A22, causes aberrant peptidoglycan synthesis and loss of the cell's rod shape (Gitai et al. 2005).

The contribution of MreB to cell mechanics has been probed in several ways. First, optical tweezers were used to bend *E. coli* cells and measure force-displacement curves (Fig. 1.2a; Wang et al. 2010). By treating the cell as an elastic rod, the **flexural rigidity** (Box 1.1) of the cell was then calculated. Remarkably, when MreB was depolymerized with A22, the flexural rigidity was reduced by ≈50%, and this effect was rapidly reversible by washing out the inhibitor. At the time of this study, it was thought that MreB formed a helical "cytoskeleton" that ran the length of the cell, and it was shown theoretically that this would be sufficient to confer the observed contribution to the flexural rigidity of the cell. We now know that MreB forms many short independent filaments rather than a single helix (Garner et al. 2011; Domínguez-Escobar et al. 2011; van Teeffelen et al. 2011). As such, it remains unclear how MreB is mechanically coupled to the cell envelope at the molecular scale such that it can contribute so strongly to flexural rigidity. It is possible that flexural rigidity depends not only on the structural state of the cell but also on active cell wall synthesis such that rigidity decreases when this process is perturbed with A22; this idea would be straightforward to test.

While MreB makes a strong contribution to flexural rigidity, its contributions to other modes of deformation are more modest. In the cell squeezing experiment (Fig. 1.2c), A22 caused the cells to move marginally more (≤10%) into the traps than untreated cells, depending on pressure (Sun 2014a). The effect of A22 on cell growth in an agarose hydrogel (Fig. 1.2d) is negligible (Tuson et al. 2012). Since the squeezing assay, but not the hydrogel assay, causes slight bending of the cell envelope, together these data suggest that MreB's sole contribution to cell mechanics could be to confer flexural rigidity to the envelope. Combined with the fact that applying bending forces to cells over many minutes caused a persistent, plastic deformation, MreB then maintains the cell's straight rod shape in two independent ways: biochemically by coordinating organized peptidoglycan synthesis and biomechanically by restricting bending.

The contributions of the other cytoskeleton homologues, FtsZ (a tubulin homolog) and crescentin (an intermediate filament homolog) to global cell mechanics have not been measured but they are less likely to be important since they form highly localized polymers that govern specific physiological functions: division and morphogenesis, respectively. Furthermore, while it is clear that polymers of both proteins can apply forces (Osawa et al. 2008; Cabeen et al. 2009), it is unclear whether these forces, per se, are important for their function.

1.4.3 The Chromosome

The mechanics of DNA in various contexts has been studied extensively (Benham and Mielke 2005). However, it is important to study the chromosome *in situ* to understand its physiology. This was done for *E. coli* by developing a hybrid microfluidics/optical tweezers assay (Fig. 1.2f; Pelletier et al. 2012). In this experiment, single bacterial cells whose chromosomes had been fluorescently labeled were trapped in long dead-end microfluidic channels, similar to those used in the microfluidic bending experiment described above. Once trapped, they were subjected to a lysis buffer that released their cytoplasm and allowed their chromosomes to expand to their rest lengths, which was found to be approximately tenfold longer than their confined lengths in the cell. The rate of expansion and

chromosome morphology depended heavily on the physiological state of the cell, with exponentially growing cells possessing globular chromosomes that expanded slowly while those from stationary phase cells possessed featureless chromosomes that expanded rapidly. Although not explicitly shown, it was suggested that these differences were due to the effect of the physiology of the chromosome (i.e., transcription and replication) on its mechanical properties.

The chromosome can be thought of as an "entropic spring": when it is confined to a small volume it gives rise to a pressure similar to that created when a gas is trapped in a balloon. By using optical tweezers to create a "micropiston" in the microfluidic channel, this magnitude of this pressure could be measured directly (Fig. 1.2f). It was found that even when the chromosome was confined to its *in vivo* size (i.e., tenfold compression), this created a pressure that was still only about one thousandth as large as the turgor pressure within the cell. This implies that the chromosome is extremely soft compared to the cell envelope, which bears the turgor pressure. In fact, it was demonstrated that forces arising from molecular crowding in the cytoplasm are alone enough to cause compaction of the chromosome to the *in vivo* size. These forces result from the fact that the chromosome excludes many proteins from within its volume, causing them to exert an entropic, osmotic pressure on the chromosome and compact it. That is, the chromosome may not even require constraint by the cell envelope!

While the mechanical properties of the chromosome are clearly correlated with the physiological state of the cell, it needs to be determined whether these properties are just a consequence of that physiology or also dictate certain physiological processes.

1.5 The Plasma Membrane

The plasma membrane is perhaps the best-studied biological structure from a biomechanics perspective, and yet there has been very little investigation into the specific mechanics of the bacterial plasma membrane. The clear exception to this statement is that the properties of stretch-activated ion channels, which are mechanically gated channels that are thought to mediate turgor pressure relief in bacteria, have been extensively studied (Martinac 2004). While mechanics at the protein level is not the focus of this review, it is likely that these ion channels actually do contribute to the gross mechanical properties of the membrane by providing "slack" (Rojas et al. 2017). When the genes encoding stretch-activated ion channels in *B. subtilis* are deleted, moderate (0.5 M) hypoosmotic shocks cause cells to swell and lyse (Hoffmann et al. 2008). However, when channels are present, cells can survive enormous (1.5 M) hypoosmotic shocks, and swell to sizes well beyond those that would cause them to lyse in the absence of channels (Rojas et al. 2017). Notably, the presence of channels does not cause cells to shrink after hypoosmotic-shock induced swelling, that is, there is no evidence that the channels actually relieve turgor pressure after shocks *in vivo*. This suggests that the role of the ion channels to "soften" the membrane by decreasing the force experienced by the phospholipid bilayer for a given extension, thereby preventing rupture. While consistent with the observed data, this mechanism needs to be tested more thoroughly.

A micropipette aspiration experiment explicitly measured the mechanical properties of the plasma membrane in *E. coli* spheroplasts (wall-less and outer membrane-less cells; Sun et al. 2014b). This measurement revealed that, as opposed to pure phospholipid bilayers, the *E. coli* membrane had viscoelastic properties, with stress relaxation occurring in about a minute. The *E. coli* membranes were also about twice as soft as pure phospholipid bilayers. While a "membrane reservoir" was invoked to rationalize these results, the protein content of the membrane, including stretch-activated ion channels, could also explain them. In any case, in concert with the ion channels, its soft viscoelastic nature likely underlies the plasma membrane's ability to accommodate large deformations and therefore confers a fitness advantage in fluctuating osmotic environments, which many bacteria regularly endure in the gut, the soil, or in natural bodies of water.

1.6 The Cell Wall

If the bacterial plasma membrane is the least well studied bacterial structure from a mechanics perspective, the cell wall is certainly the best studied. This is because the cell wall serves two primary, critical roles that are both mechanical in nature: (i) it protects the cell from osmotic lysis and (ii) it confers shape to the cell. To accomplish these functions it has to be relatively strong (resistant to rupture) and it has to be a solid material. As such, across species, the cell wall is a covalently cross-linked macromolecule. However, while peptidoglycan is the major component of the cell wall in most bacterial species, the specific chemical composition of the wall and its microscopic structure is dependent on taxum, and this has important consequences for its mechanical properties.

A key difference between the mechanics of the cell wall and other materials in the cell is that the wall is **anisotropic** (Box 1.1), and this feature is directly dependent on its microscale architecture and directly related to its function. The glycan polymers, which are thought to be stiffer than the peptide species, are oriented circumferentially around the cell axis (Fig. 1.1b; Verwer et al. 1978; Gan et al. 2008). Two studies confirm that cell-wall stiffness is anisotropic, with a larger stiffness in the longitudinal direction (parallel to the cell axis) than in the circumferential direction. First, cell walls of *E. coli* were isolated and placed on a substrate with microscopic grooves (Yao et al. 1999). Then, atomic force microscopy was used to measure the force required to indent the cell walls into the grooves (similar to the way that standing on a trampoline causes an indentation in the trampoline surface). Importantly, this force depended on which way the cell walls were laying across the groove: the force was higher if the long axis of the wall was parallel to the groove. By using simple mechanical equations, the stiffness in the circumferential direction was found to be ≈80% higher than that in the longitudinal direction. This agreed qualitatively with a second study that used large hyperosmotic shocks (Fig. 1.2g) to plasmolyze the cells, thereby relieving their turgor pressure, and then measured the resulting contraction in the circumferential and longitudinal directions (Rojas et al. 2014). Although the contractions were roughly equal in both directions, the mechanical stress in the circumferential direction is twice as large as that in the longitudinal direction for a pressurized cylindrical surface, such as a rod-shaped cell (Love 2013). That is, the stiffness of the envelope in the circumferential direction was about twice as stiff as that in the longitudinal direction.

The circumferential orientation of glycan polymers in the cell wall is due to their oriented synthesis by the "elongosome" complex (Fig. 1.2b), which moves circumferentially along the plasma membrane as it catalyzes glycan synthesis (Garner et al. 2011; Domínguez-Escobar et al. 2011; van Teeffelen et al. 2011). When this oriented motion is chemically perturbed (but biosynthesis is allowed to continue), the cell loses its rod shape and grows amorphously (without specific shape; Gitai et al. 2005). This demonstrates that the microscopic anisotropy of the wall, and probably the resulting mechanical properties, are critical for rod-shaped maintenance.

In addition to anisotropy with respect to the circumferential and axial directions, the cell wall also likely has *helical* anisotropy. In one creative experiment, charged microspheres were adhered to opposite ends of a filamentous *E. coli* cell and it was found by measuring the relative motion of these microspheres that cells "twist" as they grow (Wang et al. 2012). Furthermore, when turgor pressure was relieved in these cells by hyperosmotic shock, the cell envelope twisted in the opposite direction as the cell envelope contracted. A mechanical model of cell wall expansion demonstrated that both the helical anisotropy and the twisting growth could result from the fact that the elongosome complexes (Fig. 1.1b) actually move with a slight helical pitch with respect to the axis of the cell (Garner et al. 2011; Domínguez-Escobar et al. 2011; van Teeffelen et al. 2011).

In addition to being highly anisotropic, the cell wall also has highly **nonlinear elastic** properties (Box 1.1). This was demonstrated most clearly by a delicate atomic force microscopy (Fig. 1.1e) experiment in which force-distance responses were measured for single *E. coli* cells (Deng et al.

2011). This measurement was performed on intact cells and on cell wall-less blebs that were induced pharmacologically, allowing for the direct measurement of turgor pressure. Additionally, applying a complex mechanical model allowed the specific mechanical properties of the cell wall to be calculated *in vivo* for the first time (rather than measuring the properties of the whole cell or the isolated cell wall). It was found that the cell wall exhibited a high degree of **strain-stiffening**, in which the additional force required to make incremental deformations increased continuously as the deformation increased (Box 1.1). This result was consistent with osmotic shock-based experiments whereby hyperosmotic shocks (relieving turgor pressure, Fig. 1.1g) caused much more contraction than hypoosmotic shocks (increasing turgor pressure) of the same magnitude caused extension of the cell wall (Rojas et al. 2014, 2017). In fact, large hypoosmotic shocks caused no extension of the *E. coli* cell envelope, although rapid down-regulation of turgor pressure by stretch-activated ion channels could also account for this result.

While the specific advantage of the cell wall's nonlinear properties has not been explicitly tested, it is reasonable to speculate that these properties are important for the wall's function in protecting the cell from osmotic lysis. If the wall is present, then any extension of the plasma membrane will be limited by the extension of the cell wall that surrounds it. That the *E. coli* cell envelope is essentially inextensible beyond the length prescribed by steady-state growth guarantees that the plasma membrane is never stretched *in vivo* by osmotic fluctuations, making it virtually impossible to lyse the cell except by chemically undermining the envelope or the plasma membrane itself.

1.7 The Outer Membrane

Historically, it was textbook dogma that the cell wall was the dominant mechanical element in the cell (Madigan et al. 1997), but this view came into question after several anomalous observations suggested that the outer membrane could also bear significant loads. First, the outer membrane is not a fluid (in the plane of the membrane) like the plasma membrane; this was concluded from the observation that outer membrane proteins do not freely diffuse in the membrane (Rassam et al. 2015). Rather, it is likely that the outer membrane is an "ionic hydrogel," a solid phase wherein neighboring divalent anionic lipopolysaccharide molecules are bound to one another via divalent magnesium cations (Hermann et al. 2015). Second, it was discovered that a protein complex that disrupts the outer membrane was required for cell lysis by bacteriophage λ (Berry et al. 2012). Without these proteins, the phage could digest the cell wall, causing spheroplasts to form, thereby transferring the entire load imposed by turgor pressure to the two membranes, but the cells did not lyse, suggesting that the outer membrane was bearing the load. Finally, it was demonstrated that treatment of *E. coli* cells with vancomycin, a cell wall-targeting antibtiotic caused blebbing of the protoplast (the plasma membrane and cytoplasm); that is, the protoplast escaped from the cell wall. However, this did not immediately cause cell lysis, which took minutes to hours after protoplast escape (Yao et al. 2012). Similar phenomena have now been observed many times in response to drug treatment of bacteria.

The mechanical properties of the *E. coli* outer membrane were explicitly assayed by using several methods to apply forces to the entire cell envelope (i.e., the composite cell wall-outer membrane complex), measuring the deformation in response to these forces, and then repeating these experiments while perturbing the outer membrane via a variety of chemical and genetic techniques to determine if the deformations were greater than they were in the absence of perturbation (Rojas et al. 2018). For example, when turgor pressure was depleted by subjecting cells to a large hyperosmotic shock, the cell envelope contracted, as expected. However, when the outer membrane was subsequently dissolved by subjecting the shocked cells to a detergent, the naked cell wall contracted again, and the two contractions were roughly equal. This suggested that the outer membrane, which is connected to

the cell wall by numerous proteins (Fig. 1.1a), was stabilizing the cell wall above its rest length after hyperosmotic shock; in order to do this it had to be bearing compressive stress commensurate with that borne by the composite cell envelope during the turgid state. A simple mathematical analysis revealed that, remarkably, the outer membrane was *at least* as stiff as the cell wall. Atomic force microscopy, a cell bending assay, and another osmotic shock assay yielded similar results. It was expected that the anionic lipid-A moiety of lipopolysaccharide (Fig. 1.1c) would be the primary load bearing species within the outer membrane because it can form intermolecular bonds in the presence of divalent cations. While this hypothesis was correct, the protein and sugar species within the outer membrane also contributed greatly to outer membrane stiffness. Finally, the Tol-Pal complex, which binds both the outer membrane and cell wall, was found to be an essential mechanical link between the two structures.

The stiffness of the outer membrane raises the obvious possibility that, like the cell wall, this structure is critical for prevention of osmotic lysis of the cell. Interestingly, it was found that during steady-state growth in chemostatic conditions, the outer membrane was under no load, even though the cell wall is highly stretched (Rojas et al. 2018). This was found by digesting the cell wall, measuring the surface area of the remaining outer membrane, and comparing this area to the surface area of cell before cell wall digestion; the areas were precisely equal. However, during osmotic fluctuations, the outer membrane was mechanically engaged and strongly protected the cells from lysis. Furthermore, outer membrane stiffness was important for L-form proliferation. L-forms are wall-less bacteria that proliferate in the presence of β-lactam antibiotics as long as the medium osmolarity is high (Lederberg and Clair 1958), and they are thought to be important to the pathology of several bacteria such as those that cause urinary tract infections (Errington et al. 2016). As hypothesized, L-form proliferation was drastically inhibited upon chemical or genetic perturbation of outer membrane stiffness.

1.8 Conclusion and Outlook

Like the mechanics of non-living material hundreds of years ago, within the last 10 years the field of bacterial mechanics began with simple yet important questions: how do bacterial cells deform when you bend, poke, squeeze and deflate them? The measurements that have addressed these questions clearly point to the fact that "bacterial materials" are mechanically rich: they include at least elastic, nonlinear elastic, viscoelastic, and plastic materials. We will surely look back on these seminal measurements just as D'arcy Thompson fondly remembered the scientists who made fundamental mechanical measurements of non-living material (Thompson 1992).

In one sense, bacteria are ideal systems with which to study the mechanics of living material because the many molecular tools available allow us to make very fine-scale perturbations to the chemical composition and architecture of the materials that constitute the cells. Additionally, bacteria are incredibly diverse in terms of their subcellular material. While *E. coli* has been used as a model system for most of the mechanical studies described above, we stand to find ever more novel materials by expanding our scope to other bacteria; just as each bacterial species has a metabolic ecological niche, so does it have a mechanical niche for which its mechanical properties are highly adapted. A good example is *Myxococcus xanthus*, which uses a unique gliding mechanism of motility to assemble into multicellular communities (Zhang et al. 2012). It is apparent from single-cell time lapse micrographs that *M. xanthus* cells are easily deformable and a theoretical analysis suggests that the flexibility of the cells is critical for their multicellular organization (Harvey et al. 2011). There are surely myriad other examples than this and the ones reviewed above where mechanical properties are adapted specifically for specialized physiological processes. Finally, even within the best-studied systems, many materials are waiting to be probed mechanically: teichoic acids, capsule, and the S-layer, for example.

From a different perspective, bacteria are the most challenging systems with which to study mechanics of living material because their size often inhibits our ability to make precise measurements of their mechanical properties, especially *in vivo*. But this is then a call for highly innovative developments in experimental technology to enable the measurement of mechanical properties as precisely as we can tune them. This will require continual collaboration between microbiologists and experimental soft condensed matter physicists.

References

Amir A, Babaeipour F, McIntosh DB, Nelson DR, Jun S (2014) Bending forces plastically deform growing bacterial cell walls. Proc Natl Acad Sci 111(16):5778–5783

Auer GK, Lee TK, Rajendram M, Cesar S, Miguel A, Huang KC, Weibel DB (2016) Mechanical genomics identifies diverse modulators of bacterial cell stiffness. Cell Syst 2(6):402–411

Benham CJ, Mielke SP (2005) DNA mechanics. Annu Rev Biomed Eng 7:21–53

Berry J, Rajaure M, Pang T, Young R (2012) The spanin complex is essential for lambda lysis. J Bacteriol 194(20):5667–5674

Billaudeau C, Yao Z, Cornilleau C, Carballido-López R, Chastanet A (2019) MreB forms subdiffraction nanofilaments during active growth in Bacillus subtilis. MBio 10(1):e01879–e01818

Cabeen MT, Charbon G, Vollmer W, Born P, Ausmees N, Weibel DB, Jacobs-Wagner C (2009) Bacterial cell curvature through mechanical control of cell growth. EMBO J 28(9):1208–1219

Chen Y-Y, Wu C-C, Hsu J-L, Peng H-L, Chang H-Y, Yew T-R (2009) Surface rigidity change of Escherichia coli after filamentous bacteriophage infection. Langmuir 25(8):4607–4614

Cho H, Uehara T, Bernhardt TG (2014) Beta-lactam antibiotics induce a lethal malfunctioning of the bacterial cell wall synthesis machinery. Cell 159(6):1300–1311

Deng Y, Sun M, Shaevitz JW (2011) Direct measurement of cell wall stress stiffening and turgor pressure in live bacterial cells. Phys Rev Lett 107(15):158101

Domínguez-Escobar J, Chastanet A, Crevenna AH, Fromion V, Wedlich-Söldner R, Carballido-López R (2011) Processive movement of MreB-associated cell wall biosynthetic complexes in bacteria. Science 333(6039):225–228

Eaton P, Fernandes JC, Pereira E, Pintado ME, Malcata FX (2008) Atomic force microscopy study of the antibacterial effects of chitosans on Escherichia coli and Staphylococcus aureus. Ultramicroscopy 108(10):1128–1134

Errington J, Mickiewicz K, Kawai Y, Wu LJ (2016) L-form bacteria, chronic diseases and the origins of life. Philos Trans R Soc B Biol Sci 371(1707):20150494

Francius G, Domenech O, Mingeot-Leclercq MP, Dufrêne YF (2008) Direct observation of Staphylococcus aureus cell wall digestion by lysostaphin. J Bacteriol 190(24):7904–7909

Gaboriaud F, Parcha BS, Gee ML, Holden JA, Strugnell RA (2008) Spatially resolved force spectroscopy of bacterial surfaces using force-volume imaging. Colloids Surf B: Biointerfaces 62(2):206–213

Galilei G (1914) Dialogues concerning two new sciences. Dover, New York

Gan L, Chen S, Jensen GJ (2008) Molecular organization of gram-negative peptidoglycan. Proc Natl Acad Sci 105(48):18953–18957

Garner EC, Bernard R, Wang W, Zhuang X, Rudner DZ, Mitchison T (2011) Coupled, circumferential motions of the cell wall synthesis machinery and MreB filaments in B. subtilis. Science 333(6039):222–225

Gitai Z, Dye NA, Reisenauer A, Wachi M, Shapiro L (2005) MreB actin-mediated segregation of a specific region of a bacterial chromosome. Cell 120(3):329–341

Harvey CW, Morcos F, Sweet CR, Kaiser D, Chatterjee S, Liu X, Chen DZ, Alber M (2011) Study of elastic collisions of Myxococcus xanthus in swarms. Phys Biol 8(2):026016

Herrmann M, Schneck E, Gutsmann T, Brandenburg K, Tanaka M (2015) Bacterial lipopolysaccharides form physically cross-linked, two-dimensional gels in the presence of divalent cations. Soft Matter 11(30):6037–6044

Hoffmann T, Boiangiu C, Moses S, Bremer E (2008) Responses of Bacillus subtilis to hypotonic challenges: physiological contributions of mechanosensitive channels to cellular survival. Appl Environ Microbiol 74(8):2454–2460

Janmey PA (1991) Mechanical properties of cytoskeletal polymers. Curr Opin Cell Biol 3(1):4–11

Lederberg J, Clair JS (1958) Protoplasts and L-type growth of Escherichia coli. J Bacteriol 75(2):143

Love AEH (2013) A treatise on the mathematical theory of elasticity. Cambridge university press, Cambridge

Madigan MT, Martinko JM, Parker J (1997) Brock biology of microorganisms, vol 11. Prentice hall, Upper Saddle River

Männik J, Driessen R, Galajda P, Keymer JE, Dekker C (2009) Bacterial growth and motility in sub-micron constrictions. Proc Natl Acad Sci 106(35):14861–14866

Margolin W (2009) Sculpting the bacterial cell. Curr Biol 19(17):R812–R822

Martinac B (2004) Mechanosensitive ion channels: molecules of mechanotransduction. J Cell Sci 117(12):2449–2460

Metzler R, Jeon JH, Cherstvy AG, Barkai E (2014) Anomalous diffusion models and their properties: non-stationarity, non-ergodicity, and ageing at the centenary of single particle tracking. Phys Chem Chem Phys 16(44):24128–24164

Milo R, Phillips R (2015) Cell biology by the numbers. Garland Science, New York

Mizuno T (1979) A novel peptidoglycan-associated lipoprotein found in the cell envelope of Pseudomonas aeruginosa and Escherichia coli. J Biochem 86(4):991–1000

Osawa M, Anderson DE, Erickson HP (2008) Reconstitution of contractile FtsZ rings in liposomes. Science 320(5877):792–794

Pelletier J, Halvorsen K, Ha B-Y, Paparcone R, Sandler SJ, Woldringh CL, Wong WP, Jun S (2012) Physical manipulation of the Escherichia coli chromosome reveals its soft nature. Proc Natl Acad Sci 109(40):E2649–E2656

Perry CC, Weatherly M, Beale T, Randriamahefa A (2009) Atomic force microscopy study of the antimicrobial activity of aqueous garlic versus ampicillin against *Escheri- chia coli* and *Staphylococcus aureus*. J Sci Food Agric 89:958–964

Parry BR, Surovtsev IV, Cabeen MT, O'Hern CS, Dufresne ER, Jacobs-Wagner C (2014) The bacterial cytoplasm has glass-like properties and is fluidized by metabolic activity. Cell 156(1–2):183–194

Persat A, Nadell CD, Kim MK, Ingremeau F, Siryaporn A, Drescher K, Wingreen NS, Bassler BL, Gitai Z, Stone HA (2015) The mechanical world of bacteria. Cell 161(5):988–997

Rassam P, Copeland NA, Birkholz O, Tóth C, Chavent M, Duncan AL, Cross SJ et al (2015) Supramolecular assemblies underpin turnover of outer membrane proteins in bacteria. Nature 523(7560):333

Rojas E, Theriot JA, Huang KC (2014) Response of Escherichia coli growth rate to osmotic shock. Proc Natl Acad Sci 111(21):7807–7812

Rojas ER, Huang KC, Theriot JA (2017) Homeostatic cell growth is accomplished mechanically through membrane tension inhibition of cell-wall synthesis. Cell Syst 5(6):578–590

Rojas ER, Billings G, Odermatt PD, Auer GK, Zhu L, Miguel A, Chang F, Weibel DB, Theriot JA, Huang KC (2018) The outer membrane is an essential load-bearing element in gram-negative bacteria. Nature 559(7715):617

Saxton MJ (1994) Anomalous diffusion due to obstacles: a Monte Carlo study. Biophys J 66(2):394–401

Shi H, Bratton BP, Gitai Z, Huang KC (2018) How to build a bacterial cell: MreB as the foreman of E. coli construction. Cell 172(6):1294–1305

Shih Y-L, Rothfield L (2006) The bacterial cytoskeleton. Microbiol Mol Biol Rev 70(3):729–754

Sonntag I, Schwarz H, Hirota Y, Henning U (1978) Cell envelope and shape of Escherichia coli: multiple mutants missing the outer membrane lipoprotein and other major outer membrane proteins. J Bacteriol 136(1):280–285

Sun X, Weinlandt WD, Patel H, Wu M, Hernandez CJ (2014a) A microfluidic platform for profiling biomechanical properties of bacteria. Lab Chip 14(14):2491–2498

Sun Y, Sun T-L, Huang HW (2014b) Physical properties of Escherichia coli spheroplast membranes. Biophys J 107(9):2082–2090

Takeuchi S, DiLuzio WR, Weibel DB, Whitesides GM (2005) Controlling the shape of filamentous cells of Escherichia coli. Nano Lett 5(9):1819–1823

Teeffelen V, Sven SW, Furchtgott L, Huang KC, Wingreen NS, Shaevitz JW, Gitai Z (2011) The bacterial actin MreB rotates, and rotation depends on cell-wall assembly. Proc Natl Acad Sci 108(38):15822–15827

Thompson D'AW (1992) Chapter: introductory. In: Bonner JT (ed) On growth and form. Cambridge University Press, Cambridge, pp 1–14. https://doi.org/10.1017/CBO9781107325852.005

Todar K (2006) Todar's online textbook of bacteriology. University of Wisconsin-Madison Department of Bacteriology, Madison

Tuson HH, Auer GK, Renner LD, Hasebe M, Tropini C, Salick M, Crone WC, Gopinathan A, Huang KC, Weibel DB (2012) Measuring the stiffness of bacterial cells from growth rates in hydrogels of tunable elasticity. Mol Microbiol 84(5):874–891

Vadillo-Rodriguez V, Dutcher JR (2009) Dynamic viscoelastic behavior of individual gram-negative bacterial cells. Soft Matter 5(24):5012–5019

Verwer RW, Nanninga N, Keck W, Schwarz U (1978) Arrangement of glycan chains in the sacculus of Escherichia coli. J Bacteriol 136(2):723–729

Wang S, Arellano-Santoyo H, Combs PA, Shaevitz JW (2010) Actin-like cytoskeleton filaments contribute to cell mechanics in bacteria. Proc Natl Acad Sci 107(20):9182–9185

Wang S, Furchtgott L, Huang KC, Shaevitz JW (2012) Helical insertion of peptidoglycan produces chiral ordering of the bacterial cell wall. Proc Natl Acad Sci 109(10):E595–E604

Weber SC, Spakowitz AJ, Theriot JA (2010) Bacterial chromosomal loci move subdiffusively through a viscoelastic cytoplasm. Phys Rev Lett 104(23):238102

Weber SC, Spakowitz AJ, Theriot JA (2012) Nonthermal ATP-dependent fluctuations contribute to the in vivo motion of chromosomal loci. Proc Natl Acad Sci 109(19):7338–7343

Whatmore AM, Reed RH (1990) Determination of turgor pressure in Bacillus subtilis: a possible role for K+ in turgor regulation. Microbiology 136(12):2521–2526

Yao X, Jericho M, Pink D, Beveridge T (1999) Thickness and elasticity of gram-negative murein sacculi measured by atomic force microscopy. J Bacteriol 181(22):6865–6875

Yao Z, Kahne D, Kishony R (2012) Distinct single-cell morphological dynamics under beta-lactam antibiotics. Mol Cell 48(5):705–712

Young KD (2006) The selective value of bacterial shape. Microbiol Mol Biol Rev 70(3):660–703

Zhang Y, Ducret A, Shaevitz J, Mignot T (2012) From individual cell motility to collective behaviors: insights from a prokaryote, Myxococcus xanthus. FEMS Microbiol Rev 36(1):149–164

Complex Diffusion in Bacteria

2

Christopher H. Bohrer and Jie Xiao

Abstract

Diffusion within bacteria is often thought of as a "simple" random process by which molecules collide and interact with each other. New research however shows that this is far from the truth. Here we shed light on the complexity and importance of diffusion in bacteria, illustrating the similarities and differences of diffusive behaviors of molecules within different compartments of bacterial cells. We first describe common methodologies used to probe diffusion and the associated models and analyses. We then discuss distinct diffusive behaviors of molecules within different bacterial cellular compartments, highlighting the influence of metabolism, size, crowding, charge, binding, and more. We also explicitly discuss where further research and a united understanding of what dictates diffusive behaviors across the different compartments of the cell are required, pointing out new research avenues to pursue.

Keywords

Diffusion · Bacteria · Crowding · Viscoelastic · Glass · Mean squared displacement · Confinement · Single particle tracking · Anomalous Diffusion · Metabolism · Charge · Velocity autocorrelation function · Cell envelope · Outer membrane · Inner membrane · Periplasm.

2.1 Introduction

Diffusion is the consequence of a particle randomly colliding with the other particles in its surroundings. The diffusion speed, directionality, and trajectory of a particle contain rich information about how the particle interacts with its surroundings, offering an invaluable window to examine molecular interactions in live cells.

In bacterial cells, random diffusion is sufficient to allow molecules to reach their desired target sites efficiently because of the small cellular volumes (on the order of $\sim 10^{-15}$ L). For example, a protein molecule with a diffusion coefficient (D) of 1 $\mu m^2/s$ can sample the entire cy-

C. H. Bohrer (✉)
Department of Biophysics and Biophysical Chemistry, Johns Hopkins School of Medicine, Baltimore, MD, USA

Department of Biophysics, Johns Hopkins University, Baltimore, MD, USA

J. Xiao (✉)
Department of Biophysics and Biophysical Chemistry, Johns Hopkins School of Medicine, Baltimore, MD, USA

G. Duménil, S. van Teeffelen (eds.), *Physical Microbiology*, Advances in Experimental Medicine and Biology 1267, https://doi.org/10.1007/978-3-030-46886-6_2

toplasm in ~100 ms. In contrast, eukaryotic cells have volumes that are three orders of magnitude larger and simple diffusion is no longer sufficient. Directional motor proteins such as kinesin and myosin are hence required to deliver molecules to different cellular addresses. Since diffusion is a major mechanism behind how molecules find their "place" in bacterial cells, it is vital to understand the characteristics of diffusion in the different compartments of bacterial cells. In this review, we present a critical summary and evaluation of commonly used methods and analyses to probe complex diffusive behaviors observed in bacterial cells, with a major focus on single-molecule tracking (SMT). We then elucidate various diffusion dynamics with specific examples in the bacterial cytoplasm, nucleoid, and membranes.

2.2 Common Methods to Characterize Diffusion in Bacterial Cells

Commonly used methods to characterize molecules' diffusion in live cells are fluorescence recovery after photobleaching (FRAP), fluorescence correlation spectroscopy (FCS) and single molecule tracking (SMT). Here we briefly describe FRAP and FCS, and then discuss SMT in depth, due to its wide use and vast potential in probing diffusion in bacterial cells.

2.2.1 Fluorescence Recovery After Photobleaching (FRAP)

In FRAP, a focused laser is used to photobleach a small region of a cell containing fluorescently labeled molecules, and subsequently the fluorescence recovery of the region is monitored (Fig. 2.1a). Depending on the diffusion speed, diffusive mode, and the geometry of the selected region and cell, the FRAP curve can be fit to specific models to extract diffusion coefficients and kinetic rates associated with particular molecular interactions (Rayan et al. 2010). As an ensemble method, FRAP is relatively simple to implement; the apparent FRAP rate serves as a straightforward measure to allow comparison of the same system under different conditions even in the absence of a specific model. Therefore, FRAP has been widely used in diffusion studies. However, one should be aware of the limitation of using FRAP to extract quantitative parameters such as diffusion coefficients and kinetics. These values are ensemble-averaged means pertinent to and only valid in specific models. Finally, FRAP is unable to depict heterogeneous diffusion properties of molecules limiting its use in terms of determining diffusive behavior (Elowitz et al. 1999) – except for "relatively" specific situations (Lorén et al. 2009).

2.2.2 Fluorescence Correlation Spectroscopy (FCS)

FCS is a methodology that monitors the fluctuations of fluorescence within a small region to determine many different parameters, including the diffusion coefficients. The mechanism behind the technique is that the fluctuations in fluorescence are due to molecules moving into and out of the illuminated region, allowing the dynamics of the system to be quantified (Fig. 2.1b). FCS often includes calculating the autocorrelation function and then fitting it to specific models to extract the desired parameters. When compared to FRAP, the theoretical interpretations of the data often have the same limitations in regards to quantifying the diffusive behavior (Elson 2011).

2.2.3 Single-Molecule Tracking (SMT)

SMT is a method where one follows the movement of individual molecules (or particles in some cases) labeled with fluorophores to determine how the molecule interacts with its surroundings and potential targets (Fig. 2.1c). Because of the single-molecule nature of the method, SMT allows one to identify not only the molecule's diffusive mode and diffusion coefficient, but also the

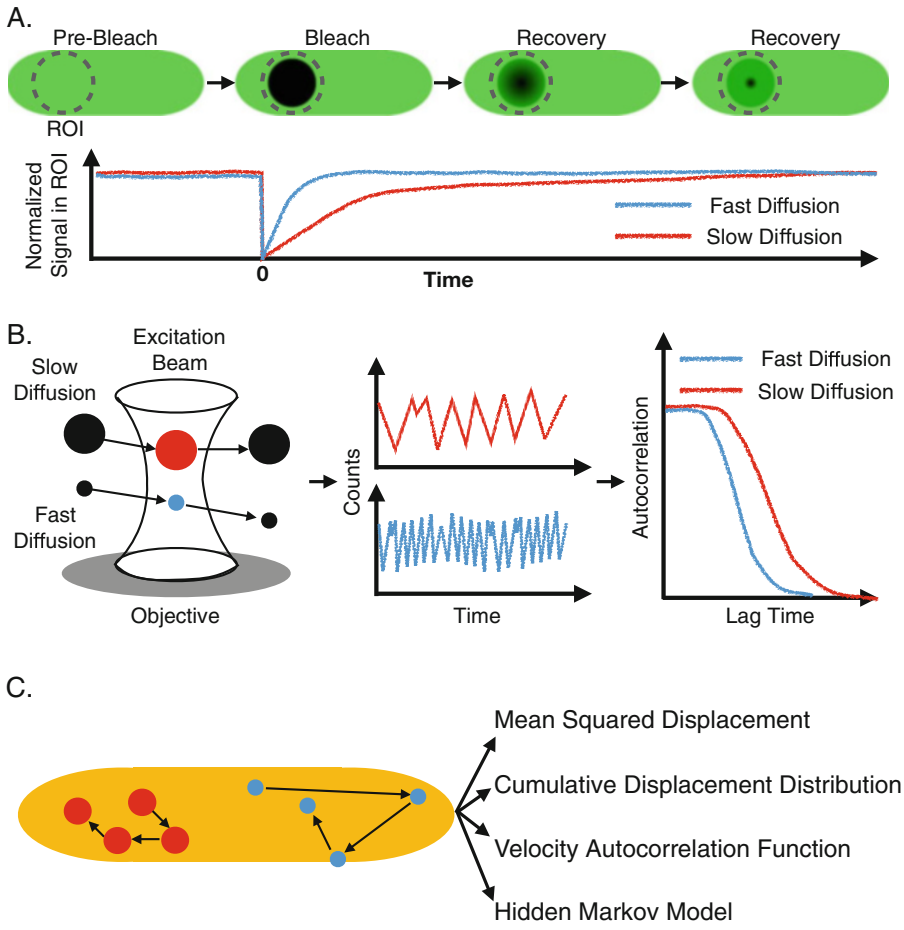

Fig. 2.1 Three most common methodologies used to quantify diffusion. (**a**) Fluorescence Recovery after Photobleaching (FRAP): the recovery of fluorescence signal (shown as green color) in a region of interest (ROI, shown as gray dashed circle) is monitored after bleaching (bleached region shown as black circle). The "rate" at which the signal recovers is related to the mobility of the particle of interest, shown as red and blue curves. (**b**) Fluorescence Correlation Spectroscopy (FCS): fluctuations within a small diffraction-limited excitation volume are monitored throughout time, illustrated as counts vs time. The fluctuations of slower diffusing particles are shown in red and the higher frequency fluctuations of the faster diffusing particles are shown in blue. The autocorrelation functions of each system can be calculated, providing information about the diffusion of the particles. (**c**) Single Molecule Tracking (SMT): The location of individual molecules or particles within a cell are monitored through time (arrows indicate direction of time). The displacements along the trajectories can then be analyzed with different methodologies, which are further illustrated in Fig. 2.2 and explained in detail in text

population heterogeneity and in vivo kinetics of switching between diffusive states, which are often indicative of specific molecular interactions.

2.3 Practical Concerns of SMT

A successful SMT experiment requires a few critical parameters be within an optimal range. These parameters are the single molecule signal to noise ratio (SNR), the length (L) and number (N) of SMT trajectories. These parameters have large influences on the theoretical limitations of quantifying diffusion coefficients and diffusive behaviors with different forms of analyses, discussed throughout (Michalet and Berglund 2012).

2.3.1 Signal to Noise Ratio (SNR)

The first parameter, SNR, is often defined as the ratio between the numbers of photons emitted by the fluorophore and the cell's autofluorescence background. SNR dictates how well one can determine the position of a molecule at each time point, i.e., the precision at which the molecule can be localized. This concept is the same as the localization precision from single-molecule localization superresolution microscopy (SMLM) (Betzig et al. 2006; Rust et al. 2006; Hess et al. 2006). In live bacterial cells, the SNR for commonly used fluorescent proteins and organic dyes are sufficient for a localization precision of ~10–30 nm (Betzig et al. 2006; Rust et al. 2006; Hess et al. 2006). When the SNR is low due to a short camera exposure time or a high cellular autofluorescence background, individual displacements along the SMT trajectory cannot be determined accurately, leading to large uncertainties in determining the corresponding D (Das et al. 2009; Bohrer et al. 2017; Persson et al. 2013; Slator and Burroughs 2018; Matsuda et al. 2018). As such, metrics used to quantify the diffusive dynamics of molecules (Weber et al. 2010a, 2012a; He et al. 2008; Condamin et al. 2008; Thapa et al. 2018) are often distorted, making the interpretation of the data difficult and complex (Weber et al. 2012a). For instance, when the SNR is low, the mean squared displacement (MSD, discussed in detail below) can show sub-diffusive behaviors at short timescales, even when the diffusion is purely Brownian (Martin et al. 2002). Additionally, the quantified diffusive states and corresponding kinetic switching rates can be ill-defined, due to the low confidence in defining D values along a trajectory (Bohrer et al. 2017; Persson et al. 2013; Michalet and Berglund 2012).

2.3.2 Trajectory Length (L)

The second parameter, L, describes how long in time a molecule can be tracked. In practice, L is limited by the time a fluorophore remains fluorescent before it photobleaches – as long as the molecule does not diffuse out of focus. Due to the stochastic nature of photobleaching (photobleaching time is usually exponentially distributed (Lee et al. 2012; Yeow et al. 2006)), only a small portion of all SMT trajectories are relatively long. As such, a large number of total SMT trajectories are often required to obtain a sufficient number of long SMT trajectories.

Long SMT trajectories are vital to determine if the diffusive behavior of molecules is ergodic, if there is dynamic heterogeneity along single trajectories, and if the molecule transitions between different diffusive states. Here ergodicity refers to whether the average behavior across all molecules equals the behavior of individual molecules over long periods of time, which can be used as a metric to discriminate between different models of diffusion (Deng and Barkai 2009; Parry et al. 2014); dynamic heterogeneity means the diffusion coefficient of an individual molecule varies through time or space (Lampo et al. 2017a); transition kinetics refer to the rates of a molecule switching from one to the other diffusive state characterized by distinct diffusion coefficients.

How long is long enough for SMT? In ensemble kinetic measurements of chemical reactions, a "rule of thumb" is to monitor the reaction for at least five reaction halftimes (so that the reaction has proceeded >95%) in order to determine the rate constant accurately. The equivalent should be applied to SMT as well. For example, for a transition rate of 1 s^{-1}, the minimal average trajectory length should be at least ~5 s long to capture a sufficient number of transition events. In practice, SMT tracking trajectories should be even longer in order to observe the two different states before and after the transition with confidence. In theory, one can also obtain a large number of shorter SMT trajectories (>10,000) and analyze the data using statistical methods to extract the kinetic information (Bohrer et al. 2017; Das et al. 2009; Persson et al. 2013). These statistical methods often require additional assumptions about the kinetic rates and steady states, and hence need to be carefully evaluated.

2.3.3 How to Achieve High SNR and Obtain Long Trajectories

To achieve a high SNR, the key is to use bright fluorophores. To obtain long trajectories, the key is to use photostable fluorophores – as it is often important to use a high frame rates, which often requires high laser intensities. Bright, red-colored organic fluorophores such as the newly developed Janelia Fluor Dyes (JFD) (Lukinavičius et al. 2013) (now commercially available) in conjunction with Halo or SNAP tag (Los et al. 2008; Cole 2013) satisfy both requirements. The unique, rigid fluorophore structure of JF646 ensures high fluorescence quantum yield and low photobleaching quantum yield, and the lengthened conjugation plane allows red-shifted excitation at 647 nm, which avoids the autofluorescence background that usually comes from flavin proteins (Xiao 2009). Halo- or SNAP-ligand modified JF646 is membrane permeable (even for Gram negative bacteria such as *E. coli*) and can be directly added into cell's growth medium and subsequently washed for live cell labeling.

In the event that the Halo/SNAP-JF646 labeling system or its alike is not feasible (for example, the fusion protein is not functional or there is a high level of nonspecific dye binding), other strategies can be employed. Fluorescent proteins (FPs) usually tolerate fusions well and do not require the addition of exogenous fluorophore, simplifying sample preparation. In our experience, the red-colored fluorescent protein TagRFP-t (Beilharz et al. 2015), even though not comparable to JF646, is sufficiently bright and is the most photostable when compared to the other FPs we tested (EGFP, EYFP, mCherry, mNeonGreen, mEos3.2, and PAmCherry) (Zhang et al. 1996, 2012; Ormö et al. 1996; Shaner et al. 2004, 2013; Subach et al. 2009). If other less bright or photostable fluorophores are the only option, one could try to [1] minimize cellular autofluorescence background by avoiding the green-colored fluorophores and by growing cells in defined (such as M9 or EZRDM) instead of complex (such as LB) media; and [2] conduct multiple rounds of SMT experiments in which the dark interval between adjacent imaging frames is systematically varied so that trajectories of different dark intervals can be computationally stitched together to cover longer time scales (Gebhardt et al. 2013). Lastly, recent advances in microscopy methodologies, such as MINFLUX, show promise for expanding the limits of SMT – as the low number of photons needed to reach a comparable resolution allows one to obtain much longer trajectories (Balzarotti et al. 2017).

2.3.4 Trajectory Number (N)

A final requirement for a successful SMT experiment is to obtain a sufficient number of trajectories. As with any single-molecule experiment, diffusive trajectories of individual molecules are inherently stochastic and therefore a large sample size is needed to quantify and account for these fluctuations. Generally speaking, to obtain a single mean diffusion coefficient (D) a hundred trajectories with an average length of at least five to ten tracking frames may be sufficient. If there are multiple populations with different Ds, a few hundred to a thousand trajectories are necessary to separate the different populations. To extract kinetic rates, greater than 10,000 trajectories may be needed (see below for more details).

The above requirement demands collecting as many trajectories from as many single cells as possible. However, SMT also requires a low labeling density in single cells so that individual molecules can be spatially isolated. A low labeling density can be achieved by carefully tuning the fusion protein's expression level using repressible promoters and/or low copy plasmids, so that on average in one bacterial cell there is only one or two fluorescent molecules. Such a low expression level leads to a low imaging throughput since the majority of cells would not have any expressed fluorescent molecules due to the Poissonian distribution of lowly expressed molecules in a population of cells. Furthermore, the expression level is often difficult to control experimentally due to the leakiness of most prokaryotic promoters.

One way to bypass this experimental difficulty is to use the Halo/SNAP-JF dye labeling system. The fusion protein can be expressed normally in cells, but the concentration of the dye can be tuned at will so that only a small percentage of fusion protein molecules are labeled to allow SMT. This strategy, however, still does not circumvent the issue of low data throughput, since one can only obtain on average one or two trajectories per cell.

The ideal strategy is to use a photoactivatable fluorophore that is not fluorescent unless activated (Stepanenko et al. 2011; Ando et al. 2002; Gurskaya et al. 2006; Subach et al. 2009). A fusion protein could thus be 100% labeled with a photoactivatable fluorophore but remain nonfluorescent; only upon a low dose of activation light one or a few molecules are stochastically turned on to be tracked. After they are photobleached, new molecules are turned on, allowing continuous SMT of many molecules in the same cells. Commonly used photoactivatable fluorophores include mEos3.2 (Zhang et al. 2012) and PAmCherry (Subach et al. 2009), but none of their photochemistry properties are as good as the stable JF646. Photoactivable JF dyes have been developed (Grimm et al. 2016), but their low activation rates require further optimization for SMT. Furthermore, continuous photoactivation using high energy light (405 or 488 nm) can cause photo-damage of cells, limiting the number of trajectories one can continuously collect from individual cells. Finally, one technology which could help in the accumulation of trajectories from a large number of cells is the mother-machine – though this technology has not yet been thoroughly utilized by the SMT community (Wang et al. 2010; Camsund et al. 2020).

2.4 Data Analysis and Interpretation of SMT

SMT trajectories can be analyzed multiple ways depending on what quantitative information one wishes to extract. Commonly used analyses include mean squared displacement (MSD), cumulative displacement distribution function (CDF), velocity autocorrelation function (VAF), and Hidden Markov Model (HMM). Below we describe each analysis and what information can be determined independently and collectively from these analyses.

2.4.1 Mean Squared Displacement (MSD)

The mean squared displacement (MSD) is the most commonly used metric to estimate the apparent diffusion coefficient D, which helps quantify the diffusion mode of single molecules (also see the section: Commonly encountered diffusion mechanisms below). The ensemble-averaged MSD is calculated by taking the squared distance a molecule travels for a certain time and then averaging over all molecules (Fig. 2.2a):

$$MSD(t) = \frac{1}{n}\sum_{i=1}^{n}(x_i(t) - x_i(0))^2 \qquad (2.1)$$

where $x(t)$ is the coordinate of the molecule at time t and n is the number of trajectories. Note that in all experimentally measured MSD curves, the square root of the y-axis intercept, or the apparent MSD value when $t = 0$, indicates the uncertainty in determining a molecule's position, hence serving as a useful indicator to estimate experimental localization precision. Because different SMT trajectories have different lengths, to ensure that each molecule contributes equally to the final MSD curve for each t, a common practice is to select trajectories that have a minimal length and truncate longer trajectories to the minimal length.

For individual trajectories, the time averaged MSD of each trajectory is computed using the following equation:

$$MSD_\tau(t) = \frac{1}{T-t}\sum_{\tau=0}^{T-t}(x(t+\tau)-x(\tau))^2, \quad (2.2)$$

where T is the total time of the individual trajectory and τ ranges over all possible values up to $T - t$ based on the time interval of the SMT experiment. If a system is ergodic, the $MSD_\tau(t) = MSD(t)$ and it can be used to discriminate

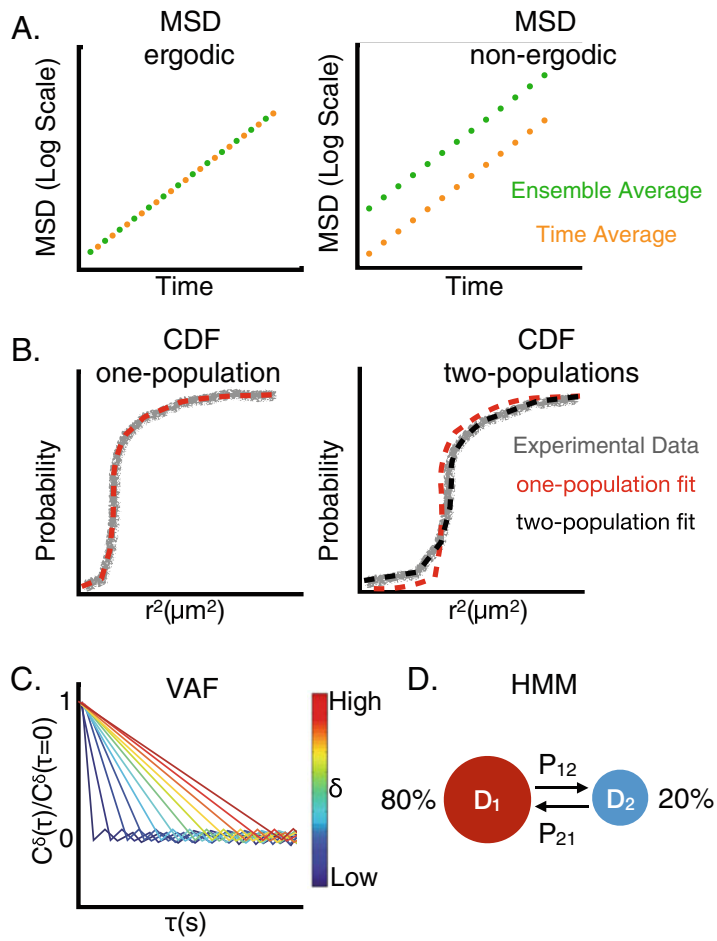

Fig. 2.2 Data analyses of SMT. (**a**) An example of an MSD for an ergodic system and for a non-ergodic system. (**b**) An example a CDF fit for a one state system and a two state system. (**c**) An example VAF for Brownian diffusion. (**d**) A two state Markov model with its corresponding diffusion coefficients, transition probabilities and percentages of each state

between different modes of diffusion, Fig. 2.2a. Note that a combination of the two can be used to examine ergodicity if trajectories are not of sufficient length (Parry et al. 2014):

$$MSD_{\tau}^{avg}(t) = \frac{1}{n}\sum_{i=1}^{n}\frac{1}{T-t}\sum_{\tau=0}^{T-t}(x_i(t+\tau)-x_i(\tau))^2. \tag{2.3}$$

2.4.2 Cumulative Displacement Distribution Function (CDF)

As mentioned above, dynamic heterogeneity means that D values of individual molecules vary through time and/or space. Dynamic heterogeneity can exist simply because the molecule of interest has multiple diffusive states depending on its interactions with other molecules. For instance, in *E. coli*, RNA polymerase (RNAP) molecules exhibit a D of $\sim 1\,\mu m^2/s$ in the cytoplasm, $\sim 0.4\,\mu m^2/s$ in the nucleoid, and $\sim 0.1\,\mu m^2/s$ when bound to chromosomal DNAs (Stracy et al. (2015) and see Section: Diffusion of DNA binding proteins). These different D values indicate different modes of DNA interactions of RNAP, with the slowest one most likely bound to DNA, the fastest one freely diffusing in the cytoplasm, and the intermediate one interacting with the nucleoid nonspecifically. Dynamic heterogeneity can also result from the molecule experiencing different local environments within the cell (Lampo et al. 2017b). When a "continuum" of heterogeneity is observed, the varying diffusive properties

could be due to the local environment changing with time or the molecule moving to a different environment.

One useful way to examine whether there are multiple diffusive populations is to inspect the single-step displacement distribution. For a single population with 1d-Brownian motion (random collisions of the molecule with other molecules within the medium), the displacement distribution for a molecule to move a distance x away from the origin in the time interval t follows a normal distribution

$$p(x,t) = \frac{e^{\frac{-x^2}{4Dt}}}{(4\pi Dt)^{\frac{1}{2}}}, \tag{2.4}$$

with a characteristic diffusion coefficient D, that is dependent upon the size of the molecule, the temperature and the viscosity of the medium. The corresponding cumulative distribution function (CDF), can also be fit to a single exponential function to extract D. When the displacement distribution cannot be described adequately with a single population, the linear combination of multiple terms with different D values and respective population fractions can be used (Vrljic et al. 2007) (Fig. 2.2b). For 2d-diffusion, the CDF for two populations of diffusing molecules can be fit with the following equation:

$$CDF(r^2,t) = 1-\alpha\times e^{\frac{-r^2}{4D_1t+4\sigma^2}} - (1-\alpha)\times e^{\frac{-r^2}{4D_2t+4\sigma^2}} \tag{2.5}$$

where D_1 and D_2 are the diffusion coefficients of the two diffusion populations, α accounts for the fraction of each population, r is the radial distance and σ is the localization precision of the experiment. Once different populations with characteristic diffusion coefficients are identified, one can analyze each population's behavior as described below.

2.4.3 Velocity Autocorrelation Function (VAF)

If one wishes to characterize the diffusive behavior and dissect the mechanisms behind it, the velocity autocorrelation function (VAF) is an important tool (Weber et al. 2012a). The function identifies the correlation in the velocity of a molecule at different timescales and allows one to distinguish between different diffusive processes and is particularly useful for sub-diffusion (Weber et al. 2012a). The function is defined as the following (Fig. 2.2c):

$$C_v^{\delta}(\tau) = \langle \vec{v}(t+\tau)\cdot\vec{v}(t)\rangle, \tag{2.6}$$

where

$$v(t) = \frac{1}{\delta}([\vec{R}(t+\delta) - \vec{R}(t)]. \tag{2.7}$$

Here $\vec{R}(t)$ is the position vector of the molecule at time t and $\langle \vec{v}(t+\tau)\cdot\vec{v}(t)\rangle$ is the mean dot product averaged over all trajectories. The values of δ and τ are varied across all possible time intervals of the trajectories. As we will describe more in detail below, specific characteristics of the VAF are indicative of different diffusion modes and when combined with other analyses, it is often possible to delineate the underlying diffusion mechanism.

2.4.4 Hidden Markov Model (HMM)

In some cases where there exist multiple "well defined" diffusive populations, it will be of interest to identify the transition kinetics between the different states of the molecule. The ability to monitor the change of a molecule's diffusive behavior in real time, which reflects its interactions with targets without perturbing the system is one of the most powerful benefits of SMT (Bohrer et al. 2017; Das et al. 2009; Persson et al. 2013). In order to extract the kinetic rates between different diffusive states, the individual states must have different diffusion coefficients and the displacement distributions need to be known (Das et al. 2009; Persson et al. 2013). One can then use likelihood and Bayesian approaches to quantify the transition kinetics of the system by fitting to a hidden Markov model (HMM, Fig. 2.2d), see Das et al. for further details (Das et al. 2009). Note: an alternative methodology,

analytical diffusion distribution analysis, was recently developed which can also extract kinetic parameters when the system of interest has two diffusive states with fast transition rates (Vink et al. 2020). Finally, the field has not yet determined a methodology for particles that exhibit non-Brownian diffusion – though methodologies are beginning to take the mechanisms responsible for non-Brownian motion into account (Bohrer et al. 2017; Slator and Burroughs 2018).

2.5 Commonly Encountered Diffusion Mechanisms

2.5.1 Brownian Motion

Brownian motion, in which a molecule randomly collides with the surrounding molecules (Fig. 2.3a), is the most common and the simplest diffusion mechanism. The MSD plot of a SMT experiment is a straight line, with the slope of the line providing the diffusion coefficient (Fig. 2.3b). The corresponding single-step displacement distribution's CDF can be well described by a single exponential function. Additionally, due to the fact that all displacements are independent of each other, the VAF decays to zero for all $\tau \geq \delta$ (Fig. 2.3c). Note, if the experiment has a low localization precision, the VAF will show a negative peak for $\tau = \delta$, which approaches zero as τ increases.

2.5.2 Anomalous Diffusion

Any type of diffusion process that does not result in a linear MSD is considered anomalous. There are two types of anomalous diffusion, sub-diffusion and super-diffusion. Most of the time, anomalous diffusion has an MSD that scales with time to an exponent, $MSD = 4Dt^{\alpha}$. (For sub-diffusion $0 < \alpha < 1$ and for super-diffusion $\alpha > 1$) Examples of the MSDs for both types of anomalous diffusion are shown in Fig. 2.3e,h,k,m,p.

Super-diffusion usually results from directional movement of molecules (Fig. 2.3d) and is rare in bacterial cells, as they do not have linear motor proteins such as kinesin or myosin. However, directional movement of cytoskeletal proteins such as MreB (Fu et al. 2018), cell wall remodeling enzymes PBP2 and PBP3 (Yang et al. 2017; Perez et al. 2019; Bisson-Filho et al. 2017) and segregating plasmid DNAs (Ringgaard et al. 2009; Hu et al. 2015) have been observed. The VAF of super-diffusion will show positive values across multiple τ values as the directionality of individual displacements is positively correlated (Fig. 2.3f) (Kim et al. 2006).

Sub-diffusion is commonly observed in bacterial cells and can result from a number of different mechanisms. A first step to differentiate different diffusion mechanism is to compare the exponent value of the MSD curve with what would be expected from the different diffusion models, as what was done previously on the diffusion of chromosomal DNA segments and mRNA molecules (Weber et al. 2010a). However, because different sub-diffusion processes can result in similar MSD curves, other metrics are normally needed to support specific models. Below we focus on a few models pertinent to diffusing molecules in bacterial cells.

2.5.2.1 Diffusion with Confinement (Sub-diffusion)

The most common mechanism behind sub-diffusion in bacterial cells is confinement, which results from diffusion in a finite space (Fig. 2.3g). With confinement, the space a molecule can explore is limited and the MSD reaches a plateau at long time scales (Fig. 2.3h), causing the MSD to scale with an exponent $\alpha < 1$. The value of the plateau can be used to extract the size of the confinement zone, which corresponds to the finite size of space where the molecule could freely diffuse (Kusumi et al. 1993). For 1d diffusion (along x) within a box of length L_x, the $MSD_x(t)$ follows:

$$MSD_x(t) = \frac{L_x^2}{6} - \frac{16L_x^2}{\pi^4} \sum_{n=1(odd)}^{\infty} \frac{1}{n^4} \times exp[-\frac{1}{2}(\frac{n\pi 2D_x}{L_x})^2 t] \quad (2.8)$$

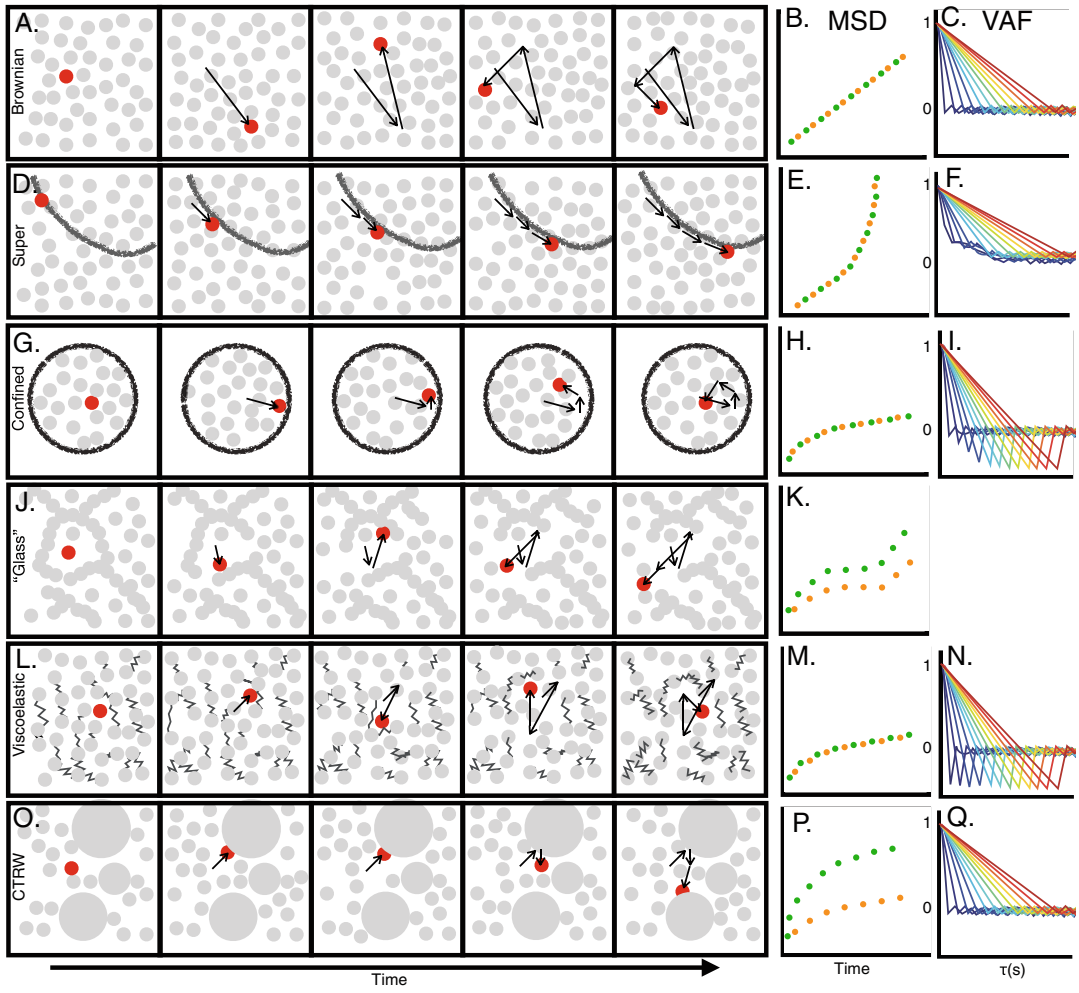

Fig. 2.3 Cartoons showing different modes of diffusion, with each row showing a different mode of diffusion through time (light gray circles illustrate the medium), the mean squared displacement (MSD, shown on a linear scale (except for K), green ensemble average, yellow time average), and the corresponding velocity autocorrelation function (VAF, color indicates δ as in Fig. 2.2). [Specifics] (**d**) Super Diffusion: dark gray line is track on which a particle travels in a directed manner (For example actin). (**g**) Confined: dark gray line indicates a barrier where the diffusion of a particle is restricted (For example the membrane). (**k**) MSD is shown on a log scale. (**l**) Viscoelastic: the springs between the particles of the medium represent the elastic property of the medium. (**o**) Continuous Time Random Walk (CTRW): the overlap between the particle of interest with a particle of the medium indicates a binding event. For all rows arrows show direction of time as well as previous locations

Here it can be seen that as $t \to \infty$ the MSD will asymptotically approach $\frac{L_x^2}{6}$, which defines the value of the plateau. If diffusion is Brownian, sub-diffusion caused by confinement will still appear Brownian at short time scales before the molecules can experience the barriers. Therefore, the single-step displacement distribution will still be approximately Gaussian. At long time scales, the displacement distribution or CDF will deviate from that expected from Brownian motion.

The characteristics of confinement can be quantified using VAF. Confinement results in an "anti-persistent" behavior, in which a molecule is reflected off of the barrier and returns to its previous position. The resulting VAF $C_v^{\delta}(\tau)$ shows a small negative peak or a zero at small

δ and τ (due to the molecule not having time to experience the barriers) and then develops into a large negative peak as δ and τ increase, Fig. 2.3i. This resulting behavior within the VAF is due to the barrier reflecting the molecule, leading to the negative velocity relative to the previous velocity.

Confinement often leads to difficulties in identifying the true diffusive behavior of molecules. For instance, confinement eliminates long timescale correlations in the VAF (Weber et al. 2012a) and reduces D values, and hence leads to mis-identified diffusion modes and states, creating error in the associated kinetic rates (Bohrer et al. 2017).

To limit the amount of confinement in rod-shaped bacterial cells, it is a common practice to take the displacements along the long axis of the cell, as it introduces less confinement when compared to the short axis of the cell due the longer length (Bohrer et al. 2017; Bakshi et al. 2013; Persson et al. 2013; Weber et al. 2010a). However, this practice eliminates a significant amount of data, leading to less accurate determination of Ds and transition kinetics of a system. Bohrer et al. developed an algorithm, termed Single-Particle tracking Improvement with Confinement Error Reduction or SPICER, to selectively incorporate the displacements along the confined dimension of the cell by quantifying the distance of a molecule to the barrier that is needed to minimize the effects of confinement. The new algorithm significantly improves the accuracy in determining both the D values of different diffusive species and also the associated kinetic transition rates of the systems (Bohrer et al. 2017).

2.5.2.2 Diffusion Near a Liquids Glass Transition (Sub-diffusion)

Another mechanism of sub-diffusion can be due to a disordered/heterogeneous medium (Havlin and Ben-Avraham 1987). For instance, it is well known that diffusion deviates from Brownian motion in amorphous solids (Hunter and Weeks 2012; Weeks and Weitz 2002). Interestingly, the bacterial cytoplasm has been reported to have "glass like properties" and changes from liquid-like to solid-like in a metabolism-dependent fashion (Fig. 2.3j) (Parry et al. 2014).

The MSD curve of molecules diffusing in a glass-forming liquid can take on a variety of different shapes, but the "characteristic curve" has three distinct characteristics: [1] At short timescales the log of the MSD displays a linear relationship; [2] at intermediate timescales, the log of the MSD approaches a plateau due to the molecules being trapped in "cages" formed by the relatively immobile solvent molecules; and [3] at long timescales the cages rearrange allowing the molecules to escape and the MSD increases again (Weeks and Weitz 2002) (Fig. 2.3k).

Additionally, diffusion within a "glass-like" medium is non-ergodic, meaning that the average MSD over all trajectories does not equal the average of individual trajectories (over time) (Equation 2.1$\neq$ Equation 2.2, Fig. 2.3k) (Cipelletti and Ramos 2005). The non-ergodicity is the result of the medium having an "infinite" phase space, in that there is an "infinite" number of ways to create local cages and unique arrangements of molecules and the timescales at which the "cages" rearrange vary greatly. A medium that is approaching its glass-like transition will have certain areas displaying glass-like properties while others display fluid-like properties, leading to heterogeneities in the diffusion modes of different molecules within the same cell. This mechanism results in individual cells having more than a single population of diffusing molecules, some confined to cages and others freely diffusing (Parry et al. 2014).

Finally, molecules diffusing in a medium approaching its glass transition also exhibit the anti-persistent behavior (Parry et al. 2014; Weeks and Weitz 2002). The anti-persistent behavior is exemplified by a strong negative correlation between adjacent displacements. For adjacent displacements there is a strong linear dependence for the magnitudes of adjacent displacements (in the direction of the first displacement) up to the "cage size" of the medium (Fig. 2.6b) (Weeks and Weitz 2002). The anti-persistent behavior arises because molecules are reflected by the cage barriers (similar to that of confinement), causing the molecules to return to their previous positions. However, analyzing the anti-persistent behavior using the relatively simple negative correlation of

adjacent displacements instead of the VAF (which has not been extensively investigated with this type of system) limits the understanding of this system, as we further discuss below (Weber et al. 2012a; Weeks and Weitz 2002; Parry et al. 2014).

2.5.2.3 Diffusion Within a Viscoelastic Medium (Sub-diffusion)

In Brownian diffusion, each step a molecule takes is independent of the previous steps. In other diffusion modes there may exist temporal correlations throughout an individual trajectory, which are thought to be a hallmark of complex systems containing many interacting components. Temporal correlations themselves lead to anomalous diffusive behavior (Balakrishnan 1985): positively correlated subsequent displacements lead to super-diffusion, whereas all other types of temporal correlations produce sub-diffusion.

One common mechanism that leads to temporally correlated sub-diffusion is diffusion within a viscoelastic medium (Fig. 2.3l). For example, the diffusive motion of bacterial chromosomal loci in the cytoplasm has been modeled as a polymer within a viscoelastic medium; the viscoelasticity of the fluid leads to "fluid memory", which propagates past "deformations" to the future (Weber et al. 2010b; Weiss 2013). Fractal calculus has been shown to be a useful tool in the modeling of mechanical memory of viscoelastic materials (Deng and Barkai 2009). Therefore, within bacteria, the viscoelasticity of the medium has been most frequently modeled with the fractional Langevin equation (Weber et al. 2012a; Lutz 2001; Deng and Barkai 2009; Weber et al. 2010a, 2012b). We should also note that the diffusion of molecules within homogeneous protein solutions have been successfully modeled using the fractional Langevin equation (Pan et al. 2009) (and the resulting MSD's of the fractional Langevin motion are ergodic, Fig. 2.3m) (Deng and Barkai 2009). Finally, as with all previously mentioned models of sub-diffusion, fractional Langevin motion also results in anti-persistent behavior, in that when a molecule moves the medium "pushes back" (Weber et al. 2010a). The corresponding VAF $C_v^{\delta}(\tau)$ shows a consistent negative peak when δ and τ are equal for all measurable δ and τ (Fig. 2.3n) (Weber et al. 2012a). This behavior indicates that there is a "restoring force", causing the anti-persistent behavior over a large range of timescales due to the elastic nature of the medium. There are two major biological implications if a cell's cytoplasm is a viscoelastic medium; (1) molecules would take longer to reach distant targets than a freely diffusing molecule; and (2) molecules would retrace their previous locations, which could have interesting implications for the timescales of any process which depends upon two molecules coming together.

2.5.2.4 Continuous Time Random Walk (Sub-diffusion)

A fourth type of sub-diffusion behavior is described by the Continuous Time Random Walk (CTRW) model. In the CTRW the diffusion of a molecule is modelled as jumps on a lattice with random waiting times between individual jumps. The waiting time distribution follows a power law probability distribution, leading to large heterogeneities when comparing the MSDs of individual molecules. The proposed biological mechanism behind the CTRW are binding events along a trajectory (Weber et al. 2010a) (Fig. 2.3o), whose power law distribution for waiting times has been observed before (Nagle 1992). The long tail of the waiting time distribution leads to the breaking of ergodicity, where the ensemble average does not equal the time averages of individual trajectories (Fig. 2.3p) (He et al. 2008). Here we should note that CTRW does not show anti-persistent behavior and the VAF does not have a negative peak (Fig. 2.3q).

2.6 Diffusion in Different Subcellular Compartments

2.6.1 Diffusion in the Cytoplasm

The cytoplasm is the largest compartment of a bacterial cell and the main reaction chamber for essential cellular processes such as signal transduction, protein degradation and gene regulation

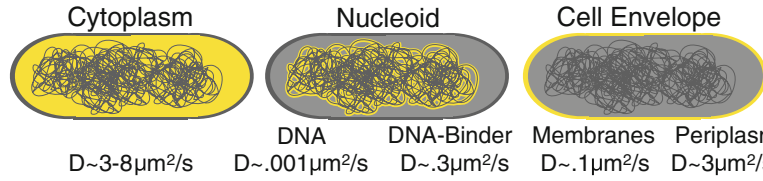

Fig. 2.4 A "simplistic" overview of diffusion within the different compartments of the cell. The three different regions of the cell are shown in yellow with their specific label. Below a characteristic diffusion coefficient is shown that has been observed for that compartment (Note: the characteristic diffusion coefficient for the nucleoid is for the DNA itself (DNA) and for a protein non-specifically binding DNA (DNA-Binder))

(Fig. 2.4). As diffusion is the main means for bacterial macromolecules to reach their target sites in the cytoplasm, it is important to understand how the properties of bacterial cytoplasm influence diffusion.

A defining difference between the cytoplasm of eukaryotic cells versus bacteria cells is the level of crowding. For instance, in bacterial cells the concentration of proteins was measured at 200 g/L in laboratory growth conditions, whereas that in mammalian cells was measured at 50–100 g/L (Cayley et al. 1991; Winick 1968). Under special conditions such as increased osmotic stress, the macromolecular concentration in bacterial cells can approach that of protein crystals (Mika and Poolman 2011). The extreme crowding of cytoplasm has a massive influence on the diffusive properties of cytoplasmic molecules and is likely the main origin of sub-diffusion.

2.6.1.1 Diffusion of Particles of Different Sizes

Early studies characterized the diffusion of fluorescent proteins (FPs) in live *E. coli* cells using FRAP (Elowitz et al. 1999). By bleaching half of a cell and monitoring the fluorescence recovery, the diffusion coefficient D of GFP was determined at $\sim 8\mu m^2/s$. This D value is ~10 times slower than that in water (Terry et al. 1995) and ~4 times slower than that in the cytoplasm of eukaryotic cells (Swaminathan et al. 1997), suggesting that the bacterial cytoplasm is indeed highly viscous, and that the diffusion of macromolecules in the cytoplasm could set the reaction timescales for certain cellular processes (Elowitz et al. 1999).

Interestingly, when a FP is fused to proteins of different molecular weights (MWs), although the trend holds true that the larger the MW is, the lower the diffusion coefficient, the quantitative relationship is different from what would be expect from the Stokes-Einstein equation (Einstein 2007). Instead of scaling with MW with an exponent of $-1/3$, the experimentally measured scaling exponent is between -0.5 to -0.8 for proteins (Mika and Poolman 2011; Kumar et al. 2010). As such, proteins exhibit a rapid reduction of D as MW increases. As we discuss below, other properties of proteins and the bacterial cytoplasm are likely responsible for this behavior.

For large and non-globular molecules such as mRNAs labeled with the MS2-FP fusion system (Golding and Cox 2006) (MW > 2 MDa), studies observed sub-diffusive motions with an MSD exponent α of ~0.7 on timescales from seconds to minutes (Golding and Cox 2006; Weber et al. 2010a, 2012b; Lampo et al. 2017b). The sub-diffusive behavior did not appear to be dependent on the growth condition or the genetic backgrounds used in the experiments, as the exponent α remained similar under various conditions (Weber et al. 2010a). In one study two diffusive states were qualitatively observed, with one essentially immobile ("trapped") and the other freely diffusing throughout the cytoplasm. With these results, the first model in which the heterogeneous, crowded cytoplasm traps/cages individual mRNA molecules was proposed for bacteria (Golding and Cox 2006). A more recent study found that the diffusion of mRNA molecules exhibited dynamic heterogeneity through time and space and was ergodic (Fig. 2.5a) (Lampo et al. 2017b). Intriguingly, the diffusion coefficients of individ-

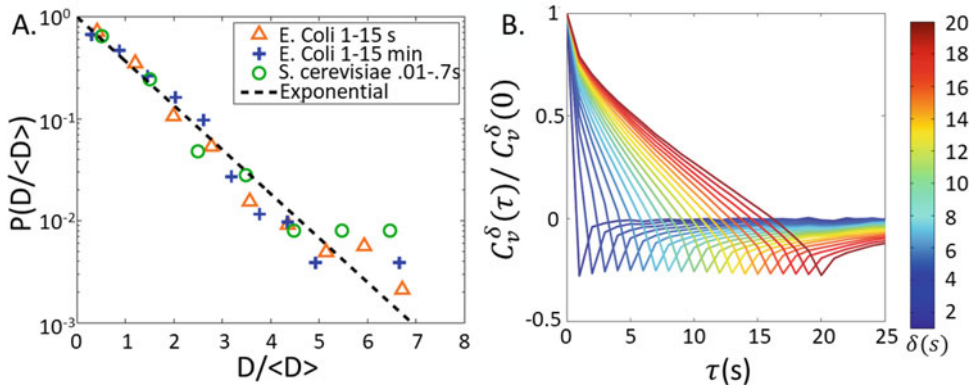

Fig. 2.5 (**a**) Dynamic Heterogeneity of individual molecules: the probability density function of the diffusion coefficient of individual mRNA molecules normalized by their mean. (Adapted from Lampo et al. 2017a). (**b**) The VAF of the mRNA resembles that of diffusion within a viscoelastic medium. (Adapted from Lampo et al. 2017a)

ual mRNA molecules followed an exponential distribution, showing more of a continuum instead of two distinct states, one immobile and one mobile. It should also be mentioned that a similar trend was also found for mRNA within Yeast cells, suggesting the behavior may be a universal trait (Fig. 2.5a). Notably, VAF analysis of these studies all showed anti-persistent behaviors over various timescales (Fig. 2.5b), suggesting that the mRNA's diffusive motion resembled that of fractional Langevin motion, i.e. mRNA molecules diffused within an viscoelastic medium (Weber et al. 2012a; Lampo et al. 2017a).

A recent study explored the diffusive properties of even larger particles in the bacterial cytoplasm (Parry et al. 2014). GFP-fused avian reovirus protein μNS, when expressed at different levels, self-assembles into large particles of different sizes. Parry et al. tracked the diffusion of these nanoparticles in *E. coli* and *C. crescentus* cells and found that these large particles exhibited different diffusion properties when compared to molecules of smaller sizes.

First, the MSD curve of these nanoparticles showed sub-diffusive behavior that was qualitatively similar to what was observed for mRNA (Golding and Cox 2006). They also exhibited two subpopulations, one immobile and one mobile. The presence of these two populations was independent of the corresponding particle size and the metabolic activity of cells, but the fractions of the two populations varied with both (Fig. 2.6a). The displacement distribution of nanoparticles was not Gaussian, and the larger the particles, the more they deviated from that expected for Brownian motion.

Second, the mobility of nanoparticles was related to the metabolic state of the cells: in metabolically inactive cells (ATP-depleted for example), there were more immobile particles (Fig. 2.6a), the MSD exhibited non-ergodic behavior, and the larger particles deviated from Brownian motion to an even greater extent when compared to smaller particles (<30–40 nm) (Parry et al. 2014). These results indicate that smaller particles within the cytoplasm "see" the cytoplasm as more of a fluid medium and the apparent diffusion coefficient of particles is greatly affected by the metabolism of the organism.

The differential diffusive behavior of small and large molecules/particles in the bacterial cytoplasm have also been reported under stressed conditions. In osmotically upshifted cells, the diffusion of GFP (quantified using FRAP) was found to decrease drastically compared to unshifted cells (Konopka et al. 2006; van den et al. 2007), while small molecules such as sugar molecules remained mobile and freely diffused throughout the cell (van den et al. 2007).

Lastly, these nanoparticles showed an anti-persistent behavior where adjacent displacements

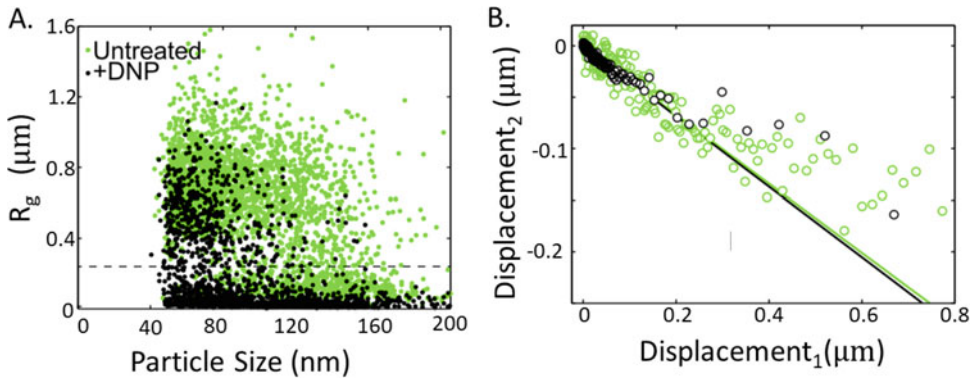

Fig. 2.6 The cytoplasm of *E. coli* has glass-like properties. (**a**) The radiation of gyration (R_g) of individual trajectories vs. the particle size for individual GFP-fused avian reovirus protein μNS particles, without (green) and with (black) ATP-depletion (DNP). (Figure from Parry et al. 2014) (The dashed line indicates the separation between the "caged" population (small R_g) and the freely diffusive population (large R_g)). (**b**) The anti-persistent behavior of adjacent displacements for the same data in (**a**). Here the directionality was assigned a negative value if the second displacement was in the opposite direction of the first. (Figure from Parry et al. 2014)

exhibited opposite directions (Fig. 2.6b), suggesting that these particles have a preference to return to their previous positions (Weeks and Weitz 2002). As such, the bacterial cytoplasm was proposed to have glass-like properties, which affects the diffusion of molecules of different sizes differentially (Parry et al. 2014).

How does the bacterial cytoplasm behave like a glass-forming liquid? The differential mobility of small and large molecules/particles, the presence of the mobile and immobile states, non-ergodicity (in metabolically inactive cells) and the anti-persistent behavior, all suggest that the highly crowded cytoplasm likely traps particles in pockets/cages and that the cytoplasm is near its glass transition, at least in the metabolically inactive cells. These cages would confine the molecules/particles until the surrounding molecules in the cages rearrange themselves, which have been proposed to be depend upon mechanic perturbations and small volume changes resulting from various enzymatic activities (Parry et al. 2014; Oyama et al. 2019). In metabolically inactive cells, the local cages would persist for a longer period of time compared to normal cells, explaining why molecules are trapped in heterogenous pockets for longer times and why the deviation from typical Brownian motion grows larger. This effect directly links the timescales at which the cytoplasmic medium rearranges to the metabolism of the cell, providing a useful window to investigate bacterial cell metabolism. Notably, similar responses of chromosomal loci and an outer membrane protein (discussed later) to the cell's metabolism (Weber et al. 2012b; Winther et al. 2009) have also been reported, suggesting that it may be a universal rule that active metabolism of the cell increases the diffusion of molecules beyond what could be caused by simple thermal motion alone.

Many questions remain unanswered. Exactly how at the molecular level does the metabolic activity of a cell perturb the local cages in the cytoplasm? How are the diffusive dynamics of trapped molecules/particles influenced by the relative sizes of the surrounding molecules and chemical compositions? Do these glass-like properties influence any cellular processes in metabolically active cells, considering that most molecules in cells are likely too small to exhibit these effects with active enzymatic activity? Also, given that the cytoplasm of metabolically active cells exhibited only a fraction of the behaviors for a medium with "glass like properties", how should the viscoelastic properties, ergodicity, and specific distributions of dynamic diffusion coefficients that were seen for the mRNA molecule (Weber et al. 2012a; Lampo et al.

2017a), chromosome (discussed later), and nucleoid associated proteins (discussed later) (Sadoon and Wang 2018) be incorporated into the theory? Finally, further studies are needed to investigate the timescales over which the μNS trajectories show anti-persistent behavior (the velocity autocorrelation function) to determine whether the behavior is consistent with the other studies/does diffusion within an "active glass" exhibit a similar VAF as a viscoelastic medium (Weber et al. 2012a; Lampo et al. 2017a; Sadoon and Wang 2018).

2.6.1.2 Diffusion of Molecules of Different Surface Properties

In the bacterial cytoplasm, the diffusive behavior has also been shown to be influenced by the surface properties of molecules. An early example came from the observation that the addition of a small (<1 kD) but highly charged 6xHis tag to GFP caused a two-fold reduction of its D value in *E. coli* cells (Elowitz et al. 1999). Another study systematically modified the surface net charge of GFP from −30 to 25 across multiple bacterial species and found that the most positively charged GFP variants had a D value 100-fold slower than those of the negatively charged ones, likely caused by their electrostatic interactions with negatively charged ribosome (Fig. 2.7). Interestingly, the study pointed out that as the majority of cytoplasmic proteins in most bacteria are negatively charged, it is possible that these organisms evolved to limit nonspecific interactions with the ribosome in order to maintain a sufficient diffusion coefficient for its cytoplasmic contents (Schavemaker et al. 2017).

A note of caution is that the D measurement of relatively small molecules such as GFP in above studies were done using FRAP. As mentioned earlier, FRAP is an ensemble method and unable to differentiate different types of diffusion and corresponding transition kinetics (Elowitz et al. 1999). SMT of freely diffusing small protein molecules in live bacterial cells has been difficult in the past because of the molecules' relative fast diffusion. However, with recent development of bright organic fluorophores such as the Halo-JF dye system, and fast, sensitive cameras such as the new generation of Scientific cMOS cameras, it is foreseeable that new information of the bacterial cytoplasm and dynamic interactions of normal-sized protein molecules with their interacting partners will emerge.

2.6.2 Diffusion in the Nucleoid

The majority of the bacterial cytoplasm volume is occupied by the nucleoid, an enormous DNA-RNA-protein complex (Fig. 2.4). The macromolecular structure and compaction of the nucleoid are maintained and regulated by small RNAs and many proteins such as histone-like nucleoid-associated proteins (NAPs) (Drlica and Rouviere-Yaniv 1987), topoisomerases (Stracy et al. 2018) and the structural maintenance of chromosome (SMC) proteins (Fudenberg et al. 2016). The chromosome also dynamically rearranges when exposed to different stimuli (Dorman and Dorman 2016). Consequently, the organization and dynamics of the nucleoid itself influences how DNA binding proteins such as RNAP and transcription factors (TFs) find their targeting DNA sites.

For instance, chromosomal DNA loops (Postow et al. 2004) play important roles in transcription regulation and the overall compaction of the chromosome (Bohrer and Roberts 2016; Chong et al. 2014). DNA loops form when specific chromosomal regions come into contact with each other in space and the ends are restrained by protein binding. Chromosomal DNA segments of different genes could also be spatially positioned in proximity with each other to form the scaffold of the so-called transcription factories for RNAP and transcription factors binding. In *E. coli* and *B. subtilis* RNA polymerases were shown to form spatial clusters, where the synthesis of rRNA takes place (Weng et al. 2018). Due to the local high concentration of RNAP, the diffusion of genes and/or transcription factors into and out of the RNAP clusters is a likely mechanism of transcription regulation. Therefore, it is important to understand the diffusive properties and associated time scales of the dynamics of the chromosome and its interacting proteins (Kapanidis et al. 2018).

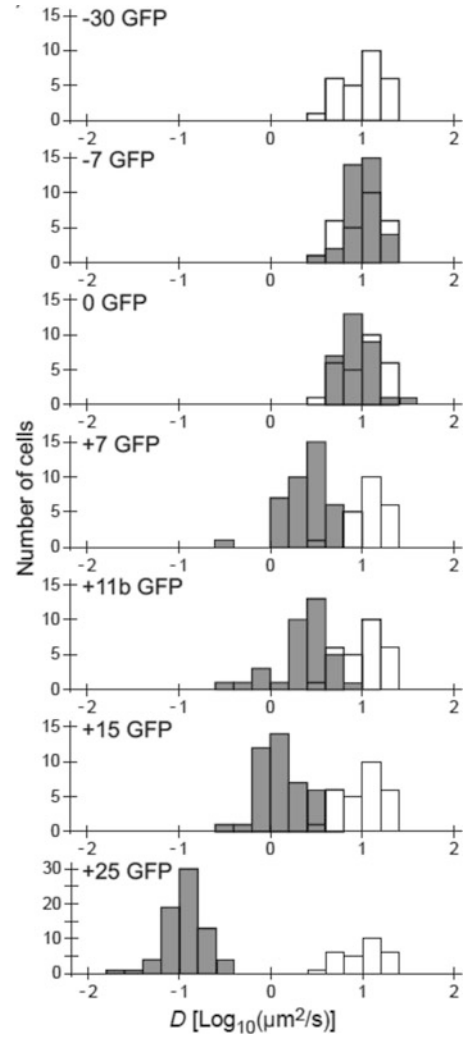

Fig. 2.7 The relation between the charge of GFP and their diffusion coefficients: the filled histogram shows the distribution for the charged particle referenced in the individual subplots and the empty histogram shows the diffusion coefficients of the −30 GFP in each subplot for reference Schavemaker et al. (2017)

2.6.2.1 Diffusion of Chromosomal DNA

One important consideration of describing the diffusion of chromosomal DNAs is that chromosomal DNA is a polymer itself, thus its diffusive dynamics are different from that of any non-tethered particles within the cytoplasm. Note that while there were only limited numbers of studies on the chromosome's dynamics in bacteria, it has been shown that the general diffusive properties of the chromosome are conserved across different bacterial species.

In one study Weber et al. (2010a) used the ParB-GFP/parS system to label chromosomal loci in both *E. coli* and *C. crescentus* (Nielsen et al. 2006). The labeled chromosomal loci exhibited sub-diffusive motion with an MSD exponent $\alpha \sim 0.4$. Under different perturbation conditions, although the D varied over $\sim$4-fold, the α value was unchanged, indicating that the dynamics of these individual loci are likely dominated by one universal physical process (Fig. 2.8a). The α value is also different from that of mRNA molecules measured using the MS2-GFP system ($\alpha \sim 0.7$) (Golding and Cox 2006; Weber et al. 2010a; Lampo et al. 2017a). This difference suggests that the physical interactions of chromosomal DNA and mRNAs with their surroundings are likely very different. Incorporating the chromosomal polymer property into the diffusion model led

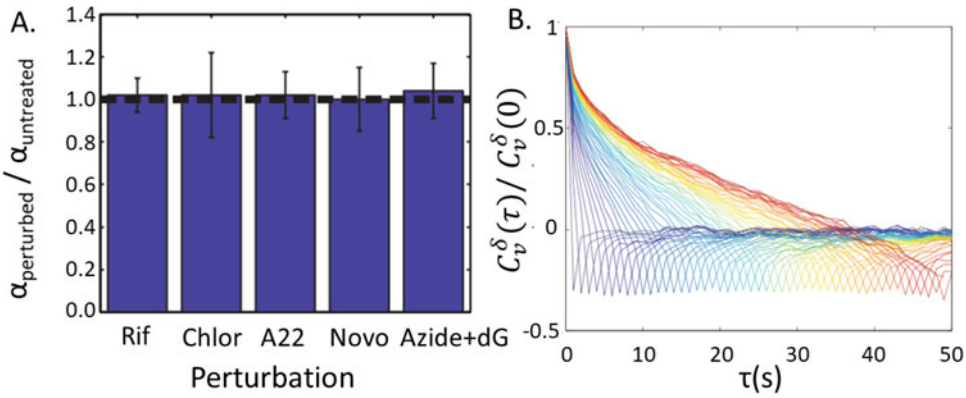

Fig. 2.8 (**a**) The behavior of the DNA's sub-diffusive diffusion (exemplified by the exponent of MSD curve α) remains the same when exposed to different perturbations. (Figure from Weber et al. 2010a). (**b**) The VAF of the DNA resembles that of diffusion within a viscoelastic medium. (Figure from Weber et al. 2012a)

to an exponent of ~ 0.5 (Weber et al. 2010b), indicating that additional factors must be at play. Interestingly, when the viscoelastic property of the cytoplasm (modelled by fractional Langevin motion Deng and Barkai 2009) was incorporated together with the polymer model, an exponent of $\alpha \sim 0.35$ was predicated, matching experimental measurements. Correspondingly, the velocity correlation function showed long timescale correlations for chromosomal loci (Fig. 2.8b, and mRNAs too, Fig. 2.5b). These results hence provide strong support that the cytoplasm possesses viscoelastic properties that create "fluid memory" (Weber et al. 2010a, 2012a).

One interesting discrepancy of this work is that a viscoelastic cytoplasm modelled by the fractional Langevin equation is fundamentally different from a cytoplasm with glass-like properties as what was proposed by Parry et al. A recent work by Sadoon et al. shed light on the discrepancy (Sadoon and Wang 2018). In this study the diffusive behavior of the DNA binding protein H-NS was investigated. The histone like H-NS oligomerizes on DNA and regulates the expression of ~5% of the *E. coli* genome. Using SMT of mEos3.2-fused H-NS, the apparent D value was determined to be similar to that of the chromosomal loci with $\alpha \sim 0.6$, suggesting that the diffusion of H-NS is likely linked to that of the chromosome. The velocity autocorrelation function showed characteristics that were consistent with previous studies (Weber et al. 2010a, 2012a; Lampo et al. 2017b) suggesting a viscoelastic cytoplasm as modeled by the fractional Langevin equation (Weber et al. 2012a). Interestingly, when they quantified the complex modulus of the medium as a function of frequency ($0.1–20\,s^{-1}$) the bacterial cytoplasm showed a glass-like transition over the different timescales, suggesting that the cytoplasm exhibited properties as reported by Parry et al. (2014). This study suggests that the cytoplasm of bacteria behaves differently at different timescales, highlighting the importance of taking timescales of different cellular processes into consideration.

In another study, Weber et al. found that their previous model of the viscoelastic cytoplasm coupled with the DNA polymer model was inadequate to capture the temperature dependence of the diffusion of labeled chromosomal DNA loci. The apparent diffusion coefficient D of chromosomal DNA loci scaled exponentially with temperature, termed "super-thermal", instead of linearly as predicted in the Stokes-Einstein equation when the system is at equilibrium (Weber et al. 2012b). Most interestingly, this super-thermal diffusion only existed in cells of active metabolism – in cells depleted of ATP, D scaled linearly with temperature as expected. These results indicate that the non-equilibrium state of the cell, most certainly caused by enzymatic activities, leads to "faster" diffusion

than what would be produced solely by thermal fluctuations. Here the influence of metabolism on diffusion is consistent with the previously discussed study done by Parry et al. (2014).

2.6.2.2 Diffusion of DNA Binding Proteins

Since the chromosome is within the same compartment as the ribosomes within bacteria, all of the components that regulate the conformation of the chromosome, transcription and translation must function together within the same environment. Since the diffusion of chromosomal DNA is very small compared to that of DNA-binding proteins, different diffusive states of DNA-binding proteins, judged by their differential apparent diffusion coefficients, are commonly used to identify the bound and unbound states, providing an invaluable technique to study protein-DNA binding kinetic and functions in live cells.

An early SMT experiment done by Elf et al. probed the binding of the transcription factor LacI to its specific chromosomal binding site lacO. While both 1d and 3d diffusion had been proposed as the mechanism for how transcription factors find their specific DNA targets in the presence of overwhelmingly nonspecific chromosomal DNA (von Hippel and Berg 1989), the authors found that the a single LacI dimer spends the majority of its time (90%) performing 1d diffusion along the DNA, demonstrating this mechanism in vivo. A similar result was found for RNAP, which spends 85% of its time binding non-specifically within the nucleoid (Stracy et al. 2014, 2015; Kapanidis et al. 2018). Furthermore, transient non-specific binding has also been observed for the nucleoid-associated protein HU and was proposed to be important for maintaining the "dynamic" nature of the chromosome (Bettridge et al. 2019) – suggesting this may be a common trait of many DNA associating proteins.

In another recent study, the diffusion dynamics of gyrase in *E. coli* was investigated using SMT (Stracy et al. 2018). Gyrase helps maintain the supercoiling state of the chromosome, which has a large effect on transcription (Dorman and Dorman 2016; Bohrer and Roberts 2016). It was found that the average time gyrase molecules spent in the specific DNA bound states is ~2 s, with replication-proximal gyrase molecules having longer dwell times (~ 8 s). Such a difference suggests that different gyrase molecules may work at different capacities depending on the local topological need, highlighting the unique power of SMT as an imaging technique to identify spatial information in live cells.

Along the same line, SMT studies helped resolve a discrepancy between biochemical and microscopic data regarding the spatial arrangement between transcription and translation in bacterial cells (Hobot et al. 1985; Wang et al. 2011; Bakshi et al. 2012). Biochemical studies showed that in bacterial cells translation occurs co-transcriptionally when mRNA is still being transcribed and physically attached to the DNA. Fluorescence microscopy however showed that ribosomes are excluded from the nucleoid while RNAP is predominately nucleoid-associated (Stracy et al. 2015; Bakshi et al. 2012). Using SMT of the ribosomal protein L1 and S2 tagged with mEos2, the diffusion coefficients of the free subunit and the incorporated, translating ribosome were found to be significantly different, and that the free subunits could diffuse freely throughout the nucleoid. Therefore, ribosome could assemble inside the nucleoid to initiate translation. Fully assembled, translating ribosomes, however, are mainly excluded from the nucleoid, suggesting that as translation is initiated, the transcribing mRNA could gradually move out of the nucleoid to continue translation. Indeed, such movement of actively transcribing gene loci has been observed in *E. coli* cells (Stracy et al. 2014).

2.6.3 Diffusion in the Cell Envelope

The cell envelope of gram-negative bacteria has three layers, the outer membrane (OM), and the inner membrane (IM), and the space in between where the cell wall resides (periplasm) (Fig. 2.4). Gram-positive bacteria do not have an outer membrane but have a thick cell wall and an inner membrane. The outer membrane acts as the first

barrier between the cell and the environment for gram-negative bacteria. It is rich in β-barrel proteins, which allows small molecules to access the periplasm and cytoplasm through the inner membrane (Ruiz et al. 2006). Another function of the outer membrane comes from its mechanical properties, as a recent study predicts that the outer membrane's β-barrel proteins play a large part in the ability of the cell to handle external forces (Lessen et al. 2018). The periplasm of gram-negative bacteria is often described as being "highly viscous" (Cho et al. 2014; Ruiz et al. 2006; Goemans et al. 2014; Denoncin et al. 2014; Mas et al. 2019; Grote et al. 2018) and contains a thin layer of peptidoglycan, or cell wall, although in reality it is likely not much more viscus than the cytoplasm (Foley et al. 1989; Mullineaux et al. 2006; Sochacki et al. 2011). The peptidoglycan layer dictates the cell shape and allows the cell to survive osmotic stress. The incorporation of this layer during division has been shown to be a major driving force for proper constriction (Yang et al. 2017). Finally, the inner membrane directly links molecules in the cytoplasm to the environment on the outside and is important for a multitude of different signal transduction processes. The organization of bacterial membranes has been shown to be highly regulated and likely composed of many scattered microdomains (Rudner and Losick 2010; Lopez and Koch 2017; Dempwolff et al. 2016).

2.6.3.1 Diffusion Within the Outer Membrane

Despite the importance of the outer membrane and its associated outer membrane proteins (OMPs), there are relatively few studies in which the diffusive behaviors of OMPs were investigated when compared to that of cytoplasmic proteins.

In an early work, where OMPs were nonspecifically labeled with a dye-conjugated reactive succinimidyl ester and chased with dye-free medium, it was found that a significant proportion of the outer membrane proteins OMPs remained immobile in particular at the cell poles (de Pedro et al. 2004). This observation is consistent with the notion that cell poles are essentially metabolically inert and stable.

For OMPs not specifically targeted to cell poles, many of them were found to be largely confined as well. SMT experiments of the outer membrane λ receptor protein tagged with large beads (20–500 nm) showed that that a subpopulation of the receptor was confined in small domains of 20–50 nm, and that a relatively faster population explored regions about 100–300 nm in size (Fig. 2.9a) (Oddershede and Dreyer 2002; Gibbs et al. 2004). SMT of two other outer membrane proteins labeled with fluorescent antibodies, the porin OmpF and the cobalamin receptor BtuB, showed that OmpF was confined to domains of ~100 nm in diameter, similar to the λ receptor, while BtuB was much more mobile with a D of 0.05 $\mu m^2/s$, an order of magnitude larger than that of OmpF (Spector et al. 2010).

What determines the differences in the mobility of OMPs and why do some OMPs exhibit confined diffusion? On one hand, depleting ATP, or inhibiting cell wall synthesis, caused a significant further reduction of the mobility of the λ receptor at long time scales (Winther et al. 2009), similar to what was observed for cytoplasmic proteins and the chromosome (Parry et al. 2014; Weber et al. 2012b). On the other hand, because λ receptor is anchored to the cell wall covalently, it was proposed that the constant and dynamic energy-consuming reconstruction of the peptidoglycan layer underlies the diffusive behavior of the λ receptor (Winther et al. 2009). A later study that quantified the dynamics of OmpA with and without the ability to bind the cell wall however showed essentially the same immobility, arguing against this hypothesis (Verhoeven et al. 2013).

Later the work of Rassam et al. showed that protein-protein interactions within the outer membrane appear to play an important role in restricting OMP diffusion. Using SMT, a mutated BtuB protein unable to interact with its cytoplasmic membrane protein partner TonB showed >10-fold increase of mobility. Interestingly, even nonspecific protein-protein interactions were shown to be important. Rassam

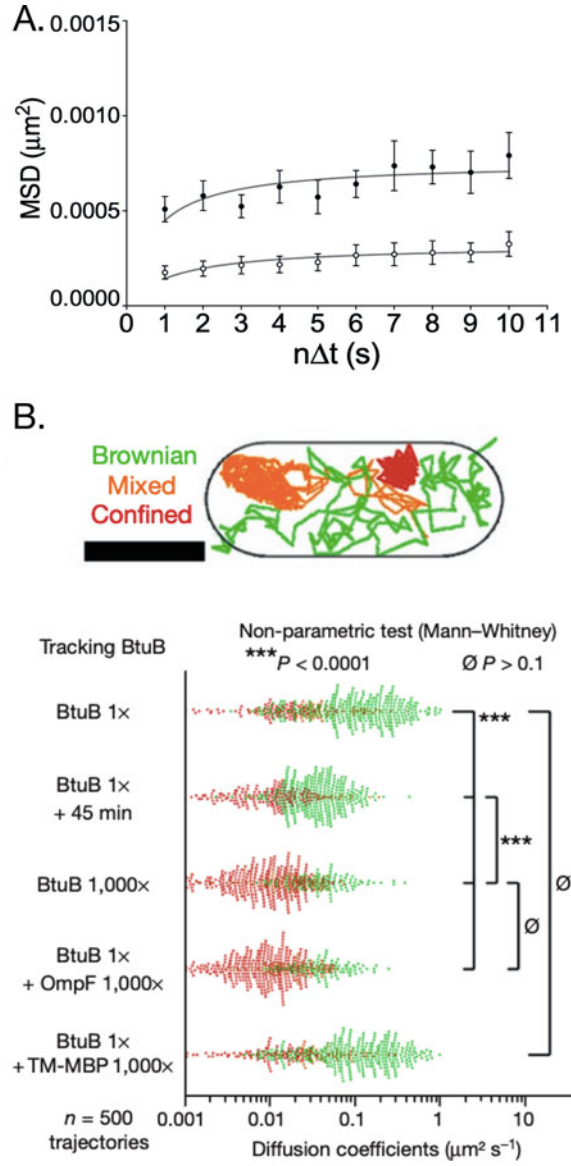

Fig. 2.9 (**a**) The confined diffusion of the OMP λ receptor with the filled circles calculated using the fast particles and the open circles the slow. (Figure from Gibbs et al. 2004). (**b**) Top shows an illustration of the colors representing the diffusive states of the individual molecules. Bottom shows how the diffusion of individual BtuB (OMP) was affected by the addition of different amounts of more BtuB or non-interacting OmpF. The addition of an engineered maltose binding protein with a single transmembrane helix (TM-MBP) was also used as a control. (Figure from Rassam et al. 2015)

et al. further showed that two other OMPs, Cir and BamA, which do not interact with BtuB directly, clustered with BtuB in 0.5-μ m diameter "islands" on the outer membrane of *E. coli* cells. When the diffusion of BtuB was measured in vitro in a supported lipid bilayer made from *E. coli* membrane extract (Fig. 2.9b), SMT of BtuB showed Brownian diffusion at low concentrations. When the concentration of BtuB or a non-interacting OMP (OmpF) increased, BtuB exhibited orders of magnitude reduced diffusion and increased confinement. These results strongly suggest that the mechanism behind the previously observed confined diffusion was due to the "promiscuous" interactions among OMPs in confined areas of the outer membrane, which was proposed to be individual islands of different molecular compositions (Rassam et al. 2015). The proposed OMP islands formed by non-specific protein-protein interactions however need to be further verified. In particular, it would be interesting to

examine whether all or just a few specific OMPs make up these islands, whether the characteristics of these OM islands vary with metabolism, and how the response changes the diffusion of other OMPs.

2.6.3.2 Diffusion Within the Periplasm

Even fewer studies have investigated the diffusive behaviors of proteins in the periplasm. In an early study where the diffusion of the maltose-binding protein (MBP) within the periplasm of *E. coli* was monitored using FRAP, the lateral diffusion coefficient of MBP was found to be at $0.009\,\mu m^2/s$ (Brass et al. 1986). The extremely small diffusion coefficient was later shown to result from the harsh experimental conditions used to permeabilize the cells. Later FRAP studies found that the diffusion coefficients of FP tagged periplasmic proteins were $\sim 3\,\mu m^2/s$ (Foley et al. 1989; Mullineaux et al. 2006; Sochacki et al. 2011), only "slightly"smaller than that in the cytoplasm. Additionally, when under osmotic stress (water leaves the cytoplasm and moves into the periplasm), the diffusion coefficient of these periplasmic proteins increased ~ 3 fold, similar to what was observed for the cytoplasm (Sochacki et al. 2011). Most interestingly, the periplasms of multiple gram-negative bacteria have been shown to form heterogenous, diffusion-confined domains, suggesting that the proteins in the periplasm likely exhibit a level of crowding that influences each other's diffusion dynamics (Foley et al. 1989; Zhang et al. 2008, 2013). Clearly, further investigations especially with SMT methodologies are needed to elucidate the diffusion dynamics of proteins in the periplasm.

While no SMT studies have been done on a purely periplasmic protein at this time, various studies have quantified the diffusive properties of the enzymes responsible for maintaining the peptidoglycan layer during cell division (mostly inner membrane proteins). Of particular interest to the study of diffusive behavior within bacteria, many of these proteins show super-diffusion, whose corresponding velocities are likely directly linked to their state. Furthermore, studies are beginning to show how the information within the dynamic behavior of molecular assemblies within the cytoplasm are propagated into the periplasmic compartment.

In most bacteria, for cell division to take place, a large macromolecular complex, the divisome, must form and direct the synthesis of septal peptidoglycan. The formation of this complex is initiated by FtsZ, a tubulin homolog, which polymerizes at the middle of dividing cells. While FtsZ SMT studies have shown that the individual monomers of the FtsZ filaments are stationary (Niu and Yu 2008), recent works utilizing total internal reflection fluorescence microscopy have shown that the filaments themselves show directional movement, the result of treadmilling (Yang et al. 2017; Bisson-Filho et al. 2017). The FtsZ filaments' dynamics are thought to direct/-coordinate the incorporation of the peptidoglycan and organize many of the other proteins in the divisome.

Interestingly, even though many of the enzymes important for septal peptidoglycan incorporation show the same super-diffusive motion, the mechanisms behind their motions seem to vary between different bacterial species. In *Bacillus subtilis* it was found that the velocity of bPBP2b (penicillin-binding protein) was directly linked with the velocity of the FtsZ filaments and that the velocities of these components were directly linked to septum closure (Bisson-Filho et al. 2017). Similarly, in *E. coli* it was shown that the velocity of the synthase enzyme bPBP3 (FtsI) was also directly correlated with the velocity of the FtsZ filaments, but interestingly the velocity of the two were not limiting in terms of septum closure (Yang et al. 2017). Lastly, unlike the other two species in *Streptococcus pneumoniae* it was recently found that the bPBP2x:FtsW complex exhibits directional motion, but its velocity is independent of the velocity of the FtsZ filaments (Perez et al. 2019). Considering the similarities in the diffusion dynamics and the rarity of directional motion within bacteria future work quantifying the mechanisms responsible for the diffusion of these enzymes is an exciting direction of study.

2.6.3.3 Diffusion Within the Inner Membrane

Compared to proteins in the outer membrane, inner membrane proteins (IMPs) appear to be more mobile. The first SMT study of an IMP tracked the membrane-bound histidine kinase PleC fused with a YFP in *C. crescentus* cells. PleC localizes to the cell pole of Caulobacter cells and was shown to be important for the asymmetric cell division (Wheeler and Shapiro 1999). A subpopulation of PleC-YFP indeed was found at the cell pole and was largely immobile, and the other subpopulation diffused within the cell body with normal Brownian motion with a D of $\sim 0.01\,\mu m^2/s$. This observation suggests that at least some IMPs can freely diffuse throughout the entire inner membrane within *C. crescentus* cells (Deich et al. 2004). Another IMP, TatA, forms large complexes (~600 KDa) with itself and the other two proteins TaB and TacC in the twin-arginine translocon (Bolhuis et al. 2001). TatA diffused faster than PleC with an apparent D of $\sim 0.13\,\mu m^2/s$ measured by FRAP (Mullineaux et al. 2006). Such a high mobility is comparable to what was observed within Eukaryotic membranes (Zhang et al. 1993). SMT of TatA-YFP in another study showed similar Brownian motion with a comparable D value, although the trajectories were not long enough to identify whether there were other diffusive modes at long time scales (Leake et al. 2008).

The relationship between the size of an IMP and its diffusion coefficient was also investigated. For TatA-YFP, for example, SMT found that the apparent diffusion coefficient value decreased when the number of TatA-YFP molecules in self-assembled complexes increased from ~10 to 100. Interestingly, the relationship can be strictly described as logarithmic, mimicking what has been observed for the relationship between the size of cytoplasmic proteins and the corresponding diffusion coefficient (Leake et al. 2008; Kumar et al. 2010). Another work by Oswald et al. investigated the diffusion coefficients of eight different inner membrane proteins and showed a clear relationship between the apparent diffusion coefficient and the radii, but not the molecular weight, of each protein (Fig. 2.10) (Oswald et al. 2016). This interesting finding suggested that it is the "amount/volume of the protein" that interacts with the membrane that dictates the apparent diffusion coefficient (Saffman and Delbrück 1975). A more recent and exhaustive study has verified this finding, which investigated ~200 membrane proteins within *Bacillus subtilis* (Lucena et al. 2018).

Not all IMPs exhibit Brownian motion. The cytochrome bd-I complex (CydB), when fused to GFP, was found to form clusters of ~100 nm in diameter and contain approximately 76 cydB-GFP proteins per cluster. A similar logarithmic relationship between the apparent diffusion coefficient and the number of CydB within the complex as that of TatA-YFP was also observed. However, some CydB-GFP clusters clearly exhibited confined diffusion. By fitting the MSD curves to a mobility-confinement model, the confinement zone of CydB-GFP, defined as an area in which the molecules can diffuse freely and above which a barrier confines the diffusion of the molecules was determined to have a diameter of 160 nm (Lenn et al. 2008). A similar confinement zone was observed for another IMP, Tsr, a chemotaxis proteins that forms clusters at cell poles (Oh et al. 2014). A few other IMPs that do not form clusters also showed sub-diffusive behavior based on their MSD plots, suggesting that sub-diffusion may be a common feature of IMPs.

What contributes to the confinement of IMPs? The inner membranes of *B. subtilis* and *E. coli* stained with membrane dyes Nile Red and DiI-C12 respectively, showed a clustered, heterogenous fluorescence distribution (Strahl et al. 2014; Oswald et al. 2016). As it is known that both dyes are more specific for fluid rather than rigid regions of the membrane, it is likely that there existed fluid macrodomains on the membrane, and that these macrodomains may be responsible for the confined movement of IMPs. In eukaryotic cells it is known that cytoskeleton proteins such as actin are involved in the formation of membrane microdomains (Chichili and Rodgers 2009). Therefore, it is not surprising that when the polymerization of the bacterial actin homolog MreB was inhibited, the apparent Ds of many IMPs increased, confinement disappeared, and

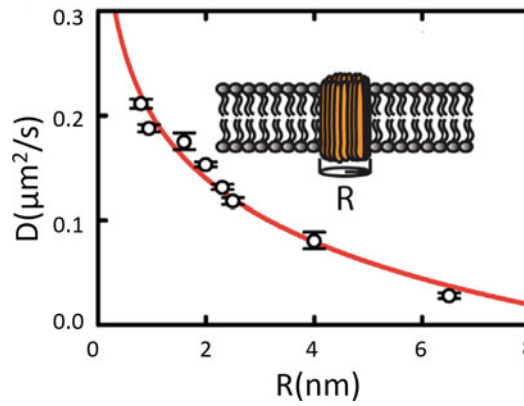

Fig. 2.10 Diffusion coefficients of IMPs vs. the radius of the IMP (R). (Figure from Oswald et al. 2016)

that the proportion of Tsr molecules that experienced confined diffusion diminished significantly (Oswald et al. 2016).

Based on these results, a general model behind the confinement caused by MreB was proposed (Oswald et al. 2016), similar to what was proposed for actin in eukaryotic cells (Goiko et al. 2016). Filaments formed by MreB and its membrane anchors may act as diffusion barriers/fences for inner membrane proteins, leading to their apparent confinement observed in the MSD plots. However, Lucena et al. found that the diffusion of >200 IMPs along the long axis of the cell and the short axis did not exhibit any markable differences, arguing that the MreB filaments, which mainly form along the short axis of the cell, may not be confining the diffusion of the proteins using the same mechanism as actin, or that MreB filaments may not be as dense or well organized as long actin filaments in eukaryotic cells (Lucena et al. 2018).

2.7 Summary

Within this review we have described the various methodologies used to characterize diffusion within bacteria with a primary focus on single molecule tracking. We have described the different forms of analysis one can use to determine the behavior of diffusion as well as described the most common models of diffusion within bacteria. We then went into detail, describing the studies that have characterized the diffusion within the different compartments of bacteria, and several different themes emerged from the various studies. First, in every compartment of the cell, diffusion is much more complicated than normal Brownian motion, with a vast array of different mechanisms leading to sub-diffusion. Second, the metabolism of the cell can have a large impact on the diffusion of particles in any compartment of the cell, where the higher the metabolism the faster the diffusion of the particles. Third, the cytoplasm likely has viscoelastic properties and influences the diffusion of particles on a variety of different timescales. Fourth, diffusion within the cell envelope has not been quantified as in depth as within the other compartments. And fifth, different protein-protein interactions can lead to different types of diffusion, including confinement. Finally, we would like to emphasize that no real consensus has been made for any compartment and no model can yet explain all the experimental work at this time, leaving room for many new discoveries.

Acknowledgments We would like to thank Dr. Xinxing Yang and Nicolas Yehya for their comments and feedback.

References

Ando R, Hama H, Yamamoto-Hino M, Mizuno H, Miyawaki A (2002) An optical marker based on the UV-induced green-to-red photoconversion of a fluorescent protein. Proc Natl Acad Sci 99:12651–12656

Bakshi S, Siryaporn A, Goulian M, Weisshaar JC (2012) Superresolution imaging of ribosomes and RNA polymerase in live Escherichia coli cells. Mol Microbiol 85:21–38

Bakshi S, Dalrymple RM, Li W, Choi H, Weisshaar JC (2013) Partitioning of RNA polymerase activity in live Escherichia coli from analysis of single-molecule diffusive trajectories. Biophys J 105:2676–2686

Balakrishnan V (1985) Anomalous diffusion in one dimension. Phys A Stat Mech Appl 132:569–580

Balzarotti F, Eilers Y, Gwosch KC, Gynnå AH, Westphal V, Stefani FD, Elf J, Hell SW (2017) Nanometer resolution imaging and tracking of fluorescent molecules with minimal photon fluxes. Science 355:606–612

Beilharz K, van Raaphorst R, Kjos M, Veening J-W, Pettinari MJ (2015) Red fluorescent proteins for gene expression and protein localization studies in streptococcus pneumoniae and efficient transformation with DNA assembled via the Gibson assembly method. Appl Environ Microbiol 81:7244–7252

Bettridge K, Verma S, Weng X, Adhya S, Xiao J (2019) Single molecule tracking reveals the role of transitory dynamics of nucleoid-associated protein HU in organizing the bacterial chromosome. BioRxiv 181:2019.12.31.725226

Betzig E, Patterson GH, Sougrat R, Lindwasser OW, Olenych S, Bonifacino JS, Davidson MW, Lippincott-Schwartz J, Hess HF (2006) Imaging intracellular fluorescent proteins at nanometer resolution. Science 313:1642–1645

Bisson-Filho AW, Hsu Y-P, Squyres GR, Kuru E, Wu F, Jukes C, Sun Y, Dekker C, Holden S, VanNieuwenhze MS, Brun YV, Garner EC (2017) Treadmilling by FtsZ filaments drives peptidoglycan synthesis and bacterial cell division. Science 355:739–743

Bohrer CH, Roberts E (2016) A biophysical model of supercoiling dependent transcription predicts a structural aspect to gene regulation. BMC Biophys 9:1

Bohrer CH, Bettridge K, Xiao J (2017) Reduction of confinement error in single-molecule tracking in live bacterial cells using SPICER. Biophys J 112:568–574

Bolhuis A, Mathers JE, Thomas JD, Barrett CM, Robinson C (2001) TatB and TatC form a functional and structural unit of the twin-arginine translocase from Escherichia coli. J Biol Chem 276:20213–20219

Brass JM, Higgins CF, Foley M, Rugman PA, Birmingham J, Garland PB (1986) Lateral diffusion of proteins in the periplasm of Escherichia coli. J Bacteriol 165:787–795

Camsund D, Lawson MJ, Larsson J, Jones D, Zikrin S, Fange D, Elf J (2020) Time-resolved imaging-based CRISPRi screening. Nat Methods 17:86–92

Cayley S, Lewis BA, Guttman HJ, Record MT Jr (1991) Characterization of the cytoplasm of Escherichia coli K-12 as a function of external osmolarity: implications for protein-DNA interactions in vivo. J Mol Biol 222:281–300

Chichili GR, Rodgers W (2009) Cytoskeleton-membrane interactions in membrane raft structure. Cell Mol Life Sci CMLS 66:2319–2328

Cho S-H, Szewczyk J, Pesavento C, Zietek M, Banzhaf M, Roszczenko P, Asmar A, Laloux G, Hov A-K, Leverrier P, Van der Henst C, Vertommen D, Typas A, Collet J-F (2014) Detecting envelope stress by monitoring β-barrel assembly. Cell 159:1652–1664

Chong S, Chen C, Ge H, Xie XS (2014) Mechanism of transcriptional bursting in bacteria. Cell 158:314–326

Cipelletti L, Ramos L (2005) Slow dynamics in glassy soft matter. J Phys Condens Matter 17:R253–R285

Cole NB (2013) Site-specific protein labeling with SNAP-tags. Curr Protoc Protein Sci 73:30.1.1–30.1.16

Condamin S, Tejedor V, Voituriez R, Bénichou O, Klafter J (2008) Probing microscopic origins of confined subdiffusion by first-passage observables. Proc Natl Acad Sci U S A 105:5675–5680

Das R, Cairo CW, Coombs D (2009) A hidden Markov model for single particle tracks quantifies dynamic interactions between LFA-1 and the actin cytoskeleton. PLoS Comput Biol 5:e1000556

Deich J, Judd EM, McAdams HH, Moerner WE (2004) Visualization of the movement of single histidine kinase molecules in live Caulobacter cells. Proc Natl Acad Sci 101:15921–15926

Dempwolff F, Schmidt FK, Hervás AB, Stroh A, Rösch TC, Riese CN, Dersch S, Heimerl T, Lucena D, Hülsbusch N, Stuermer CAO, Takeshita N, Fischer R, Eckhardt B, Graumann PL (2016) Super resolution fluorescence microscopy and tracking of bacterial flotillin (Reggie) paralogs provide evidence for defined-sized protein microdomains within the bacterial membrane but absence of clusters containing detergent-resistant proteins. PLoS Genet 12:e1006116

Deng W, Barkai E (2009) Ergodic properties of fractional Brownian-Langevin motion. Phys Rev E 79:011112

Denoncin K, Vertommen D, Arts IS, Goemans CV, Rahuel-Clermont S, Messens J, Collet J-F (2014) A new role for Escherichia coli DsbC protein in protection against oxidative stress. J Biol Chem 289:12356–12364

de Pedro MA, Grünfelder CG, Schwarz H (2004) Restricted mobility of cell surface proteins in the polar regions of Escherichia coli. J Bacteriol 186:2594–2602

Dorman CJ, Dorman MJ (2016) DNA supercoiling is a fundamental regulatory principle in the control of bacterial gene expression. Biophys Rev 8:89–100

Drlica K, Rouviere-Yaniv J (1987) Histonelike proteins of bacteria. Microbiol Rev 51:301–319

Einstein A (2007) Über die von der molekularkinetischen Theorie der Wärme geforderte Bewegung von in ruhenden Flüssigkeiten suspendierten Teilchen, pp 1–12

Elowitz MB, Surette MG, Wolf PE, Stock JB, Leibler S (1999) Protein mobility in the cytoplasm of Escherichia coli. J Bacteriol 181:197–203

Elson EL (2011) Fluorescence correlation spectroscopy: past, present, future. Biophys J 101:2855–2870

Foley M, Brass JM, Birmingham J, Cook WR, Garland PB, Higgins CF, Rothfield LI (1989) Compartmentalization of the periplasm at cell division sites in Escherichia coli as shown by fluorescence photobleaching experiments. Mol Microbiol 3:1329–1336

Fu G, Bandaria JN, Le Gall AV, Fan X, Yildiz A, Mignot T, Zusman DR, Nan B (2018) MotAB-like machinery drives the movement of MreB filaments during bacterial gliding motility. Proc Natl Acad Sci U S A 115:2484–2489

Fudenberg G, Imakaev M, Lu C, Goloborodko A, Abdennur N, Mirny LA (2016) Formation of chromosomal domains by loop extrusion. Cell Rep 15:2038–2049

Gebhardt JCM, Suter DM, Roy R, Zhao ZW, Chapman AR, Basu S, Maniatis T, Xie XS (2013) Single-molecule imaging of transcription factor binding to DNA in live mammalian cells. Nat Methods 10:421–426

Gibbs KA, Isaac DD, Xu J, Hendrix RW, Silhavy TJ, Theriot JA (2004) Complex spatial distribution and dynamics of an abundant Escherichia coli outer membrane protein, LamB. Mol Microbiol 53:1771–1783

Goemans C, Denoncin K, Collet J-F (2014) Folding mechanisms of periplasmic proteins. Biochim Biophys Acta Mol Cell Res 1843:1517–1528

Goiko M, de Bruyn JR, Heit B (2016) Short-lived cages restrict protein diffusion in the plasma membrane. Nat Publ Group 6:34987

Golding I, Cox EC (2006) Physical nature of bacterial cytoplasm. Phys Rev Lett 96:098102

Grimm JB, English BP, Choi H, Muthusamy AK, Mehl BP, Dong P, Brown TA, Lippincott-Schwartz J, Liu Z, Lionnet T, Lavis LD (2016) Bright photoactivatable fluorophores for single-molecule imaging. Nat Methods 13:985–988

Grote GRMK, Risse JM, Friehs K (2018) Secretion of recombinant proteins from E. coli. Eng Life Sci 18:532–550

Gurskaya NG, Verkhusha VV, Shcheglov AS, Staroverov DB, Chepurnykh TV, Fradkov AF, Lukyanov S, Lukyanov KA (2006) Engineering of a monomeric green-to-red photoactivatable fluorescent protein induced by blue light. Nat Biotechnol 24:461–465

Havlin S, Ben-Avraham D (1987) Diffusion in disordered media. Adv Phys 36:695–798. Taylor & Francis

He Y, Burov S, Metzler R, Barkai E (2008) Random time-scale invariant diffusion and transport coefficients. Phys Rev Lett 101:058101

Hess ST, Girirajan TPK, Mason MD (2006) Ultra-high resolution imaging by fluorescence photoactivation localization microscopy. Biophys J 91:4258–4272

Hobot JA, Villiger W, Escaig J, Maeder M, Ryter A, Kellenberger E (1985) Shape and fine structure of nucleoids observed on sections of ultrarapidly frozen and cryosubstituted bacteria. J Bacteriol 162:960–971

Hu L, Vecchiarelli AG, Mizuuchi K, Neuman KC, Liu J (2015) Directed and persistent movement arises from mechanochemistry of the ParA/ParB system. Proc Natl Acad Sci U S A 112:E7055–64

Hunter GL, Weeks ER (2012) The physics of the colloidal glass transition. Reports on progress in physics. Phys Soc 75:066501

Kapanidis AN, Uphoff S, Stracy M (2018) Understanding protein mobility in bacteria by tracking single molecules. J Mol Biol 430:4443–4455

Kim SY, Gitai Z, Kinkhabwala A, Shapiro L, Moerner WE (2006) Single molecules of the bacterial actin MreB undergo directed treadmilling motion in Caulobacter crescentus. Proc Natl Acad Sci 103:10929–10934

Konopka MC, Shkel IA, Cayley S, Record MT, Weisshaar JC (2006) Crowding and confinement effects on protein diffusion in vivo. J Bacteriol 188:6115–6123

Kumar M, Mommer MS, Sourjik V (2010) Mobility of cytoplasmic, membrane, and DNA-binding proteins in Escherichia coli. Biophys J 98:552–559

Kusumi A, Sako Y, Yamamoto M (1993) Confined lateral diffusion of membrane receptors as studied by single particle tracking (nanovid microscopy). Effects of calcium-induced differentiation in cultured epithelial cells. Biophys J 65:2021–2040

Lampo TJ, Stylianidou S, Backlund MP, Wiggins PA, Spakowitz AJ (2017a) Cytoplasmic RNA-protein particles exhibit non-Gaussian subdiffusive behavior. Biophys J 112:532–542

Lampo TJ, Stylianidou S, Backlund MP, Wiggins PA, Spakowitz AJ (2017b) Cytoplasmic RNA-protein particles exhibit non-Gaussian subdiffusive behavior. Biophys J 112:532–542

Leake MC, Greene NP, Godun RM, Granjon T, Buchanan G, Chen S, Berry RM, Palmer T, Berks BC (2008) Variable stoichiometry of the TatA component of the twin-arginine protein transport system observed by in vivo single-molecule imaging. Proc Natl Acad Sci U S A 105:15376–15381

Lee S-H, Shin JY, Lee A, Bustamante C (2012) Counting single photoactivatable fluorescent molecules by photoactivated localization microscopy (PALM). Proc Natl Acad Sci U S A 109:17436–17441

Lenn T, Leake MC, Mullineaux CW (2008) Clustering and dynamics of cytochrome bd-I complexes in the Escherichia coli plasma membrane in vivo. Mol Microbiol 70:1397–1407

Lessen HJ, Fleming PJ, Fleming KG, Sodt AJ (2018) Building blocks of the outer membrane: calculating a general elastic energy model for β-barrel membrane proteins. J Chem Theory Comput 14:4487–4497

Lopez D, Koch G (2017) Exploring functional membrane microdomains in bacteria: an overview. Curr Opin Microbiol 36:76–84

Lorén N, Nydén M, Hermansson A-M (2009) Determination of local diffusion properties in heterogeneous biomaterials. Adv Colloid Interface Sci 150:5–15

Los GV, Encell LP, McDougall MG, Hartzell DD, Karassina N, Zimprich C, Wood MG, Learish R, Ohana RF, Urh M, Simpson D, Mendez J, Zimmerman K, Otto P, Vidugiris G, Zhu J, Darzins A, Klaubert DH, Bulleit RF, Wood KV (2008) HaloTag: a novel protein labeling technology for cell imaging and protein analysis. ACS Chem Biol 3:373–382

Lucena D,Mauri M, Schmidt F, Eckhardt B, Graumann PL (2018) Microdomain formation is a general property of bacterial membrane proteins and induces heterogeneity of diffusion patterns. BMC biology, 16(1):1–17

Lukinavičius G, Umezawa K, Olivier N, Honigmann A, Yang G, Plass T, Mueller V, Reymond L, Corrêa IR Jr, Luo Z-G, Schultz C, Lemke EA, Heppenstall P, Eggeling C, Manley S, Johnsson K (2013) A near-

infrared fluorophore for live-cell super-resolution microscopy of cellular proteins. Nat Chem 5:132–139
Lutz E (2001) Fractional Langevin equation. Phys Rev E Stat Nonlinear Soft Matter Phys 64:051106
Martin DS, Forstner MB, Käs JA (2002) Apparent subdiffusion inherent to single particle tracking. Biophys J 83:2109–2117
Mas G, Thoma J, Hiller S (2019) The periplasmic chaperones Skp and SurA. In: Kuhn A (ed) Bacterial cell walls and membranes. Springer, Cham, pp 169–186
Matsuda Y, Hanasaki I, Iwao R, Yamaguchi H, Niimi T (2018) Estimation of diffusive states from single-particle trajectory in heterogeneous medium using machine-learning methods. Phys Chem Chem Phys PCCP 20:24099–24108
Michalet X, Berglund AJ (2012) Optimal diffusion coefficient estimation in single-particle tracking. Phys Rev E Stat Nonlinear Soft Matter Phys 85:061916
Mika JT, Poolman B (2011) Macromolecule diffusion and confinement in prokaryotic cells. Curr Opin Biotechnol 22:117–126
Mullineaux CW, Nenninger A, Ray N, Robinson C (2006) Diffusion of green fluorescent protein in three cell environments in Escherichia coli. J Bacteriol 188:3442–3448
Nagle JF (1992) Long tail kinetics in biophysics? Biophys J 63:366–370
Nielsen HJ, Li Y, Youngren B, Hansen FG, Austin S (2006) Progressive segregation of the Escherichia coli chromosome. Mol Microbiol 61:383–393
Niu L, Yu J (2008) Investigating intracellular dynamics of FtsZ cytoskeleton with photoactivation single-molecule tracking. Biophys J 95:2009–2016
Oddershede L, Dreyer JK, Grego S, Brown S, Berg-Sørensen K (2002) The motion of a single molecule, the lambda-receptor, in the bacterial outer membrane. Biophys J 83:3152–3161
Oh D, Yu Y, Lee H, Wanner BL, Ritchie K (2014) Dynamics of the serine chemoreceptor in the Escherichia coli inner membrane: a high-speed single-molecule tracking study. Biophys J 106:145–153
Ormö M, Cubitt AB, Kallio K, Gross LA, Tsien RY, Remington SJ (1996) Crystal structure of the aequorea victoria green fluorescent protein. Science 273:1392–1395
Oswald F, Varadarajan A, Lill H, Peterman EJG, Bollen YJM (2016) MreB-dependent organization of the E. coli cytoplasmic membrane controls membrane protein diffusion. Biophys J 110:1139–1149
Oyama N, Kawasaki T, Mizuno H, Ikeda A (2019) Glassy dynamics of a model of bacterial cytoplasm with metabolic activities. Phys Rev Res 1:032038
Pan W, Filobelo L, Pham NDQ, Galkin O, Uzunova VV, Vekilov PG (2009) Viscoelasticity in homogeneous protein solutions. Phys Rev Lett 102:108–4
Parry BR, Surovtsev IV, Cabeen MT, O'Hern CS, Dufresne ER, Jacobs-Wagner C (2014) The bacterial cytoplasm has glass-like properties and is fluidized by metabolic activity. Cell 156:183–194
Perez AJ, Cesbron Y, Shaw SL, Bazan Villicana J, Tsui H-CT, Boersma MJ, Ye ZA, Tovpeko Y, Dekker C, Holden S, Winkler ME (2019) Movement dynamics of divisome proteins and PBP2x:FtsW in cells of Streptococcus pneumoniae. Proc Natl Acad Sci U S A 116:3211–3220
Persson F, Lindén M, Unoson C, Elf J (2013) Extracting intracellular diffusive states and transition rates from single-molecule tracking data. Nat Methods 10:265–269
Postow L, Hardy CD, Arsuaga J, Cozzarelli NR (2004) Topological domain structure of the Escherichia coli chromosome. Genes Dev 18:1766–1779
Rassam P, Copeland NA, Birkholz O, Tóth C, Chavent M, Duncan AL, Cross SJ, Housden NG, Kaminska R, Seger U, Quinn DM, Garrod TJ, Sansom MSP, Piehler J, Baumann CG, Kleanthous C (2015) Supramolecular assemblies underpin turnover of outer membrane proteins in bacteria. Nature 523:333–336
Rayan G, Guet J-E, Taulier N, Pincet F, Urbach W (2010) Recent applications of fluorescence recovery after photobleaching (FRAP) to membrane bio-macromolecules. Sensors 10:5927–5948
Ringgaard S, van Zon J, Howard M, Gerdes K (2009) Movement and equipositioning of plasmids by ParA filament disassembly. Proc Natl Acad Sci U S A 106:19369–19374
Rudner DZ, Losick R (2010) Protein subcellular localization in bacteria. Cold Spring Harb Perspect Biol 2:a000307–a000307
Ruiz N, Kahne D, Silhavy TJ (2006) Advances in understanding bacterial outer-membrane biogenesis. Nat Rev Microbiol 4:57–66
Rust MJ, Bates M, Zhuang X (2006) Sub-diffraction-limit imaging by stochastic optical reconstruction microscopy (STORM). Nat Methods 3:793–796
Sadoon AA, Wang Y (2018) Anomalous, non-Gaussian, viscoelastic, and age-dependent dynamics of histone-like nucleoid-structuring proteins in live Escherichia coli. Physical Review E, 98(4):042411
Saffman PG, Delbrück M (1975) Brownian motion in biological membranes. Proc Natl Acad Sci 72:3111–3113
Schavemaker PE, Śmigiel WM, Poolman B (2017) Ribosome surface properties may impose limits on the nature of the cytoplasmic proteome. eLife 6
Shaner NC, Campbell RE, Steinbach PA, Giepmans BNG, Palmer AE, Tsien RY (2004) Improved monomeric red, orange and yellow fluorescent proteins derived from Discosoma sp. red fluorescent protein. Nat Biotechnol 22:1567–1572
Shaner NC, Lambert GG, Chammas A, Ni Y, Cranfill PJ, Baird MA, Sell BR, Allen JR, Day RN, Israelsson M, Davidson MW, Wang J (2013) A bright monomeric green fluorescent protein derived from Branchiostoma lanceolatum. Nat Methods 10:407–409
Slator PJ, Burroughs NJ (2018) A hidden Markov model for detecting confinement in single-particle tracking trajectories. Biophys J 115:1741–1754

Sochacki KA, Shkel IA, Record MT, Weisshaar JC (2011) Protein diffusion in the periplasm of E. coli under osmotic stress. Biophys J 100:22–31

Spector J, Zakharov S, Lill Y, Sharma O, Cramer WA, Ritchie K (2010) Mobility of BtuB and OmpF in the Escherichia coli outer membrane: implications for dynamic formation of a translocon complex. Biophys J 99:3880–3886

Stepanenko OV, Stepanenko OV, Shcherbakova DM, Kuznetsova IM, Turoverov KK, Verkhusha VV (2011) Modern fluorescent proteins: from chromophore formation to novel intracellular applications. BioTechniques 51:313–4–316–318 passim

Stracy M, Uphoff S, Garza de Leon F, Kapanidis AN (2014) In vivo single-molecule imaging of bacterial DNA replication, transcription, and repair. FEBS Lett 588:3585–3594

Stracy M, Lesterlin C, Garza de Leon F, Uphoff S, Zawadzki P, Kapanidis AN (2015) Live-cell superresolution microscopy reveals the organization of RNA polymerase in the bacterial nucleoid. Proc Natl Acad Sci U S A 112:E4390–E4399

Stracy M, Wollman AJ, Kaja E, Gapinski J, Lee J-E, Leek VA, McKie SJ, Mitchenall LA, Maxwell A, Sherratt DJ, Leake MC, Zawadzki P (2018) Single-molecule imaging of DNA gyrase activity in living Escherichia coli. Nucleic Acids Res 6:11055–11

Strahl H, Bürmann F, Hamoen LW (2014) The actin homologue MreB organizes the bacterial cell membrane. Nat Commun 5:3442

Subach FV, Patterson GH, Manley S, Gillette JM, Lippincott-Schwartz J, Verkhusha VV (2009) Photoactivatable mCherry for high-resolution two-color fluorescence microscopy. Nat Methods 6:153–159

Swaminathan R, Hoang CP, Verkman AS (1997) Photobleaching recovery and anisotropy decay of green fluorescent protein GFP-S65T in solution and cells: cytoplasmic viscosity probed by green fluorescent protein translational and rotational diffusion. Biophys J 72:1900–1907

Terry BR, Matthews EK, Haseloff J (1995) Molecular characterisation of recombinant green fluorescent protein by fluorescence correlation microscopy. Biochem Biophys Res Commun 217:21–27

Thapa S, Lomholt MA, Krog J, Cherstvy AG, Metzler R (2018) Bayesian analysis of single-particle tracking data using the nested-sampling algorithm: maximum-likelihood model selection applied to stochastic-diffusivity data. Phys Chem Chem Phys PCCP 20:29018–29037

van den Bogaart G, Hermans N, Krasnikov V, Poolman B (2007) Protein mobility and diffusive barriers in Escherichia coli: consequences of osmotic stress. Mol Microbiol 64:858–871

Verhoeven GS, Dogterom M, den Blaauwen T (2013) Absence of long-range diffusion of OmpA in E. coli is not caused by its peptidoglycan binding domain. BMC Microbiol 13:66

Vink JNA, Martens KJA, Vlot M, McKenzie RE, Almendros C, Estrada Bonilla B, Brocken DJW, Hohlbein J, Brouns SJJ (2020) Direct visualization of native CRISPR target search in live bacteria reveals cascade DNA surveillance mechanism. Mol Cell 77:39–50.e10

von Hippel PH, Berg OG (1989) Facilitated target location in biological systems. J Biol Chem 264:675–678

Vrljic M, Nishimura SY, Moerner WE (2007) Single-molecule tracking. Methods Mol Biol 398:193–219

Wang P, Robert L, Pelletier J, Dang WL, Taddei F, Wright A, Jun S (2010) Robust growth of Escherichia coli. Curr Biol CB 20:1099–1103

Wang W, Li G-W, Chen C, Xie XS, Zhuang X (2011) Chromosome organization by a nucleoid-associated protein in live bacteria. Science 333:1445–1449

Weber SC, Spakowitz AJ, Theriot JA (2010a) Bacterial chromosomal loci move subdiffusively through a viscoelastic cytoplasm. Phys Rev Lett 104:238102

Weber SC, Theriot JA, Spakowitz AJ (2010b) Subdiffusive motion of a polymer composed of subdiffusive monomers. Phys Rev E 82:011913

Weber SC, Thompson MA, Moerner WE, Spakowitz AJ, Theriot JA (2012a) Analytical tools to distinguish the effects of localization error, confinement, and medium elasticity on the velocity autocorrelation function. Biophys J 102:2443–2450

Weber SC, Spakowitz AJ, Theriot JA (2012b) Nonthermal ATP-dependent fluctuations contribute to the in vivo motion of chromosomal loci. Proc Natl Acad Sci U S A 109:7338–7343

Weeks ER, Weitz DA (2002) Properties of cage rearrangements observed near the colloidal glass transition. Phys Rev Lett 89:095704

Weiss M (2013) Single-particle tracking data reveal anticorrelated fractional Brownian motion in crowded fluids. Phys Rev E 88:010101

Weng X, Bohrer CH, Bettridge K, Lagda AC, Cagliero C, Jin DJ, Xiao J (2018) RNA polymerase organizes into distinct spatial clusters independent of ribosomal RNA transcription in E. coli. BioRxiv 320481

Wheeler RT, Shapiro L (1999) Differential localization of two histidine kinases controlling bacterial cell differentiation. Mol Cell 4:683–694

Winick M (1968) Changes in nucleic acid and protein content of the human brain during growth. Pediatr Res 2:352–355

Winther T, Xu L, Berg-Soslashrensen K, Brown S, Oddershede LB (2009) Effect of energy metabolism on protein motility in the bacterial outer membrane. Biophys J 97:1305–1312

Xiao J, Elf J, LiG, Yu J, Xie XS (2007) Imaging gene expression in living cells at the single-molecule level. In Single Molecules: a laboratory manual, Edited by Selvin P and Ha T, Cold Spring Harbor Press, New York city, 149–160

Yang X, Lyu Z, Miguel A, McQuillen R, Huang KC, Xiao J (2017) GTPase activity-coupled treadmilling of the bacterial tubulin FtsZ organizes septal cell wall synthesis. Science 355:744–747

Yeow EKL, Melnikov SM, Bell TDM, Schryver FCD, Hofkens J (2006) Characterizing the fluorescence intermittency and photobleaching kinetics of dye molecules

immobilized on a glass surface. J Phys Chem A 110:1726–1734

Zhang F, Lee GM, Jacobson K (1993) Protein lateral mobility as a reflection of membrane microstructure. BioEssays News Rev Mol Cell Dev Biol 15:579–588

Zhang G, Gurtu V, Kain SR (1996) An enhanced green fluorescent protein allows sensitive detection of gene transfer in Mammalian cells. Biochem Biophys Res Commun 227:707–711

Zhang LC, Chen YF, Chen WL, Zhang CC (2008) Existence of periplasmic barriers preventing green fluorescent protein diffusion from cell to cell in the cyanobacterium Anabaena sp. strain PCC 7120. Mol Microbiol 70:814–823

Zhang M, Chang H, Zhang Y, Yu J, Wu L, Ji W, Chen J, Liu B, Lu J, Liu Y, Zhang J, Xu P, Xu T (2012) Rational design of true monomeric and bright photoactivatable fluorescent proteins. Nat Methods 9:727–729

Zhang LC, Risoul V, Latifi A, Christie JM, Zhang CC (2013) Exploring the size limit of protein diffusion through the periplasm in cyanobacterium Anabaena sp. PCC 7120 using the 13 kDa iLOV fluorescent protein. Res Microbiol 164:710–717

Physical Views on ParABS-Mediated DNA Segregation

3

Baptiste Guilhas, Antoine Le Gall, and Marcello Nollmann

Abstract

In this chapter, we will focus on ParABS: an apparently simple, three-component system, required for the segregation of bacterial chromosomes and plasmids. We will specifically describe how biophysical measurements combined with physical modeling advanced our understanding of the mechanism of ParABS-mediated complex assembly, segregation and positioning.

Keywords

DNA segregation · Super-resolution microscopy · Sub-cellular organization · Quantitative methods · DNA organization

Abbreviations

DNA	deoxyribonucleic acid
GTP	guanosine triphosphate
ATP	adenosine triphosphate
NTP	nucleoside triphosphate
CBP	centromere binding protein
Ori	replication origin region
Ter	replication termination region
nsDNA	non-specific DNA
Kb	kilobase

B. Guilhas · A. Le Gall · M. Nollmann (✉)
Centre de Biochimie Structurale, CNRS UMR 5048, INSERM U1054, Université de Montpellier, Montpellier, France
e-mail: marcelo.nollmann@cbs.cnrs.fr

3.1 Introduction

Faithful inheritance of genetic information is critical for cell viability. This process specifically requires the efficient and robust segregation and organization of DNA molecules within the sub-cellular space of the cell. To this end, most bacteria make use of active partitioning systems. These systems are typically composed of three factors: a centromere DNA sequence, a centromere binding protein (CBP), and a NTPase. The specific DNA sequence recruits an assemblage of the CBP that self-assembles into a macromolecular complex called the partition complex. This complex is segregated by the NTPase motor protein. These partitioning systems have been classified into three groups according to their NTPase (Bouet and Funnell 2019; Brooks and Hwang 2017): Type I systems are based on Walker-type ATPases, Type II code for actin-like ATPases, and Type III systems use tubulin-like GTPases.

ParAB*S* systems are members of the Type Ia partition system (Ebersbach and Gerdes 2005), a subdivision of the type I class that partly emerges from specific properties of the centromere binding protein. Binding of the CBPs (typically

G. Duménil, S. van Teeffelen (eds.), *Physical Microbiology*, Advances in Experimental Medicine and Biology 1267, https://doi.org/10.1007/978-3-030-46886-6_3

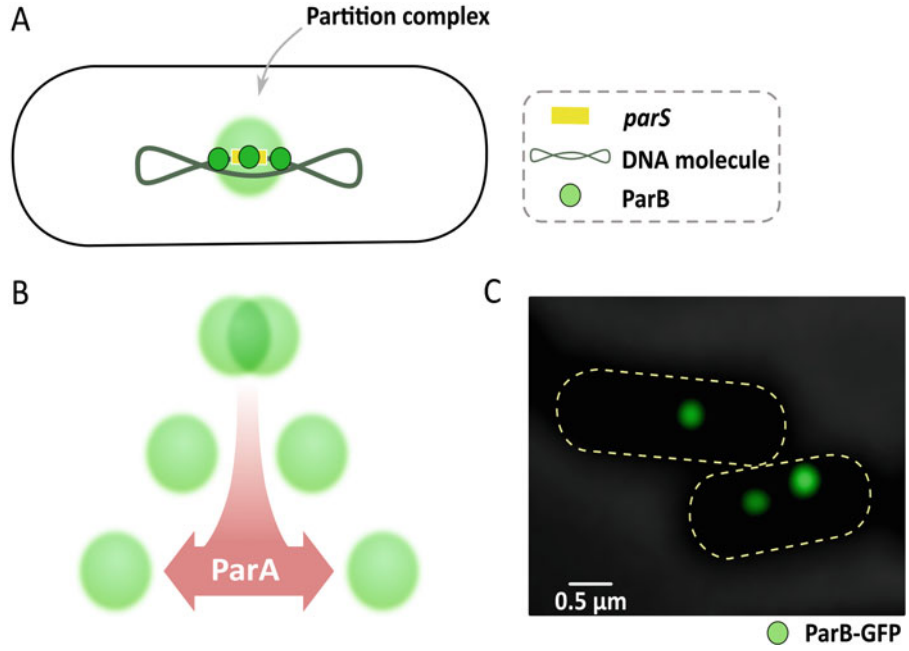

Fig. 3.1 ParAB*S*-mediated segregation of DNA molecules. (**a**) *parS* sequences (yellow) recruit several hundreds of ParB proteins (green sphere) to form the partition complex (green gradient). (**b**) Segregation of partition complexes by the ParA ATPase (red arrow) leads to the separation of DNA molecules harbouring *parS*. (**c**) Partition complexes can be imaged by visualizing ParB-GFP by fluorescence microscopy (image shows ParB-GFP from F-plasmid in *E.coli*). Partition complexes appear in green, and cell contours are represented with yellow, dashed curves

called ParB) to centromeric sequences (called *parS*) lead to the robust formation of partition complexes (also called ParB*S* complexes, Fig. 3.1a). Once DNA is replicated, *parS*-containing DNA molecules are split, segregated, and positioned at specific sub-cellular locations. These processes typically require the action of ParA, the motor protein (Ah-Seng et al. 2013; Debaugny et al. 2018) (Fig. 3.1b). ParAB*S* systems are conserved in more than 60% of sequenced bacterial species, and are the most widespread in bacteria (Gerdes et al. 2000; Livny et al. 2007). While other partition systems are exclusively dedicated to plasmid partitioning, ParAB*S* systems segregate both plasmids and bacterial chromosomes (Badrinarayanan et al. 2015; Baxter and Funnell 2014; Bouet and Funnell 2019).

3.1.1 Chromosomal ParAB*S* Systems

Bacteria are among the smallest forms of cellular life. To face the challenge of packaging their relatively large genome without compromising cellular processes, they display a complex internal organization (Fig. 3.2). This ensures that, upon cell division, cellular checkpoints may be applied in space and time to ensure that low copy number components are evenly distributed among the daughter cells. Unlike eukaryotes, bacteria generally have only one chromosome that replicates concomitantly with cell growth. Bacterial chromosomes generally fold into two main configurations: longitudinal or transverse (Badrinarayanan et al. 2015; Baxter and Funnell 2014; Bouet and

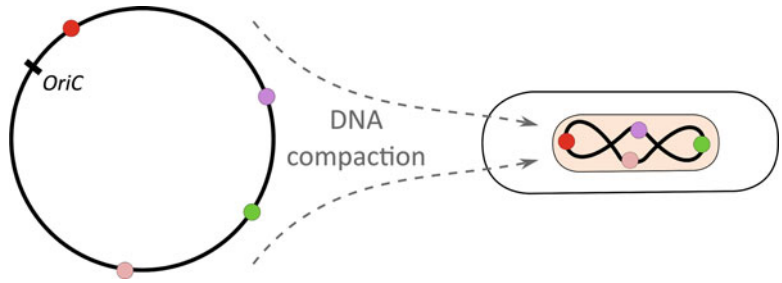

Fig. 3.2 The topologically closed bacterial chromosome (circle in left panel) is compacted into the sub-cellular space following a well-defined choreography whereby each genomic region occupies a specific sub-cellular location. This positioning is controlled by different factors, including the ParAB*S* system

Funnell 2019). In the longitudinal configuration, the origin (*Ori*) and terminus (*Ter*) of replication are located at opposite ends of the cell with left and right chromosomal arms between the two, arranged side by side. In the transverse configuration *Ori* and *Ter* are located at the middle of the cell with the left and right arms arranged in separate cell halves. In either case, the origin and terminus of replication are located at specific locations in the cellular space that must be restored during replication and maintained once replication is completed. Chromosomal ParAB*S* systems serve both for the segregation and positioning of the duplicated origin proximal region of the chromosome and were recently identified as a hub for the loading of whole-chromosome organisers, namely the SMC-ScpAB complexes.

Most chromosomal *parS* sequences are located in the immediate vicinity of *Ori* (Bouet and Funnell 2019; Livny et al. 2007). When tagged with a fluorescent reporter, ParB forms, *in vivo*, bright fluorescent foci whose dimensions are diffraction limited (Fig. 3.1). These ParB foci are referred to as partition complexes. The positioning and segregation pattern of partition complexes reflect the positioning of origin-proximal regions containing *parS* sequences, but vary among bacterial species. In *Vibrio cholerae* (Yamaichi et al. 2007), *Caulobacter crescentus* (Mohl and Gober 1997; Toro et al. 2008) or sporulating *Bacillus subtilis* (Lin et al. 1997; Webb et al. 1997), this region is anchored at the cell pole while the *Ter* is either anchored at the opposite side of the cell (notably in *Caulobacter*) or positioned at the cell center (e.g. *B. subtilis, V. cholerae or Pseudomonas aeruginosa*). Polar anchoring is mediated through direct interactions between ParB and polar proteins such as PopZ in *C. crescentus* (Bowman et al. 2008; Ebersbach et al. 2008) and HubP in *V. cholerae* (Yamaichi et al. 2012). In sporulating *B. subtilis*, ParAB*S*-mediated segregation facilitates the RacA/DivIVA-dependent polar anchoring (Ben-Yehuda et al. 2003; Wang and Rudner 2014). In *Caulobacter*, the ParAB*S* system is essential for origin segregation and for the establishment of proper chromosome choreography. After replication and splitting of *Ori* regions, one of the two replicated origins migrates to the opposite pole, crossing the cell and the nucleoid from one pole to the other (Fig. 3.3a) (Ptacin et al. 2014; Shebelut et al. 2010; Wang and Rudner 2014). ParA is known to play a key role in this segregation process. In this system, the disruption of the motor protein ParA prevents the directed movement of *Ori* and impedes it from reaching the opposite pole (Shebelut et al. 2010). Using conventional fluorescence microscopy, ParA was shown to form a wave over the nucleoid that oscillates between cell poles, however the mechanism underlying this oscillatory behavior of ParA remains unclear. In vegetative *B. subtilis*, a similar process takes place, where replicated origins are segregated bidirectionally from midcell to ¼ and ¾ of the cell main axis (Lee et al. 2003; Wang et al. 2014a) (Fig. 3.3b). The ParAB*S* system plays important roles in this micrometric-scale translocation event, however it is not essential for cell viability. Lack of ParA leads to three defects in *Ori* segregation, namely

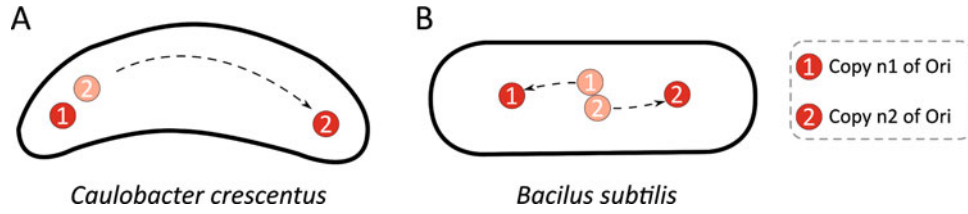

Fig. 3.3 Models for the segregation of newly replicated origins in *C. crescentus* and *B. subtilis*. (**a**) In *C. crescentus*, the partition system is essential for the Ori to cross the cell. (**b**) In *B. subtilis*, the ParABS system is required for proper resolution and segregation of replicated origins and is key to ensure the stable sub-cellular positioning of segregated origins

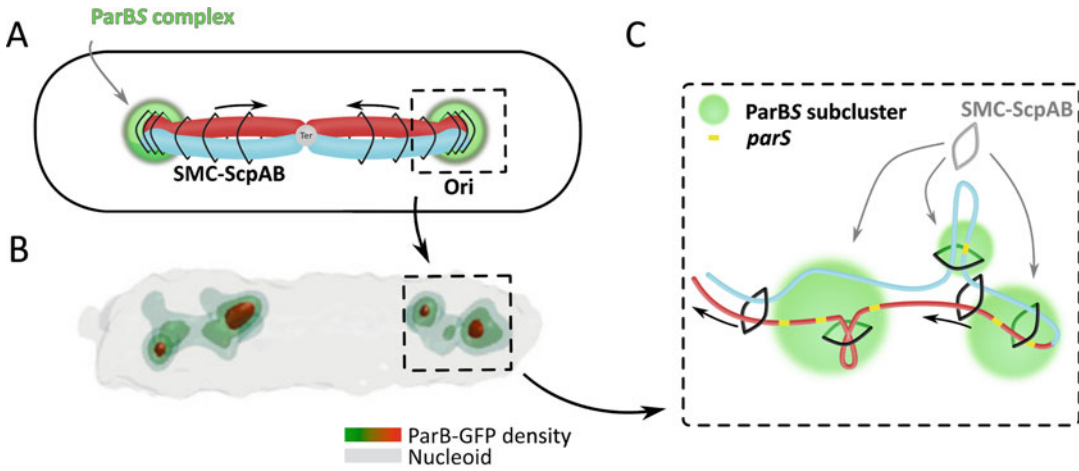

Fig. 3.4 Compaction of *B. subtilis* chromosome mediated by ParB*S* and SMC-ScpAB complexes. (**a**) Condensin complexes (black arcs) are recruited by the ParB*S* partition complex (green) to *Ori* regions. They then slide or translocate towards the terminus of replication, and pair the two replication arms (blue and red) together. (**b**) 3D-structured Illumination Microscopy image of ParB-GFP in *B. subtilis*. (**c**) Schematic representation of the folding of the origin-proximal region. ParB*S* subclusters (green) are nucleated by *parS* sites (yellow) and recruit SMC-ScpAB condensin complexes (black arcs)

an altered resolution characterized by a longer cohesion time between the two newly replicated origins (Lee et al. 2003), a loss in segregation featured by the abolishment of bi-directionnal movement, and a lack of robust positioning characterized by frequent backward movements of *Ori* towards midcell (Wang et al. 2014a).

Bacterial species harbouring ParAB*S* systems typically rely on a second factor to properly segregate and localize chromosomes: the SMC-ScpAB complex (Gruber 2018). This complex consists of two structural maintenance of chromosomes (SMC) subunits and two kleisin homologues (ScpA and ScpB). SMC-ScpAB is recruited to *Ori*-proximal regions by specific interactions with ParB bound to *parS* (Fig. 3.4a) (Gruber and Errington 2009; Miermans and Broedersz 2018; Sullivan et al. 2009; Wang et al. 2017). In *B. subtilis*, SMC-ScpAB is required for the proper resolution of freshly replicated sister origins (Gruber et al. 2014; Lee et al. 2003; Marbouty et al. 2015; Wang et al. 2014b). Recently, the use of chromosome conformation capture technologies (3C-seq) has revealed that SMC-ScpAB bridge long-range interactions between left and right replichores that extend from *Ori* to *Ter* (Fig. 3.4a) (Marbouty et al. 2015; Wang et al. 2015). ParB, *parS* and SMC-ScpAB are all essential for bridging interarm interactions and participate in the proper establishment of the longitudinal organization of bacterial chromosomes (Marbouty et al. 2015;

Wang et al. 2015). How the loading of SMC-ScpAB to *Ori*-proximal *parS* sequences leads to the global organization of the genome is still unclear. Current models point towards an active translocation of SMC-ScpAB along the chromosome by a mechanism with parallels with the DNA loop extrusion model (Alipour and Marko 2012). In addition to organizing the global folding of the genome, SMC-ScpAB plays a role in the spatial organization of the *Ori*-proximal region by bridging together distant *parS* sequences (Fig. 3.4c) (Marbouty et al. 2015). Super-resolution microscopy showed that this spatial organization changes with the cell cycle and with the sub-cellular positioning of origins, suggesting that the 3D folding of the origin region could play a role in the regulation of replication initiation (Marbouty et al. 2015) (Fig. 3.4b). Thus, in *B. subtilis*, both the ParAB*S* system (Wang and Rudner 2014) and the SMC-ScpAB complex act in concert to achieve chromosome segregation and robust chromosome choreography (Marbouty et al. 2015; Miermans and Broedersz 2018; Wang et al. 2017, 2015).

3.1.2 Plasmidic ParAB*S* Systems

Plasmids are short (5–300 kb), closed-circular DNA molecules that confer advantages to the host cell, such as antibiotic resistance, virulence attributes or new metabolic traits (Ochman et al. 2000). Plasmids can be transferred horizontally between cells in a colony to propagate beneficial qualities into the population (Ochman et al. 2000). High-copy number plasmids harbour hundreds to thousands of copies per cell, therefore random partition between daughter cells is enough to ensure their propagation (Reyes-Lamothe et al. 2014; Wang 2017). Low copy number plasmids (typically 2–3 per cell), instead, rely on partitioning systems to ensure faithful partitioning by regulating their spatial localization within the host cell.

Escherichia coli plasmids F and P1 are two low-copy number plasmids for which the ParAB*S* system is both essential and sufficient for stable inheritance (Austin and Wierzbicki 1983). The ParAB*S* system is required for their specific sub-cellular localization, ensuring the presence of at least one copy in each cell half upon cell division. Shortly after plasmid replication, the ParAB*S* system splits the single partition complex into two separate complexes (Ah-Seng et al. 2013; Fung et al. 2001; Onogi et al. 2002). The action of the ParAB*S* system also ensures that, on average, plasmids are equidistributed along the main axis of the nucleoid (Fig. 3.5) (Ringgaard et al. 2009; Sengupta et al. 2010). It is important to note that, after segregation, plasmids occupy specific sub-cellular locations, but that their movement remains highly dynamic. In fact, in rare cases segregated partition complexes can coalesce and fuse into a single partition complex (Sengupta et al. 2010). Importantly, the stable sub-cellular localization of partition complexes is severely affected in the absence of ParA (Le Gall et al. 2016). More generally, the deletion of any of the three components of the ParAB*S* system leads to the loss of the plasmid, gradually at each cell division, due to aberrant partition complex positioning.

3.2 ParA-Mediated Partitioning

In eukaryotic DNA segregation, microtubules pull chromosomes towards the poles during mitosis (Heald and Nogales 2002). In this process, the growth of filaments regulated by GTP-hydrolysis promotes chromosome partitioning between the two daughter cells. The segregation of plasmids and chromosomes by the ParAB*S* system also uses the energy of NTP hydrolysis. Early observations of ParA *in vitro* polymerization lead to models suggesting that DNA segregation by ParAB*S* may also require the formation of long filaments (Bouet et al. 2007; Ebersbach et al. 2006; Lim et al. 2005). More recent studies using super-resolution microscopy methods showed, however, that ParA does not form long filaments in living cells (Le Gall et al. 2016; Lim et al. 2014). Instead, a body of evidence now supports a chemophoresis or reaction-diffusion mechanism (see below) whereby the ParB*S* complex modulates the inhomogeneous

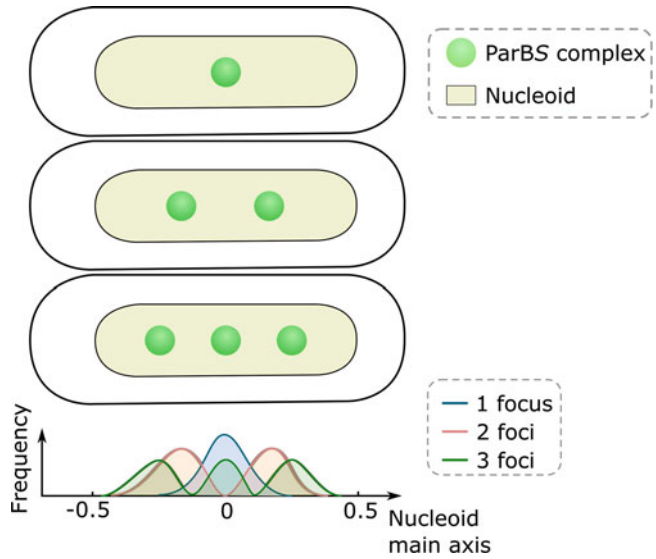

Fig. 3.5 ParAB*S*-mediated sub-cellular organization of low copy number plasmids. On average, plasmids are equidistributed along the main axis of the nucleoid, but the actual positions depend on the number of plasmids per cell. This spatial pattern ensures faithful partitioning during cell division of the host. Cell outline (black curve), nucleoid (grey), and partition complexes (green circles) are represented in the first three schemes. The bottom plot displays the average axial localization of plasmids for cells containing one, two or three partition complexes

and dynamic patterning of ParA (Vechiarelli 2010; Sugawara and Kaneko 2011; Ietswaart et al. 2014). This mechanism shares similarities with that used by PomXYZ and MinCDE to localize the division septum at mid-cell, but also differences in terms of the dynamics and sub-cellular distribution of positioning factors as well as in their mathematical descriptions (Bergeler and Frey 2018; Lutkenhaus 2007; Wingreen and Huang 2015).

Critically, ParA-ATP binds non-specific DNA (nsDNA) efficiently, while ParA-ADP displays a considerable reduction in nsDNA binding (Davey and Funnell 1994). Interestingly, ParA's ATP hydrolysis rate is low in the absence of other factors, but is synergistically stimulated by the presence of nsDNA, *parS* and ParB (Davis et al. 1992). ParA-ADP recovers its nsDNA-binding capacity after ATP re-binding and a conformational change (Davey and Funnell 1997; Libante et al. 2001; Vecchiarelli et al. 2010). This latter transition is rather slow and introduces a delay in the ParA nsDNA binding cycle (Davey and Funnell 1997; Libante et al. 2001; Vecchiarelli et al. 2010). This delay allows the ParA-ADP form to be homogeneously re-distributed over the entire nucleoid. In particular, the region depleted of ParA in the vicinity of the ParB*S* complex is not immediately refilled and a ParA distribution gradient can persist (Hwang et al. 2013). In the presence of this ParA gradient, the tethering between ParA and ParB*S* is preferably established on the direction of the ParA gradient. This results in an asymmetric tethering that biases the diffusion of the partition complex and creates a directed movement (Hwang et al. 2013; Vecchiarelli et al. 2014a, b). These observations were originally used to propose a first version of a 'diffusion-ratchet' model where plasmid motion is driven by ParA gradients (Fig. 3.6) (Vecchiarelli et al. 2010). Sugawara and Kaneko provided the first mathematical description of this model, and proposed that effective 'chemophoretic' forces exerted by ParA would be responsible for driving plasmid movement and plasmid equipartitioning (Sugawara and Kaneko 2011). More recently, Ietswaart et al. additionally showed that mid-cell and quarter-positioning of plasmids could occur due to the balancing of ParA fluxes on either side

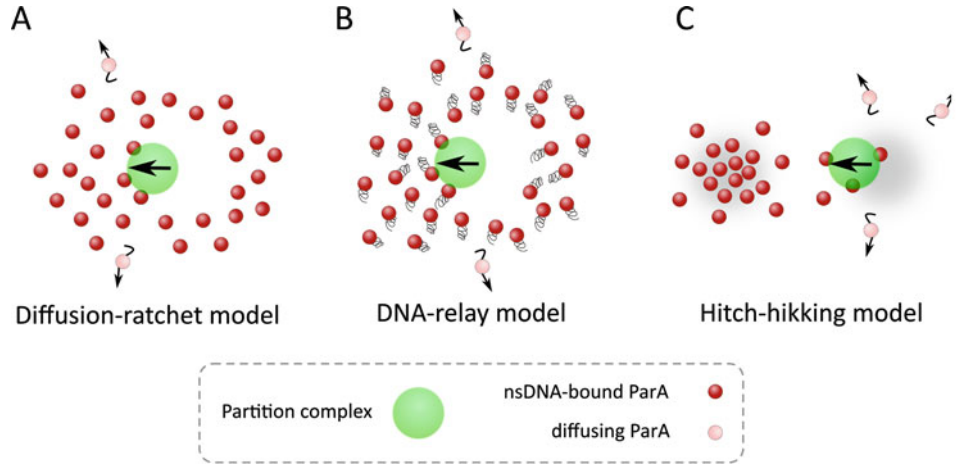

Fig. 3.6 Models of ParA-mediated segregation. (**a**) In the 'diffusion-ratchet' model, directed movement of the partition complex (green sphere) results from a thermodynamic force generated by the asymmetric DNA-bound ParA distribution (red spheres) present near the complex. (**b**) In the 'DNA-relay' model, the partition complex exploits the energy of thermal fluctuations of the DNA-bound ParA (red spheres). (**c**) The hitch-hiking model proposes that HDRs (high-density chromosomal DNA regions, shade) create pools of DNA-bound ParA that direct the movement of partition complexes

of the plasmid – giving rise to the 'flux-balance' mechanism (Ietswaart et al. 2014). The same year, the Mizzuchi lab extended their diffusion-ratchet model by introducing a chemophoresis force to direct cargo motion towards regions of higher ParA concentrations (Vecchiarelli et al. 2014a). Finally, Walter et al. coupled simple linear reaction-diffusion equations with a proteophoresis force (i.e. a volumetric chemophoresis) to describe partition complex translocation and positioning (Walter et al. 2018). Importantly, numerical simulations from all these different laboratories could faithfully reproduce the *in vivo* observation that plasmids move and reach stable sub-cellular positions without the requirement of ParA polymers.

Experimental support for these mechanisms arose, to a large extent, from elegant *in vitro* fluorescence microscopy experiments showing that ParB*S* complexes are able to move on a two-dimensional surface decorated by ParA (Vecchiarelli et al. 2013, 2014a). The topology of these experiments lead, understandably, to models where partitioning occurred on the two-dimensional surface of the nucleoid. But, it was not until it became possible to localize ParA and the partition complex within the nucleoid volume with high spatial resolution, that it was realized that plasmid partitioning rather occurs within the interior of the nucleoid (Le Gall et al. 2016). We note that this localization pattern of ParA and the partition complex do not affect the main features of the proposed models.

Recently, other studies on the chromosomal ParAB*S* system of *C. crescentus* argued for a distinct mechanism. Lim et al. (2014) performed computer simulations where they were unable to detect, in their chromosomal ParAB*S* model, *in silico* evidence for directed motion as predicted by the diffusion-reaction model. Thus, they proposed that chromosomal elasticity may represent a key actor in DNA segregation. The "DNA-relay model" posits that ParA-ATP binds to a DNA locus fluctuating in space (Fig. 3.6). These fluctuations help distant DNA-bound ParA to bind to the partition complex. At the beginning of this binding, the DNA-ParA spring is out-of-equilibrium and, under the effect of the spring's restoring force, pulls on the partition complex. Like for reaction-diffusion models, the asymmetric distribution of ParA creates a preferential direction in which more ParA-ParB interactions are formed. Critically, *C. crescentus* ParA displays a distribution gradient that points in the direction

of the main axis of the cell (Lim et al. 2014), with the lowest ParA density observed at the location of unsegregated origins. By combining computer simulations with the pre-existing biochemical properties of *C. crescentus* ParA and ParB, Lim et al. showed that the addition of DNA elasticity to their model recapitulated both the spontaneous formation of propagating ParA gradients, and their oscillation with the partition complex (Surovtsev et al. 2016a, b). While elegant, it is not clear how universal this mechanism may be, as several ParAB*S* systems (e.g. P1 plasmid, *B. subtilis*) fail to exhibit partition complex or ParA gradient oscillations *in vivo* (Hatano and Niki 2010).

A similar concept was later introduced by the Mizuuchi lab to extend their previous work with a molecular explanation of plasmid motion. In the now termed 'Brownian-ratchet' model, the ParB cargo is tethered to DNA-bound ParA through elastic bonds (Hu et al. 2015, 2017). This new ingredient allowed the authors to faithfully recapitulate and explain all the different motility behaviors observed experimentally for the plasmid, notably by varying ParA-ATP-ParB bond dissociation rate and the replenishment rate of the ParA- depletion zone.

A third model ("hitch-hiking model", Fig. 3.6) was proposed from the distribution of ParAB*S* within the volume of the nucleoid. While large macromolecular complexes –such as the RNA polymerase– are generally excluded from the nucleoid (Stracy et al. 2015), the different components of the ParAB*S* system reside within the nucleoid for the entirety of the cell cycle (Le Gall et al. 2016). Critically, this localization pattern requires the energy of ATP hydrolysis, since both the ability of ParA to hydrolyze ATP and the stimulation of ParA's ATP activity by ParB are required to maintain the partition complex confined within the volume of the nucleoid (Le Gall et al. 2016). DNA within the nucleoid is not homogeneously distributed, but instead displays regions of low and high density (HDR - for High-Density chromosomal DNA Regions) (Le Gall et al. 2016; Marbouty et al. 2015).

Interestingly, single ParA particles display static and dynamic trajectories within this inhomogeneous nucleoid, and the former population preferentially localizes to HDRs (Le Gall et al. 2016). These observations were rationalized in terms of the ability of ParA-ATP to bind nsDNA (representing static trajectories), and of Par-ADP from losing this ability (thereby representing dynamic trajectories). Thus, ParA-ATP remains bound to regions with more chromosomal DNA (HDRs), and hydrolysis of ATP leads to a conversion to a form that can diffuse freely on the nucleoid and bind (after a slow conformational change) to other HDRs. This conversion would be favoured by the stimulation of ATP hydrolysis by ParB*S*. The "hitch-hiking model" is based on a diffusion-ratchet mechanism, but incorporates the non-homogeneous, volumetric distribution of the components of the partition system within the inhomogeneous nucleoid (Fig. 3.6). Mathematical validation for this model is still awaiting.

3.3 Partition Complex Assembly

The formation of the partition complex on the centromeric sequence allows both the recognition of DNA molecules and the partitioning mechanism to proceed by promoting ParB-ParA interactions. The partition complex assembles by the binding of ParB to *parS* and the self-organization of multiple ParB dimers into higher-order structures. ParB contains three functional domains (Bouet and Funnell 2019; Funnell 2016): a C-terminal dimerization domain (Fisher et al. 2017; Leonard et al. 2004), a central helix-turn-helix domain that specifically binds *parS* (Schumacher and Funnell 2005), and a flexible N-terminal domain that interacts with ParA (Chen et al. 2015; Song et al. 2017; Zhang and Schumacher 2017). The distribution of ParB binding around *parS* was revealed by chromatin immunoprecipitation sequencing (ChIP-seq), a next-generation sequencing method that determines the binding profile of proteins to genomic DNA (Furey 2012). Surprisingly, ParB

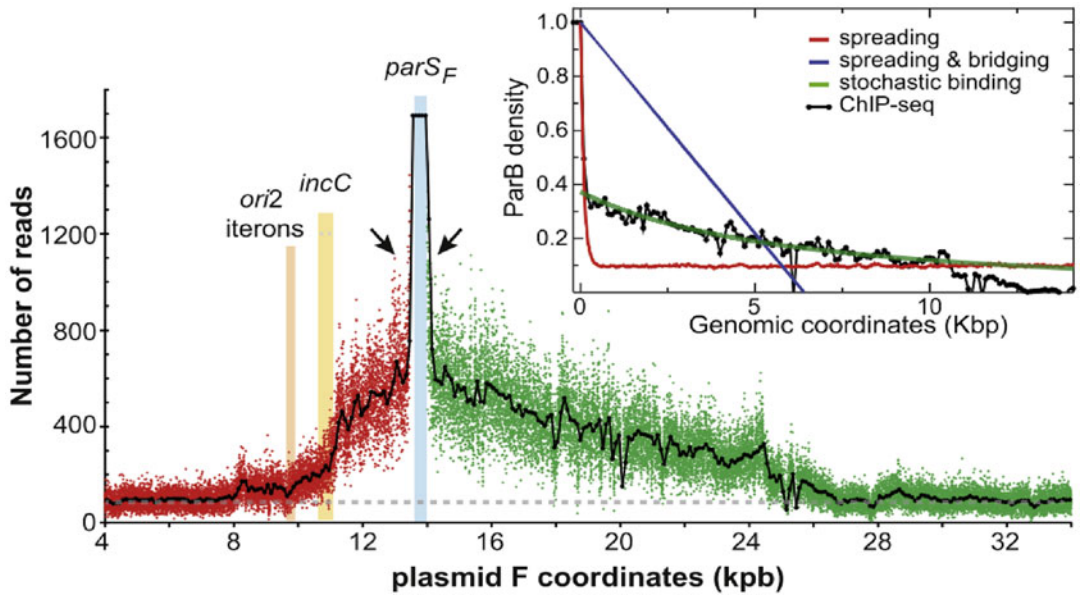

Fig. 3.7 ChIP-Seq DNA-binding profile of ParB (Sanchez et al. 2015). x-axis represents sequence coordinates in the F-plasmid. $ParS_F$ represents the *parS* locus in F-plasmid (with 10 copies of *parS*). *ori2* represents the origin of replication of the F-plasmid. Inset displays the Chip-seq binding experimental profile (black), and the binding profiles predicted by a pure 'spreading' model (red), the 'spreading and bridging' model (blue), and the 'nucleation and caging' model (green)

enrichment was observed not only at *parS* but also extended several kilobases away from the *parS* locus (Fig. 3.7) (Breier and Grossman 2007; Lagage et al. 2016; Lynch and Wang 1995; Murray et al. 2006; Rodionov et al. 1999). This extended binding of ParB is independent of ParA (Breier and Grossman 2007), and depends exclusively on the position of the *parS* sequence since ectopic *parS* sites generate similar DNA binding profiles (Debaugny et al. 2018). The existence of this extended ParB binding profile was observed for all chromosomal and plasmidic partition complexes investigated (Debaugny et al. 2018). Thus, the extended binding pattern of ParB around *parS* may be a universal property of ParAB*S* systems. Importantly, ParB mutants defective in extended binding are also unable to assemble partition complexes (Breier and Grossman 2007).

From this DNA binding profile, a first model of the partition complex structure was proposed in which ParB dimers formed a long filament that originates from *parS* sites (Murray et al. 2006; Rodionov et al. 1999). This "spreading" model was motivated by roadblock experiments that showed that the presence of a strong binding site inserted near the *parS* locus hindered the binding of ParB beyond the roadblock. However, given the number of ParB copies (300 ParB dimers per partition complex (Adachi et al. 2006; Bouet et al. 2005)), a strict linear arrangement along the DNA fibre could not generate a continuous and contiguous spreading over large genomic distances (10 kb).

Recently, single-molecule flow stretching experiments showed that the nucleation of distinct nsDNA-bound ParB complexes leads to DNA condensation (Graham et al. 2014). This and other evidence lead to a second family of models proposing that formation of partition complexes involves both spreading and also long-range, bridging interactions between distant DNA segments that contact each other by 3D looping interactions ("spreading and bridging" model, Fig. 3.8) (Broedersz et al. 2014; Debaugny et al. 2018; Song et al. 2017). Thus,

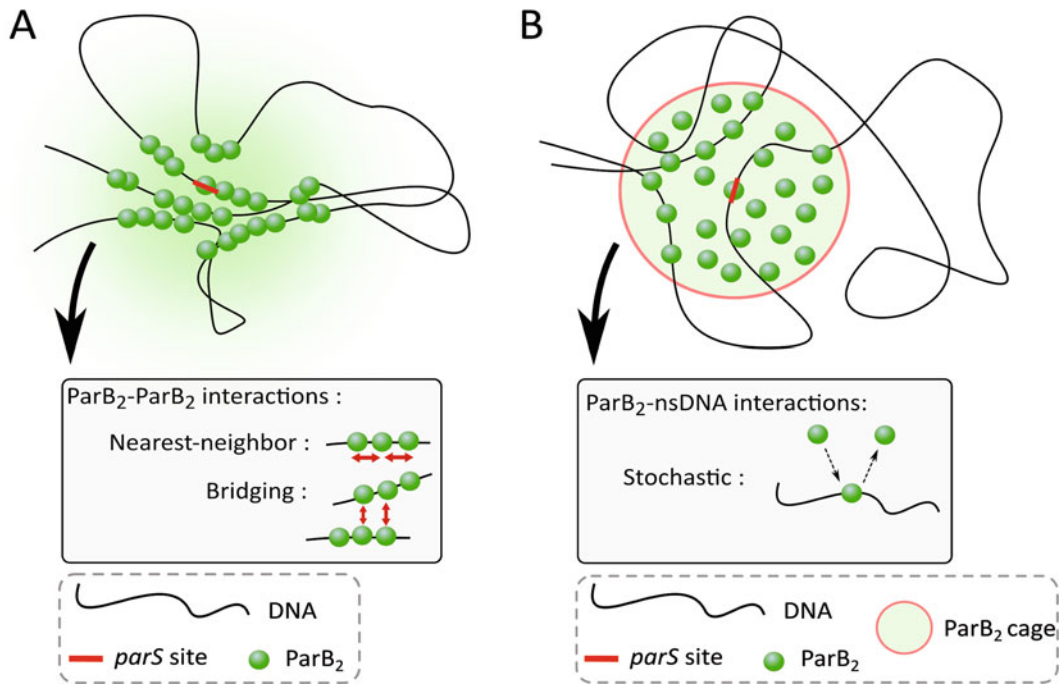

Fig. 3.8 (**a**) Schematic view of the spreading and bridging model, in which the ParB*S* complex is formed by a combination of nearest-neighbor and bridging interactions. (**b**) Schematic view of the Nucleation and Caging model, in which ParBs reside in a defined spherical region and interact stochastically with a fluctuating DNA polymer

this model posits that both nearest-neighbours and bridging interactions are required for the assembly of the partition complex. Using a coarse-grained modeling approach, Broedersz et al. proposed that these interactions are sufficient to assemble a complex composed of multiple small nucleoprotein filaments that interact and cluster together in 3D space (Broedersz et al. 2014; Debaugny et al. 2018; Song et al. 2017). Critically, other combinations of interactions ("adjacent", "bridging", "adjacent or bridging") failed to robustly assemble partition complexes.

The "spreading and bridging" model accounts for many of the key properties of the ParB*S* complex, but is, however, unable to qualitatively reproduce the ParB DNA binding profile (Sanchez et al. 2015). In fact, this profile exhibits an exponential decay from *parS*. Critically, models with only bridging or spreading interactions fail to fit this exponential decay, while the "bridging and spreading" model predicts a linear decay (Sanchez et al. 2015). In addition, evidence from footprinting analysis of ParB binding showed that *parS* sites, but not the neighboring DNA, are protected from proteolysis, suggesting that spreading interactions are not stable (Sanchez et al. 2015). Sanchez et al. proposed a new model ("Nucleation and Caging", Figure 8) that is able to reproduce the extent of ParB binding away from *parS*, as well as its exponential decay with genomic distance (Sanchez et al. 2015). In this model, ParB dimers are localized to the 3D volume surrounding *parS* sequences by: specific interactions with *parS*, weak interactions between ParB dimers, and non-specific interactions with the surrounding DNA. Within this spherical cage, the frequency of interaction of ParB with distant DNA segments is defined by the polymer physics of DNA (de Gennes and Gennes 1979; Schiessel 2013). In fact, super-resolution microscopy showed that partition complexes imprison the large majority of ParB dimers (>90%) in the

cell (Sanchez et al. 2015). More recently, Walter et al. showed that reductions in the value of spreading interactions in the "spreading and bridging model" reproduce the experimental ParB DNA binding profile more faithfully, and fit experimental profiles as well as the "Nucleation and Caging model" when spreading interactions become negligible (Walter et al. 2018). Thus, modeling suggests that long-range 3D looping interactions between ParB dimers -but not spreading interaction- are required for the assembly of the partition complex.

Recently, molecular evidence for ParB-ParB dimer interactions and their roles in DNA condensation and assembly of partition complexes has been unearthed. A co-crystal structure of *Helicobacter pylori* ParB with *parS* (Chen et al. 2015; Song et al. 2017) reveals that ParB tetramerization is mediated by *in cis* and *in trans* interactions involving the N-terminal domain. More recent studies tested the effect of systematic mutations of N-terminal domain residues located in a ParB-ParB interaction hub on DNA compaction (Song et al. 2017) and partition complex assembly (Song et al. 2017; Chen et al. 2015). These studies indicated that mutants in the ParB-ParB interaction hub exhibit abnormal DNA condensation (Song et al. 2017) and fail to assemble partition complexes (Debaugny et al. 2018).

3.4 Conclusion

The ParAB*S* system is a relatively simple apparatus -composed of only three essential components- in contrast to other bacterial machineries with tens of parts (e.g flagellar motor). Yet, despite this apparent simplicity, this system reveals an outstanding degree of complexity. Recent biophysical measurements and physical models helped us to start understanding how partition complexes assemble, and how these complexes are robustly segregated and localized in the sub-cellular space. For instance, a very recent study showed that ParBS assembles a nanometer-sized, liquid-like condensate, while ParA ATPase activity serves to prevent their fusion and ensure their robust nucleoid positioning (Guilhas et al., 2020). However, many mysteries remain unsolved: for instance, the mechanism of formation and separation of liquid-like condensates, the origin of For instance, a very recent study ParA oscillation waves or their purpose (i.e. how they contribute to segregation/positioning), For instance, a very recent study the molecular mechanisms responsible for segregation of newly replicated *parS*-harbouring DNA molecules, or how the coupling of segregation with chromosomal arm cohesion. In future, experimental and theoretical physical approaches will surely continue to provide important insights into these important questions. Importantly, they will also continue to provide a model for how these approaches can be used to study other, more complex, molecular mechanisms. such as those involved in the formation and positioning of phase condensates in eukaryotes.

References

Adachi S, Hori K, Hiraga S (2006) Subcellular positioning of F plasmid mediated by dynamic localization of SopA and SopB. J Mol Biol 356(4):850–863

Ah-Seng Y, Rech J, Lane D, Bouet J-Y (2013) Defining the role of ATP hydrolysis in mitotic segregation of bacterial plasmids. PLoS Genet 9(12):e1003956

Alipour E, Marko JF (2012) Self-Organization of Domain Structures by DNA-loop-extruding enzymes. Nucleic Acids Res 40(22):11202–11212

Austin S, Wierzbicki A (1983) Two mini-F-encoded proteins are essential for equipartition. Plasmid 10(1):73–81

Badrinarayanan A, Le TBK, Laub MT (2015) Bacterial chromosome organization and segregation. Annu Rev Cell Dev Biol 31:171–199

Baxter JC, Funnell BE (2014) Plasmid partition mechanisms. Microbiol Spectr 2(6). https://doi.org/10.1128/microbiolspec.PLAS-0023-2014

Ben-Yehuda S, Rudner DZ, Losick R (2003) RacA, a bacterial protein that anchors chromosomes to the cell poles. Science 299(5606):532–536

Bergeler S, Frey E (2018) Regulation of Pom cluster dynamics in Myxococcus Xanthus. PLoS Comput Biol 14(8):e1006358

Bouet J-Y, Funnell BE (2019) Plasmid localization and partition in Enterobacteriaceae. EcoSal Plus 8(2). https://doi.org/10.1128/ecosalplus.ESP-0003-2019

Bouet JY, Rech J, Egloff S, Biek DP (2005) Probing plasmid partition with centromere-based incompatibility. Molecular. Retrieved from https:/

/onlinelibrary.wiley.com/doi/abs/10.1111/j.1365-2958.2004.04396.x
Bouet J-Y, Ah-Seng Y, Benmeradi N, Lane D (2007) Polymerization of SopA partition ATPase: regulation by DNA binding and SopB. Mol Microbiol 63(2):468–481
Bowman GR, Comolli LR, Zhu J, Eckart M, Koenig M, Downing KH, Moerner WE, Earnest T, Shapiro L (2008) A polymeric protein anchors the chromosomal origin/ParB complex at a bacterial cell pole. Cell 134(6):945–955
Breier AM, Grossman AD (2007) Whole-genome analysis of the chromosome partitioning and sporulation protein Spo0J (ParB) reveals spreading and origin-distal sites on the Bacillus subtilis chromosome. Mol Microbiol 64(3):703–718
Broedersz CP, Wang X, Meir Y, Loparo JJ, Rudner DZ, Wingreen NS (2014) Condensation and localization of the partitioning protein ParB on the bacterial chromosome. Proc Natl Acad Sci U S A 111(24):8809–8814
Brooks AC, Hwang LC (2017) Reconstitutions of plasmid partition systems and their mechanisms. Plasmid 91:37–41
Chen B-W, Lin M-H, Chu C-H, Hsu C-E, Sun Y-J (2015) Insights into ParB spreading from the complex structure of Spo0J and parS. Proc Natl Acad Sci U S A 112(21):6613–6618
Davey MJ, Funnell BE (1994) The P1 plasmid partition protein ParA. A role for ATP in site-specific DNA binding. J Biol Chem 269(47):29908–29913
Davey MJ, Funnell BE (1997) Modulation of the P1 plasmid partition protein ParA by ATP, ADP, and P1 ParB. J Biol Chem 272(24):15286–15292
Davis MA, Martin KA, Austin SJ (1992) Biochemical activities of the parA partition protein of the P1 plasmid. Mol Microbiol 6(9):1141–1147
Debaugny RE, Sanchez A, Rech J, Labourdette D, Dorignac J, Geniet F et al (2018) A conserved mechanism drives partition complex assembly on bacterial chromosomes and plasmids. Mol Syst Biol 14(11):e8516
Ebersbach G, Briegel A, Jensen GJ, Jacobs-Wagner C (2008) A self-associating protein critical for chromosome attachment, division, and polar organization in Caulobacter. Cell 134(6):956–968
Ebersbach G, Gerdes K (2005) Plasmid segregation mechanisms. Annu Rev Genet 39:453–479
Ebersbach G, Ringgaard S, Moller-Jensen J, Wang Q, Sherratt DJ, Gerdes K (2006) Regular cellular distribution of plasmids by oscillating and filament-forming ParA ATPase of plasmid pB171. Mol Microbiol 61:1428–1442. https://doi.org/10.1111/j.1365-2958.2006.05322.x
Fisher GL, Pastrana CL, Higman VA, Koh A, Taylor JA, Butterer A, Craggs T, Sobott F, Murray H, Crump MP, Moreno-Herrero F, Dillingham MS (2017) The structural basis for dynamic DNA binding and bridging interactions which condense the bacterial centromere. elife 6. https://doi.org/10.7554/eLife.28086
Fung E, Bouet JY, Funnell BE (2001) Probing the ATP-binding site of P1 ParA: partition and repression have different requirements for ATP binding and hydrolysis. EMBO J 20(17):4901–4911
Funnell BE (2016) ParB partition proteins: complex formation and spreading at bacterial and plasmid centromeres. Front Mol Biosci 3:44
Furey TS (2012) ChIP-seq and beyond: new and improved methodologies to detect and characterize protein-DNA interactions. Nat Rev Genet 13(12):840–852
de Gennes P-G, Gennes P-G (1979) Scaling concepts in polymer physics. Cornell University Press
Gerdes K, Møller-Jensen J, Bugge Jensen R (2000) Plasmid and chromosome partitioning: surprises from phylogeny. Mol Microbiol 37(3):455–466
Graham TGW, Wang X, Song D, Etson CM, van Oijen AM, Rudner DZ, Loparo JJ (2014) ParB spreading requires DNA bridging. Genes Dev 28(11):1228–1238
Gruber S (2018) SMC complexes sweeping through the chromosome: going with the flow and against the tide. Curr Opin Microbiol 42:96–103
Gruber S, Errington J (2009) Recruitment of Condensin to replication origin regions by ParB/SpoOJ promotes chromosome segregation in B. *subtilis*. Cell 137:685–696. https://doi.org/10.1016/j.cell.2009.02.035
Gruber S, Veening J-W, Bach J, Blettinger M, Bramkamp M, Errington J (2014) Interlinked sister chromosomes arise in the absence of condensin during fast replication in B. subtilis. Curr Biol 24(3):293–298
Guilhas, B., J. C. Walter, J. Rech, G. David, N-O Walliser, J. Palmeri, C. Mathieu-Demaziere, et al. (2020) ATP-Driven Separation of Liquid Phase Condensates in Bacteria. https://doi.org/10.1101/791368
Hatano T, Niki H (2010) Partitioning of P1 plasmids by gradual distribution of the ATPase ParA. Mol Microbiol 78(5):1182–1198
Heald R, Nogales E (2002) Microtubule dynamics. J Cell Sci 115(Pt 1):3–4
Hu L, Vecchiarelli AG, Mizuuchi K, Neuman KC, Liu J (2015) Directed and persistent movement arises from mechanochemistry of the ParA/ParB system. Proc Natl Acad Sci U S A 112(51):E7055–E7064
Hu L, Vecchiarelli AG, Mizuuchi K, Neuman KC, Liu J (2017) Brownian ratchet mechanism for faithful segregation of low-copy-number plasmids. Biophys J 112(7):1489–1502
Hwang LC, Vecchiarelli AG, Han Y, Mizuuchi M, Harada Y, Funnell BE, Mizuuchi K (2013) ParA-mediated plasmid partition driven by protein pattern self-organization. EMBO J 32(9):1238–1249
Ietswaart R, Szardenings F, Gerdes K, Howard M (2014) Competing ParA structures space bacterial plasmids equally over the nucleoid. PLoS Comput Biol 10(12):e1004009
Lagage V, Boccard F, Vallet-Gely I (2016) Regional control of chromosome segregation in Pseudomonas aeruginosa. PLoS Genet 12(11):e1006428
Le Gall A, Cattoni DI, Guilhas B, Mathieu-Demazière C, Oudjedi L, Fiche J-B et al (2016) Bacterial partition

complexes segregate within the volume of the nucleoid. Nat Commun 7:12107
Lee PS, Lin DCH, Moriya S, Grossman AD (2003) Effects of the chromosome partitioning protein Spo0J (ParB) on oriC positioning and replication initiation in Bacillus subtilis. J Bacteriol 185(4):1326–1337
Leonard TA, Butler PJG, Löwe J (2004) Structural analysis of the chromosome segregation protein Spo0J from Thermus thermophilus. Mol Microbiol 53(2):419–432
Libante V, Thion L, Lane D (2001) Role of the ATP-binding site of SopA protein in partition of the F plasmid. J Mol Biol 314(3):387–399
Lim GE, Derman AI, Pogliano J (2005) Bacterial DNA segregation by dynamic SopA polymers. Proc Natl Acad Sci U S A 102(49):17658–17663
Lim HC, Surovtsev IV, Beltran BG, Huang F, Bewersdorf J, Jacobs-Wagner C (2014) Evidence for a DNA-relay mechanism in ParABS-mediated chromosome segregation. elife 3:e02758
Lin DC, Levin PA, Grossman AD (1997) Bipolar localization of a chromosome partition protein in Bacillus subtilis. Proc Natl Acad Sci U S A 94(9):4721–4726
Livny J, Yamaichi Y, Waldor MK (2007) Distribution of centromere-like parS sites in bacteria: insights from comparative genomics. J Bacteriol 189(23):8693–8703
Lutkenhaus J (2007) Assembly dynamics of the bacterial MinCDE system and spatial regulation of the Z ring. Annu Rev Biochem 76:539–562
Lynch AS, Wang JC (1995) SopB protein-mediated silencing of genes linked to the sopC locus of Escherichia coli F plasmid. Proc Natl Acad Sci U S A 92(6):1896–1900
Marbouty M, Le Gall A, Cattoni DI, Cournac A, Koh A, Fiche J-B et al (2015) Condensin- and replication-mediated bacterial chromosome folding and origin condensation revealed by Hi-C and super-resolution imaging. Mol Cell 59:588–602. https://doi.org/10.1016/j.molcel.2015.07.020
Miermans CA, Broedersz CP (2018) Bacterial chromosome organization by collective dynamics of SMC condensins. J R Soc Interface/R Soc 15(147). https://doi.org/10.1098/rsif.2018.0495
Mohl DA, Gober JW (1997) Cell cycle–dependent polar localization of chromosome partitioning proteins in Caulobacter crescentus. Cell 88(5):675–684
Murray H, Ferreira H, Errington J (2006) The bacterial chromosome segregation protein Spo0J spreads along DNA from parS nucleation sites. Mol Microbiol 61(5):1352–1361
Ochman H, Lawrence JG, Groisman EA (2000) Lateral gene transfer and the nature of bacterial innovation. Nature 405(6784):299–304
Onogi T, Miki T, Hiraga S (2002) Behavior of sister copies of mini-F plasmid after synchronized plasmid replication in Escherichia coli cells. J Bacteriol 184(11):3142–3145
Ptacin JL, Gahlmann A, Bowman GR, Perez AM, von Diezmann ARS, Eckart MR, Moerner WE, Shapiro L (2014) Bacterial scaffold directs pole-specific centromere segregation. Proc Natl Acad Sci U S A 111(19):E2046–E2055
Reyes-Lamothe R, Tran T, Meas D, Lee L, Li AM, Sherratt DJ, Tolmasky ME (2014) High-copy bacterial plasmids diffuse in the nucleoid-free space, replicate stochastically and are randomly partitioned at cell division. Nucleic Acids Res 42(2):1042–1051
Ringgaard S, van Zon J, Howard M, Gerdes K (2009) Movement and equipositioning of plasmids by ParA filament disassembly. Proc Natl Acad Sci U S A 106(46):19369–19374
Rodionov O, Lobocka M, Yarmolinsky M (1999) Silencing of genes flanking the P1 plasmid centromere. Science 283(5401):546–549
Sanchez A, Cattoni DI, Walter J-C, Rech J, Parmeggiani A, Nollmann M, Bouet J-Y (2015) Stochastic self-assembly of ParB proteins builds the bacterial DNA segregation apparatus. Cell Syst 1(2):163–173
Schiessel H (2013) Biophysics for beginners: a journey through the cell nucleus. CRC Press
Schumacher MA, Funnell BE (2005) Structures of ParB bound to DNA reveal mechanism of partition complex formation. Nature 438(7067):516–519
Sengupta M, Nielsen HJ, Youngren B, Austin S (2010) P1 plasmid segregation: accurate redistribution by dynamic plasmid pairing and separation. J Bacteriol 192(5):1175–1183
Shebelut CW, Guberman JM, van Teeffelen S, Yakhnina AA, Gitai Z (2010) Caulobacter chromosome segregation is an ordered multistep process. Proc Natl Acad Sci U S A 107(32):14194–14198
Song D, Rodrigues K, Graham TGW, Loparo JJ (2017) A network of cis and trans interactions is required for ParB spreading. Nucleic Acids Res 45(12):7106–7117
Stracy M, Lesterlin C, Garza de Leon F, Uphoff S, Zawadzki P, Kapanidis AN (2015) Live-cell superresolution microscopy reveals the organization of RNA polymerase in the bacterial nucleoid. Proc Natl Acad Sci U S A 112(32):E4390–E4399
Sugawara T, Kunihiko K (2011) Chemophoresis as a driving force for intracellular organization: theory and application to plasmid partitioning. Biophysics 7 (September): 77–88
Sullivan NL, Marquis K a, Rudner DZ (2009) Recruitment of SMC by ParB-parS organizes the origin region and promotes efficient chromosome segregation. Cell 137(4):697–707
Surovtsev IV, Campos M, Jacobs-Wagner C (2016a) DNA-relay mechanism is sufficient to explain ParA-dependent intracellular transport and patterning of single and multiple cargos. Proc Natl Acad Sci U S A 113(46):E7268–E7276
Surovtsev IV, Lim HC, Jacobs-Wagner C (2016b) The slow mobility of the ParA partitioning protein underlies its steady-state patterning in Caulobacter. Biophys J 110(12):2790–2799
Toro E, Hong S-H, McAdams HH, Shapiro L (2008) Caulobacter requires a dedicated mechanism to initiate chromosome segregation. Proc Natl Acad Sci U S A 105(40):15435–15440
Vecchiarelli AG, Han Y-W, Tan X, Mizuuchi M, Ghirlando R, Biertümpfel C, Funnell BE, Mizuuchi K (2010)

ATP control of dynamic P1 ParA-DNA interactions: a key role for the nucleoid in plasmid partition. Mol Microbiol. https://doi.org/10.1111/j.1365-2958.2010.07314.x

Vecchiarelli AG, Hwang LC, Mizuuchi K (2013) Cell-free study of F plasmid partition provides evidence for cargo transport by a diffusion-ratchet mechanism. Proc Natl Acad Sci U S A 110(15):E1390–E1397

Vecchiarelli AG, Neuman KC, Mizuuchi K (2014a) A propagating ATPase gradient drives transport of surface-confined cellular cargo. Proc Natl Acad Sci U S A 111(13):4880–4885

Vecchiarelli AG, Seol Y, Neuman KC, Mizuuchi K (2014b) A moving ParA gradient on the nucleoid directs subcellular cargo transport via a chemophoresis force. BioArchitecture 4(4–5):154–159

Walter J-C, Walliser N-O, David G, Dorignac J, Geniet F, Palmeri J, Parmeggiani A, Parmeggiani A, Wingreen NS, Broedersz CP (2018) Looping and clustering model for the organization of protein-DNA complexes on the bacterial genome. New J Phys 20:035002. https://doi.org/10.1088/1367-2630/aaad39

Wang Y (2017) Spatial distribution of high copy number plasmids in bacteria. Plasmid 91:2–8

Wang X, Rudner DZ (2014) Spatial organization of bacterial chromosomes. Curr Opin Microbiol 22:66–72

Wang X, Montero Llopis P, Rudner DZ (2014a) Bacillus subtilis chromosome organization oscillates between two distinct patterns. Proc Natl Acad Sci U S A 111(35):12877–12882

Wang X, Tang OW, Riley EP, Rudner DZ (2014b) The SMC condensin complex is required for origin segregation in Bacillus subtilis. Curr Biol 24(3):287–292

Wang X, Le TBK, Lajoie BR, Dekker J, Laub MT, Rudner DZ (2015) Condensin promotes the juxtaposition of DNA flanking its loading site in Bacillus subtilis. Genes Dev 29(15):1661–1675

Wang X, Brandão HB, Le TBK, Laub MT, Rudner DZ (2017) Bacillus subtilis SMC complexes juxtapose chromosome arms as they travel from origin to terminus. Science 355(6324):524–527

Webb CD, Teleman A, Gordon S, Straight A, Belmont A, Lin DC et al (1997) Bipolar localization of the replication origin regions of chromosomes in vegetative and sporulating cells of B. subtilis. Cell 88(5):667–674

Wingreen NS, Huang KC (2015) Physics of intracellular organization in Bacteria. Annu Rev Microbiol 69:361–379

Yamaichi Y, Bruckner R, Ringgaard S, Möll A, Cameron DE, Briegel A, Jensen GJ, Davis BM, Waldor MK (2012) A multidomain hub anchors the chromosome segregation and chemotactic machinery to the bacterial pole. Genes Dev 26(20):2348–2360

Yamaichi Y, Fogel MA, Waldor MK (2007) Par genes and the pathology of chromosome loss in Vibrio cholerae. Proc Natl Acad Sci U S A 104(2):630–635

Zhang H, Schumacher MA (2017) Structures of partition protein ParA with nonspecific DNA and ParB effector reveal molecular insights into principles governing Walker-box DNA segregation. Genes Dev 31(5):481–492

4 Efficiency and Robustness of Processes Driven by Nucleoid Exclusion in *Escherichia coli*

Ines Baptista, Vatsala Chauhan, Bilena Almeida, Vinodh Kandavalli, and Andre S. Ribeiro

Abstract

The internal spatial organization of prokaryotic organisms, including *Escherichia coli*, is essential for the proper functioning of processes such as cell division. One source of this organization in *E. coli* is the nucleoid, which causes the exclusion of macromolecules – e.g. protein aggregates and the chemotaxis network – from midcell. Similarly, following DNA replication, the nucleoid(s) assist in placing the Z-ring at midcell. These processes need to be efficient in optimal conditions and robust to suboptimal conditions. After reviewing recent findings on these topics, we make use of past data to study the efficiency of the spatial constraining of Z-rings, chemotaxis networks, and protein aggregates, as a function of the nucleoid(s) morphology. Also, we compare the robustness of these processes to nonoptimal temperatures. We show that Z-rings, Tsr clusters, and protein aggregates have temperature-dependent spatial distributions along the major cell axis that are consistent with the nucleoid(s) morphology and the volume-exclusion phenomenon. Surprisingly, the consequences of the changes in nucleoid size with temperature are most visible in the kurtosis of these spatial distributions, in that it has a statistically significant linear correlation with the mean nucleoid length and, in the case of Z-rings, with the distance between nucleoids prior to cell division. Interestingly, we also find a negative, statistically significant linear correlation between the efficiency of these processes at the optimal condition and their robustness to suboptimal conditions, suggesting a trade-off between these traits.

Keywords

Chemotaxis · Protein aggregates · Cell division · Nucleoid exclusion · *Escherichia coli* · Efficiency and robustness · Optimal and nonoptimal temperatures

I. Baptista · V. Chauhan · B. Almeida · V. Kandavalli
Laboratory of Biosystem Dynamics, Faculty of Medicine and Health Technology, Tampere University, Tampere, Finland

A. S. Ribeiro (✉)
Laboratory of Biosystem Dynamics, Faculty of Medicine and Health Technology, Tampere University, Tampere, Finland

CA3 CTS/UNINOVA. Faculty of Science and Technology, NOVA University of Lisbon, Caparica, Portugal
e-mail: andre.sanchesribeiro@tuni.fi

4.1 Introduction

Advances in microscopy and in the engineering of synthetic fluorescent proteins have facilitated the observation of cellular components and, thus,

G. Duménil, S. van Teeffelen (eds.), *Physical Microbiology*, Advances in Experimental Medicine and Biology 1267, https://doi.org/10.1007/978-3-030-46886-6_4

of the dynamics of bioprocesses in live cells. These observations have established that, even in prokaryotes, which lack internal walls separating the nucleus from the cytoplasm (Alberts et al. 2008), there is a far-from-random internal spatial organization, which is now considered to play a key role in proper cell functioning, including in critical processes, such as cell division and cell-to-cell communication (Mulder and Woldringh 1989; Wang et al. 2005).

Interestingly, proteins responsible for transport within the cytoplasm have not been identified in prokaryotes (Elowitz et al. 1999). As such, any internal spatial organization is likely maintained by (largely) energy-free processes. Recent studies, including those using *Escherichia coli* as a model organism, have provided evidence that one critical component of the internal spatial organization of prokaryotic cells is the nucleoid, located at midcell (see e.g. (Gupta et al. 2014a; Neeli-Venkata et al. 2016a, b, 2018) and references within).

The key biophysical feature of the nucleoid that allows it to affect the internal organization of prokaryotic cells is its compaction (de Vries 2010; Wang et al. 2013; van der Berg et al. 2017). This, along with the presence of nucleoid-associated proteins (Dillon and Dorman 2010), excludes large cellular components from the region where the nucleoid is located. In the model organism *Escherichia coli*, since the nucleoid occupies from 50% to 80% of the cell (Fisher et al. 2013) (and even larger regions when replicated), the components excluded from midcell will be located at the cell poles, near to the cell extremities. Even ribosomes tend to be located at the poles, performing most translation in those regions (Bakshi et al. 2012). Nucleoid replication allows for cellular components to become spatially located in between the two nucleoids, prior to cell division (see e.g. (Neeli-Venkata et al. 2018)), including the Z-ring, which is critical to determine the point of cell division (Bernhardt and de Boer 2005).

As noted, the functionality of several critical cellular processes has been recently shown to depend on this energy-free process of nucleoid exclusion (see e.g. (Stylianidou et al. 2014)). Here we focus on the functionality and efficiency of three such processes. One is the formation of the Z-ring at midcell that assists the cell, during division, to establish where to locate the cell wall responsible for dividing the cell into two daughter cells. The second process is chemotaxis, which depends on a system of several proteins and whose efficiency likely partially relies on their localization at one of the poles of the cell (Maddock and Shapiro 1993). The third is the segregation of non-functional protein aggregates to the cell poles. It has been hypothesized that this process may be associated with the perpetuation of cell lineages, by cleansing most cells of non-functional protein aggregates, at the expense of a few individuals (Lindner et al. 2008; Gupta et al. 2015; Lloyd-Price et al. 2014).

Here we discuss the degree with which the efficiency of each of these processes depends (among other factors) on biophysical parameters of the nucleoid, such as its size relative to cell size, density, and its location at any given moment of the cell cycle. In particular, we address two questions. First, does the efficiency of these processes differ similarly with temperature? Second, what is the balance between efficiency in optimal conditions and robustness to fluctuating temperatures?

Following a description of present knowledge of these phenomena, to address these questions, we quantified the efficiency with which each of the three processes is carried out in optimal temperature conditions. Further, we quantified their robustness to suboptimal temperatures. For this, we start by introducing each of these processes based on past studies, followed by a description of some of our recent results based on analyses of their dynamics as a function of the physical properties of the nucleoid(s) in optimal and suboptimal temperatures. Next, we define parameters to quantify the efficiency of the processes based on the localization of the cellular components that need to be placed on specific regions of the cells. Finally, we compare their efficiency in optimal and nonoptimal temperatures, as well as their robustness to temperature shifts.

4.2 Heterogeneities in the Internal Composition of *Escherichia coli*

As a prokaryote, *E. coli* does not have membrane-bound organelles (Golding and Cox 2006). Their only organelle is the nucleoid, a cell-confined, ellipsoidal region that is typically located at mid-cell (Fisher et al. 2013). In it reside several substances essential for the cell's functioning, such as DNA, RNA and nucleoid associated proteins (NAPs). These substances interact by diffusion since *E. coli* cells lack internal transport mechanisms (Winkler et al. 2010; Golding and Cox 2006).

Due to this apparently simple internal structure, any internal heterogeneities must emerge from the biophysical properties of the cells. Particularly, any nonhomogeneous spatial organization ought to emerge from three features: the presence of the nucleoid at midcell (Fisher et al. 2013), the shape of the cell (Coquel et al. 2013), and the physical properties of the interacting components (Mondal et al. 2011).

E. coli cells can survive to a particularly wide range of environmental conditions. In general, its endurance is achieved at the expense of its growth rate, due to physiological and morphological changes (Farewell and Neidhardt 1998; Shehata and Marr 1975). For example, at low temperatures, the viscosity of the cytoplasm is increased (Oliveira et al. 2016), causing it to acquire glass-like properties (Parry et al. 2014). This change impairs chromosome partitioning (Weart et al. 2007; Männik and Bailey 2015) and adds uncertainty to the location of the point of cell division, likely due to the increased distance between the replicated nucleoids or due to higher asymmetry in their locations (Gupta et al. 2014b; Lloyd-Price et al. 2012).

Overall, the main aspects considered here are that there are spatial heterogeneities in the internal composition of *E. coli* – resulting from the physical properties of the cell and of its components – and that these heterogeneities are not free from change due to fluctuating temperatures. As such, it is expected that processes relying on the heterogeneities will also have temperature-dependent efficiencies.

4.2.1 Z-ring Formation and Localization

Cell division is a complex process that results from the sequential timely execution of several processes that are independent in origin, such as DNA replication and chromosome segregation (Margolin 2005; Adams and Errington 2009; Lutkenhaus et al. 2012). One of these processes is the emergence of the Z-ring, an integral structure of the divisome. The divisome is a protein complex responsible for synthesizing the septal envelope and for constricting the Z-ring to divide the inner and outer membranes of the cell (Margolin 2005; Adams and Errington 2009; Lutkenhaus et al. 2012; Bi and Lutkenhaus 1991). Its assembly begins with the polymerization of FtsZ protofilaments that form a constriction plane (Errington et al. 2003; Goehring and Beckwith 2005; Harry et al. 2006). These proteins are then organized into a Z-ring that contracts in the later stages of the cell cycle and disassembles once the septal wall is formed (Adams and Errington 2009; Addinall et al. 1996).

While the Z-ring assembles and disassembles relatively quickly (Addinall et al. 1997), its formation starts early in the cell cycle. This process has three distinct phases (Ma et al. 1996): first, there is no apparent ring with its future components being near-uniformly distributed in the cytoplasm; next, two dots appear at the center of the cell and on opposite sides of the minor cell axis (open ring state); finally, a band is formed at the geometrical center of the major axis (closed ring state).

Interestingly, although the Z-ring positioning seems to be a largely stochastic process (Gupta et al. 2014b), the septum is consistently located precisely in the geometric center of the major axis of the cell in the vast majority of *E. coli* cells (Trueba and Woldringh 1980; Errington et al. 1965; Cullum and Vicente 1978). This allows for the high degree of symmetry in cell division (Trueba 1982; Yu and Margolin 1999; Hiraga

et al. 1989; Guberman et al. 2008; Männik et al. 2012).

The Z-ring positioning is coordinated by the Min system (Lutkenhaus 2007; Rothfield et al. 2005), formed by the MinC protein that inhibits Z-ring formation, and MinD and MinE proteins that regulate the MinC's position, guiding the divisome to the middle of the cell (Hu and Lutkenhaus 1999; Raskin and de Boer 1999). The Min system is believed to be responsible for locating the division point in between the replicated nucleoids. The precision of the geometrical symmetry is then significantly enhanced by nucleoid occlusion (Gupta et al. 2014b), made possible by the binding of the SlmA protein to the DNA (Cho et al. 2011; Tonthat et al. 2011) which inhibits the assembly of the Z-ring in the region occupied by the nucleoids (Raskin and de Boer 1999).

4.2.2 Segregation of Nonfunctional Protein Aggregates

Nonoptimal conditions increase the rate of production of malfunctioning proteins (Miot and Betton 2004), which, in turn, negatively impacts on other cellular processes (Maisonneuve et al. 2008; Dai et al. 2009). To decrease the numbers of non-functional proteins, *E. coli* makes use of an intricate machinery. First, chaperones catalyse the correct folding of proteins and aid in the rescue of misfolded proteins (Carrió et al. 1999; Wickner 1999). A protease network also destroys misfolded proteins (Gottesman and Maurizi 1992), allowing error correction and ensuring the existence of 'raw material' to produce new proteins (Willetts 1967; Goldberg 1972).

When these mechanisms fail and protein degradation is impaired (which occurs mostly when in nonoptimal conditions), *E. coli* resorts to protein aggregation (Sabate et al. 2010; Tyedmers et al. 2010; Winkler et al. 2010), which renders non-functional proteins inactive (Bednarska et al. 2013). The aggregation is regulated (Laskowska et al. 2004), protein-specific (Speed et al. 1996) and it requires energy (Govers et al. 2014). The existence of these costs suggests that it is important to cell functioning. Once created, the aggregates migrate to the poles (Gupta et al. 2014a). Finally, cell division generates a bias towards the old pole of the cells, since newly formed poles are free from aggregates (Stewart et al. 2005; Ackermann et al. 2003).

It has been suggested that the gathering of aggregates at the poles can interfere with the cell's health (Maisonneuve et al. 2008; Lindner et al. 2008) and diminish the growth rate (Stewart et al. 2005). As such, this resembles an aging phenomenon (Stewart et al. 2005), as it is characterized by a decrease of the organism's functionality and increased probability of death (due to reduced or null growth rate).

The segregation of non-functional protein aggregates does not require active transport mechanisms (Coquel et al. 2013) and the diffusion process by which it occurs seems to be independent from the substance that is being segregated (Lindner et al. 2008). Therefore, the aggregates' spatial distribution – which affects their partitioning in division – is expected to result from morphological features in *E. coli*, particularly the nucleoid's presence in midcell, which facilitates a volume exclusion phenomenon responsible for driving aggregates to the poles of the cell (Winkler et al. 2010; Coquel et al. 2013).

4.2.3 Localization of Serine Chemoreceptors

In *E. coli,* chemoreceptor proteins are responsible for sensing chemical gradients (Sourjik and Berg 2004), temperatures changes (Lee et al. 1988), and oxygen concentrations (Rebbapragada et al. 1997). Chemoreceptors form clusters that are stabilized by the CheW protein and the kinase CheA (Sourjik and Berg 2004; Wadhams and Armitage 2004; Parkinson et al. 2005) (Fig. 4.1).

The chemoreceptor clusters tend to locate at the cell poles (Maddock and Shapiro 1993; Sourjik and Berg 2000; Zhang et al. 2007), even though they first form at midcell (Thiem et al. 2007). This phenomenon has been attributed to a diffusion-and-capture mechanism (Rudner et al. 2002) by the trans-envelope Tol-Pal complex (Santos et al. 2014).

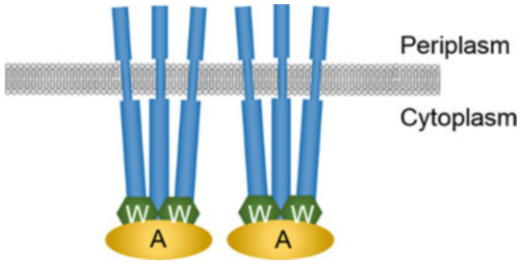

Fig. 4.1 Chemotaxis complex. The chemoreceptors are inserted in the cytoplasmic membrane and are organized in trimer-of-dimers with the assistance of proteins CheW (*W*) and CheA (*A*)

Particularly, the Tsr protein – a serine chemoreceptor in *E. coli* (Lee et al. 1988) – migrates and remains in the same pole for several rounds of cell division, where it moves freely (Thiem et al. 2007), which suggests that the propensity for chemoreceptor clusters to accumulate at the poles is not due solely to the Tol-Pal complexes. In this regard, there is evidence that the tendency for locating at the poles is enhanced by the ability of these protein clusters to match the curved shape of the cell poles (Huang et al. 2006). Further, recently, evidence was presented to support that the tendency of the chemoreceptors for the cell poles is also enhanced by the presence of the nucleoid at midcell, due to the volume exclusion phenomenon (Neeli-Venkata et al. 2016a).

4.3 Effects of Suboptimal and Critically Low Temperatures

All processes described above have recently been shown to have a temperature-dependent efficiency, given their loss of robustness following temperature shifts, particularly when at critically low temperatures. In this section, we briefly describe some of the evidences supporting these conclusions, which are consistent with the hypothesis that all these processes are driven by nucleoid exclusion from midcell.

4.3.1 Temperature-Dependent Segregation of Protein Aggregates to the Cell Poles

The formation of non-functional protein aggregates is known to be more common in cells under nonoptimal conditions (Lindner et al. 2008; Maisonneuve et al. 2008; Winkler et al. 2010; Govers et al. 2014). A past study (Gupta et al. 2014a), showed that nucleoid occlusion is the main cause for the proneness by non-functional protein aggregates to locate at the cell poles. In addition, significant evidence was provided that, at lower-than-optimal temperatures, several variables are altered, which explains differences in the behavior of the aggregates. One relevant parameter in the dynamics of these events is the size of the nucleoid(s) relative to midcell. Another is the rate of diffusion of the aggregates, which alters, among other, the escape time of the aggregates from the poles. Overall, this study suggests that the prediction of the robustness to temperature shifts of processes based on nucleoid exclusion is a complex, multi-variable problem.

4.3.2 Temperature-Dependent Placement of the Z-ring at Midcell

In a recent study (Neeli-Venkata et al. 2018), we used fluorescence microscopy, GFP-tagged FtsZ proteins and DAPI-stained nucleoids to study the robustness of the process of placement of the Z-ring at midcell to suboptimal and critical temperatures. We observed that as temperature is lowered, the distance between nucleoids following DNA replication increases. Consistently, it was observed a slow loss of symmetry in division at the single-cell level (displacement from the geometric center) at a single-cell level. As temperature is further lowered (below 24 °C to as low as 10 °C) it was observed a sharp loss of symmetry, indicating that the process is not robust to such temperature shifts. Following this, it was

shown that, in this range, the consistent increase in distance between replicated nucleoids further enhances a loss of density in the Z-ring. Similar observations were made at high temperatures complemented with high media richness.

Interestingly, evidence suggests that, within certain ranges, the effects of nonoptimal temperatures on the Z-ring morphology are reversible (Neeli-Venkata et al. 2018). Specifically, temporal microscopy measurements of cells subject to temperature shifts from optimal to non-optimal, followed by the inverse shift, showed that the cells quickly re-established typical distances between nucleoids, as well as the shape and location of Z-rings (see Tables 7 and 8 in (Neeli-Venkata et al. 2018)). Importantly, the changes in Z-rings morphology and location are gradual and occur at the same temperature threshold, regardless of the transition being from high to low or low to high. This implies that the system dynamics does not exhibit hysteresis, which is not common in biological decision-making processes. This suggests that the abnormalities in Z-rings at non-optimal temperatures have biophysical (rather than physiological) causes.

In support, the changes in Z-rings emerged soon after the temperature shifts (1 to a few minutes (Neeli-Venkata et al. 2018)), implying that they are not likely to be due to changes in the proteome, as protein numbers take at least tenths of minutes to change, given natural protein maturation times, among other reasons (see, e.g. (Hebisch et al. 2013)). Similarly, the fast reversibility following the inverse temperature shifts also implies that, again, no proteome modifications were necessary. Finally, it was also observed that increasing temperature in cells in rich media has cumulative effects on these features of Z-rings (Table 6 in (Neeli-Venkata et al. 2018)).

4.3.3 Temperature-Dependent Localization of Serine Chemoreceptors

In another study (Neeli-Venkata et al. 2016b), we provided evidence that the intracellular location of clusters of Venus-tagged Tsr (associated to chemotaxis networks) cannot be explained solely by a diffusion-and-capture mechanism based on Tol-Pal complexes at the cell poles. First, we observed that, in anucleate cells, Tsr clusters tend to locate closer to midcell than in wild type cells. Further, we observed that deleting the Tol-Pal complex only slightly decreases the fraction of Tsr clusters that are at the poles. These and additional evidence (Neeli-Venkata et al. 2016b) suggest that the nucleoid excludes clusters from midcell, partially explaining their tendency for locating at the cell poles.

Interestingly, in cells lacking Tol-Pal, the fraction of clusters at the poles decreased with decreasing temperature. This would be consistent with a process that initiates with the formation of clusters at the cytoplasm, and that has an increased failure rate as the cytoplasm viscosity increases with decreasing temperature (Oliveira et al. 2016). Overall, we concluded that the processes of diffusion-and-capture made possible by Tol-Pal complexes and exclusion from the midcell by nucleoid(s) have complementary effects. Due to this, below, to compare the efficiency of nucleoid exclusion of Tsr complexes and non-functional protein aggregates, we make use of deletion mutants for Tol-Pal.

4.4 Efficiency at Optimal Temperatures and Robustness to Suboptimal Temperatures

The three processes above share a common criterion for proper functioning, which is the ability to place a specific cellular component at a specific cell location. Further, in all, this depends on (but not only on) nucleoid(s) exclusion. As such, their efficiency is expected to differ with the nucleoid(s) size and position, as well as with the component (e.g. aggregates) size and mobility in the cytoplasm (Kuwada et al. 2015). Temperature shifts affect all these biophysical variables (Maclean and Munson 1961) and, thus, the efficiencies are expected to be temperature dependent.

In the case of protein aggregates and chemotaxis networks, the 'aim' is to drive and maintain them at the cell pole(s). Meanwhile, Z-rings should be placed at the geometric center of the major cell axis, in between the replicated nucleoids.

As such, the Efficiency (E) of these processes can be quantified from the distance between the real position of the component along the major cell axis and its optimal position in that axis. For that, let D be the distance of the component from midcell, scaled by the cell length, L. Next, for a given cell i, let $E_Z(i)$ be its efficiency in placing the Z-ring at midcell, $E_A(i,j)$ be its efficiency in placing a given non-functional protein aggregate at one of the cell poles (with j being the aggregate, when more than 1 exists), and $E_{Tsr}(i,j)$ be its efficiency in placing the chemotaxis network at a cell pole (where j is a Tsr-Venus cluster, when more than 1 exists). Given this, if $\langle x \rangle$ and $|x|$ are, respectively, the average and the absolute value of x, and n is the number of components j in the cell one has:

$$0 \leq E_Z^i = \frac{1}{2} - \left| D^i \right| \leq \frac{1}{2} \tag{4.1}$$

$$0 \leq E_A^i = \sum_{j=1}^{n} \frac{\left\langle \left| D_j^i \right| \right\rangle}{n} \leq \frac{1}{2} \tag{4.2}$$

$$0 \leq E_{Tsr}^i = \sum_{j=1}^{n} \frac{\left\langle \left| D_j^i \right| \right\rangle}{n} \leq \frac{1}{2} \tag{4.3}$$

From (4.1), (4.2), and (4.3), E_i is optimal when equaling 0.5 and minimal when equaling 0.

Similarly, we define Robustness, R, as the ability to maintain the behavior in nonoptimal conditions similar to that in the optimal condition. Assuming n conditions besides the control/optimal condition, we quantify R as:

$$R = \frac{1}{n} \cdot \sum_{j=1}^{n} \frac{E_j}{E_{control}} \tag{4.4}$$

4.5 Moments of the Distributions

From the distributions of distance of the cellular components from their optimal position, as measured by microscopy, we extract the mean (M) coefficient of variation (CV) skewness (S) and kurtosis (K), as follows. Let x_i be a variable (e.g. distance of Z-ring i from midcell). Then, the mean distance of Z-rings from midcell, M(x), for a set of N Z-rings, equals:

$$M(x) = \frac{1}{N} \cdot \sum_{i=1}^{N} x_i \tag{4.5}$$

Given this, if σ is the standard deviation and $\langle x \rangle$ stands for M(x):

$$CV(x) = \frac{\sigma_x}{\langle x \rangle} \tag{4.6}$$

$$S = \frac{\left\langle (x - \langle x \rangle)^3 \right\rangle}{\sigma_x^3} \tag{4.7}$$

$$K = \frac{\left\langle (x - \langle x \rangle)^4 \right\rangle}{\sigma_x^4} \tag{4.8}$$

4.6 Measurements

Microscopy images of nucleoids were obtained by DAPI staining. For a detailed description, see (Neeli-Venkata et al. 2016a). The data used to study Z-rings was obtained from (Neeli-Venkata et al. 2018) and is based on FtsZ proteins tagged with GFP (FtsZ-GFP). Meanwhile, to study non-functional protein aggregates, we used RNA molecules tagged with 96 MS2-GFP proteins (RNA-MS2-GFP, Fig. 4.2), using the data from (Gupta et al. 2014a). Finally, the data on chemotaxis networks was obtained from (Neeli-Venkata et al. 2016b) and is based on tagging Tsr proteins with the fluorescent Venus protein (Tsr-Venus).

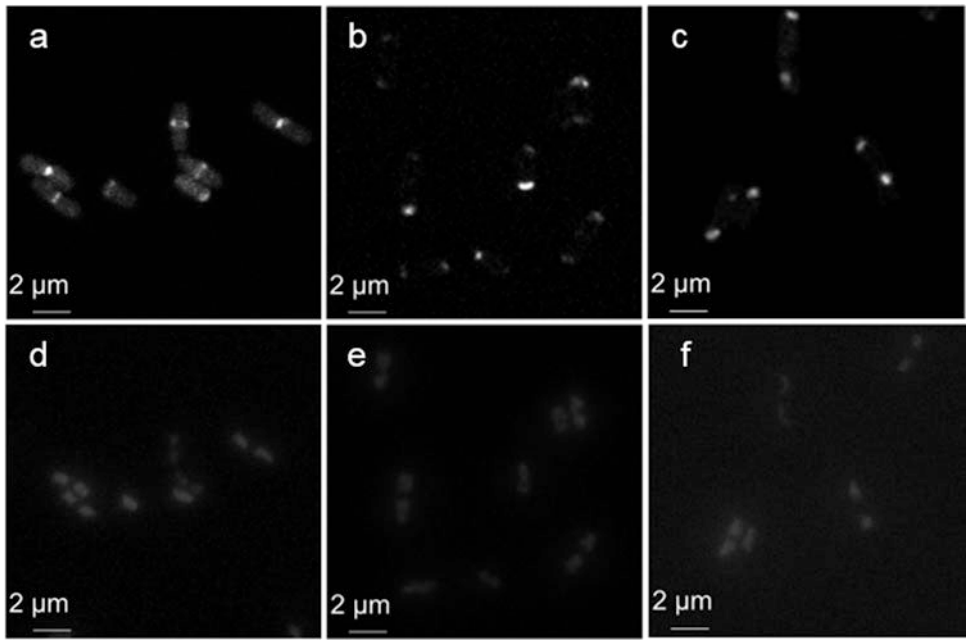

Fig. 4.2 Example microscopy images of *E. coli* cells using a 100 × objective. For images with DAPI-stained nucleoids, the cells were fixed with formaldehyde. (**a**) Example image of cells grown in LB media at 37 °C expressing FtsZ-GFP proteins, which become particularly visible when forming a Z-ring at midcell, (**b**) Example image of cells grown in M9 media at 37 °C expressing Tsr-Venus proteins, causing the chemotaxis networks to become visible at the cell poles, (**c**) Example image of cells grown in LB media at 37 °C expressing MS2-GFP proteins along with the RNA target for these proteins, making MS2-GFP tagged RNAs visible as bright spots, (**d**) Example image of the cells in the same field of view as Fig. **a** and their DAPI-stained nucleoids, (**e**) Example image of the cells in the same field of view as Fig. **b** and their DAPI-stained nucleoids, (**f**) Example image of the cells in the same field of view as Fig. **c** and their DAPI-stained nucleoids

In detail, to observe FtsZ fluorescently tagged with GFP, we used *E. coli* MG1655-derived strain BS001 which expresses FtsZ-GFP under the control of the P_{lac} promoter. To observe RNAs tagged with multiple MS2-GFP we used the strain DH5α-PRO, which contains a multi-copy plasmid carrying $P_{LtetO-1}$-MS2d-GFP and a single-copy plasmid carrying $P_{lac/ara-1}$-mRFP1-MS2-96bs (Golding and Cox 2004). Finally, to observe the spatial distribution of Tsr-Venus proteins, in the absence of Tol-Pal complexes, we used an isogenic derivative of the *E. coli* strain MG1655 (MG1655 Δ*tolpal*), to which we added a medium-copy plasmid carrying a gene coding for Tsr-Venus, under the control of the P_{lac} promoter.

Cells expressing FtsZ-GFP and cells expressing RNA-MS2-GFP were grown in Lysogeny broth (LB). Cells expressing Tsr-Venus were grown in M9-glucose medium. Overnight culture cells were diluted to 1:1000 in the respective fresh media, supplemented with the appropriate antibiotics. Cells were then placed in the incubator at 37 °C with shaking (250 r.p.m.) until reaching an OD_{600} of ≈ 0.3.

Afterwards, we induced target and reporter genes. FtsZ-GFP expression was induced with 2.5 μM isopropyl β-d-1-thiogalactopyranoside (IPTG) and the cells were then incubated at 37 °C for 30 min. Induction of MS2-GFP was achieved by 100 ng ml^{-1} of anhydrotetracycline (aTc) and 0.1% L-arabinose for 50 min, after which it was added 1 mM IPTG for 10 min for the induction of $P_{lac/ara-1}$. Tsr-Venus was induced with 50 mM ml^{-1} IPTG for 1 h at 37 °C. The induction processes lasted until cells reached an OD_{600} of ≈ 0.4–0.6.

Next, cells were shifted to the incubator at specific temperatures (10 °C, 24 °C, 37 °C and 43 °C) for 1 h. Subsequently, the nucleoids were stained with 4′,6-diamidino-2-phenylindole (DAPI). For this, cells were fixed with 3.7% formaldehyde in phosphate-buffered saline (PBS) for 30 min. Next, they were resuspended in PBS and DAPI (2 mg ml^{-1}) was added to the suspension. After the cells were in the incubator for 20 min, they were washed twice with PBS to remove DAPI in excess.

Finally, cells were resuspended in PBS and suitable amounts of these samples (5 μl for cells expressing FtsZ-GFP and RNA-MS2-GFP and 8 μl for cells expressing Tsr-Venus) were placed on 1% agarose gel pad prepared in the respective media (LB medium for cells expressing FtsZ-GFP and RNA-MS2-GFP, and M9-glucose medium otherwise) for microscopy observation.

Cells were visualized using a Nikon Eclipse inverted microscope (Ti-E, Nikon, Japan) with a C2 confocal laser scanning system using a 100× Apo TIRF (1.49 NA, oil) objective. GFP fluorescence was visualized under the confocal microscope using a 488 nm argon ion laser (Melles-Griot) and a 515/30 nm detection filter. DAPI-stained nucleoids were observed by epifluorescence microscopy using a mercury lamp with a DAPI filter (Nikon). Images were acquired using a medium pinhole, 90 gain, and 3.36 μs pixel dwell. The software used for image acquisition was NIS-elements (Nikon, Japan). The size of the phase contrast and epifluorescence images was 2560 × 1920 pixels, where a pixel corresponds to 0.048 μm. For confocal images, the size of a pixel corresponds to 0.062 μm using a scan resolution of 2048 × 2048 pixels.

Microscopy images were analyzed using the software 'CellAging' (Häkkinen et al. 2013) and 'SCIP' (Martins et al. 2018). Cells and nucleoid(s) segmentation were performed as in (Oliveira et al. 2016), while RNA-MS2-GFP spot detection was performed as in (Häkkinen and Ribeiro 2015). From the images, we extracted the lengths of the major and minor axes of cells and nucleoids, to obtain the ratio between them, which is used here as a measure of their 'shapes'. Also, the positioning of Tsr clusters responsible for chemotaxis was measured from the positioning of the largest cluster (usually only one exists per cell) of Tsr proteins tagged with a Venus protein (Yu et al. 2006; Neeli-Venkata et al. 2016b). An example microscopy image is shown in Fig. 4.2b. Similarly, we identified the Z-ring positioning from cells expressing FtsZ tagged with GFP (Neeli-Venkata et al. 2018) (Fig. 4.2a). Finally, we used a multi-copy plasmid expressing MS2-GFP proteins, along with a single-copy plasmid coding for an RNA target for 96 MS2-GFP proteins, to produce visible protein aggregates whose spatial location can be tracked (Oliveira et al. 2016) (Fig. 4.2c). Finally, to observe nucleoids, we performed DAPI staining (Fig. 4.2d–f).

Finally, growth rates were measured by a spectrophotometer (Ultrospec 10; GE Healthcare). Cultures were grown overnight with continuous shaking. Next, overnight cultures were diluted into fresh medium to an optical density at 600 nm (OD_{600}) of 0.04. We recorded the OD_{600} values every 30 min for 5 h to obtain growth curves. We performed 3 technical replicates per condition. No significant differences were found between replicates.

Table 4.1 Shows the number of cells analyzed in each condition.

Table 4.1 Number of cells analyzed, from each of the three strains studied, in each temperature condition

Cells	Temperature (°C)	Number of cells
MG1655 BS001	10	169
	24	115
	37	144
	43	90
DH5α-PRO	10	166
	24	71
	37	171
	43	464
MG1655 Δ*tolpal*	10	142
	24	119
	37	280
	43	175

4.7 Results

We studied the efficiency with which *E. coli* cells impose a preferential spatial location to Z-rings, protein clusters responsible for chemotaxis, and non-functional protein aggregates, when under critically low up to critically high temperatures. From the quantified efficiency at the various temperatures, we also quantified the robustness to these nonoptimal temperatures (Eq. 4.4). For simplicity, the length of the major axis of the cells is normalized to 1 (Fig. 4.3).

Measurements of mean cell growth rates in each temperature condition are shown in Fig. 4.4a–c, and measurements to assess whether temperature shifts affect cell shapes are shown in Fig. 4.4d, e.

We started by testing whether adverse temperature conditions cause morphological changes in the cells and/or nucleoids shapes or physiological changes (in growth rates). From Fig. 4.4a–c, temperature affects growth rates. Meanwhile, to assess whether temperature affects cells or nucleoids shapes, we calculated the ratios between their lengths and widths, at each temperature. Results in Fig. 4.4d, e show that these ratios suffer only small changes with temperature, in agreement with observations from the images, implying that the cells' or nucleoids' shapes are not strongly affected by temperature, within this range of conditions.

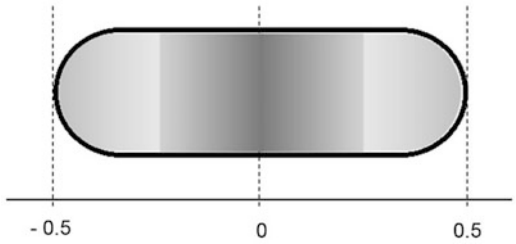

Fig. 4.3 Normalization of the major cell axis of an *E. coli* cell. The midcell region with the nucleoid(s) and the space in between (when applicable) is represented by dark grey color, while the two polar regions are represented in light grey. The size of the regions differs between cells and with temperature

4.7.1 Temperature Dependence of the Nucleoid(s) Morphology

We first measured differences in nucleoid(s) morphology (size and positioning along the major cell axis) between temperature conditions. Data of nucleoid(s) sizes was obtained using DAPI staining (Oliveira et al. 2016) (see Sect. 4.6 for the measurements' protocols). Since we found little to no changes in the cells or nucleoid(s) length along the minor cell axis with changing temperature, here we report only on the lengths along the major cell axis.

From images at each temperature condition, we extracted the length of cells and nucleoid(s) within (Sect. 4.6). Here we report on the length(s) of the nucleoid(s) and the distance between nucleoids (for cells with two nucleoids) relative to the cell length. We also report on the length between the two outer borders of the nucleoids (which includes the space in between the nucleoids) in cells with two nucleoids. Finally, we report on absolute cell lengths. Results are shown in Fig. 4.5.

From Fig. 4.5, both the length of nucleoid(s) relative to the cell length, as well as the distance between nucleoids relative to the cell length (when two exist) are temperature dependent (in agreement with (Gupta 2014b) (Oliveira et al.2016)). For example, in cells with one nucleoid, the relative nucleoid size along the major cell axis differs by 10–15% between 10 °C and 43 °C. Similarly, the distance between nucleoids (relative to the major cell axis) differs by 5% between 10 °C and 37 °C. Interestingly, while the relative nucleoid size is minimized at the highest temperature tested, the distance between nucleoids is minimized at the control condition, 37 °C. In addition, from Fig. 4.5d we find that this change is not solely due to changes in the cell length (if only the latter changed, the relative nucleoid size would increase for increasing temperature, not the opposite). Given this and the above, it is expected that temperature shifts will affect the spatial locations of Z-rings, protein aggregates, and Tsr clusters.

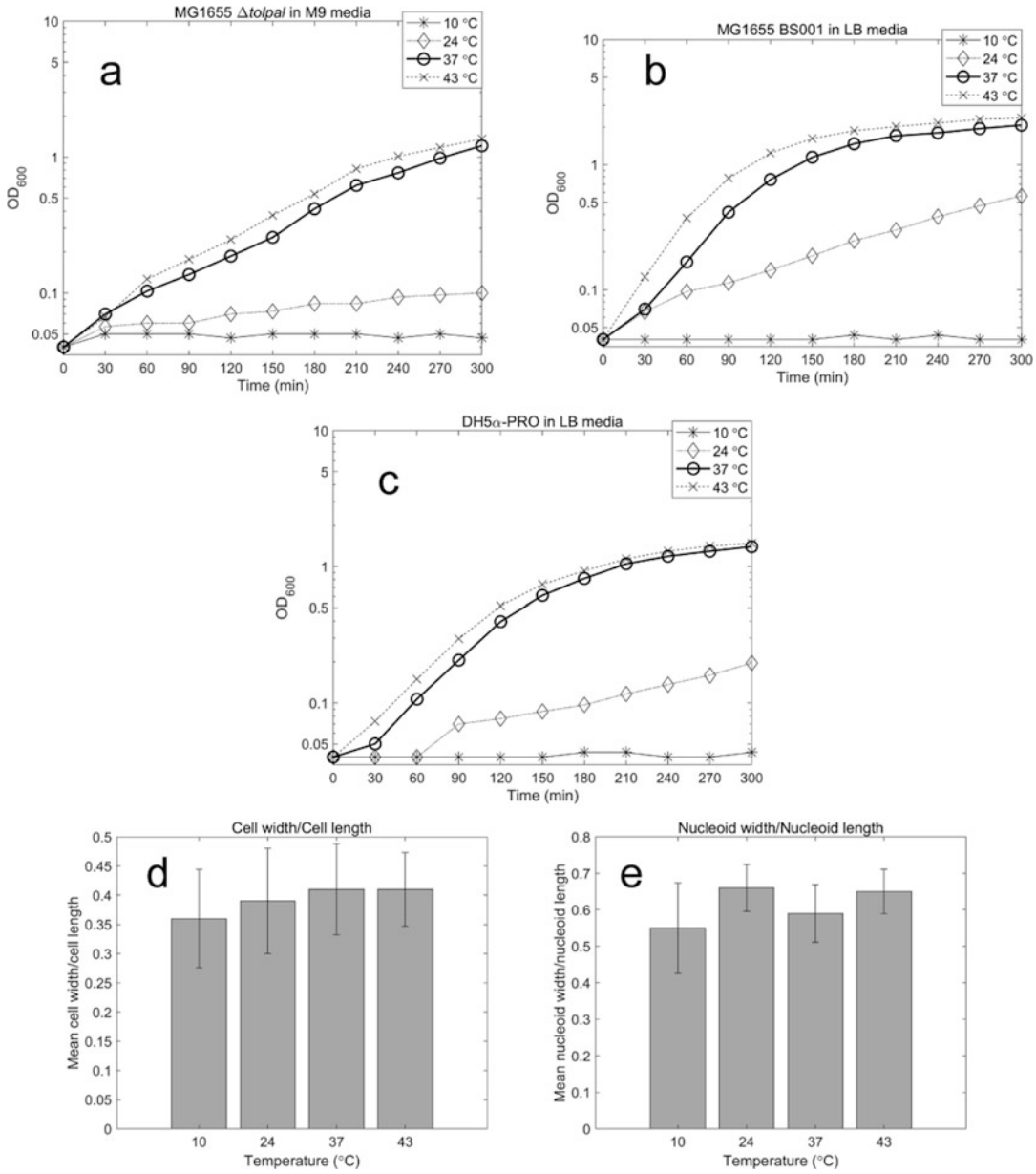

Fig. 4.4 (**a**) Growth curve (OD_{600}) of MG1655 BS001 cells in LB media at 10 °C, 24 °C, 37 °C and 43 °C, (**b**) Growth curve (OD_{600}) of MG1655 Δ*tolpal* cells in M9 media at 10 °C, 24 °C, 37 °C and 43 °C, (**c**) Growth curve (OD_{600}) of DH5α-PRO cells in LB media at 10 °C, 24 °C, 37 °C and 43 °C, (**d**) Mean and standard deviation of the ratio between cell length and width as a function of temperature, (**e**) Mean and standard deviation of the ratio between nucleoid length and width as a function of temperature. Data for Figs. **d** and **e** was obtained by analyzing 631 (10 °C), 803 (24 °C), 622 (37 °C) and, 1000 (43 °C) cells

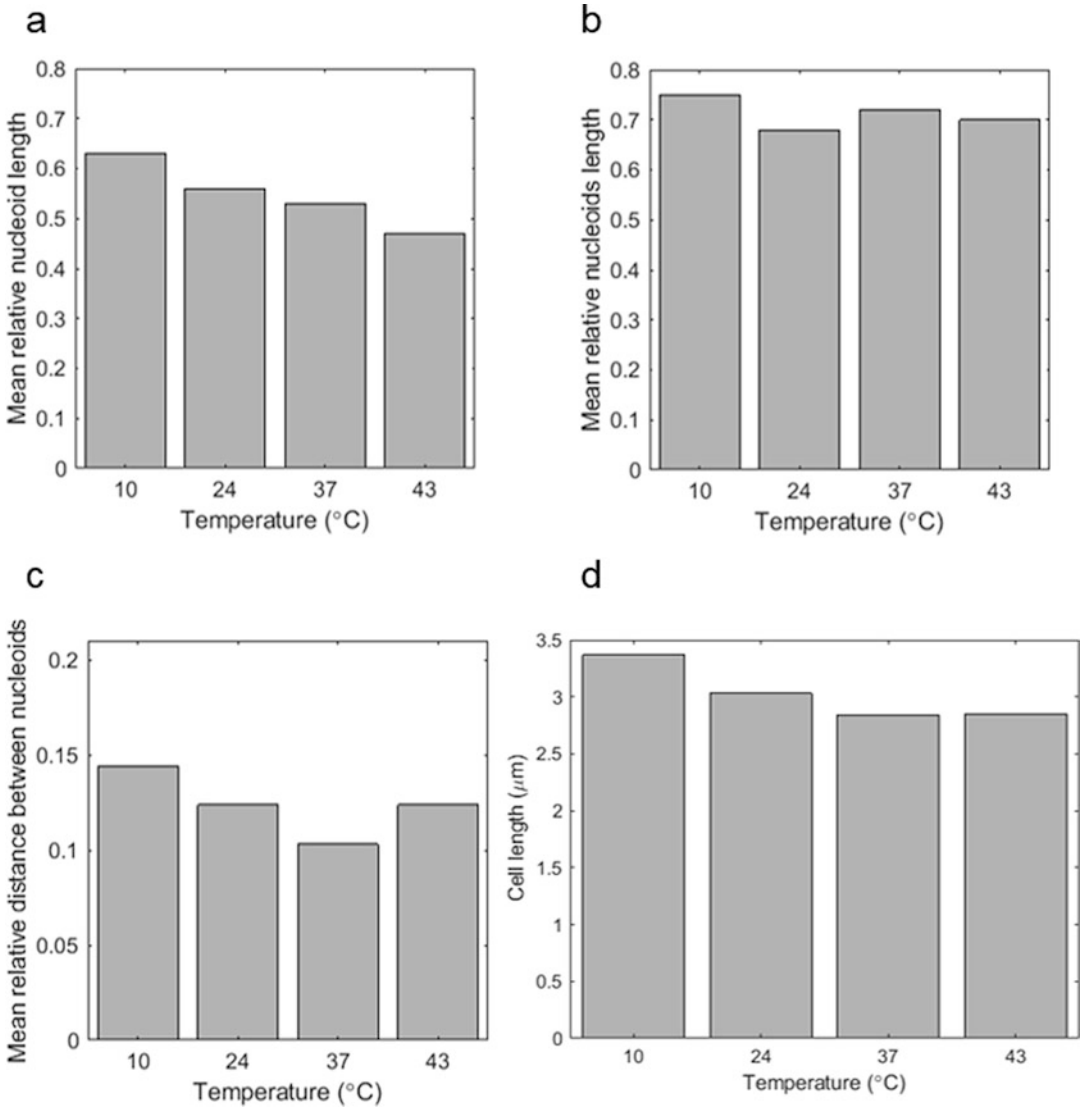

Fig. 4.5 (**a**) Mean nucleoid length relative to the cell length at each temperature in cells with one nucleoid, (**b**) Mean length of the two nucleoids and the space in between relative to the cell length in cells with two nucleoids at each temperature, (**c**) Mean relative distance between the inner borders (i.e. the closest to midcell) of the two nucleoids at each temperature, (**d**) Mean absolute cell length (in μm) at each temperature. Table 4.1 shows the number of cells that were analyzed in each condition

4.7.2 Spatial Distributions of Cellular Components along the Major Cell Axis

From images of multiple cells (Sect. 4.6 and Fig. 4.2), we obtained the empirical spatial distributions along the major cell axis of the centers of Z-rings (Fig. 4.6, see also Table 4.1 for the number of cells analyzed in each condition). Similarly, we obtained the spatial distributions of MS2-GFP tagged RNAs (protein aggregates, Fig. 4.7) and of the centers of Tsr-Venus clusters (Fig. 4.8). In each figure, we show also the mean distance of the border of the nucleoid from midcell (extracted from the images used for Fig. 4.5). In the case of the Z-ring, we instead show the mean distance of the borders of the nucleoids from midcell.

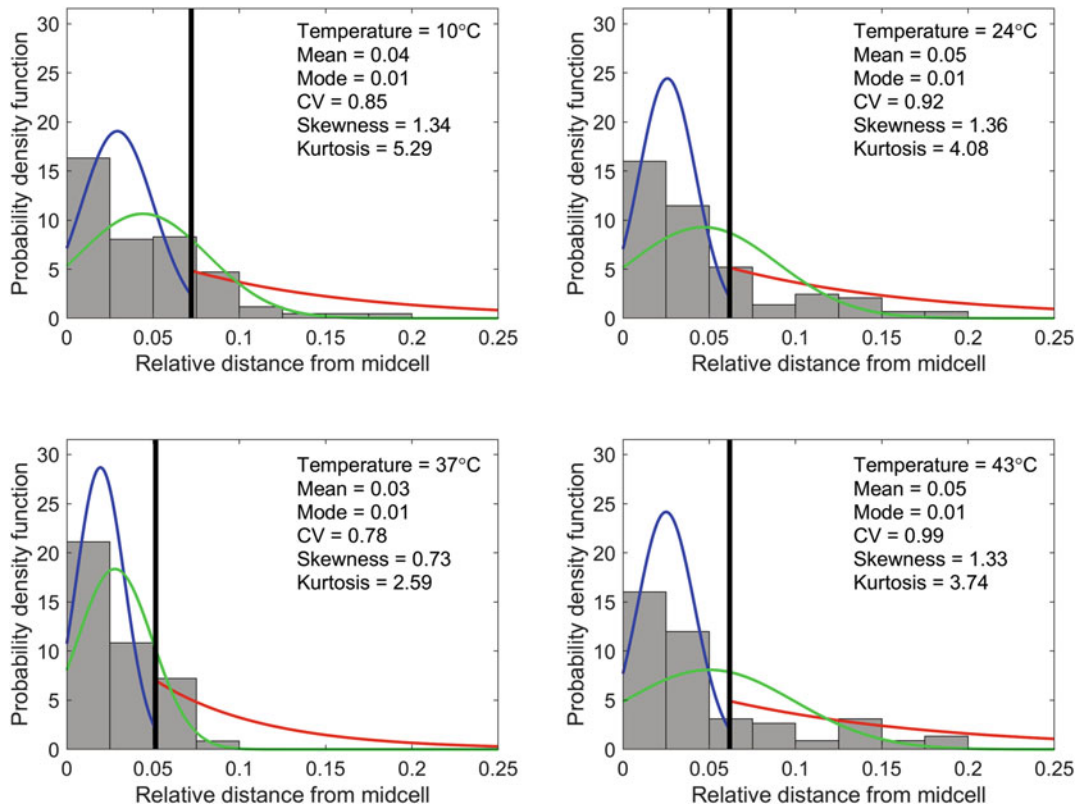

Fig. 4.6 Probability density functions (grey bars) of the distance (relative to the cell length) of the Z-ring center from midcell, at different temperatures (10 °C, 24 °C, 37 °C, 43 °C). All cells analyzed have two nucleoids at the moment the microscopy image was collected. In each plot, we also show the temperature, along with the mean, mode, coefficient of variation (CV), skewness and kurtosis of the single-cell distribution of distances. Meanwhile, the black vertical line represents the mean distance of the borders of the nucleoids from midcell, averaged over all cells in each condition (data from Fig. 4.5c). A few cells with Z-rings distanced by more than 0.2 from midcell were not included, since the ring formed outside the region between the two nucleoids, and thus will not result in two viable cells. Finally, the blue line is the best half-normal distribution fitting to the data trimmed at the black vertical line, the red line is the best exponential fitting to the data starting from the black vertical line, and the green line is the best half-normal distribution fitting to all data. Table 4.1 shows the number of cells analyzed in each condition

From Fig. 4.6, the spatial distribution of the relative distance of the Z-rings from midcell along the major cell axis changes gradually as temperature increases. This change is consistent with the changes in the mean relative distance between the borders of the two nucleoids at each temperature (Fig. 4.5c). Namely, as the temperature is increased until 37 °C, there is a gradual compaction of the distribution towards midcell, consistent with the decreasing distance between the nucleoids (Fig. 4.5c). At 43 °C, the distribution expands when compared to the control, in accordance with the increased distance between nucleoids (Fig. 4.5c).

Figure 4.6 also shows best fits to the empirical data to the left (blue lines) and the data to the right (red lines) of the nucleoids' borders (marked by the black vertical lines). Also shown are the best fits to the whole data (green lines). We opted for fitting a half-normal distribution to the left, an exponential distribution to the right, and a half-normal distribution to the whole data, to show that the latter is only a good fit at the 37 °C condition, where the containment of FtsZ-GFP proteins in between the nucleoids is more efficient. This efficiency decreases at both lower-than- as well as higher-than-optimal temperatures. Namely, one observes two distinct behaviors by these proteins (from those in between nucleoids and from

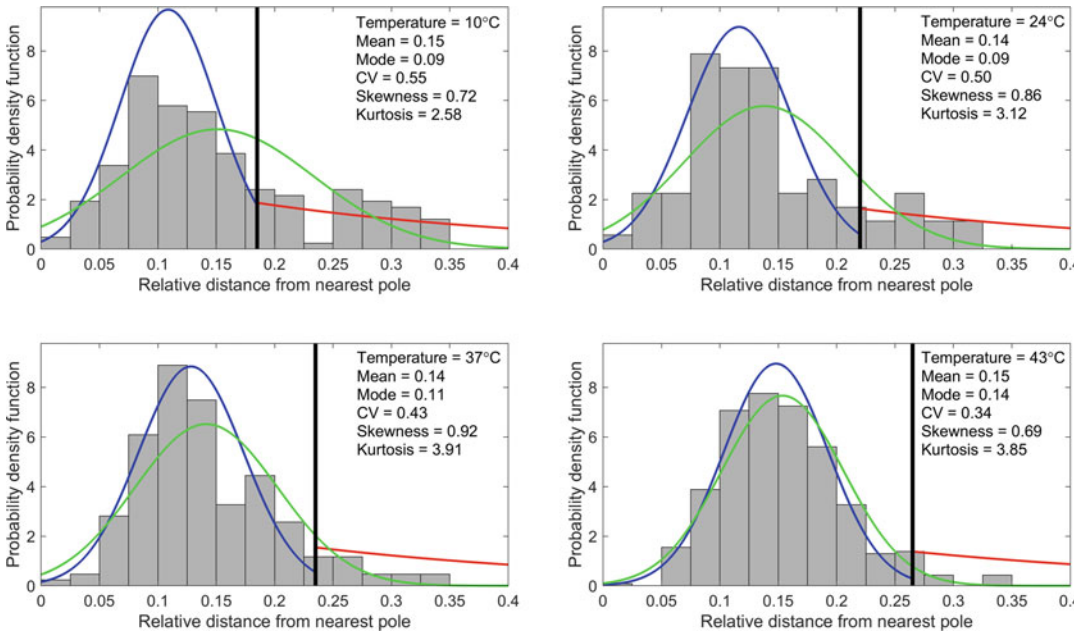

Fig. 4.7 Probability density functions of the distances of protein aggregates from the nearest pole (relative to the cell length) in individual cells at different temperatures (10 °C, 24 °C, 37 °C, 43 °C). All cells analyzed have one nucleoid at the moment the microscopy image was collected. In each plot we also show the temperature, along with the mean, mode, coefficient of variation (CV), skewness and kurtosis of the single-cell distribution of distances. Meanwhile, the black vertical line represents the distance of the border of the nucleoid from midcell, averaged over all cells in each condition. Note that the aggregates distanced more than 0.15 from midcell were excluded as, in those cases, the complexes were assumed to be confined between two nucleoids and thus unable to migrate to the cell poles (see Fig. 4.5c). Finally, the blue line is the best Gaussian fitting to the data trimmed at the black vertical line, the red line is the best exponential fitting to the data starting from the black vertical line, and the green line is the best Gaussian fitting to all data. Table 4.1 shows the number of cells that were analyzed in each condition

those not in that region). These behaviors are, respectively, well captured by a half-Gaussian distribution (with lower variance than the half-Gaussian fitted to the whole distribution) and by an exponential distribution that captures the presence of FtsZ-GFP proteins no longer in between the nucleoids, as well as the decrease in propensity of finding them as the distance from midcell increases.

Such spatial distributions can be expected by assuming a stochastic model where, aside from Markovian-like motion, FtsZ proteins (weakly) attract one another to form a ring and are strongly excluded from the poles by the action of the Min system (Meinhardt and de Boer 2001; Bernhardt and de Boer 2005; Adams and Errington 2009). To complete the model, one should consider that the nucleoids exclude (large enough) FtsZ clusters (which provides more accuracy in centering the ring at midcell than the Min system alone) (Neeli-Venkata et al. 2018). A similar model was recently implemented in Neeli-Venkata et al. (2016b) to mimic the spatial dynamics of Tsr clusters. Meanwhile, it is less clear why there is a loss of efficiency at sub-optimal temperatures. Likely it is due to several factors, such as the increased viscosity of the cytoplasm at low temperatures and the effects of such temperature on nucleoid(s) size (Oliveira et al. 2016), among other.

Figure 4.7 shows the spatial distribution along the major cell axis of non-functional protein aggregates (MS2-GFP tagged RNAs) relative distance to the nearest pole at the same temperatures as above. Visibly, the point of least energy of the protein aggregates (i.e. the mode of the distribution) is approximately at midpoint between the cell border and the nucleoid outer bor-

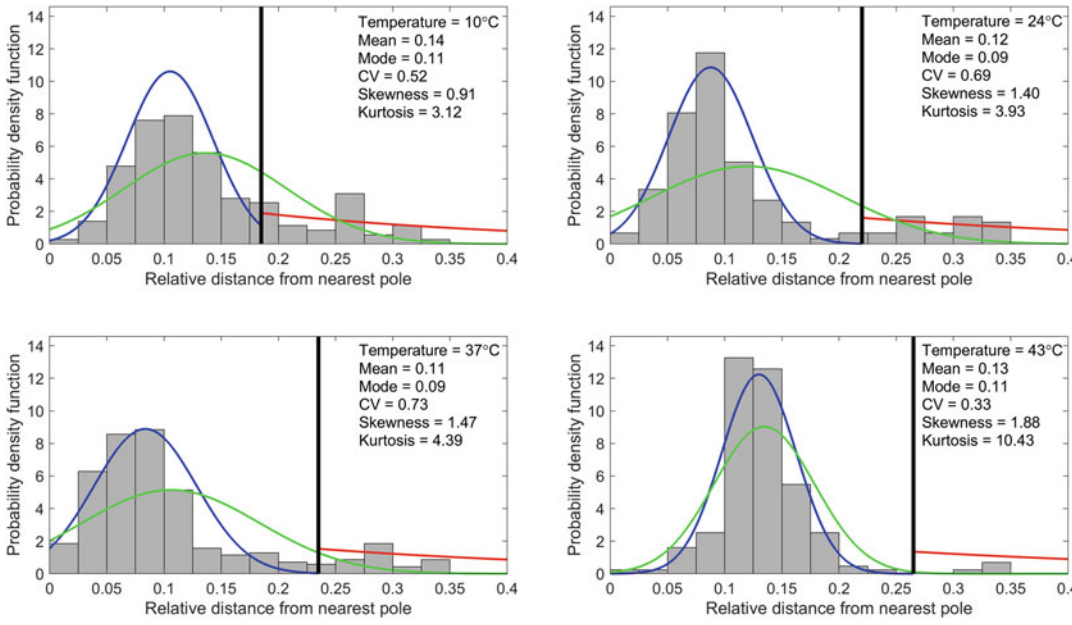

Fig. 4.8 Probability density functions of the distances of Tsr clusters from the nearest pole (relative to the cell length) in individual Δ*tolpal* cells at different temperatures (10 °C, 24 °C, 37 °C, 43 °C). All cells analyzed have one nucleoid at the moment the microscopy image was collected. In each plot, we also show the temperature along with the mean, mode, coefficient of variation (CV), skewness and kurtosis of the single-cell distribution of distances. Meanwhile, the black vertical line represents the distance of the border of the nucleoid from midcell, averaged over all cells in each condition. Note that the clusters that were distanced more than 0.15 from midcell were excluded as, in those cases, the complexes were assumed to be confined between two nucleoids and thus unable to migrate to the cell poles (see Fig. 4.5c). Finally, the blue line is the best Gaussian fitting to the data trimmed at the black vertical line, the red line is the best exponential fitting to the data starting from the black vertical line, and the green line is the best Gaussian fitting to all data. Table 4.1 shows the number of cells that were analyzed in each condition

der (Fig. 4.5a). Interestingly, as temperature is decreased, there is a consistent increase in the number of aggregates at midcell, even though the nucleoid size increases. This has been explained in a past work (Oliveira et al. 2016) as being due to increased cytoplasm viscosity, which hampers significantly nucleoid exclusion of aggregates from midcell by weakening the effects of the segregation of aggregates by nucleoid occlusion from midcell.

Meanwhile, the Gaussian and exponential best fits (blue and red lines, respectively) in Fig. 4.7 provide evidence that the spatial distribution of the protein aggregates differs significantly between the regions occupied and not occupied by the nucleoid. This supports the assumption that the nucleoid excludes these aggregates from midcell. Interestingly, by observing the best fits one finds that, as temperature increases, the 'blue' and 'green' lines gradually become similar. This can be explained by the decreasing viscosity of the cytoplasm with increasing temperature (Oliveira et al. 2016), which allows aggregates to more quickly reach the least energy position (the poles), implying that they will more commonly be observed at that location.

4.7.3 Correlation to Nucleoids Size and/or Distance Between Nucleoids

To establish a quantitative relationship between the mean relative size of the nucleoid and the spatial distributions of Z-rings, Tsr-Venus clusters and, protein aggregates, we considered the effects of changing temperature on the shapes of these distributions. Visibly, from Figs. 4.6, 4.7, and 4.8, the main apparent difference in these shapes with temperature is in the tail of the dis-

tribution. This is expected since, e.g. with relatively smaller nucleoids, more components will tend to appear in the cylindrical region(s) of the cell where the nucleoid(s) is located, resulting in increased tails.

Such changes are expected to reflect mostly on K, rather than M, CV, and S, since K specifically quantifies the size of the tail of the distribution. As such, we searched for linear correlations between K of the spatial distribution of the cellular components and the mean size of the nucleoids along the major cell axis (or, in the case of Z-rings, the distance between nucleoids).

Results in Fig. 4.9 show that there is a goodness of fit between the value of K of the distribution of distances of the Z-ring from midcell and the mean relative distance between nucleoids for various temperatures. We argue that this statistically significant correlation (p-value of the linear least-squares regression fit equal to 0.01) is a strong argument that nucleoids exclusion drives, to a significant extent, the positioning of Z-rings.

Contrary to Z-rings, protein aggregates and chemotaxis networks tend to locate at the poles, due to nucleoid exclusion from midcell, as they form throughout the cell cycle and only rarely first appear in between the two nucleoids. Further, it is expected that as the mean nucleoid length decreases with increasing temperature (Fig. 4.5a), the kurtosis of the spatial distribution of aggregates and Tsr clusters should increase, as the polar regions increase in size relative to the cell length. Thus, one expected a negative correlation between K and mean nucleoid size. Results in Fig. 4.10 confirm these predictions for protein aggregates (p-value of the linear least-squares regression fit equal to 0.09).

Figure 4.11 shows the results for the Tsr clusters. Here the linear fit is not statistically significant (p-value of 0.13). This could be due to insufficient data or due to the existence of additional parameter(s) influencing significantly the positioning of the clusters, such as the ability of Tsr clusters to match the curved shape of the cell poles, which may enhance their propensity for polar location, thus reducing their sensitivity to temperature changes when compared to protein aggregates (Huang et al. 2006).

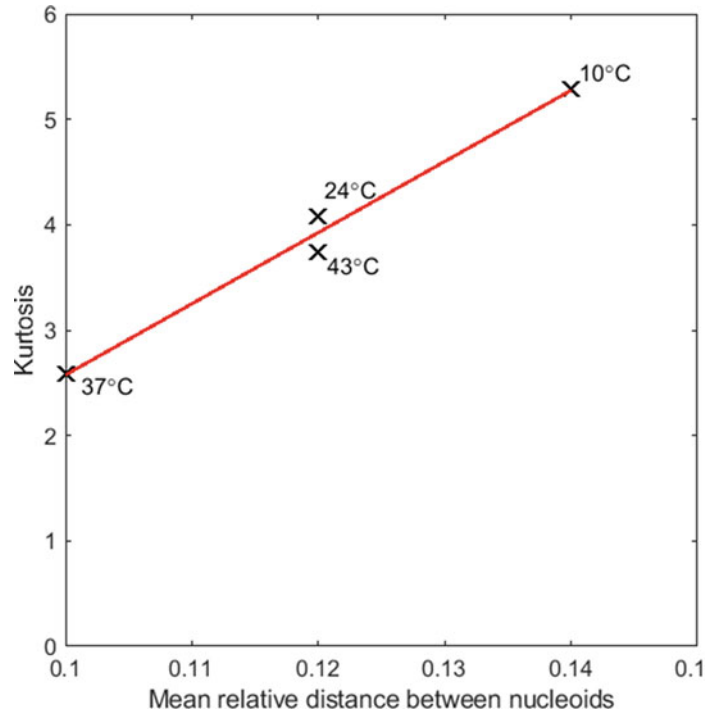

Fig. 4.9 Kurtosis of the distribution of distances of the Z-ring from midcell (relative to the cell length) plotted against the mean distance between nucleoids relative to the cell length. Data obtained at different temperatures (10 °C, 24 °C, 37 °C, 43 °C) from cells with 2 nucleoids. The solid red line is the best linear fit by least-squares regression. Its goodness of fit is quantified by the p-value (which here equals 0.01). For p-values smaller than 0.1, we reject the null hypothesis that there is no relationship between the two variables. Finally, the temperature of each condition is shown near to the data point it corresponds to

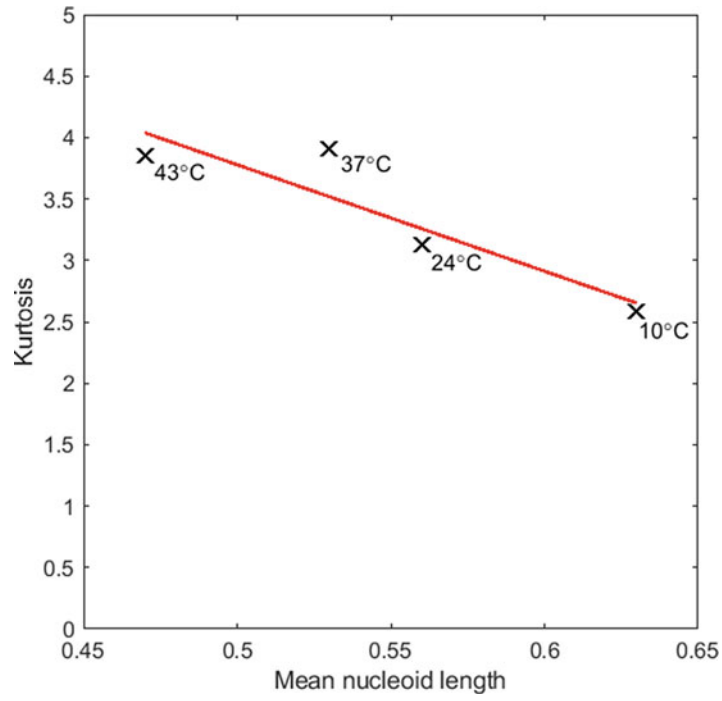

Fig. 4.10 Kurtosis of the distribution of distances of protein aggregates from the nearest pole (relative to the cell length) plotted against the mean nucleoid length relative to the cell length. Data at different temperatures (10 °C, 24 °C, 37 °C, 43 °C) from cells with 1 nucleoid. The solid red line is the best linear fit by least-squares regression, whose goodness of fit is quantified by the p-value (which equals 0.09). For p-values smaller than 0.1, we reject the null hypothesis that there is no relationship between the two variables. The temperature of each condition is shown near to the data point it corresponds to

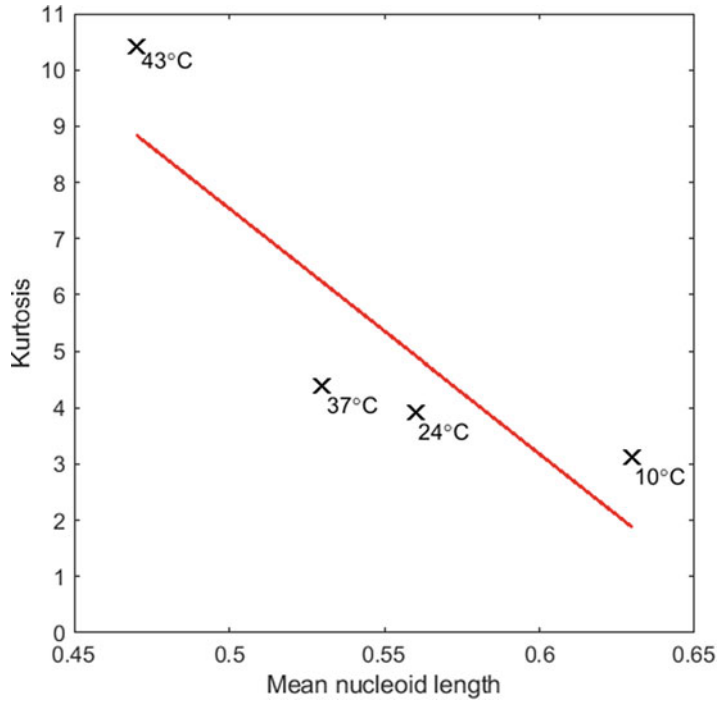

Fig. 4.11 Kurtosis of the distribution of distances of Tsr clusters from the nearest pole (relative to cell length) plotted against the mean nucleoid length relative to cell length. Data at different temperatures (10 °C, 24 °C, 37 °C, 43 °C) from cells with 1 nucleoid. The solid red line is the best linear fit by least-squares regression. Its goodness of fit is quantified by the p-value (which equals 0.13). For p-values smaller than 0.1, we reject the null hypothesis that there is no relationship between the two variables. Finally, the temperature of each condition is shown near to the data point it corresponds to

4.7.4 Efficiency of the Positioning as a Function of Temperature and Robustness to Nonoptimal Temperatures

Using Eqs. 4.1–4.3 and data in Figs. 4.6, 4.7, and 4.8, for each temperature we calculated the efficiency with which Z-rings, protein aggregates and, Tsr clusters are placed in their 'optimal' position in the cells. Results are shown in Fig. 4.12.

From Fig. 4.12, temperature does not affect the efficiency of the three processes equally. This is particularly surprising when comparing protein aggregates and Tsr clusters, due to their similar preferential location. While future research is needed to assert the causes, one potential explanation is a difference in the effects of changing temperature on the clustering process of Tsr and protein aggregates. Meanwhile, the changes in efficiency with temperature in Z-rings placement agrees with the hypothesis that the smaller the distance between nucleoids (Fig. 4.5c), the more efficient the process is.

Overall, the efficiency of positioning of Z-rings appears to be most perturbed by high temperatures, perhaps due to increased hampering of the clustering process of the proteins forming the ring. In the case of protein aggregates and Tsr clusters, critically low temperatures seem to cause the strongest perturbations, likely due to the increased viscosity of the media (Oliveira et al. 2016).

Finally, from Fig. 4.12 and Eq. 4.4, we obtained the quantitative robustness of these processes, within the range of temperatures tested. We find it to equal, specifically, 0.88 for the Z-ring, 0.93 for Tsr clusters, and 0.94 for protein aggregates. These results are, to some extent, surprisingly similar (particularly between Tsr clusters and protein aggregates), given the differences on how these processes (and their efficiency) respond to temperature changes.

Finally, from Fig. 4.13, we find a negative linear correlation (p-value of 0.04) between the efficiency at the optimal temperature and the robustness to changing temperatures, within in the ranges considered.

4.8 Discussion

Recent reports provide strong evidences that the far-from-random spatial distribution within *Es-*

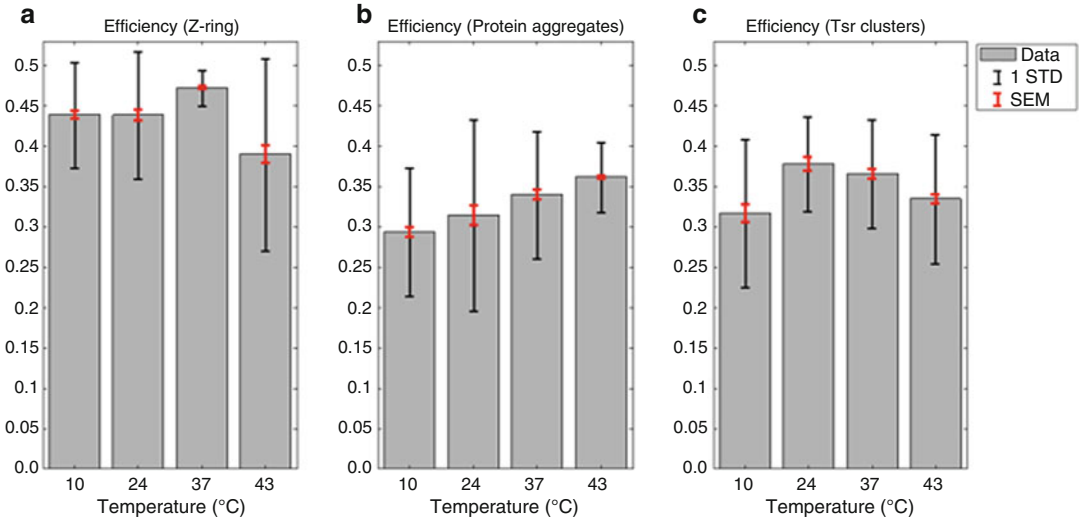

Fig. 4.12 Mean (*grey bars*), single-cell variability as measured by one standard deviation (*black error bars*), and standard error of the mean obtained by bootstrapping (*red error bars*) of the efficiency of 'optimal' localization at different temperatures (10 °C, 24 °C, 37 °C, 43 °C) of: (**a**) Z-rings, (**b**) Protein aggregates, (**c**) Tsr clusters

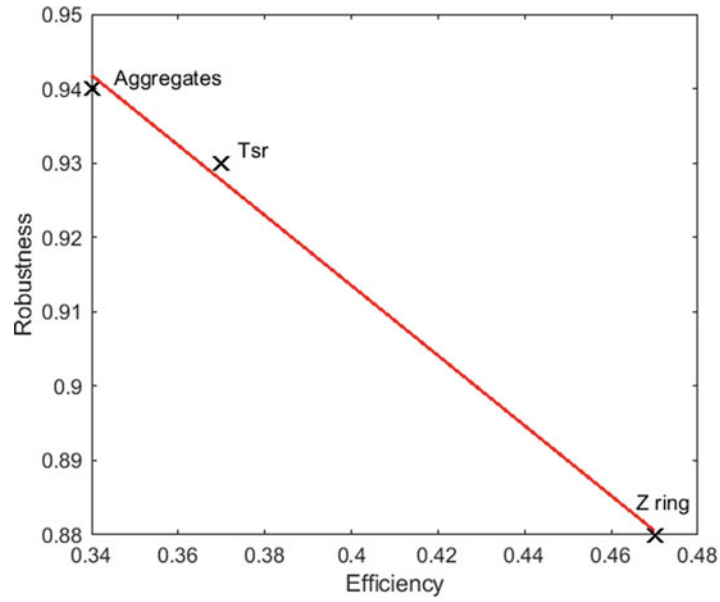

Fig. 4.13 Robustness to nonoptimal temperatures (10 °C, 24 °C, and 43 °C) of each segregation process to a specific region of the cell plotted against their efficiency at the optimal temperature (37 °C). The solid red line is the best fit by linear least-squares regression, whose goodness of fit is quantified by the p-value (equals 0.04). For p-values smaller than 0.1, we reject the null hypothesis that there is no relationship between the two variables. The process is shown near to the data point it corresponds to

cherichia coli cells of Z-rings, Tsr protein clusters (associated to chemotaxis networks), and nonfunctional protein aggregates are generated by a volume exclusion phenomenon, caused by the presence of the nucleoid(s) at midcell. In addition, evidence has been presented that this phenomenon is temperature dependent.

After reviewing the literature on this topic, we made use of empirical data to quantify the efficiency in optimal conditions and the robustness to nonoptimal temperatures of these processes. For this, following a summary of the present knowledge on the biophysics of positioning along the major cell axis of these three cellular components, we first characterized the morphology (size and positioning) of nucleoid(s) at various temperatures. Next, we studied the distributions of distances from optimal position along the major cell axis of Z-rings, Tsr protein clusters, and protein aggregates.

Next, we proposed a methodology for quantifying the efficiency of these processes, based on the definition of potentially optimal positions in the cells for those components. Also, from the efficiency at different temperatures, we proposed a means to quantify the robustness to changing temperatures, within a given range of temperatures.

Overall, we found a correlation between the positioning of nucleoid(s) and the positioning of the aforementioned cellular components. This, and previous findings, are evidence that the nucleoid provides a means to produce non-random spatial distributions of relatively large cellular components in *E. coli*.

Interestingly, while similar, the distributions of the three cellular components considered are not identical (this is particularly interesting in the case of protein aggregates and Tsr clusters in cells lacking Tol-Pal). These differences resulted in a different correlation between the kurtosis of the distributions of distances from the optimal position of the cellular components and the mean size of the nucleoid. Another difference between the behavior of the three components is in their responses to temperature shifts. For instance, while increasing temperature always increase the efficiency of the segregation to the poles of protein aggregates, it has the opposite effect in Tsr clusters. Research is needed to better determine whether these differences are due to differences between the biophysical properties of the components (e.g. weight and shape), or due to the action of other factors affecting their positioning.

Another interesting result presented here is the linear, negative correlation between efficiency at the control (optimal temperature) condition and the robustness to nonoptimal temperatures. This result is very common in both Engineering and Biology (see e.g. (Prajapat and Ribeiro 2018)), yet the reasons to occur in the phenomena studied here are so far unclear, since all three processes have efficiencies in all temperatures that are far from that of a random process.

In the future it will be of interest to evaluate if, when accounting for additional cellular components also subject to segregation by nucleoid exclusion, the efficiency-robustness relationship observed here is conserved and, in the opposite case, study the reasons why it is not.

References

Ackermann M, Stearns SC, Jenal U (2003) Senescence in a bacterium with asymmetric division. Science 300(5627):1920

Adams DW, Errington J (2009) Bacterial cell division: assembly, maintenance and disassembly of the Z ring. Nat Rev Microbiol 7:642–653

Addinall SG, Bi E, Lutkenhaus J (1996) FtsZ ring formation in fts mutants. J Bacteriol 178(3):3877–3884

Addinall SG, Cao C, Lutkenhaus J (1997) Temperature shift experiments with an ftsZ84(Ts) strain reveal rapid dynamics of FtsZ localization and indicate that the Z ring is required throughout septation and cannot reoccupy division sites once constriction has initiated. J Bacteriol 179(13):4277–4284

Alberts B et al (eds) (2008) Molecular biology of the cell, 5th edn. Garland Science, New York

Bakshi S, Siryaporn A, Goulian M et al (2012) Superresolution imaging of ribosomes and RNA polymerase in live *Escherichia coli* cells. Mol Microbiol 85(1):21–38

Bednarska NG, Schymkowitz J, Rousseau F et al (2013) Protein aggregation in bacteria: the thin boundary between functionality and toxicity. Microbiology 159:1795–1806

Bernhardt TG, de Boer PAJ (2005) SlmA, a nucleoid-associated, FtsZ binding protein required for blocking septal ring assembly over chromosomes in *E coli*. Mol Cell 18(5):555–564

Bi E, Lutkenhaus J (1991) FtsZ ring structure associated with division in *Escherichia coli*. Nature 354:161–164

Carrió MM, Corchero JL, Villaverde A (1999) Proteolytic digestion of bacterial inclusion body proteins during dynamic transition between soluble and insoluble forms. Biochim Biophys Acta 1434(1):170–176

Cho H, McManus HR, Dove SL et al (2011) Nucleoid occlusion factor SlmA is a DNA-activated FtsZ polymerization antagonist. Proc Natl Acad Sci USA 108(9):3773–3778

Coquel A-S, Jacob J-P, Primet M et al (2013) Localization of protein aggregation in *Escherichia coli* is governed by diffusion and nucleoid macromolecular crowding effect. PLoS Comput Biol 9:e1003038

Cullum J, Vicente M (1978) Cell growth and length distribution in *Escherichia coli*. J Bacteriol 134(1):330–337

Dai X, Healy D, Yli-Harja O et al (2009) Tuning cell differentiation patterns and single cell dynamics by regulating proteins' functionalities in a toggle switch. J Theor Biol 261(3):441–448

de Vries (2010) DNA condensation in bacteria: interplay between macromolecular crowding and nucleoid proteins. Biochimie 92(1):1715–1721

Dillon SC, Dorman CJ (2010) Bacterial nucleoid-associated proteins, nucleoid structure and gene expression. Nat Rev Microbiol 8(3):185–195

Elowitz MB, Surette MG, Leibler S et al (1999) Protein mobility in the cytoplasm of *Escherichia coli*. J Bacteriol 181(1):197–203

Errington FP, Powell EO, Thompson N (1965) Growth characteristics of some gram-negative bacteria. J Gen Microbiol 39:109–123

Errington J, Daniel RA, Scheffers DJ (2003) Cytokinesis in bacteria. Microbiol Mol Biol Rev 67:52–65

Farewell A, Neidhardt FC (1998) Effect of temperature on in vivo protein synthetic capacity in *Escherichia coli*. J Bacteriol 180(17):4704–4710

Fisher JK, Bourniquel A, Witz G et al (2013) Four-dimensional imaging of *E. coli* nucleoid organization and dynamics in living cells. Cell 153:882–895

Goehring NW, Beckwith J (2005) Diverse paths to midcell: assembly of the bacterial cell division machinery. Curr Biol 15(13):514–526

Goldberg A (1972) Degradation of abnormal proteins in *Escherichia coli*. Proc Natl Acad Sci USA 69(2):422–426

Golding I, Cox EC (2004) RNA dynamics in live Escherichia coli cells. Proc Natl Acad Sci USA 101(31):11310–11315

Golding I, Cox EC (2006) Physical nature of bacterial cytoplasm. Phys Rev Lett 96(6):098102

Gottesman S, Maurizi MR (1992) Regulation by proteolysis: energy-dependent proteases and their targets. Microbiol Rev 56(4):592–621

Govers SK, Dutré P, Aertsen A (2014) In vivo disassembly and reassembly of protein aggregates in *Escherichia coli*. J Bacteriol 196:2325–2332

Guberman JM, Fay A, Dworkin J et al (2008) PSICIC: noise and asymmetry in bacterial division revealed by computational image analysis at sub-pixel resolution. PLoS Comput Biol 4(11):e1000233

Gupta A, Lloyd-Price J, Neeli-Venkata R et al (2014a) In vivo kinetics of segregation and polar retention of MS2-GFP-RNA complexes in *Escherichia coli*. Biophys J 106(9):1928–1937

Gupta A, Lloyd-Price J, Neeli-Venkata R et al (2014b) Robustness of the division symmetry in *Escherichia*

coli and functional consequences of symmetry breaking. Phys Biol 11(6):066005
Gupta A, Llyod-Price J, Ribeiro AS (2015) In silico analysis of division times of *Escherichia coli* populations as a function of the partitioning scheme of non-functional proteins. Silico Biol 1(2):9–21
Häkkinen A, Ribeiro AS (2015) Estimation of GFP-tagged RNA numbers from temporal fluorescence intensity data. Bioinformatics 31(1):69–75
Häkkinen A, Muthukrishnan AB, Mora A et al (2013) CellAging: a tool to study segregation and partitioning in division in cell lineages of *Escherichia coli*. Bioinformatics 29:1708–1709
Harry E, Monahan L, Thompson L (2006) Bacterial cell division: the mechanism and its precison. Int Rev Cyt 253:27–94
Hebisch E, Knebel J, Landsberg J, Frey E, Leisner M (2013) High variation of fluorescence protein maturation times in closely related *Escherichia coli* strains. PLoS One 8(10):e75991
Hiraga S, Niki H, Ogura T et al (1989) Chromosome partitioning in *Escherichia coli*: novel mutants producing anucleate cells. J Bacteriol 171(3):1496–1505
Hu Z, Lutkenhaus J (1999) Topological regulation of cell division in *Escherichia coli* involves rapid pole to pole oscillation of the division inhibitor MinC under the control of MinD and MinE. Mol Microbiol 34(1):82–90
Huang KC, Mukhopadhyay R, Wingreen NS (2006) A curvature-mediated mechanism for localization of lipids to bacterial poles. PLoS Comput Biol 2:e151
Kuwada N, Traxler B, Wiggins PA (2015) Genome-scale quantitative characterization of bacterial protein localization dynamics throughout the cell cycle. Mol Microbiol 95(1):64–79
Laskowska E, Bohdanowicz J, Kuczyńska-Wiśnik D et al (2004) Aggregation of heat-shock-denatured, endogenous proteins and distribution of the IbpA/B and Fda marker-proteins *in Escherichia coli* WT and grpE280 cells. Microbiology 150:247–259
Lee L, Mizuno T, Imae Y (1988) Thermosensing properties of *Escherichia coli* tsr mutants defective in serine chemoreception. J Bacteriol 170:4769–4774
Lindner AB, Madden R, Demarez A et al (2008) Asymmetric segregation of protein aggregates is associated with cellular aging and rejuvenation. Proc Natl Acad Sci USA 105(8):3076–3081
Lloyd-Price J, Gupta A, Ribeiro AS (2012) SGNS2: a compartmentalized stochastic chemical kinetics simulator for dynamic cell populations. Bioinformatics 28(22):3004–3005
Lloyd-Price J, Tran H, Ribeiro AS (2014) Dynamics of small genetic circuits subject to stochastic partitioning in cell division. J Theo Biol 356:11–19
Lutkenhaus J (2007) Assembly dynamics of the bacterial MinCDE system and spatial regulation of the Z ring. Annu Rev Biochem 76:539–562
Lutkenhaus J, Pichoff S, Du S (2012) Bacterial cytokinesis: from Z ring to divisome. Cytoskeleton (Hoboken) 69(10):778–790
Ma X, Ehrhardt DW, Margolin W (1996) Colocalization of cell division proteins FtsZ and FtsA to cytoskeletal structures in living *Escherichia coli* cells by using green fluorescent protein. Proc Natl Acad Sci USA 93(23):12998–13003
Maclean FI, Munson RJ (1961) Some environmental factors affecting the length *of Escherichia coli* organisms in continuous cultures. J Gen Microbiol 25:17–27
Maddock JR, Shapiro L (1993) Polar location of the chemoreceptor complex in the *Escherichia coli* cell. Science 259(5102):1717–1723
Maisonneuve E, Ezraty B, Dukan S (2008) Protein aggregates: an aging factor involved in cell death. J Bacteriol 190(18):6070–6075
Männik J, Bailey MW (2015) Spatial coordination between chromosomes and cell division proteins in *Escherichia coli*. Front Microbiol 6:306
Männik J, Wu F, Hol FGH et al (2012) Robustness and accuracy of cell division in Escherichia coli in diverse cell shapes. Proc Natl Acad Sci USA 109(18):6957–6962
Margolin W (2005) FtsZ and the division of prokaryotic cells and organelles. Nat Rev Mol Cell Biol 6:862–871
Martins L, Neeli-Venkata R, Oliveira SMD et al (2018) SCIP: a single-cell image processor toolbox. Bioinformatics 34(24):4318–4320
Meinhardt H, de Boer PAJ (2001) Pattern formation in Escherichia coli: a model for the pole-to-pole oscillations of min proteins and the localization of the division site. Proc Natl Acad Sci USA 98(25):14202–14207
Miot M, Betton JM (2004) Protein quality control in the bacterial periplasm. Microb Cell Factories 3:4
Mondal J, Bratton BP, Li Y et al (2011) Entropy-based mechanism of ribosome-nucleoid segregation in *E. coli cells*. Biophys J 100(11): 2605–2613
Mulder E, Woldringh CL (1989) Actively replicating nucleoids influence positioning of division sites in *Escherichia coli* filaments forming cells lacking DNA. J Barcteriol 171(8):4303–4314
Neeli-Venkata R, Martikainen A, Gupta A et al (2016a) Robustness of the process of nucleoid exclusion of protein aggregates in *Escherichia coli*. J Bacteriol 198(6):898–906
Neeli-Venkata R, Startceva S, Teppo A et al (2016b) Polar localization of the serine chemoreceptor of *Escherichia coli* is nucleoid exclusion-dependent. Biophys J 111(11):2512–2522
Neeli-Venkata R, Oliveira SMD, Martins L et al (2018) The precision of the symmetry in Z-ring placement in *Escherichia coli* is hampered at critical temperatures. Phys Biol 15(5):056002
Oliveira SMD, Neeli-Venkata R, Goncalves NS et al (2016) Increased cytoplasm viscosity hampers aggregate polar segregation in *Escherichia coli*. Mol Microbiol 99(4):686–999
Parkinson JS, Ames P, Studdert CA (2005) Collaborative signaling by bacterial chemoreceptors. Curr Opin Microbiol 8:116–121

Parry BR, Surovtsev IV, Cabeen MT et al (2014) The bacterial cytoplasm has glass-like properties and is fluidized by metabolic activity. Cell 156:183–194

Prajapat MK, Ribeiro AS (2018) Added value of autoregulation and multi-step kinetics of transcription initiation. R Soc Open Sci 5(11):181170

Raskin DM, de Boer PA (1999) Rapid pole-to-pole oscillation of a protein required for directing division to the middle of *Escherichia coli*. Proc Natl Acad Sci USA 96(9):4971–4976

Rebbapragada A, Johnson MS, Harding GP et al (1997) The Aer protein and the serine chemoreceptor Tsr independently sense intracellular energy levels and transduce oxygen, redox, and energy signals for *Escherichia coli* behavior. Proc Natl Acad Sci USA 94:10541–10546

Rothfield L, Taghbalout A, Shih YL (2005) Spatial control of bacterial division-site placement. Nat Rev Microbiol 3:959–968

Rudner DZ, Pan Q, Losick RM (2002) Evidence that subcellular localization of a bacterial membrane protein is achieved by diffusion and capture. Proc Natl Acad Sci USA 99(13):8701–8706

Sabate R, de Groot NS, Ventura S (2010) Protein folding and aggregation in bacteria. Cell Mol Life Sci 67(16):2695–2715

Santos TMA, Lin TY, Rajendran M et al (2014) Polar localization of *Escherichia coli* chemoreceptors requires an intact Tol-pal complex. Mol Microbiol 92(5):985–1004

Shehata TE, Marr AG (1975) Effect of temperature on the size of Escherichia coli cells. J Bacteriol 124(2):857–862

Sourjik V, Berg HC (2000) Localization of components of the chemotaxis machinery of *Escherichia coli* using fluorescent protein fusions. Mol Microbiol 37(4):740–751

Sourjik V, Berg HC (2004) Functional interactions between receptors in bacterial chemotaxis. Nature 428:437–441

Speed MA, Wang DI, King J (1996) Specific aggregation of partially folded polypeptide chains: the molecular basis of inclusion body composition. Nat Biotechnol 14(10):1283–1287

Stewart EJ, Madden R, Gregory P et al (2005) Aging and death in an organism that reproduces by morphologically symmetric division. PLoS Biol 3(2):e45. https://doi.org/10.1371/journal.pbio.0030045

Stylianidou S, Kuwada NJ, Wiggins PA (2014) Cytoplasmic dynamics reveals two modes of nucleoid-dependent mobility. Biophys J 107(11):2684–2692

Thiem S, Kentner D, Sourjik V (2007) Positioning of chemosensory clusters in *E. coli* and its relation to cell division. EMBO J 26(6):1615–1623

Tonthat NK, Arold ST, Pickering BF et al (2011) Molecular mechanism by which the nucleoid occlusion factor, SlmA, keeps cytokinesis in check. EMBO J 30:154–164

Trueba FJ (1982) On the precision and accuracy achieved by *Escherichia coli* cells at fission about their middle. Arch Microbiol 131(1):55–59

Trueba FJ, Woldringh CL (1980) Changes in cell diameter during the division cycle of *Escherichia coli*. J Bacteriol 142(3):869–878

Tyedmers J, Mogk A, Bukau B (2010) Cellular strategies for controlling protein aggregation. Nat Rev Mol Cell Biol 11(11):777–788

van den Berg J, Boersma AJ, Poolman B (2017) Microorganisms maintain crowding homeostasis. Nat Rev Microbiol 15(5):309–318

Wadhams GH, Armitage JP (2004) Making sense of it all: bacterial chemotaxis. Nat Rev Mol Cell Biol 5:1024–1037

Wang X, Possoz C, Sherratt DJ (2005) Dancing around the divisome: asymmetric chromosome segregation in *Escherichia coli*. Genes Dev 19:2367–2377

Wang X, Llopis PM, Rudner DZ (2013) Organization and segregation of bacterial chromosomes. Nat Rev Genet 14(3):191–203

Weart RB, Lee AH, Chien AC et al (2007) A metabolic sensor governing cell size in bacteria. Cell 130(2):335–347

Wickner S (1999) Posttranslational quality control: folding, refolding, and degrading proteins. Science 286(5446):1888–1893

Willetts NS (1967) Intracellular protein breakdown in nongrowing cells of *Escherichia coli*. Biochem J 103(2):453–461

Winkler J, Seybert A, König L et al (2010) Quantitative and spatio-temporal features of protein aggregation in *Escherichia coli* and consequences on protein quality control and cellular aging. EMBO J 29(5):910–923

Yu XC, Margolin W (1999) FtsZ ring clusters in min and partition mutants: role of both the Min system and the nucleoid in regulating FtsZ ring localization. Mol Microbiol 32(2):315–326

Yu J, Xiao J, Ren X, Lao K, Xie XS (2006) Probing gene expression in live cells, one protein molecule at a time. Science 311(5767):1600–1603

Zhang P, Khursigara CM, Hartnell LM et al (2007) Direct visualization of *Escherichia coli* chemotaxis receptor arrays using cryo-electron microscopy. Proc Natl Acad Sci USA 104(10):3777–3781

Mechanisms and Dynamics of the Bacterial Flagellar Motor

5

A. L. Nord and F. Pedaci

Abstract

Many bacteria are able to actively propel themselves through their complex environment, in search of resources and suitable niches. The source of this propulsion is the Bacterial Flagellar Motor (BFM), a molecular complex embedded in the bacterial membrane which rotates a flagellum. In this chapter we review the known physical mechanisms at work in the motor. The BFM shows a highly dynamic behavior in its power output, its structure, and in the stoichiometry of its components. Changes in speed, rotation direction, constituent protein conformations, and the number of constituent subunits are dynamically controlled in accordance to external chemical and mechanical cues. The mechano-sensitivity of the motor is likely related to the surface-sensing ability of bacteria, relevant in the initial stage of biofilm formation.

Keywords

Bacterial flagellar motor · Bacterial motility · Biofilm · Chemosensing · Cooperativity · Ion motive force · Mechanosensing · Molecular motor · Protein exchange · Surface sensing

A. L. Nord · F. Pedaci (✉)
Centre de Biochimie Structurale (CBS), INSERM, CNRS, University of Montpellier, Montpellier, France

Abbreviations

BFM	Bacterial Flagellar Motor
CW, CCW	Clock-Wise, Counter Clock-Wise
ECT	Electron Cryotomography
FLIM	Fluorescence Loss in Photobleaching
FRAP	Fluorescence Recovery After Photobleaching
GFP	Green Flourescent Protein
IMF	Ion Motive Force
MCP	Methyl-Accepting Chemoreceptor Protein
PG	Peptidoglycan
PMF	Proton Motive Force
SMF	Sodium Motive Force
SNR	Signal to Noise Ratio
TIRF	Total Internal Reflection Fluorescence

5.1 Introduction

Active movement gives an important evolutionary advantage for survival, especially when embedded within a feedback loop which includes the ability to sense the environment and bias the displacement accordingly (Wei et al. 2011). Such directed movement in living systems appears even at the smallest scale, where many bacteria have evolved mechanisms to propel them-

G. Duménil, S. van Teeffelen (eds.), *Physical Microbiology*, Advances in Experimental Medicine and Biology 1267, https://doi.org/10.1007/978-3-030-46886-6_5

selves, sense their environment, and control their displacement. This allows them to explore and find suitable niches in complex inhomogeneous environments. Since inertia plays a negligible role at the microscopic level (Purcell 1997), directed motion requires continuous energy consumption, and this is likely one reason why today we observe highly efficient molecular motors at work in living cells. Here we focus on a striking example of efficiency and power evolved to provide bacteria with motility: the rotary Bacterial Flagellar Motor (BFM).

Found in many motile bacteria, the BFM is a large protein complex (∼11 MDa) in the membrane at the base of each flagellum. The BFM is one of the rare examples where rotation around an axis emerged in living systems, despite the requirement of two distinct parts, which must be in close proximity yet topologically separated in order to allow force generation and continuous rotation. By rotating the flagellum, the BFM propels the cell and, finely regulated by the chemotaxis network, allows cellular motility and chemotaxis, the ability of bacteria to move and follow chemical gradients (Berg 2003; Sowa and Berry 2008; Morimoto and Minamino 2014).

Yet, far from being resigned to being a simple propeller for the cell, the BFM is an extraordinarily active and dynamic player in different contexts. In the following, we will focus on the studies that have revealed the intricate mechanisms by which the BFM senses the local extracellular environment and adjusts its output power, thrust, and direction of rotation, by dynamically changing the stoichiometry and structure of the protein complex. Such dynamicity may even play a role in triggering drastic changes in the lifestyle of the cell.

5.2 Architecture of the Bacterial Flagellar Motor

The BFM complex (described in this chapter pertaining to *Escherichia coli* (*E. coli*), unless otherwise noted) is composed of at least 13 different component proteins, and a further ∼25 proteins are required for its expression and assembly. As every rotary motor, it is composed by two main parts which rotate with respect to each other, a rotor and a stator. The rotor broadly consists of three major parts: (1) the intracellular "basal body", formed by a set of linked ring structures (of ∼50 nm maximum diameter) spanning the cell membranes and peptidoglycan (PG) layer, (2) the long (∼10 μm) external flagellum, formed mainly by the protein FliC, and (3) a short (∼50 nm) flexible universal joint termed the "hook", which connects the basal body to the flagellum and allows the extracellular components to bend while rotating. The cytosolic part of the basal body, termed the C ring, is composed by multiple copies of the three proteins, FliG, FliM, and FliN, and plays an important role in torque generation and switching between clock-wise (CW) and counter clock-wise (CCW) rotation (Fig. 5.1).

Rotation of the rotor, and thus the flagellum, is the result of the collective effort of a dozen unitary motors, the *stator units*, ion channels located in the inner membrane and firmly anchored to the rigid PG layer. Torque is produced at the interface between each stator unit and the section of the C ring facing the inner membrane and formed by FliG. As a microtubule is the track for kinesin, the FliG ring can be seen as a circular common track over which the different stator units independently step (Sowa and Berry 2008; Samuel and Berg 1996).

The BFM is an electric motor: the stator units consume energy from the cellular *Ion Motive Force* (IMF), the ion-specific electro-chemical potential sustained by the cell across its membrane. In *E. coli*, *Salmonella enterica* (*S. enterica*), and many other bacteria, the source of energy is specifically the *Proton Motive Force* (PMF), the potential (which can attain a couple hundred mV) generated by the cell during respiration, which is a complex series of processes controlled by a wide variety of membrane-associated enzymes that act as either sources or sinks of proton flux. In other bacteria, the stator units consume other ions, depending upon their environment. A popular model system is the stator of *Vibrio alginolyticus* (*V. alginolyticus*) and *Vibrio*

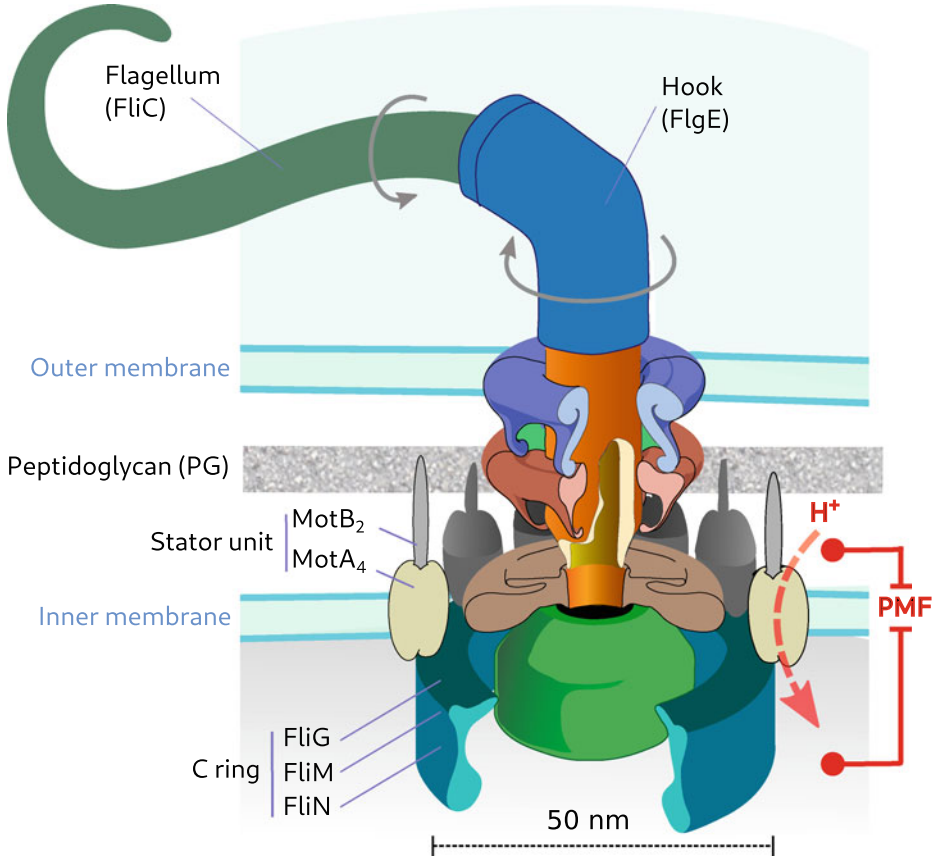

Fig. 5.1 Schematic structure of the BFM

cholerae (*V. cholerae*), which are Na^+ specific. Other bacteria have been reported to consume K^+, and even divalent ions (Terahara et al. 2012; Imazawa et al. 2016). Most stator units are specific to a single ion, though some are capable of coupling two different ions (Terahara et al. 2008, 2012). While most bacteria contain a single type of stator unit, some bacteria contain two or more different types of stator units, either with the same or different ion specificity (Thormann and Paulick 2010).

Each stator unit in E.coli is believed to be a hetero-hexamer a MotA homo-tetramer which engulfs a MotB dimer (see Note). Each MotA extends mainly into the cytosol, with a domain that is involved in torque generation. The two MotB are each composed of a single transmembrane helix, with their N-terminals likely enclosed within the four MotA cytosolic domains, and their C-terminals extending in the periplasm. The C-terminus of MotB is involved in the anchoring of the stator unit to the rigid PG layer when the stator unit is incorporated into the BFM, and in the opening and closing of the ion channel which permits ion translocation and the downstream torque generation (Sowa and Berry 2008; Kojima et al. 2009).

5.2.1 A Highly Dynamic Complex

The BFM does not blindly produce torque to rotate the rotor. In the last few years, the emerging picture of the BFM shows that the propeller is also a mechanical sensor, and that its structure is not fixed and unchangeable but capable of varying both structure and stoichiometry of its various components, both in the stator and rotor. More-

over, the long flagellum is not simply a passive producer of thrust. It can dynamically switch between several global structures depending on the force and torque applied to it (Darnton and Berg 2007), and it can act as a tether to external surfaces. The features of dynamic complexity which have been uncovered so far can be summarized by the following examples:

- The mechanical properties of the long flagellum and the flexible hook are a product of their structures. The flagellum and hook exhibit dynamic global conformational changes between several discrete helical forms, triggered by force and torque (Darnton and Berg 2007; Calladine et al. 2013; Son et al. 2013). (See Sects. 5.3.1 and 5.3.2).
- Chemotaxis is based on the controlled switch of the direction of rotation of each BFM, which occurs on the order of milliseconds. The fascinating molecular origin of this directional switching comes from the ability of the FliG ring to dynamically and cooperatively change its global conformation during rotation, a phenomenon triggered by extracellular mechanochemical cues (Lam et al. 2012; Lee et al. 2010; Bai et al. 2010, 2012). (See Sect. 5.3.2).
- In *E. coli*, *V. alginolyticus*, *Shewanella oneidensis* (*S. oneidensis*), *P. aeruginosa aeruginosa* (*P. aeruginosa*) and possibly many other strains (Baker and O'Toole 2017), the stator units are not fixed modules of the BFM, but are observed to dynamically exchange: on one hand, anchored to the cell wall at the periphery of the rotor, the stator units actively produce torque which rotates the rotor; on the other hand, unbound from the complex and PG, they passively diffuse in the membrane, closing their ion-specific pore so as not to waste the IMF (Block and Berg 1984; Leake et al. 2006; Kojima et al. 2009). (See Sect. 5.3.3.1).
- Stator unit dynamics were recently revealed to be even richer when it was demonstrated that their recruitment to the BFM is *mechanosensitive*, i.e. dependent on the mechanical load the motor must rotate. A higher resistance to rotation has been observed to promote the recruitment of more stator units (Lele et al. 2013; Tipping et al. 2013; Che et al. 2014). Such a system is analogous to a car whose engine incorporates new pistons when running uphill, and releases them when running downhill (Mandadapu et al. 2015). (See Sect. 5.3.3.2).
- Surprisingly, an exchange has also been observed for the proteins FliM and FliN (Delalez et al. 2010, 2014), two components of the rotor. By tailoring its stoichiometry in accordance to the output of the chemotaxis network, the BFM attains a hypersensitivity that is, to our knowledge, unmatched by other allosteric protein complexes (Yuan and Berg 2013). (See Sect. 5.3.3.4).

5.3 Mechanisms of the Motor with Respect to Motility and Chemotaxis

5.3.1 Mechanism of Propulsion

Up to a dozen stator units are found at the periphery of the rotor (Reid et al. 2006), spanning the inner membrane and bound to the PG by an OmpA-like domain within the periplasmic domain of MotB (Chun and Parkinson 1988; De Mot and Vanderleyden 1994). Each stator unit contains two ion channels (Braun and Blair 2001). Ions in the periplasm bind to a conserved charged residue of MotB (Zhou et al. 1998) and are translocated across the inner membrane and released into the cytoplasm. While no atomic level crystal structure exists for the stator complex (see Note), making it difficult to pinpoint the site of torque generation, biochemical crosslinking and site-directed mutagenesis studies have located the active regions. An interaction between two charged residues on the cytoplasmic domain of MotA and five charged residues on the C-terminal domain of FliG generates torque (Zhou and Blair 1997; Lloyd and Blair 1997; Zhou et al. 1998). Introducing charge-reversing mutations in both proteins compensates, suggesting an electrostatic interaction between FliG and MotA in H^+-driven *E. coli* (Zhou et al. 1998), and a similar pattern is seen in PomA and FliG in the Na^+-

driven BFM of *V. alginolyticus* (Yakushi et al. 2006).

Each stator unit, while functionally independent, applies torque to a common track, the FliG subunits of the C ring. Consequently, the rotational speed of the BFM is proportional to the number of stator units present around the rotor (Block and Berg 1984; Blair and Berg 1988). It has been postulated that ion translocation modulates the cyclic conformation of MotA (Zhou et al. 1998; Kojima and Blair 2001; Kim et al. 2008), causing a power-stroke or ratchet-like interaction with the rotor, applying torque via electrostatic and steric forces (Mandadapu et al. 2015; Nishihara and Kitao 2015), leading to rotation. However, the exact mechanochemical cycle describing how a stator unit uses the energy of the IMF to rotate the BFM has yet to be elucidated. Indirect evidence for a stepping mechanism in the BFM came from applying Poisson statistics to the mean and variance of motor rotation speeds of the motor, yielding an upper limit of 50 mechanical steps per stator unit per rotation of the BFM (Samuel and Berg 1995, 1996). Individual steps of the motor have since been directly resolved in a Na^+-driven chimeric strain of *E. coli*. These experiments were performed under deenergized conditions where the number of stator units was low (but not quantified) (Sowa et al. 2005). Individual steps of BFM rotation have yet to be resolved under physiological conditions, a task rendered complicated by the speed of the motor, the small angular size of a step, and the flexibility of the hook.

Rotation of the C ring is coupled to the rod, the central driveshaft of the rotor, then to the hook, and finally to the flagellum. While the helical nature of the hook and flagellum are similar, structural differences elicit very different mechanical properties. The hook is flexible (Block et al. 1991), and acts as a universal joint, allowing the flagella of multiple motors to bundle together (Samatey et al. 7012; Brown 2012). The flagellum is much less flexible, and dynamically adopts a range of discrete helical forms, from tightly right-handed, to straight, to tightly left-handed, each with distinct propulsive characteristics (Turner et al. 2000; Asakura 1970). This observed polymorphism, which is dependent upon force and torque as well as the pH and ionic strength of the environment (Hotani 1976; Darnton and Berg 2007; Kamiya and Asakura 1976a,b), has been explained in terms of a bi-stable molecular "switch" at the interface between neighboring flagellin molecules (Yamashita et al. 1998; Yonekura et al. 2003; Maki-Yonekura et al. 2010), a property believed to be indispensable to bacterial motility.

The 'fingerprint' of any rotary motor is the relationship of the torque produced as a function of rotational speed. A variety of biophysical assays have been used to measured the torque-speed relationship of the BFM of *E. coli* (see Sect. 5.3.4 for details). Torque-speed curves have generally been characterized by a concave-down shape (Chen and Berg 2000), and this has served as one of the prime constraints for physical models of the mechanism of torque production. However, such measurements have assumed that the average number of stator units is constant, an assumption that we now know not to be true (details below). While measurements of the torque-speed curve in BFMs driven by a single Na^+ chimeric stator unit in *E. coli* also demonstrate a concave-down shape (Lo et al. 2013), more work will be necessary to provide a full characterisation of the motor's capabilities as a function of the number of stator units (Nord et al. 2017; Sato et al. 2019).

Depending on the bacterial species, the motor can rotate at speeds up to at least 1700 Hz and switch rotational direction within milliseconds (Sowa and Berry 2008). The rotation of the flagellum via the BFM ultimately serves to propel the cell through its environment, which can be either a liquid environment or on a surface. When swimming in an aqueous environment, the helical conformation adopted by the flagellum provides a nonreciprocal or time-irreversible motion necessary for propulsion in the low Reynolds number environment of the bacterium (Purcell 1997). While swimming occurs at the level of an individual bacterium, groups of bacteria can also collectively propel themselves along surfaces, a widespread but less well studied type of motility called swarming (Partridge and Harshey 2013). Many bacteria dynamically and reversibly transition between swimming and swarming, a

transition which involves distinct changes in cell morphology, such as a change in the number of flagella per cell (Harshey 2003).

5.3.2 Mechanism of Chemotaxis

Propulsion from the BFM bestows upon the cell the ability to actively explore its environment. While active movement in itself may be slightly beneficial (Wei et al. 2011), the ability to bias such exploration in response to external stimuli confers a much greater advantage. Chemotaxis is the processes by which bacteria temporally sense the chemical composition of their environment and bias their movement towards favorable conditions, either towards attractants or away from toxins (Adler 1966; Eisenbach 2011).

Chemosensory signals alter the rotary behavior of the BFM, causing it to switch direction, slow down, or stop (depending on the species) (Armitage and Schmitt 1997). The average *E. coli* cell has about six motors (Fukuoka et al. 2010), randomly positioned on the cell body, each turning a single flagellum. The motors are bidirectional. During swimming motility, when all of the motors of a cell rotate in the CCW direction, the flagella interact hydrodynamically to form a bundle that propels the cell smoothly forwards. Upon reversal of a single motor to the CW direction, a torsional shock propagates along the flagellum, triggering a conformational change of the entire flagellum, causing the bundle to splay, and causing a random reorientation of the cell, or 'tumble' (Turner et al. 2000; Macnab and Ornston 1977; Hotani 1982). Upon the return of this motor to the CCW direction, the bundle reforms and the cell swims forwards again, albeit in a new direction. Chemotaxis is achieved via regulation of the concentration of an intracellular response regulator, CheY-P, which subsequently controls the ratio of swimming versus tumbling; as a cell moves towards attractant or away from repellent, the CheY-P concentration decreases, decreasing the frequency of re-orientations and biasing the random walk along the chemical gradient (Berg 2003). Interestingly, it remains unclear whether chemotaxis plays a role in swarmer-cell migration, with evidence suggesting that it is actually suppressed during swarming (Harshey 1994). How and why chemotaxis suppression occurs remains unknown.

The chemotaxis network of *E. coli* has been intensively studied over the last 50 years and serves as a model system for biological signal processing (Wadhams and Armitage 2004; Vladimirov and Sourjik 2009). The input of the network consists of co-operative arrays of transmembrane methyl-accepting chemoreceptor proteins (MCPs). Clusters of MCPs, located primarily near the cell poles, bind small chemoeffector molecules which pass through porins in the outer cell membrane. MCP activation, due to a decrease in attractant binding or an increase in repellent binding, induces the trans autophosphorylation of the cytoplasmic histidine protein kinase CheA. CheA subsequently transfers it phosphoryl group to CheY (Li et al. 1995). Phosphorylated CheY (CheY-P) binds first to FliM (Welch et al. 1993; Toker and Macnab 1997; Lee et al. 2001) and then to FliN of the C ring (Sarkar et al. 2010), inducing a conformational change in FliG, ultimately enhancing the probability of CW rotation of the rotor (Dyer et al. 2009). The output of the chemotaxis network is the rotational bias of the motor (time spent in CW with respect to CCW rotation). Thus, while the stator units act as actuators, the topology of FliG sets the rotation direction. CheZ, an allosteric activator of CheY dephosphorylation, decreases the half-life of CheY-P from $\sim$20 s to $\sim$200 ms, allowing for rapid signal termination (Wadhams and Armitage 2004).

The chemotaxis system demonstrates both remarkable adaptation to stimuli and extreme sensitivity. Adaptation emerges from the regulation of MCP activity by CheR and CheB, enzymes which methylate and demethylate the receptors, respectively. Upon the addition or removal of an attractant, the change in ligand binding is compensated for via methylation, returning the system to its prestimulus state with respect to MCP activation, [CheY-P], and motor bias. A crucial ingredient of adaptation is the fact that signal termination, the dephosphorylation of CheY-P by CheZ, occurs

on a timescale faster than MCP regulation; all together, this provides the cell a memory mechanism for extracellular chemoeffector concentrations (Berg and Brown 1972) which is necessary for chemotaxis. Sensitivity emerges from two methods of signal amplification, enabling the network to sense nanomolar changes in chemoeffectors (Mao et al. 2003). One source of signal amplification is the cooperative interactions of neighboring MCPs within clusters (Sourjik and Berg 2002). The second is a steep dependence of BFM rotational bias upon [CheY-P] (with a Hill coefficient of 10-20) (Cluzel et al. 2000; Yuan and Berg 2013). Together, these traits allow the cell to retain high sensitivity to extracellular chemoeffectors over a wide range, from nanomolar to millimolar concentrations (Vladimirov and Sourjik 2009).

Binding of CheY-P to the C ring is much less cooperative than the change of the rotational direction of the BFM (Sourjik and Berg 2002; Sagi et al. 2003), leading to the well-accepted proposal that the change in the rotational direction of the motor occurs via the conformational spread (Duke et al. 2001) of individual FliG subunits (Bai et al. 2010; Ma et al. 2016). In this model, the binding of CheY-P to a single C ring protomer (likely composed of four FliN, one FliM, and one FliG, though we note a potential stoichiometry mismatch between FliG and FliM Minamino and Imada 2015, Stock et al. (2012)), causes a conformational change in FliG of that protomer, flipping from the native structural orientation to an alternate structural orientation. Under the assumption of a free-energy penalty for neighboring protomers in opposing orientations, conformational spread describes the stochastic growth of the conformational state around the C ring until each protomer is in the altered orientation (Bai et al. 2010; Ma et al. 2016). Due to the electrostatic interactions between the conserved residues of FliG with respect to the relevant residues on MotA of the stator unit, a ring of natively oriented FliGs leads to CCW rotation of the motor, while a ring of FliGs in the alternate orientation leads to CW rotation (Lee et al. 2010).

However, [CheY-P] is not the only determinant of the rotational bias of the motor. It has been shown that the switching rate of the motor is non-monotonically dependent upon the external load on the flagella, first increasing and then decreasing with increasing external load (Fahrner et al. 2003; Yuan et al. 2009). This relationship has been successfully reproduced by a model in which the instantaneous torque applied by an individual stator unit onto a FliG subunit accelerates the rate of switching of the protomer (Bai et al. 2012). The number of FliG subunits which are flipped with the mechanical aid of the stator unit depends upon the applied single-stator unit torque (a function of IMF and motor speed), and the time that each stator unit interacts with a single FliG (a function of motor speed). Thus, the rotational bias of the motor, the crucial ingredient of chemotaxis, is regulated by both chemical and mechanical signals.

5.3.3 Mechanisms of Motor Regulation and Adaptation

Over the last decade, single-molecule in vivo microscopy has revealed that many protein complexes, once believed to be compositionally stable, are surprisingly dynamic, on a broad continuum of time scales (Tusk et al. 2018). The BFM is no exception to this trend. Multiple components of the BFM demonstrate dynamic protein exchange with a pool of cellular "spare parts". While the reasons for such exchange are not fully elucidated, it is becoming clear that it serves as a mechanism for regulation and adaptation.

5.3.3.1 Stator Exchange

The first hint of the dynamic nature of the stator units came from experiments performed in an *E. coli* strain which lacked functional stator unit proteins. While the motors were initially nonfunctional, the expression of the stator proteins from inducible plasmids restored the functionality of the BFMs. In such "resurrection" experiments, rotation of the BFM was restored in a series of ~8–11 discrete increases in speed, each interpreted as the inclusion of a new stator unit, leading to the conclusion that the stator units act

independently on the C ring (Blair and Berg 1988; Ryu et al. 2000; Reid et al. 2006; Block and Berg 1984).

The first direct observation of stator unit exchange under steady state conditions used fluorescence recovery after photobleaching (FRAP) and fluorescence loss in photobleaching (FLIM) to observe a constant exchange between green fluorescent protein (GFP) labeled stator units which were co-localized with a rotating motor, and a pool of about 200 stator units which were freely diffusing in the inner membrane (Leake et al. 2006). These experiments also counted an average number of 11 stator units co-localized with the motor, in good agreement with the number of discrete speed increases seen in resurrection experiments. Steady-state measurements of the rotation of the BFM show stochastic discrete increases and decreases in speed (Ryu et al. 2000; Sowa et al. 2005; Nord et al. 2017), interpreted as individual stator unit association and dissociation events, consistent with the idea that there is a constant exchange of stator units between an active state, localized with the motor and applying torque, and an inactive state, diffusing in the inner membrane. The magnitude of these speed changes has been used to quantify the amount of speed and torque that an individual stator unit contributes to the complex as a function of the viscous load on the motor (Nord et al. 2017).

Aside from *E. coli*, stator unit exchange in functional motors has also been directly observed in *S. enterica* (Partridge et al. 2015), *S. oneidensis* (Paulick et al. 2015), and *B. subtilis* (Terahara et al. 2017a,b). Three-dimensional structures of in situ BFMs from multiple species have been obtained via electron cryotomography (ECT) coupled with subtomogram averaging. Structures of certain species show a clear density which corresponds to the ring of stator units; depending on the species, this stator unit ring shows variable radii and symmetries (Chen et al. 2011). However, the stator ring is absent in other species, including the enteric bacteria, *E. coli* and *S. enterica*. The absence of this ring in ECT structures may prove to be an indicator of stator unit exchange. If so, one might predict that species such as *V. fischeri* and *C. jejuni*, which show distinct rings of 13-fold and 17-fold symmetry respectively (Beeby et al. 2016), are characterized by fixed stator units which do not exchange. However, we note that recently a stator ring was imaged in *S. oneidensis* (Kaplan et al. 2019), which expresses two different types of stator units that display turnover (Paulick et al. 2015).

5.3.3.2 Stator Mechanosensing

Stator unit exchange gives the cell the ability to adapt to the chemical and mechanical characteristics of its environment. Motor speed is proportional to the IMF in both H^+ and Na^+ motors (Manson et al. 1980; Fung and Berg 1995; Gabel and Berg 2003; Sowa et al. 2003; Lo et al. 2007, 2013), and when the IMF is collapsed, motors no longer turn (Sowa et al. 2005, 2014). Upon reinstatement of the IMF, motor speed increases in a step-wise fashion, similar to that seen in resurrection experiments, and this has typically been interpreted as the stochastic assembly of stator units which had dissociated from the motor in the absence of IMF (Fung and Berg 1995; Sowa et al. 2005, 2014; Tipping et al. 2013). However, one could imagine that a stator unit could disengage from the rotor without dissociating from the BFM complex, and determining how stator unit localization depends upon the chemical environment has proven to be difficult. Experiments employing mutations in the periplasmic conserved ion-binding site of MotB/PomB which prohibit ion conduction and lead to non-functional motors have concluded that ion conduction is not necessary for stator units to localize to the motor in *S. enterica* or *E. coli* (Morimoto et al. 2010; Zhou et al. 1998; Kojima and Blair 2001), but that it is necessary in *V. alginolyticus* (Fukuoka et al. 2009). Stator unit localization probed via fluorescent protein fusions of stator proteins have shown that the SMF is necessary for stator unit incorporation in *V. alginolyticus* (Fukuoka et al. 2009), whereas the PMF is unnecessary for incorporation in *S. enterica* (Morimoto et al. 2010; Suzuki et al. 2019), and conflicting studies disagree on the necessity of the PMF for stator unit incorporation in *E. coli* (Tipping et al. 2013; Suzuki et al. 2019). Recently, fluorescent studies have suggested that stator unit incorporation is dependent upon external pH (Suzuki et al. 2019).

It has also recently been shown in *E. coli* that the stator unit number is a function of external load on the flagellum, with an increase in viscous load leading to an increase in stator unit number (Lele et al. 2013; Tipping et al. 2013; Che et al. 2014; Nord et al. 2017). We have measured the load-dependent association and dissociation rates of the stator units (Nord et al. 2017), showing little to no dependence of the association rate with load and a dissociation rate that decreases with increasing external load. Measurements of the force applied by a single stator unit upon the rotor show that it scales with external load. By reaction, the force with which the stator unit pulls on its attachment to the PG also scales with external load. The observation that force appears to strengthen, instead of weaken, the stator unit's association with the motor has led to the speculation that stator dynamics may be governed by a catch bond mechanism (Nord et al. 2017; Chawla et al. 2017). An in-frame deletion of residues 72–100 of MotB of *S. enterica* has been shown to reduce the number of active stator units except at high load, thereby impacting the mechanosensitivity of the stator unit (Castillo et al. 2013). A mutation in the conserved ion-binding site of MotB which reduces ion conductivity (Che et al. 2008) has been shown to reduce the number of stator units in a load-dependent manner, thus also impacting the mechanosensitivity of the stator unit (Che et al. 2014). Aside from *E. coli*, there is direct and indirect evidence that the stators of *S. enterica* and *B. subtilis* share similar mechanosensitive features (Che et al. 2014; Terahara et al. 2017a).

The over-expression of stator proteins does not inhibit growth (Stolz and Berg 1991), suggesting that stator units in the inactive state do not exhibit high ion-conductivity. The ion channels are connected to the PG binding domain by an intrinsically disordered and highly flexible linker (Terahara et al. 2017b). Mutational studies have identified a region in this linker that appears to act as a plug, limiting ion translocation prior to association to the rotor (Hosking et al. 2006; Li et al. 2011). Various mutations in MotA and FliG have been identified as important for proper stator unit assembly around the rotor (Morimoto et al. 2010, 2013), and structural evidence suggests that assembly involves a large conformational change in the periplasmic region of MotB, stretching upwards towards the PG and opening the plug (Kojima 2015).

Recently, high speed scanning measurements have shown that an isolated (Na^+ consuming) MotPS stator unit in *B. subtilis* can rapidly switch between conformations that are compatible with an extension of the PG binding domain, activated by the presence of the ion (Terahara et al. 2017b). The authors have suggested the following mechanism for MotPS stator assembly and activation (Terahara et al. 2017b) (Fig. 5.2). Unbound stators diffuse with their plug closed, and in the absence of the coupling ions, they present an unfolded PG binding region. The presence of ions promotes the folding and dimerization of this region. Once in proximity to a rotor, an interaction between FliG and MotP likely stabilizes the recruitment, allowing the opening of the channel and the binding to the PG layer. This mechanism would predict that the stator units dissociate if the SMF is depleted (as seen in the Na^+ stators of *V. alginolyticus* Fukuoka et al. 2009), but does not explicitly include the observed effect of force on the lifetime of the stator units bound in the BFM (Nord et al. 2017). We speculate that, in strains such as *E. coli* where stator units exchange and mechanosensing takes place, the following elements could complete the model. When the stator unit is in proximity to the rotor, the initial mechano-chemical cycles perform work on the rotor, and by reaction, build tension in the stator unit (between its cytoplasmic face and the PG binding domain). By a catch-bond mechanism, the lifetime of the bond to the PG increases in a load-dependent manner, possibly via structural changes in the PG binding domain of MotB. In this way, any mechanism that decreases the force applied by the stator (lower load (Nord et al. 2017; Yuan and Berg 2008), decrease in IMF (Zhu et al. 2014; Fukuoka et al. 2009; Sowa et al. 2014, 2005; Tipping et al. 2013), slowed ion translocation (Che et al. 2008, 2014), mutations (Pourjaberi et al. 2017; Nakamura et al. 2014; Morimoto et al. 2010; Fukuoka et al. 2009; Zhu et al. 2014; Zhou et al. 1998; Kojima and Blair

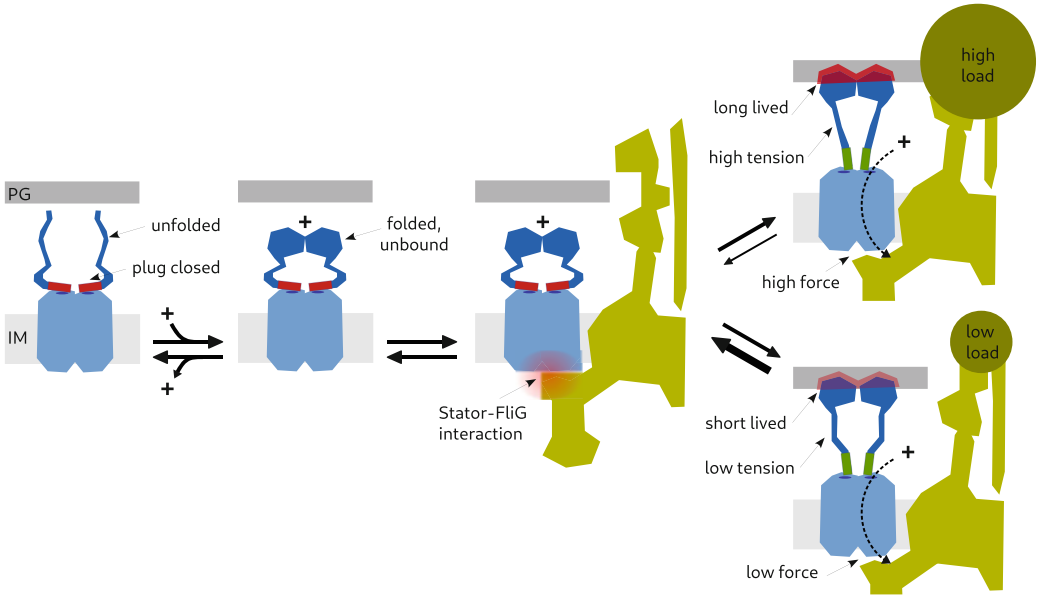

Fig. 5.2 Schematic model of stator unit recruitment and mechanosensitivity. The three leftmost states correspond to the model proposed for (Na^+) MotPS stator of *B. subtilis* (Terahara et al. 2017b). The two rightmost states correspond to the catch-bond model proposed for the mechanosensitivity of (H^+) MotAB stator of *E. coli* (Nord et al. 2017)

2001; Chawla et al. 2017)) would result in a decrease of the number of bound stators.

5.3.3.3 The Role of FliL and c-di-GMP

Many studies have suggested that another player, an inner membrane protein called FliL, may also affect the dynamics of stator unit exchange, although the role of FliL appears to vary greatly depending on the bacterial species. For example, the deletion of FliL abolishes swarming in *Proteus mirabilus* (*P. mirabilus*) (Cusick et al. 2012; Belas and Suvanasuthi 2005), abolishes swimming in *P. mirabilus*, *Caulobacter crescentus* (*C. crescentus*), and *Pseudomonas putida* (*P. putida*) (Jenal et al. 1994; Segura et al. 2001; Belas and Suvanasuthi 2005), and reduces the swimming ability in *Borrelia burgdorferi* (*B. burgdorferi*), *Rhodobacter sphaeroides* (*R. sphaeroides*), and *V. alginolyticus* (Motaleb et al. 2011; Suaste-Olmos et al. 2010; Zhu et al. 2015). Conflicting studies report that the deletion of FliL leads either to decreased swimming and abolished swarming in *E. coli* and *S. enterica* (Attmannspacher et al. 2008; Partridge et al. 2015), or to no affect whatsoever on either swimming or swarming in these bacteria (Raha et al. 1994; Chawla et al. 2017). FliL is an inner-membrane protein which has been shown to localize with the basal body in *S. enterica* and *V. alginolyticus* (Schoenhals and Macnab 1999; Zhu et al. 2015). In-situ cryo-electron tomography of *B. burgdorferi* has placed FliL between the stator and rotor (Motaleb et al. 2011), and two-hybrid and pulldown assays have shown that it interacts with FliF, FliG, and MotAB in *S. enterica* (Partridge et al. 2015) and MotB in *Campylobacter jejuni* (*C. jejuni*) and *Helicobacter* (Rajagopala et al. 2007). An interaction between FliL and the stator is also suggested in *V. alginolyticus*, where FliL localization at the motor is dependent upon stator unit localization, and stator unit localization is decreased in a ΔFliL strain (Zhu et al. 2015). In *V. alginolyticus* the stator to FliL stoichiometry is estimated to be 1:1 (Zhu et al. 2015), whereas in *S. enterica* it is suggested to be is 1:2 (Partridge et al. 2015). Fluorescence microscopy has been used to show that, in *V. alginolyticus*, the exchange rate of the stator units decreases in the absence of FliL (Lin et al. 2018),

yet in *E. coli*, stator unit stoichiometry is unaffected by the absence of FliL (Chawla et al. 2017). Overall, there is mounting but still incomplete evidence that, depending on the species, FliL plays a role in recruiting or stabilizing the stator units or increasing their efficiency, thereby increasing motor torque, especially at high load.

The interactions between the stator units and the motor are also regulated by a ubiquitous bacterial second messenger, cyclic di-GMP (c-di-GMP), which regulates a diverse set of cellular processes, including the transition between the motile, planktonic state and the sedentary state, such as within a biofilm (Hengge 2009; Jenal and Malone 2006; Römling et al. 2005; Schirmer and Jenal 2009). Aside from exerting transcriptional control over expression of flagellar genes (Hengge 2009; Hickman and Harwood 2008; Krasteva et al. 2010), c-di-GMP also affects motility at a post-transcriptional level, though the exact mechanisms remain to be elucidated. The steady-state intracellular levels of c-di-GMP are controlled by diguanylate cyclases and phosphodiesterases, which produce and degrade c-di-GMP, respectively, in response to environmental and intracellular cues (Schirmer and Jenal 2009). In general, low levels of c-di-GMP promote motility, whereas higher levels inhibit motility (Ryjenkov et al. 2006; Wolfe and Visick 2008; Boehm et al. 2010; Paul et al. 2010; Fang and Gomelsky 2010) and stimulate surface attachment and biofilm formation (Caiazza et al. 2007; Simm et al. 2004; Wang et al. 2018). On the level of an individual motor, elevated levels of c-di-GMP slow motor speed and increase the CCW bias of the motor (Paul et al. 2010; Wang et al. 2018). In *E. coli* and *S. enterica*, YcgR is a PilZ domain protein which binds c-di-GMP (Ryjenkov et al. 2006). Upon binding to c-di-GMP, YcgR then binds to either the rotor (Wang et al. 2018; Paul et al. 2010; Fang and Gomelsky 2010) or the stator (Boehm et al. 2010), exerting a brake-like mechanism on the motor, inhibiting swimming and swarming and facilitating surface attachment (Paul et al. 2010; Boehm et al. 2010). While the mechanism by which this occurs remains unclear, models propose that YcgR disrupts the rotor-stator interface (Boehm et al. 2010; Fang and Gomelsky 2010; Paul et al. 2010). Interestingly, a similar but distinct system exists in *B. subtilis*, wherein EpsE binds to c-di-GMP and then interacts with the rotor via a clutch mechanism, disengaging the rotor from the stator units and facilitating biofilm formation (Blair et al. 2008). Such mechanisms allow motor control on a much shorter timescale than gene expression or assembly, and they are reversible: motors inhibited by c-di-GMP bound YcgR may function again upon YcgR dissociation, for example, upon biofilm dispersal.

5.3.3.4 Rotor Protein Exchange

The stator units are not the only component of the BFM complex that actively exchange; surprisingly, at least two components of the rotor dynamically exchange with cytoplasmic spares. FRAP experiments have shown that fluorescently tagged FliM and FliN show active exchange on a similar timescale as the stator units (Delalez et al. 2010; Fukuoka et al. 2010). Surprisingly, the stoichiometry and dynamics of FliM and FliN exchange depend upon the rotation direction of the motor (Lele et al. 2012). Using FliG mutations which lock the rotor in either the CW or CCW direction, it has been shown that there are fewer FliM and FliN subunits in motors locked in the CW direction and more in motors locked in the CCW direction (Yuan et al. 2012; Branch et al. 2014). Moreover, the binding of CheY-P induces the dissociation of FliM/N subunits (Yuan et al. 2012; Yuan and Berg 2013; Branch et al. 2014). These results show a mechanism by which the active remodeling allows the BFM to fine tune its response to chemoattractants. As CheY-P levels drop, CCW bias increases, and additional FliM are recruited to the C ring, providing additional CheY-P binding sites. This increases the motor's sensitivity to CheY-P, and this sensitivity continues to be tuned on the second timescale (Yuan and Berg 2013), increasing the speed with which the chemosensory system adapts to changes in chemoattractants (Zhang et al. 2018). Recent measurements give a Hill coefficient around 20, the highest yet to be discovered amongst allosteric protein complexes (Yuan and Berg 2013).

How does the rotor of the motor balance high stability with high variability and adaptability? Measurements of FliG and FliF have shown that they do not display exchange (at least over timescales of ∼2 h and 10 min, respectively) (Fukuoka et al. 2010; Li et al. 2011), likely providing a central stable core to the rotor. Both the mechanisms of FliM and FliN exchange as well as the structural details of the compositionally varying C ring remain to be elucidated.

5.3.4 Microscopy Techniques to Study the BFM Dynamics

Uncovering the dynamical behavior of the BFM and of its components over the last few decades has required the development of special techniques based on optical microscopy. Here we briefly introduce them (see Fig. 5.3), together with a discussion about their potential and limitations.

In *tethered-cell assays* (Silverman and Simon 1974), a single flagellum (usually carrying a mutation to become "sticky" to glass) adheres to the microscope slide, resulting in the rotation of the cell body around the tethering point (Fig. 5.3c). By measuring the cell's rotational speed and geometry, one can calculate the drag coefficient of the cell and the torque generated by the BFM. In such an assay, the viscous load of the motor is high, and the rotational speed is low. In *bead assays*, (Chen and Berg 2000; Ryu et al. 2000) the cell adheres to the surface and a micro bead is tethered either to a short flagellar stub or to the hook in the absence of the flagellum (via non-covalent chemistry) (Fig. 5.3d). The viscous load experienced by the motor is then controlled by the size of the bead used or the viscosity of the surrounding media. Using darkfield microscopy, the detection of plasmonic nanoparticles is possible, enabling access to the extremely low load region (Yuan and Berg 2008; Nord et al. 2017). An external torque can also be used to manipulate the motor. Using *electrorotation* (Fig. 5.3e) on a spinning tethered cell, a fast rotating electric field can impose torque on the cell body (Berg and Turner 1993; Iwazawa et al. 1993; Berry et al. 1995). Optical tweezers can be employed to apply a force to the cell body of a tethered cell, rotating it about its tether (Block et al. 1989, 1991; Berry and Berg 1997) (Fig. 5.3f). Using super paramagnetic beads in bead assays, an external magnetic field can orient the bead and the motor in a Magnetic Tweezers setup (Tipping et al. 2013; van Oene et al. 2017; Nord et al. 2017) (Fig. 5.3g).

When specifically interested in the dynamics of the stator units, it is worth noting that the above techniques have some limitations. Speed of the BFM is often used as a proxy for stator unit activity, and is often assumed to be a direct proxy of stator unit presence. However, we should consider the possibility of a bound-inactive state of the stator unit, which would make the speed a valuable proxy only for stator activity Shi et al. (2019). Fluorescence is a natural extension to these techniques (Fig. 5.3a,b). Fluorescently tagged stator units of immobilized cells often exhibit immobile fluorescent spots which indicate the presence of multiple tagged proteins, and is often assumed to indicate the presence of a functional motor. However, this interpretation is complicated by the possibility that the fluorescently tagged stator units may cluster in regions outside the motor complex, or that the presence of the fluorescent tag may inhibit or perturb motor functionality (Heo et al. 2017). Moreover, the motors on the side of the cell in contact with the coverslip are likely stalled due to interactions between the flagellum and surface. These complications can be overcome in tethered cell and bead assays. Detection of fluorescent fusion motor proteins in total internal reflection fluorescent (TIRF) microscopy can be coupled to tethered cell assays (Leake et al. 2006; Tipping et al. 2013), as the motor remains in a fixed position close to the surface while the cell body rotates. This ensures that only functional motors are considered, while retaining high fluorescence signal to noise ratio (SNR), yielding information on the stoichiometry and dynamics of the tagged protein. In bead assays, the viscous load is more easily controlled over a population of cells, making the results easily comparable across different motors. However, the

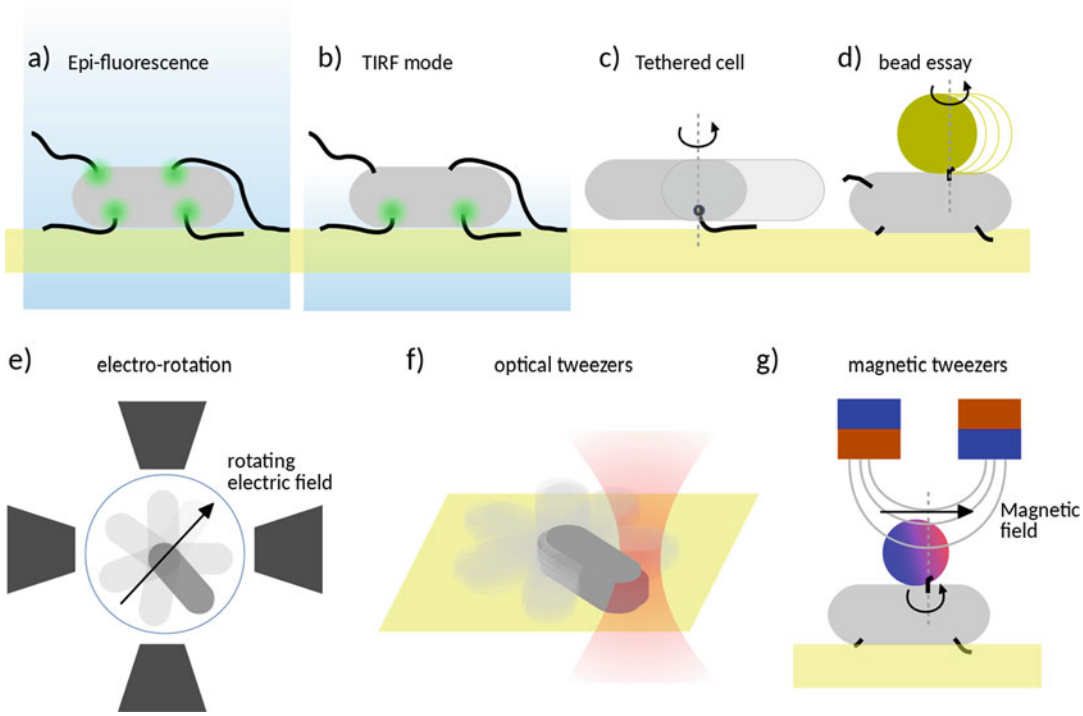

Fig. 5.3 Optical microscopy techniques used to study the activity and composition of the BFM. (**a**,**b**) Fluorescence detection in epi and TIRF mode, respectively. (**c**) Tethered cell assay: the cell body is rotated by the BFM via a single flagellum adhered to the coverslip. (**d**) Bead assay: the cell body is stuck to the coverslip and a microscopic bead is bound to a flagellar stub (or hook), and is rotated by the BFM. (**e**) Electro-rotation: in a tethered cell assay, the cell body is rotated by the BFM and by an external torque imposed by a fast rotating electric field. (**f**) External torque is exerted on a tethered cell via Optical tweezers. (**g**) In a bead assay, using a magnetic tweezers setup, an external torque can be applied to a super-paramagnetic bead, and to the BFM tethered to it, by an external controlled magnetic field

motor is located far ($\sim$1 μm) from the surface, necessitating epi illumination, which decreases the SNR of the measurement. Ideally, coupling fast electrorotation and TIRF detection, or magnetic bead assays and confocal fluorescence detection (centered on the BFM) could provide versatile techniques to study the dynamics of motor components, combining external manipulation and high SNR, while minimizing the possibility for artefacts.

5.4 The Motor as a Mechanical Sensor

We have seen that the BFM can dynamically adapt both its structure and its power output as a function of both biochemical and mechanical signals. With respect to the latter, several observations in different bacterial species suggest that the BFM may also be involved in cellular mechano-responses which drastically affect the cell motility and lifestyle when a single bacterium adheres to a surface or interface. This is relevant in the initial stage of *biofilm formation*, when a single cell adheres to a surface and, switching its lifestyle from motile to sessile, generates a surface-attached microbial community. Mature biofilms, which can attain macroscopic dimensions, adhere strongly to surfaces and are protected by a matrix of secreted polymers, thereby acquiring resistance to biochemical and mechanical attacks (Berne et al. 2018). For this reason, biofilms have major clinical and economical implications, and strategies to fight them are

actively sought (Koo et al. 2017). Alternatively, surface-adhered bacteria can either retain or reacquire motility via swarming, a collective surface motility driven by diverse strategies (Partridge and Harshey 2013; Harshey and Partridge 2015).

While several cellular mechanisms have been identified in biofilm and swarming initiation upon recognition of the surface, it is still not clear how the individual cell initially recognizes that it is in contact with the surface, what signals originate from such mechanical attachment, and whether general mechanisms can be identified (Berne et al. 2018; Belas 2014; Persat 2017; Dorel 2010; Harapanahalli et al. 2015). For many species, flagellar motility has been shown to be crucial to surface colonization and biofilm formation (Berne et al. 2018), potentially playing multiple roles in the swimming to sessile transition. The BFM can promote surface binding simply by actively propelling the cell towards the surface (whereas, in the absence of an active propeller, the cell would rely upon passive diffusion), helping to overcome the repulsive forces near the surface, and by prolonging surface proximity (Berne et al. 2018; Lauga 2016). Similarly, the flagellum can be involved in tethering the cell to the surface by aspecific interactions, again increasing the proximity time and promoting surface adhesion. However, while these roles of the BFM and flagellum in promoting surface adhesion are perhaps expected, they are challenged by observations which reveal a more complex picture. For example, *Listeria monocytogenes* (*L. monocytogenes*) mutants which carry an intact flagellum but a non-functional BFM, do not form biofilms as efficiently as fully motile cells, even when forcibly brought in contact with the surface by centrifugation (reviewed in Chaban et al. 2015). This suggests that the role of the BFM extends beyond merely bringing the cell in close proximity with the surface to facilitate adhesion; if it were this simple, a defective BFM could be replaced by an external force (such as centrifugation) acting on the cell.

How can a BFM facilitate surface adhesion, inducing the cellular response necessary for biofilm formation, only when it is active? A popular hypothesis starts from the reasoning that the flagellum of a recently adhered cell quickly becomes constrained, stalling or inhibiting the rotation of the corresponding BFM. An influential result in the BFM literature suggests that BFM rotation is tightly coupled to ion flux thorough the stator units (Meister et al. 1987), i.e. that a fixed number of ions are translocated through the stator units during each revolution. As such, it is often assumed that, during motor stall, the absence of rotation precludes ion flux through the BFM. Considering the BFM is a substantial IMF sink in the membrane (Lo et al. 2006), the sudden variation of ionic influx due to the stalled flagellum, where respiration and ion outflux remain unchanged, could quickly produce a hyper-polarization of the cell. Therefore, such a mechanically-induced electro-chemical stimulus is hypothesized to trigger, via yet to be determined pathways, the intracellular signals required for biofilm initiation (Belas 2014; Persat 2017; Van Dellen et al. 2008; Dorel 2010).

To further complicate this emerging picture, it has been shown that *C. crescentus* can still efficiently bind to surfaces in the absence of all the extracellular parts of the motor (including the flagellum), but strikingly, only if the remaining intracellular BFM, working at extremely low load, is fully functional (Hug et al. 2017). The authors conclude that their observations cannot support a simple model for surface sensing by means of a surface-mediated obstruction of flagellar rotation, as described above. Rather, they suggest that the need for a functional BFM in the absence of the outer motor indicates that the stator units (whether their number at low load is affected by mechano-sensing is not known in *C. crescentus*) may act as mechanosensitive channels. Surface-mediated membrane deformations could produce local strain which causes structural changes in the stator units. The authors hypothesize that this would translate to a decrease of BFM ion influx and a consequent increase in internal pH, which is associated, in vitro, to the activation of the surface program (Abel et al. 2011).

Regardless of whether the initial mechanical clue which signals the presence of the surface comes from the stall of the flagellum, or from the local strain upon the adhered membrane, it

is worth noting that the tight-coupling between the BFM rotation and its ion flux is an essential hypothesis to link the mechanical stall to the hyper-polarization of the cell. Measurements of the BFM ion flux at the single-cell and single-motor level are still technically challenging, but they will be able to directly test this (widely accepted) model, which is based on measurements at the population level.

In the context of swarming, an alternative scenario for surface sensing involving the BFM has been proposed (Harshey and Partridge 2015), which does not rely on an electro-chemical perturbation induced by the BFM. Surface sensing could be explained by the existence of regulator proteins of the downstream response, still not identified, which are sequestered by the normally functioning and ion-conducting BFM. The effect of the external surface would then be to modify the "normal" interaction between stator units and rotor, releasing the regulators. This could happen for a stalled motor as well as for conditions where the stators are not present (e.g. in mutants, or with depleted IMF). Only new experiments and measurements will be able to test these models, and hopefully will shed light on the common or diverse strategies used by different bacteria in mechanosensing.

Note

While this chapter was under review, two works, submitted to biorxiv and not yet peer-reviewed Deme et al. (2020); Santiveri et al. (2020), present the first high resolution structure of the stator unit. Remarkably, a pentameric stoichoimetry is observed for MotA, challenging the long-standing belief of 4:2 stoichiometry in MotAB.

Acknowledgments This work was supported by the ANR FlagMotor project grant ANR-18-CE30-0008 of the French *Agence Nationale de la Recherche*. The CBS is a member of the France-BioImaging (FBI) and the French Infrastructure for Integrated Structural Biology (FRISBI), 2 national infrastructures supported by the French National Research Agency (ANR-10-INBS-04-01 and ANR-10-INBS-05, respectively).

References

Abel S, Chien P, Wassmann P, Schirmer T, Kaever V, Laub MT, Baker TA, Jenal U (2011) Regulatory cohesion of cell cycle and cell differentiation through interlinked phosphorylation and second messenger networks. Mol Cell 43(4):550–560

Adler J (1966) Chemotaxis in bacteria. Science 153(3737):708–716

Armitage JP, Schmitt R (1997) Bacterial chemotaxis: Rhodobacter sphaeroides and Sinorhizobium meliloti–variations on a theme? Microbiology 143:3671–3682

Asakura S (1970) Polymerization of flagellin and polymorphism of flagella. Adv Biophys 1:99–155

Attmannspacher U, Scharf BE, Harshey RM (2008) FliL is essential for swarming: motor rotation in absence of FliL fractures the flagellar rod in swarmer cells of Salmonella enterica. Mol Microbiol 68(2):328–341

Bai F, Branch RW, Nicolau DV, Pilizota T, Steel BC, Maini PK, Berry RM (2010) Conformational spread as a mechanism for cooperativity in the bacterial flagellar switch. Science 327(5966):685–689

Bai F, Minamino T, Wu Z, Namba K, Xing J (2012) Coupling between switching regulation and torque generation in bacterial flagellar motor. Phys Rev Lett 108(17):178105

Baker AE, O'Toole GA (2017) Bacteria, rev your engines: stator dynamics regulate flagellar motility. J Bacteriol 199(12):e00088–e00017

Beeby M, Ribardo DA, Brennan CA, Ruby EG, Jensen GJ, Hendrixson DR (2016) Diverse high-torque bacterial flagellar motors assemble wider stator rings using a conserved protein scaffold. Proc Natl Acad Sci USA 113(13):E1917–E1926

Belas R (2014) Biofilms, flagella, and mechanosensing of surfaces by bacteria. Trends Microbiol 22(9):517–527

Belas R, Suvanasuthi R (2005) The ability of Proteus mirabilis to sense surfaces and regulate virulence gene expression involves FliL, a flagellar basal body protein. J Bacteriol 187(19):6789–6803

Berg CH (2003) The rotary motor of bacterial flagella. Annu Rev Biochem 72(1):19–54

Berg HC, Brown DA (1972) Chemotaxis in Escherichia coli analysed by three-dimensional tracking. Nature 239(5374):500–504

Berg HC, Turner L (1993) Torque generated by the flagellar motor of Escherichia coli. Biophys J 65(5):2201–2216

Berne C, Ellison CK, Ducret A, Brun YV (2018) Bacterial adhesion at the single-cell level. Nat Rev Microbiol 16:616–27

Berry RM, Berg HC (1997) Absence of a barrier to backwards rotation of the bacterial flagellar motor demonstrated with optical tweezers. Proc Natl Acad Sci USA 94(26):14433–14437

Berry RM, Turner L, Berg HC (1995) Mechanical limits of bacterial flagellar motors probed by electrorotation. Biophys J 69(1):280–286

Blair DF, Berg HC (1988) Restoration of torque in defective flagellar motors. Science 242(4886):1678–1681

Blair KM, Turner L, Winkelman JT, Berg HC, Kearns DB (2008) A molecular clutch disables flagella in the Bacillus subtilis biofilm. Science 320(5883):1636–1638

Block SM, Berg HC (1984) Successive incorporation of force-generating units in the bacterial rotary motor. Nature 309(5967):470–472

Block SM, Blair DF, Berg HC (1989) Compliance of bacterial flagella measured with optical tweezers. Nature 338(6215):514–518

Block SM, Blair DF, Berg HC (1991) Compliance of bacterial polyhooks measured with optical tweezers. Cytometry 12(6):492–496

Boehm A, Kaiser M, Li H, Spangler C, Kasper CA, Ackermann M, Kaever V, Sourjik V, Roth V, Jenal U (2010) Second messenger-mediated adjustment of bacterial swimming velocity. Cell 141(1):107–116

Branch RW, Sayegh MN, Shen C, Nathan VSJ, Berg HC (2014) Adaptive remodelling by FliN in the bacterial rotary motor. J Mol Biol 426(19):3314–3324

Braun TF, Blair DF (2001) Targeted disulfide cross-linking of the MotB protein of Escherichia coli: evidence for two h+channels in the stator complex. Biochemistry 40(43):13051–13059

Brown MT, Steel BC, Silvestrin C, Wilkinson DA, Delalez NJ, Lumb CN, Obara B, Armitage JP, Berry RM (2012) Flagellar hook flexibility is essential for bundle formation in swimming Escherichia coli cells. J Bacteriol 194(13):3495–3501

Caiazza NC, Merritt JH, Brothers KM, O'Toole GA (2007) Inverse regulation of biofilm formation and swarming motility by Pseudomonas aeruginosa PA14. J Bacteriol 189(9):3603–3612

Calladine CR, Luisi BF, Pratap JV (2013) A "mechanistic" explanation of the multiple helical forms adopted by bacterial flagellar filaments. J Mol Biol 425(5):914–928

Castillo DJ, Nakamura S, Morimoto YV, Che Y-S, Kamiike N, Kudo S, Minamino T, Namba K (2013) C-terminal periplasmic domain of MotB is responsible for load-dependent control of the number of stators of the bacterial flagellar motor. Biophysics 9:173–181

Chaban B, Velocity Hughes H, Beeby M (2015) The flagellum in bacterial pathogens: for motility and a whole lot more. In: Seminars in cell & developmental biology, vol 46. Elsevier, Amsterdam, pp 91–103

Chawla R, Ford KM, Lele PP (2017) Torque, but not FliL, regulates mechanosensitive flagellar motor-function. Sci Rep 7(1):5565

Che YS, Nakamura S, Kojima S, Kami-Ike N, Namba K, Minamino T (2008) Suppressor analysis of the MotB(D33E) mutation to probe the bacterial flagellar motor dynamics coupled with proton translocation. J Bacteriol 190:6660–6667

Che Y-S, Nakamura S, Morimoto YV, Kami-ike N, Namba K, Minamino T (2014) Load-sensitive coupling of proton translocation and torque generation in the bacterial flagellar motor. Mol Microbiol 91(1):175–184

Chen X, Berg HC (2000) Torque-speed relationship of the flagellar rotary motor of Escherichia coli. Biophys J 78(2):1036–1041

Chen S, Beeby M, Murphy GE, Leadbetter JR, Hendrixson DR, Briegel A, Li Z, Shi J, Tocheva EI, Müller A, Dobro MJ, Jensen GJ (2011) Structural diversity of bacterial flagellar motors. EMBO J 30(14):2972–2981

Chun SY, Parkinson JS (1988) Bacterial motility: membrane topology of the Escherichia coli MotB protein. Science 239(4837):276–278

Cluzel P, Surette M, Leibler S (2000) An ultrasensitive bacterial motor revealed by monitoring signaling proteins in single cells. Science 287(5458):1652–1655

Cusick K, Lee Y-Y, Youchak B, Belas R (2012) Perturbation of FliL interferes with Proteus mirabilis swarmer cell gene expression and differentiation. J Bacteriol 194(2):437

Darnton NC, Berg HC (2007) Force-extension measurements on bacterial flagella: triggering polymorphic transformations. Biophys J 92(6):2230–2236

Delalez NJ, Wadhams GH, Rosser G, Xue Q, Brown MT, Dobbie IM, Berry RM, Leake MC, Armitage JP (2010) Signal-dependent turnover of the bacterial flagellar switch protein FliM. Proc Natl Acad Sci USA 107(25):11347–11351

Delalez NJ, Berry RM, Armitage JP (2014) Stoichiometry and turnover of the bacterial flagellar switch protein FliN. mBio 5(4):e01216–e01214

De Mot R, Vanderleyden J (1994) The C-terminal sequence conservation between OmpA-related outer membrane proteins and MotB suggests a common function in both gram-positive and gram-negative bacteria, possibly in the interaction of these domains with peptidoglycan. Mol Microbiol 12(2):333–334

Deme, Justin and Johnson, Steven and Vickery, Owen and Muellbauer, Amy and Monkhouse, Holly and Griffiths, Thomas and Hennell-James, Rory and Berks, Ben and Coulton, James and Stansfeld, Phillip James and others (2020) Structures of the stator complex that drives rotation of the bacterial flagellum. BioRxiv, Cold Spring Harbor Laboratory

Dorel C (2010) Manipulating bacterial cell fate: key role of surface-sensing and signal transduction. In: Méndez-Vilas A (ed) Current research, technology and education topics in applied microbiology and microbial biotechnology. Formatex, Badajoz, pp 791–800

Duke TA, Le Novere N, Bray D (2001) Conformational spread in a ring of proteins: a stochastic approach to allostery. J Mol Biol 308(3):541–553

Dyer CM, Vartanian AS, Zhou H, Dahlquist FW (2009) A molecular mechanism of bacterial flagellar motor switching. J Mol Biol 388(1):71–84

Eisenbach M (2011) Bacterial chemotaxis. American Cancer Society

Fahrner KA, Ryu WS, Berg HC (2003) Biomechanics: bacterial flagellar switching under load. Nature 423(6943):938

Fang X, Gomelsky M (2010) A post-translational, c-di-GMP-dependent mechanism regulating flagellar motility. Mol Microbiol 76(5):1295–1305

Fukuoka H, Wada T, Kojima S, Ishijima A, Homma M (2009) Sodium-dependent dynamic assembly of membrane complexes in sodium-driven flagellar motors. Mol Microbiol 71(4):825–835

Fukuoka H, Inoue Y, Terasawa S, Takahashi H, Ishijima A (2010) Exchange of rotor components in functioning bacterial flagellar motor. Biochem Biophys Res Commun 394(1):130–135

Fung DC, Berg HC (1995) Powering the flagellar motor of Escherichia coli with an external voltage source. Nature 375(6534):809–812

Gabel CV, Berg HC (2003) The speed of the flagellar rotary motor of Escherichia coli varies linearly with protonmotive force. Proc Natl Acad Sci USA 100(15):8748–8751

Harapanahalli AK, Younes JA, Allan E, van der Mei HC, Busscher HJ (2015) Chemical signals and mechanosensing in bacterial responses to their environment. PLoS Pathog 11(8):e1005057

Harshey RM (1994) Bees aren't the only ones: swarming in gram-negative bacteria. Mol Microbiol 13(3):389–394

Harshey RM (2003) Bacterial motility on a surface: Many ways to a common goal. Annu Rev Microbiol 57(1):249–273

Harshey RM, Partridge JD (2015) Shelter in a swarm. J Mol Biol 427(23):3683–3694

Hengge R (2009) Principles of c-di-GMP signalling in bacteria. Nat Rev Microbiol 7(4):263–273

Heo M, Nord AL, Chamousset D, van Rijn E, HJE Beaumont, Pedaci F (2017) Impact of fluorescent protein fusions on the bacterial flagellar motor. Sci Rep 7(1):12583

Hickman JW, Harwood CS (2008) Identification of FleQ from Pseudomonas aeruginosa as a c-di-GMP-responsive transcription factor. Mol Microbiol 69(2):376–389

Hosking ER, Vogt C, Bakker EP, Manson MD (2006) The Escherichia coli MotAB proton channel unplugged. J Mol Biol 364(5):921–937

Hotani H (1976) Light microscope study of mixed helices in reconstituted Salmonella flagella. J Mol Biol 106(1):151–166

Hotani H (1982) Micro-video study of moving bacterial flagellar filaments: III. Cyclic transformation induced by mechanical force. J Mol Biol 156(4):791–806

Hug I, Deshpande S, Sprecher KS, Pfohl T, Jenal U (2017) Second messenger–mediated tactile response by a bacterial rotary motor. Science 358(6362):531–534

Imazawa R, Takahashi Y, Aoki W, Sano M, Ito M (2016) A novel type bacterial flagellar motor that can use divalent cations as a coupling ion. Sci Rep 6:19773

Iwazawa J, Imae Y, Kobayasi S (1993) Study of the torque of the bacterial flagellar motor using a rotating electric field. Biophys J 64(3):925–933

Jenal U, Malone J (2006) Mechanisms of cyclic-di-GMP signaling in bacteria. Annu Rev Genet 40:385–407

Jenal U, White J, Shapiro L (1994) Caulobacter flagellar function, but not assembly, requires FliL, a non-polarly localized membrane protein present in all cell types. J Mol Biol 243(2):227–244

Kamiya R, Asakura S (1976a) Helical transformations of Salmonella flagella in vitro. J Mol Biol 106(1):167–186

Kamiya R, Asakura S (1976b) Flagellar transformations at alkaline pH. J Mol Biol 108(2):513–518

Kaplan M, Ghosal D, Subramanian P, Oikonomou CM, Kjaer A, Pirbadian S, Ortega DR, Briegel A, El-Naggar MY, Jensen GJ (2019) The presence and absence of periplasmic rings in bacterial flagellar motors correlates with stator type. eLife 8:e43487

Kim EA, Price-Carter M, Carlquist WC, Blair DF (2008) Membrane segment organization in the stator complex of the flagellar motor: implications for proton flow and proton-induced conformational change. Biochemistry 47(43):11332–11339

Kojima S (2015) Dynamism and regulation of the stator, the energy conversion complex of the bacterial flagellar motor. Curr Opin Microbiol 28:66–71

Kojima S, Blair DF (2001) Conformational change in the stator of the bacterial flagellar motor. Biochemistry 40(43):13041–13050

Kojima S, Imada K, Sakuma M, Sudo Y, Kojima C, Minamino T, Homma M, Namba K (2009) Stator assembly and activation mechanism of the flagellar motor by the periplasmic region of MotB. Mol Microbiol 73(4):710–718

Koo H, Allan RN, Howlin RP, Stoodley P, Hall-Stoodley L (2017) Targeting microbial biofilms: current and prospective therapeutic strategies. Nat Rev Microbiol 15(12):740

Krasteva PV, Fong JCN, Shikuma NJ, Beyhan S, Navarro MVAS, Fitnat H. Yildiz, Sondermann H (2010) Vibrio cholerae VpsT regulates matrix production and motility by directly sensing cyclic di-GMP. Science 327(5967):866–868

Lam K-H, Ip W-S, Lam Y-W, Chan S-O, Ling TK-W, Au SW-N (2012) Multiple conformations of the FliG C-terminal domain provide insight into flagellar motor switching. Structure (London, England, 1993) 20(2):315–325

Lauga E (2016) Bacterial hydrodynamics. Annu Rev Fluid Mech 48:105–130

Leake MC, Chandler JH, Wadhams GH, Bai F, Berry RM, Armitage JP (2006) Stoichiometry and turnover in single, functioning membrane protein complexes. Nature 443(7109):355–358

Lee SY, Cho HS, Pelton JG, Yan D, Henderson RK, King DS, Huang L, Kustu S, Berry EA, Wemmer DE (2001) Crystal structure of an activated response regulator bound to itsytarget. Nat Struct Biol 8(1): 52–56

Lee LK, Ginsburg MA, Crovace C, Donohoe M, Stock D (2010) Structure of the torque ring of the flagellar motor and the molecular basis for rotational switching. Nature 466(7309):996–1000

Lele PP, Branch WR, Nathan JVS, Berg CH (2012) Mechanism for adaptive remodeling of the bacterial flagellar switch. Proc Natl Acad Sci USA 109(49):20018–20022

Lele PP, Hosu BG, Berg HC (2013) Dynamics of mechanosensing in the bacterial flagellar motor. PNAS 110(29):11839–11844

Li J, Swanson RV, Simon MI, Weis RM (1995) The response regulators CheB and CheY exhibit competitive binding to the kinase CheA. Biochemistry 34(45):14626–14636

Li N, Kojima S, Homma M (2011) Characterization of the periplasmic region of PomB, a Na+-driven flagellar stator protein in Vibrio alginolyticus. J Bacteriol 193(15):3773–3784

Lin T-S, Zhu S, Kojima S, Homma M, Lo C-J (2018) FliL association with flagellar stator in the sodium-driven Vibrio motor characterized by the fluorescent microscopy. Sci Rep 8(1):11172

Lloyd SA, Blair DF (1997) Charged residues of the rotor protein FliG essential for torque generation in the flagellar motor of Escherichia coli. J Mol Biol 266(4):733–744

Lo CJ, Leake MC, Berry RM (2006) Fluorescence measurement of intracellular sodium concentration in single escherichia coli cells. Biophys J 90(1):357–365

Lo CJ, Leake MC, Pilizota T, Berry RM (2007) Nonequivalence of membrane voltage and ion-gradient as driving forces for the bacterial flagellar motor at low load. Biophys J 93(1):294–302

Lo CJ, Sowa Y, Pilizota T, Berry RM (2013) Mechanism and kinetics of a sodium-driven bacterial flagellar motor. Proc Natl Acad Sci USA 28(110):2544

Macnab RM, Ornston MK (1977) Normal-to-curly flagellar transitions and their role in bacterial tumbling. Stabilization of an alternative quaternary structure by mechanical force. J Mol Biol 112(1):1–30

Ma Q, Sowa Y, Baker MAB, Bai F (2016) Bacterial flagellar motor switch in response to CheY-P regulation and motor structural alterations. Biophys J 110(6):1411–1420

Maki-Yonekura S, Yonekura K, Namba K (2010) Conformational change of flagellin for polymorphic supercoiling of the flagellar filament. Nat Struct Mol Biol 17(4):417–422

Mandadapu KK, Nirody JA, Berry RM, Oster G (2015) Mechanics of torque generation in the bacterial flagellar motor. Proc Natl Acad Sci USA 112(32):E4381–E4389

Manson MD, Tedesco PM, Berg HC (1980) Energetics of flagellar rotation in bacteria. J Mol Biol 138(3):541–561

Mao H, Cremer PS, Manson MD (2003) A sensitive, versatile microfluidic assay for bacterial chemotaxis. Proc Natl Acad Sci USA 100(9):5449–5454

Meister M, Lowe G, Berg HC (1987) The proton flux through the bacterial flagellar motor. Cell 49(5):643–650

Minamino T, Imada K (2015) The bacterial flagellar motor and its structural diversity. Trends Microbiol 23(5):267–274

Morimoto YV, Minamino T (2014) Structure and function of the bi-directional bacterial flagellar motor. Biomolecules 4:217–234

Morimoto VY, Nakamura S, Kami-ike N, Namba K, Minamino T (2010) Charged residues in the cytoplasmic loop of MotA are required for stator assembly into the bacterial flagellar motor. Mol Microbiol 78(5):1117–1129

Morimoto YV, Nakamura S, Hiraoka KD, Namba K, Minamino T (2013) Distinct roles of highly conserved charged residues at the MotA-FliG interface in bacterial flagellar motor rotation. J Bacteriol 195(3):474–481

Motaleb MA, Pitzer JE, Sultan SZ, Liu J (2011) A novel gene inactivation system reveals altered periplasmic flagellar orientation in a Borrelia burgdorferi fliL mutant. J Bacteriol 193(13):3324

Nakamura S, Minamino T, Kami-ike N, Kudo S, Namba K (2014) Effect of the MotB(D33N) mutation on stator assembly and rotation of the proton-driven bacterial flagellar motor. Biophysics 10:35–41

Nishihara Y, Kitao A (2015) Gate-controlled proton diffusion and protonation-induced ratchet motion in the stator of the bacterial flagellar motor. Proc Natl Acad Sci USA 112:7737–7742

Nord AL, Sowa Y, Steel BC, Lo C-J, Berry RM (2017) Speed of the bacterial flagellar motor near zero load depends on the number of stator units. Proc Natl Acad Sci USA 114(44):11603–11608

Nord AL, Gachon E, Perez-Carrasco R, Nirody JA, Barducci A, Berry RM, Pedaci F (2017) Catch bond drives stator mechanosensitivity in the bacterial flagellar motor. Proc Natl Acad Sci USA 114(49):12952–12957

Partridge JD, Harshey RM (2013) Swarming: flexible roaming plans. J Bacteriol 195(5):909–918

Partridge JD, Nieto V, Harshey RM (2015) A new player at the flagellar motor: FliL controls both motor output and bias. mBio 6(2):e02367

Paul K, Nieto V, Carlquist WC, Blair DF, Harshey RM (2010) The c-di-GMP binding protein YcgR controls flagellar motor direction and speed to affect chemotaxis by a "backstop brake" mechanism. Mol Cell 38(1):128–139

Paulick A, Delalez NJ, Brenzinger S, Steel BC, Berry RM, Armitage JP, Thormann KM (2015) Dual stator dynamics in the Shewanella oneidensis MR-1 flagellar motor. Mol Microbiol 96(5):993–1001

Persat A (2017) Bacterial mechanotransduction. Curr Opin Microbiol 36:1–6

Pourjaberi SNS, Terahara N, Namba K, Minamino T (2017) The role of a cytoplasmic loop of MotA in load-dependent assembly and disassembly dynamics of the MotA/B stator complex in the bacterial flagellar motor. Mol Microbiol 106(4):646–658

Purcell EM (1977) Life at low reynolds number. Am J Phys 45(1):3–11

Raha M, Sockett H, Macnab RM (1994) Characterization of the fliL gene in the flagellar regulon of Escherichia coli and Salmonella typhimurium. J Bacteriol 176(8):2308–2311

Rajagopala SV, Titz B, Goll J, Parrish JR, Wohlbold K, McKevitt MT, Palzkill T, Mori H, Finley RL, Uetz P (2007) The protein network of bacterial motility. Mol Sys Biol 3:128

Reid SW, Leake MC, Chandler JH, Lo CJ, Armitage JP, Berry RM (2006) The maximum number of torque-generating units in the flagellar motor of escherichia coli is at least 11. Proc Natl Acad Sci USA 103(21):8066–8071

Römling U, Gomelsky M, Galperin MY (2005) C-di-GMP: the dawning of a novel bacterial signalling system. Mol Microbiol 57(3):629–639

Ryjenkov DA, Simm R, Römling U, Gomelsky M (2006) The PilZ domain is a receptor for the second messenger c-di-GMP: the PilZ domain protein YcgR controls motility in enterobacteria. J Biol Chem 281(41):30310–30314

Ryu WS, Berry RM, Berg HC (2000) Torque-generating units of the flagellar motor of Escherichia coli have a high duty ratio. Nature 403(6768):444–447

Sagi Y, Khan S, Eisenbach M (2003) Binding of the chemotaxis response regulator CheY to the isolated, intact switch complex of the bacterial flagellar motor: lack of cooperativity. J Biol Chem 278(28):25867–25871

Samatey FA, Matsunami H, Imada K, Nagashima S, Shaikh TR, Thomas DR, Chen JZ, Derosier DJ, Kitao A, Namba K (2004) Structure of the bacterial flagellar hook and implication for the molecular universal joint mechanism. Nature 431(7012):1062–1068

Samuel AD, Berg HC (1995) Fluctuation analysis of rotational speeds of the bacterial flagellar motor. Proc Natl Acad Sci USA 92(8):3502–3506

Samuel AD, Berg HC (1996) Torque-generating units of the bacterial flagellar motor step independently. Biophys J 71(2):918–923

Santiveri, Mònica and Roa-Eguiara, Aritz and Kuhne, Caroline and Wadhwa, Navish and Berg, Howard C and Erhardt, Marc and Taylor, Nicholas MI (2020) Structure and function of stator units of the bacterial flagellar motor. bioRxiv, Cold Spring Harbor Laboratory

Sarkar MK, Paul K, Blair D (2010) Chemotaxis signaling protein CheY binds to the rotor protein FliN to control the direction of flagellar rotation in Escherichia coli. Proc Natl Acad Sci USA 107(20):9370–9375

Sato K, Nakamura S, Kudo S, Toyabe S (2019) Evaluation of the duty ratio of the bacterial flagellar motor by dynamic load control. Biophys J 116(10):1952–1959

Schirmer T, Jenal U (2009) Structural and mechanistic determinants of c-di-GMP signalling. Nat Rev Microbiol 7(10):724–735

Schoenhals GJ, Macnab RM (1999) FliL is a membrane-associated component of the flagellar basal body of Salmonella. Microbiology 145(Pt 7):1769–1775

Segura A, Duque E, Hurtado A, Ramos JL (2001) Mutations in genes involved in the flagellar export apparatus of the solvent-tolerant Pseudomonas putida DOT-T1E strain impair motility and lead to hypersensitivity to toluene shocks. J Bacteriol 183(14):4127–4133

Shi, Hui and Ma, Shuwen and Zhang, Rongjing and Yuan, Junhua (2019) A hidden state in the turnover of a functioning membrane protein complex. Science advances, American Association for the Advancement of Science 5(3):eaau6885

Silverman M, Simon M (1974) Flagellar rotation and the mechanism of bacterial motility. Nature 249(5452):73

Simm R, Morr M, Kader A, Nimtz M, Römling U (2004) GGDEF and EAL domains inversely regulate cyclic di-GMP levels and transition from sessility to motility. Mol Microbiol 53(4):1123–1134

Son K, Guasto JS, Stocker R (2013) Bacteria can exploit a flagellar buckling instability to change direction. Nat Phys 9(8):494–498

Sourjik V, Berg HC (2002) Receptor sensitivity in bacterial chemotaxis. Proc Natl Acad Sci USA 99(1):123–127

Sowa Y, Berry RM (2008) Bacterial flagellar motor. Q Rev Biophys 41(2):103–132

Sowa Y, Hotta H, Homma M, Ishijima A (2003) Torque-speed relationship of the Na+-driven flagellar motor of Vibrio alginolyticus. J Mol Biol 327(5):1043–10451

Sowa Y, Rowe AD, Leake MC, Yakushi T, Homma M, Ishijima A, Berry RM (2005) Direct observation of steps in rotation of the bacterial flagellar motor. Nature 437(7060):916–919

Sowa Y, Homma M, Ishijima A, Berry RM (2014) Hybrid-fuel bacterial flagellar motors in Escherichia coli. Proc Natl Acad Sci USA 111(9):3436–3441

Stolz B, Berg HC (1991) Evidence for interactions between MotA and MotB, torque-generating elements of the flagellar motor of Escherichia coli. J Bacteriol 173(21):7033–7037

Stock D, Namba K, Lee LK (2012) Nanorotors and self-assembling macromolecular machines: the torque ring of the bacterial flagellar motor. Current opinion in biotechnology, Elsevier 23(4):545–554

Suaste-Olmos F, Domenzain C, Mireles-Rodríguez JC, Poggio S, Osorio A, Dreyfus G, Camarena L (2010) The flagellar protein FliL is essential for swimming in Rhodobacter sphaeroides. J Bacteriol 192(23):6230

Suzuki Y, Morimoto YV, Oono K, Hayashi F, Oosawa K, Kudo S, Nakamura S (2019) Effect of the MotA(M206I) mutation on torque generation and stator assembly in the Salmonella H+-driven flagellar motor. J Bacteriol 201(6):e00727–e00718

Terahara N, Krulwich TA, Ito M (2008) Mutations alter the sodium versus proton use of a Bacillus clausii flagellar motor and confer dual ion use on Bacillus subtilis motors. Proc Natl Acad Sci USA 105(38):14359–14364

Terahara N, Sano M, Ito M (2012) A Bacillus flagellar motor that can use both Na+ and K+ as a coupling ion is converted by a single mutation to use only Na+. PloS one 7(9):e46248

Terahara N, Noguchi Y, Nakamura S, Kami-Ike N, Ito M, Namba K, Minamino T (2017) Load- and polysaccharide-dependent activation of the Na-type MotPS stator in the Bacillus subtilis flagellar motor. Sci Rep 7:46081

Terahara N, Kodera N, Uchihashi T, Ando T, Namba K, Minamino T (2017) Na+-induced structural transition of MotPS for stator assembly of the Bacillus flagellar motor. Sci Adv 3(11):eaao4119

Thormann KM, Paulick A (2010) Tuning the flagellar motor. Microbiology 156:1275–1283

Tipping MJ, Delalez NJ, Lim R, Berry RM, Armitage JP (2013) Load-dependent assembly of the bacterial flagellar motor. mBio 4(4):e00551–e00513

Tipping JM, Steel CB, Delalez JN, Berry MR, Armitage PJ (2013) Quantification of flagellar motor stator dynamics through in vivo proton-motive force control. Mol Microbiol 87(2):338–347

Toker AS, Macnab RM (1997) Distinct regions of bacterial flagellar switch protein FliM interact with FliG, FliN and CheY. J Mol Biol 273(3):623–634

Turner L, Ryu WS, Berg HC (2000) Real-time imaging of fluorescent flagellar filaments. J Bacteriol 182(10):2793–2801

Tusk SE, Delalez NJ, Berry RM (2018) Subunit exchange in protein complexes. J Mol Biol 430:4557–4579

Van Dellen KL, Houot L, Watnick PI (2008) Genetic analysis of Vibrio cholerae monolayer formation reveals a key role for $\delta\psi$ in the transition to permanent attachment. J Bacteriol 190(24):8185–8196

van Oene MM, Dickinson LE, Cross B, Pedaci F, Lipfert J, Dekker NH (2017) Applying torque to the Escherichia coli flagellar motor using magnetic tweezers. Sci Rep 7:43285

Vladimirov N, Sourjik V (2009) Chemotaxis: how bacteria use memory. J Biol Chem 390:1097

Wadhams GH, Armitage JP (2004) Making sense of it all: bacterial chemotaxis. Nat Rev Mol Cell Biol 5(12):1024–1037

Wang R, Wang F, He R, Zhang R, Yuan J (2018) The second messenger c-di-GMP adjusts motility and promotes surface aggregation of bacteria. Biophys J 115(11):2242–2249

Wei Y, Wang X, Liu J, Nememan I, Singh AH, Weiss H, Levin BR (2011) The population dynamics of bacteria in physically structured habitats and the adaptive virtue of random motility. Proc Natl Acad Sci USA 108(10):4047–4052

Welch M, Oosawa K, Aizawa S, Eisenbach M (1993) Phosphorylation-dependent binding of a signal molecule to the flagellar switch of bacteria. Proc Natl Acad Sci USA 90(19):8787–8791

Wolfe AJ, Visick KL (2008) Get the message out: Cyclic-di-GMP regulates multiple levels of flagellum-based motility. J Bacteriol 190(2):463–475

Yakushi T, Yang J, Fukuoka H, Homma M, Blair DF (2006) Roles of charged residues of rotor and stator in flagellar rotation: comparative study using H+-driven and Na+-driven motors in Escherichia coli. J Bacteriol 188(4):1466–1472

Yamashita I, Hasegawa K, Suzuki H, Vonderviszt F, Mimori-Kiyosue Y, Namba K (1998) Structure and switching of bacterial flagellar filaments studied by X-ray fiber diffraction. Nat Struct Biol 5(2): 125–132

Yonekura K, Maki-Yonekura S, Namba K (2003) Complete atomic model of the bacterial flagellar filament by electron cryomicroscopy. Nature 424(6949):643–650

Yuan J, Berg HC (2008) Resurrection of the flagellar rotary motor near zero load. Proc Natl Acad Sci USA 105(4):1182–1185

Yuan J, Berg CH (2013) Ultrasensitivity of an adaptive bacterial motor. J Mol Biol 425:1760–1764

Yuan J, Fahrner KA, Berg HC (2009) Switching of the bacterial flagellar motor near zero load. J Mol Biol 390(3):394–400

Yuan J, Branch RW, Hosu BG, Berg HC (2012) Adaptation at the output of the chemotaxis signalling pathway. Nature 484(7393):233–236

Zhang C, He R, Zhang R, Yuan J (2018) Motor adaptive remodeling speeds up bacterial chemotactic adaptation. Biophys J 114(5):1225–1231

Zhou J, Blair DF (1997) Residues of the cytoplasmic domain of mota essential for torque generation in the bacterial flagellar motor. J Mol Biol 273(2):428–439

Zhou J, Sharp LL, Tang HL, Lloyd SA, Billings S, Braun TF, Blair DF (1998) Function of protonatable residues in the flagellar motor of Escherichia coli: a critical role for Asp 32 of MotB. J Bacteriol 180(10):2729–2735

Zhou J, Lloyd SA, Blair DF (1998) Electrostatic interactions between rotor and stator in the bacterial flagellar motor. Proc Natl Acad Sci USA 95(11):6436–6441

Zhu S, Takao M, Li N, Sakuma M, Nishino Y, Homma M, Kojima S, Imada K (2014) Conformational change in the periplamic region of the flagellar stator coupled with the assembly around the rotor. Proc Natl Acad Sci USA 111(37):13523–13528

Zhu S, Kumar A, Kojima S, Homma M (2015) FliL associates with the stator to support torque generation of the sodium-driven polar flagellar motor of Vibrio. Mol Microbiol 98(1):101–110

Dewetting: From Physics to the Biology of Intoxicated Cells

6

David Gonzalez-Rodriguez, Camille Morel, and Emmanuel Lemichez

Abstract

Pathogenic bacteria colonize or disseminate into cells and tissues by inducing large-scale remodeling of host membranes. The physical phenomena underpinning these massive membrane extension and deformation are poorly understood. Invasive strategies of pathogens have been recently enriched by the description of a spectacular mode of opening of large transendothelial cell macroaperture (TEM) tunnels correlated to the dissemination of EDIN-producing strains of *Staphylococcus aureus* via a hematogenous route or to the induction of gelatinous edema triggered by the edema toxin from *Bacillus anthracis*. Remarkably, these highly dynamic tunnels close rapidly after they reach a maximal size. Opening and closure of TEMs in cells lasts for hours without inducing endothelial cell death. Multidisciplinary studies have started to provide a broader perspective of both the molecular determinants controlling cytoskeleton organization at newly curved membranes generated by the opening of TEMs and the physical processes controlling the dynamics of these tunnels. Here we discuss the analogy between the opening of TEM tunnels and the physical principles of dewetting, stemming from a parallel between membrane tension and surface tension. This analogy provides a broad framework to investigate biophysical constraints in cell membrane dynamics and their diversion by certain invasive microbial agents.

Keywords

Bacterial · TEM-transcellular · RhoA GTPase · CAMP · EZRIN · MIM · ABBA · Membrane tension

Abbreviations

BAR	Bin Amphiphysin Rvs167 domain
EDIN	Epidermal cell Differentiation Inhibitor
HUVEC	Human umbilical vein endothelial cell
I-BAR	Inverse-BAR domain
MIM	Missing in metastatis

D. Gonzalez-Rodriguez (✉)
Université de Lorraine, LCP-A2MC, Metz, France
e-mail: david.gr@univ-lorraine.fr

C. Morel
Unité des Toxines Bactériennes, Institut Pasteur, UMR CNRS 2001, Paris, France

Paris Diderot, Sorbonne Paris Cité, Paris, France

E. Lemichez (✉)
Unité des Toxines Bactériennes, Institut Pasteur, UMR CNRS 2001, Paris, France
e-mail: emmanuel.lemichez@pasteur.fr

G. Duménil, S. van Teeffelen (eds.), *Physical Microbiology*, Advances in Experimental Medicine and Biology 1267, https://doi.org/10.1007/978-3-030-46886-6_6

SNARE Soluble NSF attachment protein receptor
TEM Transendothelial cell macroaperture

6.1 Introduction

Interfacial forces such as surface tension dominate the physics at the micrometric scale, which is characteristic of cellular objects. Indeed, surface tension in liquids has led to two different biophysical analogies in living systems. The first type of analogy has been proposed for multicellular systems, such as multicellular aggregates (Steinberg 1963) or biofilms (Oldewurtel et al. 2015). In this analogy, the cells or bacteria forming the multicellular system are identified to the molecules of a liquid. Such units attract each other through intercellular adhesion, similar to molecular interactions in a liquid. A force imbalance arises at the system's interface, where cells (molecules) only have neighbors to one side. This imbalance is energetically unfavorable and leads the units to spontaneously reorganize to reduce the total surface of the interface. This is the molecular origin of surface tension that describes both the behavior of a liquid drop and of a multicellular system. Thus, surface tension has been characterized and measured for cellular aggregates (Phillips and Steinberg 1978, Forgacs et al. 1988, Guevorkian et al. 2010), soft tissues (Maitre et al. 2015), and bacterial colonies (Rühs et al. 2013). The physical similarities between multicellular systems and liquid drops have led to studying the collective dynamics of multicellular systems through analogies with wetting (Douezan and Brochard-Wyart 2011, Gonzalez-Rodriguez et al. 2012a) and dewetting (Douezan and Brochard-Wyart 2012). A second type of analogy has been proposed at the scale of a single cell. The cell is modeled as a viscous liquid drop (Yeung and Evans 1989) and an analogy is established between liquid surface tension and membrane tension of cells. The idealized picture of a tense membrane to conceptualize liquid surface tension becomes here an actual tense membrane. Importantly, the effective membrane tension in the cell is the sum of two different contributions, one arising from the plasma membrane itself and the other from the actin cortex, to which the plasma membrane is attached (Sheetz and Dai 1996; Diz-Muñoz et al. 2013). The analogy with surface tension is valuable to understand cell shape (Fischer-Friedrich et al. 2014), cell adhesion (Sackmann and Bruinsma 2002), or cell dewetting, which is the topic of this chapter.

A liquid film forced to spread on a non-wettable substrate may spontaneously withdraw from the substrate, leading to the formation of dry patches (Fig. 6.1). This phenomenon is known as dewetting. The phenomenon of dewetting is observed for example when placing a thin layer of oil on a non-sticking pan. Dewetting is driven by a difference in interfacial energies of the liquid between wet and dry regions, the wetting zone being favored. This energy difference translates into tension driving the motion of the liquid surface. The liquid surface can be pictured as a tense membrane whose tension will spontaneously tend to minimize the liquid surface by forming dry patches. By analogy with liquid dewetting, cellular dewetting refers to the process of nucleation and enlargement of transendothelial cell macroaperture (TEM) tunnel observed in endothelial cells (Lemichez et al. 2013) (Fig. 6.1). Several exoenzymes and AB toxins from pathogenic bacteria have the property to induce a cellular dewetting of endothelial cells. They comprise EDIN-like factors from *Staphylococcus aureus* and *Clostridium botulinum* that inactivate RhoA as well as cyclic-AMP producing adenylate cyclase toxins from *Bacillus anthracis* and *Bordetella pertussis*. Formation of TEM tunnels occurs upon relaxation of the actomyosin cytoskeleton as a result of (i) inhibition of the small GTPase RhoA by mono-ADP-ribosylating toxins, (ii) inhibition of the Rho kinase (ROCK) with the Y27632 compound or (iii) a rise of intracellular cyclic-AMP concentration (Boyer et al. 2006; Maddugoda et al. 2011). Video microscopy studies of the dynamics of TEM tunnel formation have revealed the remarkable transient nature of their opening (Fig. 6.2). Tunnels open and

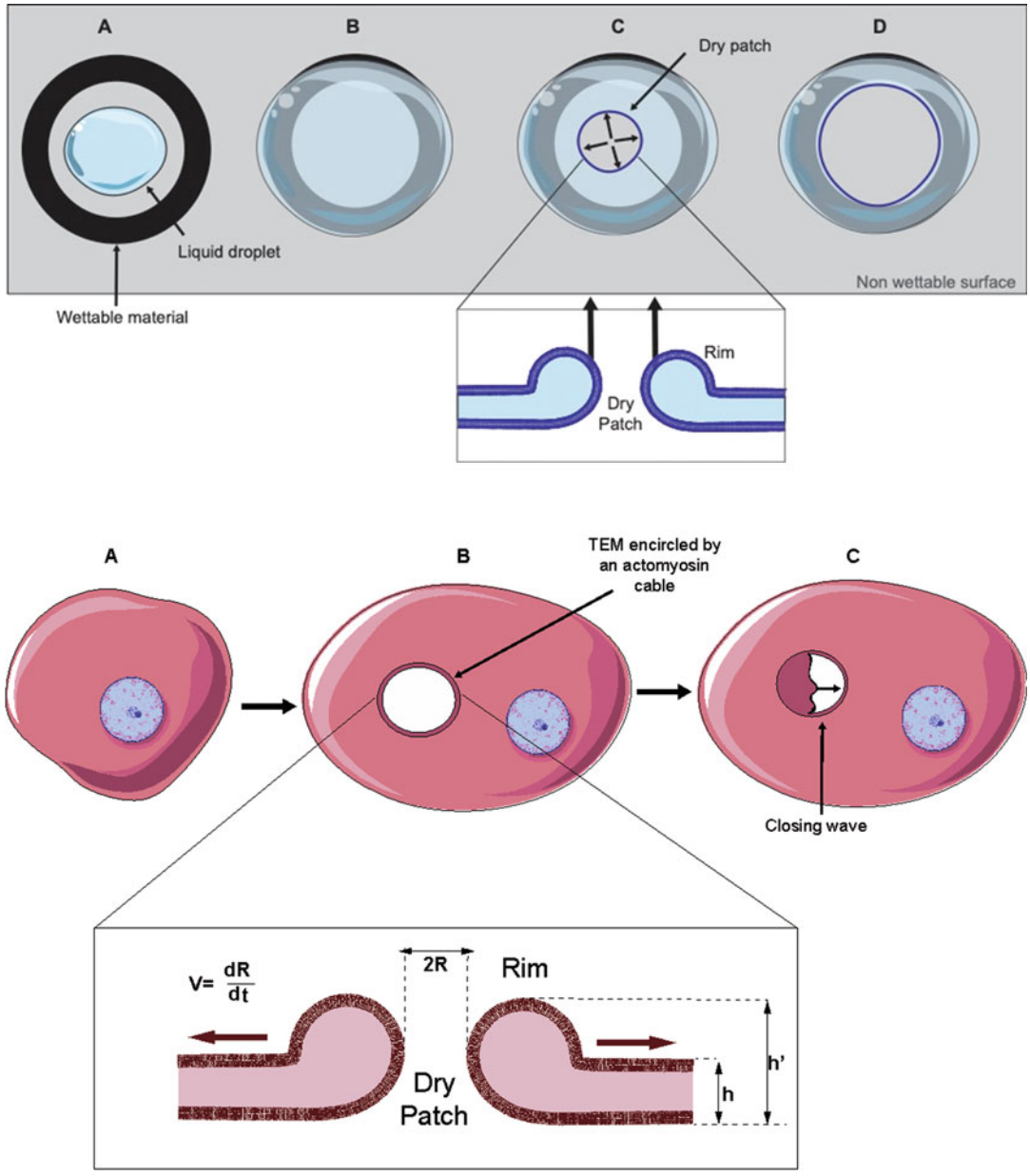

Fig. 6.1 Physical process of liquid dewetting compared to biological cellular dewetting. Upper panel: dewetting phenomenon. (**a**) A liquid droplet is deposited at the center of a non-wettable surface, surrounded by a black region that has been rendered wettable. (**b**) The droplet is mechanically forced to spread and gets pinned by the wettable region, created by a localized substrate treatment. Thus, a metastable state is reached. (**c**) Nucleation of a dry patch destabilizes the system. The dry patch opens up spontaneously so that free energy is minimized. (**d**) The dry patch grows until it fully withdraws from the non-wettable zone. The liquid removed from the dry zone accumulates in a rim. Lower panel: cellular dewetting phenomenon. (**a**) An untreated cell with its nucleus (in blue). (**b**) Upon RhoA inhibiting exoenzyme treatment, the cell spreads thereby increasing membrane tension. A TEM forms and enlarges up to a maximal size, also displaying the formation of a rim along the TEM. The formation of a rigid actin cable encircling the TEM allows its stabilization. (**c**) TEMs open transiently owing to the formation of membrane waves invading the dry patch up to complete resealing of the TEM.(**d**) Schematic side-view showing characteristic dimensions (h = 50 nm, h' = 100 nm, t: time, R: radius, V: opening speed).

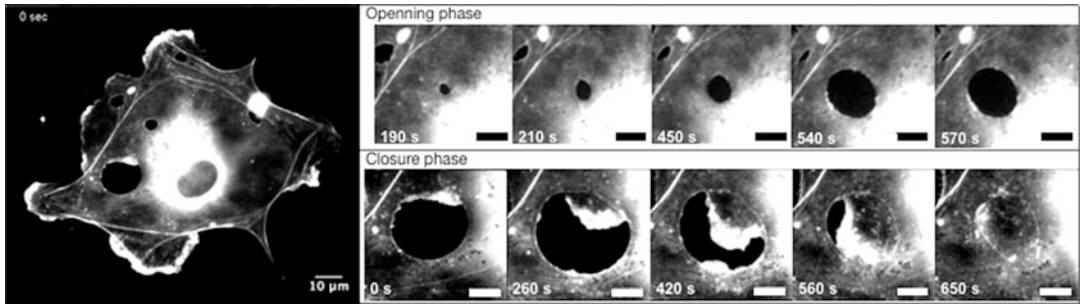

Fig. 6.2 Human Umbilical Vein Endothelial cell (HUVEC) expressing pLifeAct-GFP intoxicated 24 h with edema toxin (ET) from *Bacillus anthracis* was imaged with a spinning-disk microscope (60×) at a rate of one image every 10 s during 1 h (Published in Maddugoda et al. 2011). Right panels show series of snapshots taken at the indicated time. It displays the opening (upper panel) and closure (lower panel) phase of two TEMs. The TEM opens and reaches its maximum size in a few tenths of seconds. Closure typically involves lamellipodia-like actin-rich membrane extension. Note the presence after closure of a persistent actin cable encircling TEMs. Scale bar represent 5 µm

enlarge in about 2 min before reaching a maximal radius of about 10 µm. After the tunnels have stabilized they undergo a phase of closure of about 3 min that involves the extension of membrane waves from their edges invading progressively the dry patch up to complete closure (Fig. 6.2) (Maddugoda et al. 2011). Cycles of TEM opening and closure occur for hours without induction of cell death or detectable leakage of cytosolic material (Boyer et al. 2006). *In vivo,* the expression of EDIN in a clinically relevant strain of *S. aureus* engineered to emit bioluminescence allows visualizing the resulting increase dissemination of bacteria through the vasculature tree forming more infectious foci in various tissues (Munro et al. 2010). Direct injection of EDIN or of the edema toxin from *B. anthracis* into the vasculature induces the loss of endothelium barrier integrity (Boyer et al. 2006; Maddugoda et al. 2011). *Ex vivo*, EDIN promotes the opening of large tunnels through the endothelium layer of vessels thereby unmasking the extracellular matrix fibers (Boyer et al. 2006). The formation of transcellular tunnels is not just a component of several infectious diseases. More broadly, transendothelial tunnels form during the diapedesis of leukocytes through the endothelium lining lymphatic and blood vessels (Alon and van Buul 2017). They also form in cells lining the Schlemm's canal, fulfilling an essential function in the transfer of aqueous humor from the eye chamber to the blood circulation (Braakman et al. 2014).

In this chapter, we review how the analogy with the physics of liquids has allowed a physical interpretation of the opening and enlargement phases of TEMs, yielding the name "cellular dewetting" (Gonzalez-Rodriguez et al. 2012b). While powerful, the analogy between liquid and cellular dewetting is not complete, as some physical aspects of cellular dewetting differ from liquid dewetting due to the intrinsic activity of living matter (Stefani et al. 2017). Here we review the physics of cellular dewetting in parallel to liquid dewetting. Through this parallel, we show the successes of the analogy and we also discuss physical aspects of liquid dewetting for which a cellular dewetting counterpart has not yet been described. This provides clues for future work to address several remaining open questions in the physics of living matter.

6.2 Physical Model of Cellular Dewetting

In this section we summarize the key ideas for the physical modeling of TEM opening arising from

an analogy with liquid dewetting. The driving force for cellular dewetting is

$$F_d = 2\sigma - \frac{T}{R}. \tag{6.1}$$

Here σ is the membrane tension, which tends to open up a TEM and plays the role of the surface tension in liquid dewetting. Membrane tension is estimated to be of the order of 10^{-5} N/m (Raucher and Sheetz 2000). The factor of 2 in the equation reflects the existence of upper and lower membranes. T is the line tension that builds up at the edge of TEMs, when they enlarge. It arises from the energetic cost of forming the TEM edge, where the membrane is deformed to a very high curvature. While negligible in liquid dewetting, line tension plays an important role in cellular dewetting. R is the radius of the TEM. Eq. (6.1) may suggest that the line tension term becomes negligible for large TEMs. This is however not the case, because σ and T do not remain constant during the opening process, as discussed below. Spontaneous dewetting occurs when the driving force F_d is positive. This positive driving force arises from membrane tension increase due to the spreading of cells, but it can also be enhanced by externally applied equibiaxial strain, *i.e.* a strain of equal magnitude imposed along the two perpendicular directions on the sample plane (Braakman et al. 2014). Eq. (6.1) shows that $F_\mathrm{d} > 0$ requires generating an initial TEM whose radius is larger than a certain threshold, $R > R_\mathrm{n} = T/(2\sigma)$. This threshold for initiation of dewetting R_n is known as the nucleation radius. The calculated value of nucleation radius is of the order of 0.1 μm (Gonzalez-Rodriguez et al. 2012b), below photonic microscopy resolution, and its generation mechanisms remain incompletely described so far. As the TEM opens up, the membrane relaxes and membrane tension decreases. It can be assumed that this decrease of membrane tension is rather local given that meanwhile other TEMs open in the cells. Consistent with this notion, recent findings highlighted the local nature of membrane tension in cells (Shi et al. 2018). Moreover, line tension increases due to biological changes occurring around TEM perimeter, such as accumulation of scaffolding proteins (Gonzalez-Rodriguez et al. 2012b) and/or actin assembly (Stefani et al. 2017). As a result, the net driving force decreases and eventually becomes zero. Therefore, the TEM reaches a maximum size, at which spontaneous dewetting stops.

Physical models based on Eq. (6.1) have been developed to explain static aspects of the physics of TEM formation, the maximum size of TEMs, and the role of curvature-sensing proteins (Gonzalez-Rodriguez et al. 2012b, Stefani et al. 2017, Fedorov and Shemesh 2017). Similar to liquid dewetting, the dynamics of TEM opening are governed by a balance between the driving force in Eq. (6.1) and the dynamic resisting force arising from viscous dissipation (see Eq. 6.5 below). By using a viscous dissipation model, previous theoretical studies have described the experimentally observed dynamics of TEM opening (Gonzalez-Rodriguez et al. 2012a, b).

6.3 Characteristics of Cell Dewetting

After having discussed the general framework of the physical modeling of cellular dewetting, in this section we discuss in more detail the building blocks of the model, i.e. driving and resisting forces, nucleation, enlargement, reaching of a maximal size and closure of TEMs. We analyze the analogy between liquid dewetting and cellular dewetting and discuss the similarities and differences between the two. The reader interested in a more detailed overview of the physics of liquid dewetting is referred to the seminal book by P.-G. de Gennes and collaborators (de Gennes et al. 2003).

6.3.1 Driving Force

It has been hypothesized that the driving force for a cell to dewet is powered by an abnormal in-

crease of membrane tension, for example during cell stretching. In support of the role of membrane tension increase as a driver for TEM opening, *in vitro* observations highlight that mechanical stretching can induce tunnel formation. A monolayer of endothelial Schlemm's canal cells were cultured on a stretchable substrate and exposed to equibiaxial strain of up to 20%, which induced the formation of transcellular tunnels, as well as paracellular pores at cell junctions (Braakman et al. 2014). Similarly, the bacterial toxin EDIN induces a massive spreading of endothelial cells due to RhoA inhibition and downstream disruption of stress fibers. By analogy, the inhibition of NMII-dependent symmetric traction forces between opposite cell edges induces a sustained spreading of fibroblasts that likely tenses the membrane up to either a rupture of cell edges, which undergo retractions and adopt a C-shape, or the formation of intracelluar TEM-like gaps (Cai et al. 2010).

A major difference between TEMs that widen to reach a maximum size and holes in liquids that dewet completely arises from the characteristics of the driving force. The surface tension in liquid dewetting remains constant until the hole enlarges up to a complete disruption of the film. In contrast, membrane tension σ is related to the TEM radius R by Helfrich's law (Helfrich 1975):

$$\sigma = \sigma_0 \exp\left\{-\frac{\mathrm{R}^2}{\mathrm{R}_\mathrm{c}^2}\right\}, \tag{6.2}$$

where σ_0 is the undisturbed value of the surface tension, in the absence of a TEM. The characteristic radius in the equation $R_c^2 = R_t^2 \left(k_B\hat{T}\right) / (8\pi\kappa)$, where R_t is the radius of the whole cell, $k_B\hat{T}$ is the thermal agitation energy, and κ is the membrane's bending rigidity. Equation (6.2) is obtained by considering all possible membrane fluctuation modes, whose energy scales as $k_B\hat{T}$ (equipartition theorem). The smallest possible fluctuation wavelength corresponds to the size of a membrane lipid molecule, whereas the largest possible fluctuation wavelength corresponds to the cell size, R_t. The thermal energy of the membrane fluctuations is used to stretch the membrane (work done against the membrane tension σ) and to bend the membrane (work done against its bending rigidity κ). The mathematical formulation of these concepts leads to Eq. (6.2) (Helfrich 1975, Helfrich and Servuss 1984).

Helfrich's law is applicable to membranes subjected to thermal fluctuations. The law is also at play in pore formation in phospholipid vesicles (Sandre et al. 1999, Karatekin et al. 2003), which are are also transient. Opening of the hole is limited by reduction of surface tension as the pore opens and by line tension.

By injecting Eq. (6.2) into Eq. (6.1) and equating the driving force to zero, two equilibrium solutions for the TEM size are obtained. The smaller of them is the nucleation radius, R_n, and the largest of them is the maximum radius, R_m. For $R_\mathrm{n} < R < R_\mathrm{m}$, the driving force is positive and cellular dewetting proceeds spontaneously. The first physical model of cell dewetting showed that by combining the dewetting equation, Eq. (6.1), with Helfrich's law, Eq. (6.2), one can explain spontaneous TEM opening and the existence of a maximum TEM size (Gonzalez-Rodriguez et al. 2012b). This first result raised the question of the exact nature of line tension around TEMs.

TEM opening does not usually occur in isolation. Rather, it is observed that endothelial cells successively open TEMs at different locations. The opening of one TEM does not significantly impair further TEM opening in the cell. Interestingly, a recent study has provided evidence that membrane tension in cells is a local rather than a global parameter (Shi et al. 2018). According to this study, transmembrane proteins bound to the cytoskeleton act as an obstacle to the propagation of membrane tension variations. Thus, local perturbations in effective cell membrane tension require a time scale of the order of tenths of minutes to propagate to the whole cell, which is the same time scale required for TEMs to close back. This can explain why a local drop in membrane tension due to the opening of a TEM does not preclude subsequent TEM opening elsewhere in the cell.

Laser ablation experiments showed that TEMs having reached their maximum size resume opening when their periphery is perturbed (Stefani et al. 2017). Since laser ablation does

not modify membrane tension, these experiments demonstrated that membrane tension reduction does not suffice to explain TEM equilibrium size. This rather pointed to a key role of cytoskeletal-mediated line tension variations in the arrest of TEM enlargement.

6.3.2 Line Tension

Line tension is a force that acts around the edge of a dewetting hole to oppose its widening. In liquids, this force arises from the energetic cost needed to form a highly curved edge. The finding that TEMs stabilize has unveiled the importance of line tension to maintain the cellular integrity, i.e. prevent the extension of a TEM that would finally rupture the edge of cells. The origin of line tension in cell dewetting is a subject of ongoing research. To date, several mechanisms of line tension generation have been proposed: membrane-bending resistance, curvature-sensing proteins forming a scaffold stabilizing the periphery, and actomyosin cable assembly (Gonzalez-Rodriguez et al. 2012b, Stefani et al. 2017).

Membrane bending resistance is responsible for line tension in stretched vesicles (Sandre et al. 1999). When a pore is opened on a vesicle, the lipid molecules along the edge of the pore must curve with a very small radius of curvature that scales as the membrane thickness. This line tension induces the closure of transient pores in vesicles, where it is increased by inclusion of cholesterol and decreased by the addition of detergents (Karatekin et al. 2003). In the case of TEMs, the contribution of membrane bending to line tension is (Gonzalez-Rodriguez et al. 2012b):

$$T_{\mathrm{mb}} = \frac{2\kappa}{\mathrm{h}}. \tag{6.3}$$

As captured by Eq. (6.3), the relevant radius of curvature of the membrane at the TEM border scales as the cell thickness h. Toxins that induce TEM formation perturb the cell cytoskeleton, leading to a very flat morphology, with a typical thickness $h \sim 50$ nm. Thus, with an estimate of the membrane bending rigidity of $\kappa \sim 40\, k_B \hat{T}$, the membrane bending contribution to line tension is of the order of $T_{\mathrm{mb}} \sim 5$ pN. This value is probably greater if one takes into account the force required to deform the cortical cytoskeleton. It is noted that line tension induced by membrane bending rigidity is smaller in TEM opening than it is in pores, because in TEMs the relevant radius for membrane bending is the endothelial cell thickness, whereas at pore edges the lipid membrane bends over itself to join the inner and outer leaflets. Line tension in TEMs arises from the bending rigidity of the whole membrane, similar to the line tension described at the edges of adherent cells (Oakes et al. 2014). This difference with pore opening leads to a significantly different value of h in Equation (6.3), and thus to a smaller line tension for TEMs (note that the relevant membrane bending rigidity is also different). However, line tension generation in TEM opening can also be mediated by other mechanisms that are absent in pore formation, as we discuss next.

Curvature-sensing by proteins such as Inverse-BAR domain (I-BAR)-containing proteins may enhance line tension (Saarikangas et al. 2009; Gonzalez-Rodriguez et al. 2012b). Association of these proteins to the TEM edge may increase the energetic cost of forming a border. Indeed, these proteins have a preferred spontaneous curvature that may deviate from the actual radius. An increase of the radius may thus force them to an unfavorable configuration, which would translate into a line tension. Interestingly, high-rate video acquisition showed that the I-BAR domain of MIM starts to accumulate along TEM edges a few hundred milliseconds after opening (Maddugoda et al. 2011). The size of TEMs increases upon depletion of the curvature-sensing protein MIM, which can be explained by a decrease of line tension (Maddugoda et al. 2011, Gonzalez-Rodriguez et al. 2012b).

Line tension is primarily provided by local actin reorganization around the TEM edges. It has been shown that an actomyosin cable encircles the TEMs as they open (Stefani et al.

2017). Laser ablation nano-surgery has revealed that cutting the actomyosin cable resumes TEM enlargement up to actomyosin cable formation at the edge of the enlarged zone. Line tension arising from the actomyosin cable limits TEM opening by opposing membrane tension, leading to TEM stabilization at a maximum size. Consistently, the introduction of a break in the cable by a laser nanosurgery-based approach promotes further widening of the hole until a new equilibrium state is reached (Stefani et al. 2017). Indeed, a new breaking then induces a second phase of TEM enlargement. The role of this cable in limiting TEM size in cellular dewetting can be expressed as an actomyosin contribution to the line tension, T_{am}. The actin scaffold is not present when the TEM nucleates, but rather it is recruited over time, leading to a time-dependent contribution to line tension, $T_{am} = T_{am}(t)$.

Stefani and collaborators have investigated the quantitative dependence of line tension on actomyosin cable formation, by combining physical modeling with experiments of TEM opening after laser ablation of the cable (Stefani et al. 2017). The predictions of different empirical models of line tension evolution were compared to experimental measurements of TEM opening after ablation. One such model assumed that T_{am} arises from the bending resistance of the cable. Another model supposed that the cable strengthens due to filamentous actin recruitment by convective sweeping of the cell cortex by the moving cable. These two models yielded predictions in contradiction with experimental data showing that the size increase of the TEM after ablation does not depend on its initial size, but it is rather a constant increment. In contrast, good experimental agreement was achieved by a third model that supposed a constant rate of increase of line tension over time, $T_{am} = \alpha t$, corresponding to a constant strengthening of the cable due to actin polymerization and bundling. These descriptions remain empirical, and a full quantitative understanding of the mechanisms by which actomyosin cable assembly leads to line tension generation is still lacking.

6.3.3 Nucleation

The mechanism of nucleation of these structures is probably the most fascinating and difficult question to address. Physical models can guide the response. According to Eq. (6.1), a TEM will open up if its size is larger than a certain threshold, known as the minimal nucleation radius R_n, which is estimated to be of the order of 0.1 μm (Gonzalez-Rodriguez et al. 2012b). The mechanism of TEM nucleation, i.e., of formation of the initial tunnel, remains incompletely understood. Even at the cellular scale, a systematic statistical investigation of a population of TEM nucleation events and a comparison with nucleation in classical liquid dewetting is still lacking. At the subcellular scale, TEM nucleation is probably enabled by thermal fluctuations of the two membranes. Because TEMs form in regions where the cells are very thin, the distance between the upper and lower cell membranes (~50 to 100 nm) is comparable to the amplitude of membrane fluctuations (Chen et al. 2009), which would allow the two membranes to meet. As the two inner leaflets meet, their fusion may be mediated by fusogenic proteins such as SNAREs (Carman and Springer 2008, Carman 2009) or by cations (Mondal Roy and Sankar 2011). In normal endothelial cells, cytoskeletal resistance to deformation is probably the main barrier to membrane fusion. Indeed, TEMs occur in intoxicated cells whose cytoskeleton is significantly perturbed, leading to a drop of the cell's elastic modulus, as measured by atomic force microscopy (Ng et al. 2017). Moreover, Ng and collaborators measured a lower penetration work to form TEMs in EDIN-treated cells. In contrast, direct ROCK inhibition has no impact on the penetration force required to form TEMs. This points toward the importance of other RhoA effectors than ROCK for example implicated in actin filaments polymerization and forming a viscous physical barrier to membrane fusion. The contributing role of the dynamics of cortical cytoskeleton in the initiation of tunnels is less defined. More broadly, one can

speculate that the formation of a dense network of branched actin filaments triggered by Arp2/3 at the interface of membranes also serves as a natural barrier to prevent membrane interaction and opening of TEMs.

Transcellular tunnel opening can also be induced by leukocytes during transmigration, a process in which leukocytes exert forces on endothelial cells through protrusions known as podosomes (Carman et al. 2007, Carman and Springer 2008). By analogy, it has been shown that the application of a mechanical force at the apical side of cells can overcome cytoskeletal resistance to membrane fusion and induce tunnel formation (Ng et al. 2017). In the experiments by Ng et al., compressive forces applied by means of an AFM tip on endothelial cells induced TEM nucleation. Interestingly, control endothelial cells respond to compression by actin polymerization that opposes TEM nucleation, whereas actin polymerization is impaired in intoxicated cells and TEMs open. These tunnels close like those induced by the toxin but are much less wide. The size of the AFM tip is comparable to the size of leukocyte podosomes, and the compression force required to induce TEM opening in AFM experiments (5–100 pN) is also comparable to the forces applied by podosomes during leukocyte transcellular diapedesis (Labernadie et al. 2014).

6.3.4 Maximum Size

Typical TEMs open up to a maximum size of the order of several micrometers. TEMs remain at their maximum size for a few tenths of seconds or minutes, before starting to close down. Closure is a slower process, typically lasting for a few minutes, and it is associated to the formation of lamellipodia-like actin-rich membrane waves for a majority of TEMs, whereas other close by a purse-string mechanism (Fig. 6.2).

The existence of a maximum size is a specific feature of cellular dewetting. The tunnels remain stably open when the cell is depleted of the MIM protein, showing that cell activity is required for the closure. In contrast, liquid dewetting is irreversible, as dry patches continue to grow until the liquid has completely withdrawn from the non-wettable surface. In lipid vesicles, pore opening is also transient, but unlike TEMs no durable stabilization at a maximum size is observed between the opening and closure stages (Sandre et al. 1999). Stabilization of a dewetting hole is however observed in liquid dewetting over a rough surface (de Gennes et al. 2003), although such stabilization arises from surface heterogeneities and not from the system itself, as in the process of cellular dewetting.

The maximum size of TEMs results from balance between membrane tension and the kinetics of line tension increase. It corresponds to $F_d = 0$ in Eq. (6.1). In a configuration where membrane tension variations dominate over line tension, the maximum radius would scale as

$$R_m \sim R_c \left(-\ln \frac{T}{2\sigma_0 R_c} \right)^{1/2}. \qquad (6.4)$$

As discussed in the section on line tension above, the assumption of a constant line tension, arising from membrane bending resistance, satisfactorily predicts the typical size attained by TEMs formed *ex novo* (Gonzalez-Rodriguez et al. 2012b). However, this simple picture does not suffice to explain experimental observations of *de novo* TEM opening following laser ablation (Stefani et al. 2017), which requires accounting for a time-varying line tension provided by the assembly of an actin cable around the TEM. With this improvement, the cellular dewetting model can explain quantitatively the increase of TEM size following laser ablation (Stefani et al. 2017). It also provides a physical framework to our hypothesis that ezrin, a member of the FERM-domain containing protein family encompassing ezrin, radixin and moesin, specifically drives the formation of the actin cable encircling TEMs. Ezrin has a tendency to accumulate around TEMs, especially when phosphorylated on T567 (Tsai et al. 2018; Stefani et al. 2017). Ablation of ezrin leads to a higher turnover of F-actin around TEMs and the formation of TEMs of wider size. Taking into account a kinetic parameter in the line tension increase offers a theoretical framework

to the observation that a TEM opening *de novo* stabilizes to a maximal size while laser ablation-mediated disruption of the actin cable induced a widening of TEMs that is no longer limited. This particular case indicates that a major difference between viscous liquid dewetting and cellular dewetting comes from cytoskeletal-mediated line tension buildup at curved membranes, which stabilizes newly formed cell borders generated by the opening of TEMs.

6.3.5 Rim Formation

In classical liquid dewetting, the liquid removed from the dry patch accumulates in a rim that forms along the border of the hole (Redon et al. 1991, de Gennes et al. 2003). Such a liquid rim typically has a circular cross-section, and it increases in both height and width as dewetting proceeds, due to mass conservation.

Rim formation is also observed in cellular dewetting, as it has been evidenced by AFM profiles (Maddugoda et al. 2011). The rim appears to correspond to the accumulation of cytoplasmic material that has been displaced as the TEMs open (Gonzalez-Rodriguez et al. 2012b), see Fig. 6.1. Typical rim dimensions are about 100 nm in height and about 1 micrometer in width, whereas the cell height at the location of the tunnels is about 50 nm (measured with AFM operated at constant force of 100 pN, 0.3–1 Hz) (Maddugoda et al. 2011). A numerical model that accounts for membrane bending rigidity, membrane tension and cytoplasmic pressure explained the shape of the rim profile by free energy minimization (Fedorov and Shemesh 2017).

6.3.6 Viscous Dissipation and Opening Dynamics

During TEM opening, the driving force in Eq. (6.1) is positive. At the small length scales of TEM opening, this positive driving force cannot be balanced by inertia as in the macroscopic world. Indeed, the relevant Reynolds number for TEM opening is very small, of the order of 10^{-6}, indicating that inertial effects are negligible. Therefore, the positive driving force must be balanced out by viscous dissipation, same as in viscous liquid dewetting.

In the study of viscous liquid dewetting, different scenarios have been described (de Gennes et al. 2003). For very thin films, where gravity effects are negligible, placed on a smooth and homogeneous solid substrate, liquid removed from the dry patch accumulates in a rim of circular cross-section. Viscous dissipation is mainly due to fluid flow within the rim. This scenario leads to a constant velocity of dewetting, $v = \mathrm{d}R / \mathrm{d}t = \text{constant}$ (Redon et al. 1991).

A second liquid dewetting scenario arises at longer time scales, once enough liquid has accumulated in the rim and gravity effects are no longer negligible. In this regime, the rim's cross-section becomes a flat pancake, with a maximum thickness equal to e_c, the critical thickness below which a liquid film dewets. This critical thickness scales as the capillary length, of the order of a millimeter. In this regime, viscous dissipation is concentrated at the wedges of the flat pancake, which leads to a law of dewetting of the form $R^2 = D.t$, where D is a constant (Brochard-Wyart et al. 1988).

A third scenario, which inspired the original analogy with cellular dewetting, is the dewetting on a slippery substrate, such as ultra-viscous liquid PDMS on a smooth and passive surface. It has been shown that ultra-viscous liquids slide over smooth, passive surfaces (Redon et al. 1994). Unlike the usual velocity profile of a viscous flow, where velocity vanishes at contact with the substrate due to the no-slip boundary condition, ultra-viscous liquids adopt a plug flow, with a constant velocity profile over the height. In this case, friction dissipation is given by

$$F_v \sim k\, l\, v, \tag{6.5}$$

where l is the width of the rim, $v = \mathrm{d}R / \mathrm{d}t$ is the velocity, and $k \approx \eta / a$ is a friction coefficient, with η the liquid viscosity and a the size of a monomer in the polymeric liquid. In this scenario, the rim has a circular cross-section. The resulting opening dynamics scale as $R \sim t^{2/3}$ (Redon et al. 1994).

It has been proposed that cellular dewetting resembles this latter scenario (Gonzalez-Rodriguez et al. 2012a, b). As the TEM opens, the rim advances over the substrate. Due to the disturbed cytoskeleton of intoxicated cells, adhesion with the substrate is reduced, and the membrane may slip over the substrate. This is the rationale to model friction dissipation in dewetting using Eq. (6.5). The friction coefficient k is expected to be of the order of $k \approx 10^8$ Pa.s.m.$^{-1}$, an estimate obtained from experiments that measured friction between a cell and a substrate (Guevorkian et al. 2010, Douezan and Brochard-Wyart 2011).

Different dynamics are observed in liquid dewetting on a slippery substrate and in cell dewetting, which is attributed to a different shape of the rim. The rim's cross-section is circular in the slippery liquid dewetting and flat in cellular dewetting. This difference modifies the equations of motion, leading to a cellular dewetting law that scales as $R \sim t^{1/2}$. Thus, cellular dewetting has diffusion-like opening dynamics, same as in the second liquid dewetting scenario discussed above. Interestingly, these two phenomena also share the common feature of a pancake-shaped rim. However, these apparent similarities correspond to different physics: the flat pancake rim in liquid dewetting is due to gravity effects, whereas in cell dewetting it is due to the cell's mechanical properties.

The cellular dewetting dynamics model summarized above is thus based on the assumptions of a pancake-shaped rim of constant height and membrane slipping on the substrate (Gonzalez-Rodriguez et al. 2012b). Its validity is supported by good agreement with the dynamics of opening observed in experiments. However, direct experimental investigation of the rim shape evolution is limited, and the flow field of the cell membrane during TEM opening has not been quantified. Future experiments could aim at experimentally characterizing these two aspects of TEM opening, in order to directly test the model's hypotheses.

6.3.7 Closure

Over longer time scales, of the order of several minutes, TEMs completely close down (Fig. 6.2). Unlike transient pore closure in vesicles, the interplay between surface tension and line tension do not suffice to explain the dynamics of TEM closure, which is driven by extension of actomyosin-dependent processes. TEM closure has been related to the formation of lamellipodia-like projections via local Arp2/3-dependent branched-actin polymerization driven by MIM (Maddugoda et al. 2011). Closure driven by actin polymerization has been described by a physical model (Fedorov and Shemesh 2017). This model related actin polymerization dynamics to local curvature of the TEM edge. The model predicted that actin polymerization is slower in regions where the TEM edge has positive curvature (the curvature of a circular TEM) and faster in regions of negative curvature (such as a protrusion). This curvature effect is due to the effect of line tension, which promotes protrusion at a negatively curved edge, and to the lower compressive stress experienced by actin filaments in such regions, which results in a higher polymerization rate. The model successfully explains the observed instability of the circular TEM shape, which forms protrusions during the closure. The TEM closure mechanism described in this model does not require myosin motor activity for TEM repair.

An open question is the role of the actomyosin cable in the dynamics of TEM closure. Although a majority of the TEMs close by extension of membrane waves, we have also observed closure of TEMs by a purse-string phenomenon. Laser ablation experiments have shown that the cable after ablation retains its original length, indicating that it is under tension but does not undergo significant elastic deformation (Stefani et al. 2017). The absence of the contractility of the cable may dependent on the level of RhoA inactivation in intoxicated cells. In some circumstances the actomyosin cable that forms around the TEM (Stefani et al. 2017) could provide an additional mechanism to drive TEM closure by a purse-string mechanism similar to that described in wound healing of epithelial tissues (Vedula et al. 2015). In this case, it is not excluded that another type of contractile ring forms around TEMs when they stabilize prior to the closure by a purse-string mechanism.

6.4 Future Developments and Conclusions

In this section we discuss several physical phenomena observed in liquid dewetting for which an analogy in cellular dewetting has not yet been identified. These unexplored analogies, if pertinent, may lead to advancements in our understanding of the physics of TEMs.

6.4.1 Critical Thickness

Spontaneous dewetting of a liquid film on a solid substrate depends on the value of the spreading parameter S, which is the difference in energy between a wet patch and a dry patch (de Gennes et al. 2003). For $S > 0$ a liquid film is always stable and dewetting does not occur. For $S < 0$ dewetting occurs when the film thickness e is smaller than a critical threshold thickness e_c. The balance between capillarity and gravity defines this critical thickness. For $e < e_c$, a configuration where the liquid accumulates in patches of thickness e_c by leaving dry patches elsewhere is energetically favored, and dewetting can occur spontaneously. The continuous film of thickness $e < e_c$ is thus at a metastable state. Experiments perturbing the film destabilize its metastable state thereby initiating dewetting.

In cellular dewetting, the role of the liquid film is played by the whole cell. In the cell dewetting model, there is no direct analogy with the critical threshold thickness. This is because gravitational forces in liquid dewetting, which set the critical thickness, are negligible in cell dewetting, where they are much smaller than viscous and membrane forces. Nevertheless, it is observed that cellular dewetting occurs in cells that are abnormally thin, of the order of 50–100 nm or when pushing on the membranes to bring them in close proximity. This suggests the possible existence of a critical cell thickness for dewetting, although arising from different physics. Existence of a critical thickness would not simply mean that it is harder to nucleate a TEM in a thicker cell. Rather, we suggest that if the cell thickness is larger than a certain threshold, any nucleated tunnel would immediately disappear, implying that TEM opening is observed only when the cell thickness is smaller than this threshold. In physics terms, the cell would be metastable below this critical thickness and stable above. In cellular dewetting, such critical thickness would not be set by gravity, but by a different force opposing TEM opening, such as actin cytoskeletal resistance.

6.4.2 Spinodal Dewetting

Very thin liquid films of $e << e_c$ are unstable to capillary waves. Driven by van der Waals forces, perturbations get amplified at certain wavelengths, and the liquid films breaks up into multiple droplets. This dewetting mechanism is known as spinodal dewetting (Reiter 1992, de Gennes et al. 2003). It is a different dewetting mechanism from the nucleation and growth of dry patches.

Spinodal dewetting in cells has not been described. Whereas a direct physical analogy may not be pertinent, spinodal decomposition processes may play a role in cell dewetting. Similar to spinodal dewetting arising from the growth of surface perturbations in the liquid film, cellular dewetting appears to arise from perturbations in the cell membrane. Rather than studying out-of-plane perturbations of the film thickness like in spinodal liquid dewetting, it appears more pertinent to investigate heterogeneities in cell membrane composition. Indeed, spinodal decomposition leading to phase separation has been reported in multicomponent lipid vesicles (Veatch and Keller 2003). Such membrane heterogeneities may create preferential spots for TEM nucleation, as well as barriers between membrane domains that limit TEM opening. These considerations suggest studying how the locations of successive TEM opening within one cell correlate with heterogeneities in membrane composition.

In spinodal dewetting, a thin liquid film may be perturbed by the wavy topography of the substrate, if the wavelength of such geometrical substrate variations is large enough. Similarly, there could be a role of substrate geometry in cellular

dewetting. This analogy points to a possible effect of substrate patterning and of substrate curvature on inducing membrane perturbations and TEM nucleation. In the next section, we further consider how surface characteristics may affect cell dewetting.

6.4.3 Irregular and Soft Substrates

There are large variations in the fibrillar composition and mechanical properties of the extracellular matrix that is in direct contact with endothelial cells (Marchand et al. 2018). Substrate irregularities induce hysteresis in liquid dewetting (de Gennes et al. 2003). The origin for such hysteresis is the existence of two different contact angles for a drop placed on a textured surface, depending on whether the wetting front advances or recedes. Due to hysteresis, liquid dewetting on a textured surface may lead to stable configurations, where a dry patch keeps a constant size, and neither opens up nor closes. Hysteretic effects in cellular dewetting have not yet been described, but they could arise in cellular dewetting over patterned or heterogeneous substrates, which are known to significantly modify cell properties (Curtis and Wilkinson 1997, Anderson and Hinds 2011).

Liquid wetting and dewetting phenomena are also affected by substrate stiffness. If the substrate is sufficiently soft to be deformed by surface tension forces, elasto-capillary phenomena arise (Bico et al. 2018). To date, cellular dewetting on substrates of different stiffness has not been studied. However, we expect that substrate rigidity may affect cellular dewetting through physical mechanisms, such as elasto-capillarity, and through biological mechanisms, such as actin reorganization in response to mechanosensing. We also anticipate the role of biophysical mechanisms by which rigidity modifies the wetting properties of a substrate by a cell. It has been shown that the wetting of cellular aggregates can be equivalently modulated by substrate chemistry (as in classic liquid wetting) or by substrate rigidity (which is specific to biological wetting) (Douezan et al. 2012). Substrate coating and rigidity also affect wetting-dewetting transitions in cellular monolayers (Perez-Gonzalez et al. 2019). Substrate coating and rigidity are known to affect the height of membrane undulations (Chang et al. 2017), which likely contribute to membrane collision for fusion and opening of TEMs. Taken together, these previous observations suggest an effect of substrate characteristics on cellular dewetting.

In conclusion, the analogy made between the dynamics of TEMs and the physics of liquid dewetting on non-wettable surfaces has been instrumental in deciphering essential parameters of TEM opening and stabilization. A challenge for the upcoming years will certainly encompass the comparison of this phenomenon to leukocyte diapedesis through the endothelium and the study of these phenomena in 3D models reflecting the physiological conditions of vessels. It will also be interesting to define the intrinsic cellular parameters that limit the formation of TEMs in cells. This should ultimately lead to progress in our understanding of spontaneous bleeding vascular diseases not due to platelet deficiencies.

Acknowledgements We warmly thank all our colleagues who have contributed to unveiling the importance of the cellular dewetting phenomenon and the biophysical mechanisms underlying it. We are particularly grateful to Patricia Bassereau and Françoise Brochard-Wyart for pointing out the analogy between the opening of TEMs and the physics of dewetting and for their contributions to modeling this biological phenomenon. We also thank Cécile Leduc, Patricia Bassereau and two anonymous reviewers, who read earlier versions of this chapter and provided valuable ideas and suggestions. Studies on TEMs are funded by a grant ANR-15-CE18-0016.

References

Alon R, van Buul JD (2017) Leukocyte breaching of endothelial barriers: the actin link. Trends Immunol 38:606–615

Anderson DE, Hinds MT (2011) Endothelial cell micropatterning: methods, effects, and applications. Ann Biomed Eng 39(9):2329–2345

Bico J, Reyssat E, Roman B (2018) Elastocapillarity: when surface tension deforms elastic solids. Annu Rev Fluid Mech 50:629–659

Boyer L, Doye A, Rolando M, Flatau G, Munro P, Gounon P, Clément R, Pulcini C, Popoff MR, Mettouchi A, Landraud L, Dussurget O, Lemichez E (2006) Induction of transient macroapertures in endothelial cells through

RhoA inhibition by Staphylococcus aureus factors. J Cell Biol 173(5):809–819

Braakman ST, Pedrigi RM, Read AT, Smith JAE, Stamer WD, Ethier CR, Overby DR (2014) Biomechanical strain as a trigger for pore formation in Schlemm's canal endothelial cells. Exp Eye Res 127:224–235

Brochard-Wyart F, Redon C, Rondelez F (1988) Démouillage: régime de gravité. C R Acad Sci Paris 306(II):1143–1146

Cai Y, Rossier O, Gauthier NC, Biais N, Fardin MA, Zhang X, Miller LW, Ladoux B, Cornish VW, Sheetz MP (2010) Cytoskeletal coherence requires myosin-IIA contractility. J Cell Sci 123:413–423

Carman CV (2009) Mechanisms for transcellular diapedesis: probing and pathfinding by "invadosome-like protrusions.". J Cell Sci 122:3025–3035

Carman CV, Springer TA (2008) Trans-cellular migration: cell-cell contacts get intimate. Curr Opin Cell Biol 20:533–540

Carman CV, Sage PT, Sciuto TE, de la Fuente MA, Geha RS, Ochs HD, Dvorak HF, Dvorak AM, Springer TA (2007) Transcellular diapedesis is initiated by invasive podosomes. Immunity 26:784–797

Chang CH, Lee HH, Lee CH (2017) Substrate properties modulate cell membrane roughness by way of actin filaments. Sci Rep 7:9068

Chen CH, Tsai FC, Wang CC, Lee CH (2009) Three-dimensional characterization of active membrane waves on living cells. Phys Rev Lett 103(23):238101

Curtis A, Wilkinson C (1997) Topographical control of cells. Biomaterials 18(24):1573–1583

de Gennes PG, Brochard-Wyart D, Quéré D (2003) Capillarity and wetting phenomena. Drops, Bubbles, Pearls, Waves. Springer

Diz-Muñoz A, Fletcher DA, Weiner OD (2013) Use the force: membrane tension as an organizer of cell shape and motility. Trends Cell Biol 23(2):47–53

Douezan S, Brochard-Wyart F (2011) Spreading dynamics and wetting transition of cellular aggregates. Proc Natl Acad Sci USA 108(18):7315–7320

Douezan S, Brochard-Wyart F (2012) Dewetting of cellular monolayers. Eur Phys J E 35(5):34

Douezan S, Dumond J, Brochard-Wyart F (2012) Wetting transitions of cellular aggregates induced by substrate rigidity. Soft Matter 8(17):4578–4583

Fedorov EG, Shemesh T (2017) Physical model for stabilization and repair of trans-endothelial apertures. Biophys J 112(2):388–397

Fischer-Friedrich E, Hyman AA, Jülicher F, Muller DJ, Helenius J (2014) Quantification of surface tension and internal pressure generated by single mitotic cells. Sci Rep 4:6213

Forgacs G, Foty RA, Shafrir Y, Steinberg MS (1988) Viscoelastic properties of living embryonic tissues: a quantitative study. Biophys J 74(5):2227–2234

Gonzalez-Rodriguez D, Guevorkian K, Douezan S, Brochard-Wyart F (2012a) Soft matter models of developing tissues and tumors. Science 338:910–917

Gonzalez-Rodriguez D, Maddugoda MP, Stefani C, Janel S, Lafont F, Cuvelier D, Lemichez E, Brochard-Wyart F (2012b) Cellular dewetting: opening of macroapertures in endothelial cells. Phys Rev Lett 108(21):218105

Guevorkian K, Colbert MJ, Durth M, Dufour S, Brochard-Wyart F (2010) Aspiration of biological viscoelastic drops. Phys Rev Lett 104:218101

Helfrich W (1975) Out-of-plane fluctuations of lipid bilayers. Zeitschrift für Naturforschung C 30(11–12):841–842

Helfrich W, Servuss RM (1984) Undulations, steric interaction and cohesion of fluid membranes. Il Nuovo Cimento D 3(1):137–151

Karatekin E, Sandre O, Guitouni H, Borghi N, Puech PH, Brochard-Wyart F (2003) Cascades of transient pores in Giant vesicles: line tension and transport. Biophys J 84(3):1743–1749

Labernadie A, Bouissou A, Delobelle P, Balor S, Voituriez R, Proag A, Fourquaux I, Thibault C, Vieu C, Poincloux R, Charrière GM, Maridonneau-Parini I (2014) Protrusion force microscopy reveals oscillatory force generation and mechanosensing activity of human macrophage podosomes. Nat Commun 5:5343

Lemichez E, Gonzalez-Rodriguez D, Bassereau P, Brochard-Wyart F (2013) Transcellular tunnel dynamics: control of cellular dewetting by actomyosin contractility and I-BAR proteins. Biol Cell 105(3):109–117

Maddugoda MP, Stefani C, Gonzalez-Rodriguez D, Saarikangas J, Torrino S, Janel S, Munro P, Doye A, Prodon F, Aurrand-Lions M, Goossens PL, Lafont F, Bassereau P, Lappalainen P, Brochard F, Lemichez E (2011) cAMP signaling by anthrax edema toxin induces transendothelial cell tunnels, which are resealed by MIM via Arp2/3-driven actin polymerization. Cell Host Microbe 10(5):464–474

Maitre JL, Niwayama R, Turlier H, Nédélec F, Hiiragi T (2015) Pulsatile cell-autonomous contractility drives compaction in the mouse embryo. Nat Cell Biol 17(7):849–855

Marchand M, Monnot C, Muller L, Germain S (2018) Extracellular matrix scaffolding in angiogenesis and capillary homeostasis. Semin Cell Dev Biol S1084-9521(17):30578–30575

Mondal Roy S, Sarkar M (2011) Membrane fusion induced by small molecules and ions. J Lipids 2011: e528784

Munro P, Benchetrit M, Nahori MA, Stefani C, Clement R, Michiels JF, Landraud L, Dussurget O, Lemichez E (2010) Staphylococcus aureus EDIN toxin promotes formation of infection foci in a mouse model of bacteremia. Infect Immun 78:3404–3411

Ng WP, Webster KD, Stefani C, Schmid EM, Lemichez E, Bassereau P, Fletcher DA (2017) Force-induced transcellular tunnel formation in endothelial cells. Mol Biol Cell 28(20):2589–2745

Oakes PW, Banerjee S, Marchetti MC, Gardel ML (2014) Geometry regulates traction stresses in adherent cells. Biophys J 107(4):825–833

Oldewurtel ER, Kouzel N, Dewenter L, Henseler K, Maier B (2015) Differential interaction forces govern bacterial sorting in early biofilms. elife 4:e10811

Pérez-González C, Alert R, Blanch-Mercader C, Gómez-González M, Kolodziej T, Bazellieres E, Casademunt J, Trepat X (2019) Active wetting of epithelial tissues. Nat Phys 15:79–88

Phillips HM, Steinberg MS (1978) Embryonic tissues as elasticoviscous liquids. I. Rapid and slow shape changes in centrifuged cell aggregates. J Cell Sci 30:1–20

Raucher D, Sheetz MP (2000) Cell spreading and lamellipodial extension rate is regulated by membrane tension. J Cell Biol 148:127–136

Redon C, Brochard-Wyart F, Rondelez F (1991) Dynamics of dewetting. Phys Rev Lett 66(6):715–718

Redon C, Brzoska JB, Brochard-Wyart F (1994) Dewetting and slippage of microscopic polymer films. Macromolecules 27:468–471

Reiter G (1992) Dewetting of thin polymer films. Phys Rev Lett 68(1):75–78

Rühs PA, Böni L, Fuller GG, Inglis RF, Fischer P (2013) In-situ quantification of the interfacial rheological response of bacterial biofilms to environmental stimuli. PLoS One 8(11):e78524

Saarikangas J, Zhao H, Pykalainen A, Laurinmaki P, Mattila PK, Kinnunen PK, Butcher SJ, Lappalainen P (2009) Molecular mechanisms of membrane deformation by I-BAR domain proteins. Curr Biol 19: 95–107

Sackmann E, Bruinsma RF (2002) Cell adhesion as wetting transition? Chem Phys Chem 3:262–269

Sandre O, Moreaux L, Brochard-Wyart F (1999) Dynamics of transient pores in stretched vesicles. Proc Natl Acad Sci USA 96(19):10591–10596

Sheetz MP, Dai J (1996) Modulation of membrane dynamics and cell motility by membrane tension. Trends Cell Biol 6:85–89

Shi Z, Graber ZT, Baumgart T, Stone HA, Cohen AE (2018) Cell membranes resist flow. Cell 175:1769–1779

Stefani C, Gonzalez-Rodriguez D, Senju Y, Doye A, Efimova N, Janel S, Lipuma J, Tsai MC, Hamaoui D, Maddugoda MP, Cochet-Escartin O, Prévost C, Lafont F, Svitkina T, Lappalainen P, Bassereau P, Lemichez E (2017) Ezrin enhances line tension along transcellular tunnel edges via NMIIa driven actomyosin cable formation. Nat Commun 23(8):15839

Steinberg MS (1963) Reconstruction of tissues by dissociated cells. Science 141(3579):401–408

Tsai FC, Bertin A, Bousquet H, Manzi J, Senju Y, Tsai MC, Picas L, Miserey-Lenkei S, Lappalainen P, Lemichez E, Coudrier E, Bassereau P (2018) Ezrin enrichment on curved membranes requires a specific conformation or interaction with a curvature-sensitive partner. Elife 7:e37262

Veatch SL, Keller SL (2003) Separation of liquid phases in Giant vesicles of ternary mixtures of phospholipids and cholesterol. Biophys J 85(5):3074–3083

Vedula SR, Peyret G, Cheddadi I, Chen T, Brugués A, Hirata H, Lopez-Menendez H, Toyama Y, de Almeida LN, Trepat X, Lim CT, Ladoux B (2015) Mechanics of epithelial closure over non-adherent environments. Nat Commun 6:6111

Yeung A, Evans E (1989) Cortical shell-liquid core model for passive flow of liquid-like spherical cells into micropipets. Biophys J 56:139–149

Physical Mechanisms of Bacterial Killing by Histones

7

Tory Doolin, Steven Gross, and Albert Siryaporn

Abstract

Antibiotic resistance is a global epidemic, becoming increasingly pressing due to its rapid spread. There is thus a critical need to develop new therapeutic approaches. In addition to searching for new antibiotics, looking into existing mechanisms of natural host defense may enable researchers to improve existing defense mechanisms, and to develop effective, synthetic drugs guided by natural principles. Histones, primarily known for their role in condensing mammalian DNA, are antimicrobial and share biochemical similarities with antimicrobial peptides (AMPs); however, the mechanism by which histones kill bacteria is largely unknown. Both AMPs and histones are similar in size, cationic, contain a high proportion of hydrophobic amino acids, and possess the ability to form alpha helices. AMPs, which mostly kill bacteria through permeabilization or disruption of the biological membrane, have recently garnered significant attention for playing a key role in host defenses. This chapter outlines the structure and function of histone proteins as they compare to AMPs and provides an overview of their role in innate immune responses, especially regarding the action of specific histones against microorganisms and their potential mechanism of action against microbial pathogens.

Keywords

Mammalian histones · Antimicrobial peptides · LL-37 · Neutrophil extracellular traps · Antimicrobial synergy · Host-microbe interactions

T. Doolin
Department of Developmental and Cell Biology, UC Irvine, Irvine, CA, USA

S. Gross (✉)
Department of Developmental and Cell Biology, UC Irvine, Irvine, CA, USA

Department of Physics & Astronomy, UC Irvine, Irvine, CA, USA
e-mail: sgross@uci.edu

A. Siryaporn (✉)
Department of Physics & Astronomy, UC Irvine, Irvine, CA, USA

Department of Molecular Biology & Biochemistry, UC Irvine, Irvine, CA, USA
e-mail: asirya@uci.edu

Abbreviations

H1	Histone H1
H2A	Histone H2A
H2B	Histone H2B
H3	Histone H3
H4	Histone H4
AMP	Antimicrobial Peptide

G. Duménil, S. van Teeffelen (eds.), *Physical Microbiology*, Advances in Experimental Medicine and Biology 1267, https://doi.org/10.1007/978-3-030-46886-6_7

NETs	Neutrophil Extracellular Traps
LDs	Lipid Droplets
LPS	Lipopolysaccharide
LTA	Lipoteichoic acid
PAD4	Peptidyl arginine deiminase, type IV
MIC	Minimum inhibitory concentration
CRAMP	Cathelin-related antimicrobial peptide
NMDA	N-methyl-D-aspartate

7.1 Introduction

In 1922, Alexander Fleming discovered lysozyme from nasal mucus (Fleming 1922). This was the first human antimicrobial protein to be reported; however, the discovery of penicillin in 1928 (Fleming 1980) overshadowed this finding, and ushered the world into the "Golden Age" of antibiotics. Recently, the rise of antibiotic resistance, combined with the stagnation in discovering new, viable antimicrobial agents, has sparked renewed interest in natural host defenses. The antimicrobial activity of histones was first reported in 1942 (Miller et al. 1942) and *in vitro* histone killing of bacteria was further characterized in 1958 using *Escherichia coli* (Hirsch 1958). However, despite originally being proposed to function as antimicrobial agents, the role of histones in condensing eukaryotic DNA became seen as their primary function and little is known about their antimicrobial role and the possible mechanisms by which they kill bacteria. The discovery that histones have a central role in innate immune responses (Brinkmann 2004) has renewed interest into understanding their antimicrobial functions.

Eukaryotic organisms possess a cell nucleus and other organelles enclosed within a membrane. Their nuclei contain genetic material, typically encoded in DNA, within a nuclear envelope. Within the nucleus, small, alkaline histone proteins are used to package the DNA into 5 nm nucleosomes that condense chromatin, the chromosomal material in eukaryotic cells that is composed protein, DNA, and a small amount of RNA. The basic structural unit of chromatin is made up of 146 DNA base pairs wrapped roughly 1.5 times around a histone core. This histone core structure is made up of eight histone components: two H2A-H2B dimers and a H3-H4 tetramer (Luger et al. 1997). These core histones are highly conserved through evolution, containing the 'helix turn helix turn helix' central motif, named the histone fold, and an unstructured amino-terminal tail (DeLange and Smith 1971). The structure of H2A, which is representative of the structure of the four core histones, is shown in Fig. 7.1. Histones contain the positively-charged amino acids lysine and arginine, which facilitate their interactions with negatively-charged DNA. The histones are grouped into two classes: lysine-rich (H1, H2A, H2B) and arginine-rich (H3, H4) (DeLange and Smith 1971). The nucleosome complex, which contains the segment of DNA wrapped around the histone core, forms the repeating units of chromatin, facilitates higher order chromatin structure, and is necessary for eukaryotic survival. Histone H1 functions as a linker that binds to 20 base pairs of DNA, forming a chromatosome (Allan et al. 1980). The structure of H1, with a long C-terminal tail, a short N-terminal tail, and a central globular domain with a winged helix domain (Zhou et al. 2013), is shown in Fig. 7.1. Linker DNA from one chromatosome binds to linker DNA from another chromatosome, further condensing the DNA into 30 nm chromatin fiber.

7.2 Innate Immune Responses for Combating Bacterial Infections

When histones were believed to be solely in the nucleus, it was hard to imagine how they might play an antimicrobial role. More recently, the observation of histones localizing outside of the cell nucleus, across multiple species, allows one to speculate that they may have roles in addition to chromosome condensation (Brinkmann 2004; Anand et al. 2012). For instance, histones are observed inside cytoplasmic granules in human neutrophils (Lominadze et al. 2005). Further, they are likely functional: H2A and H2B purified from the fetal membranes of the human placenta show dose-dependent inhibition of LPS endotoxin activity, by binding the core and lipid A portions

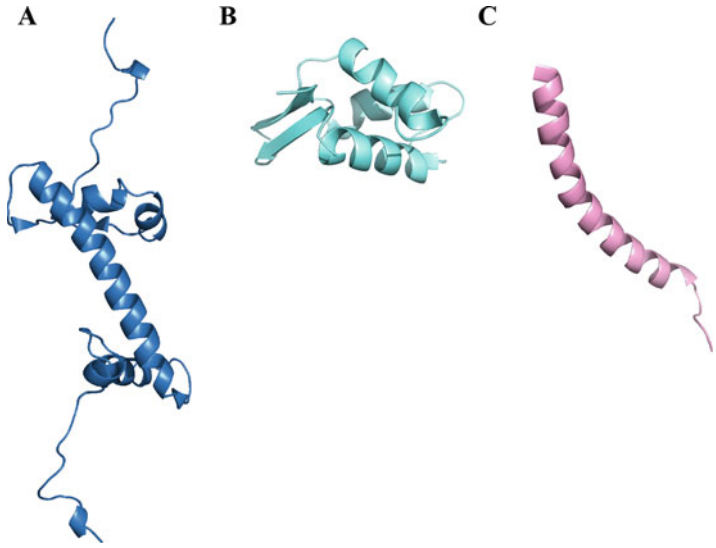

Fig. 7.1 Structure of the core histone H2A, the linker histone H1, and the antimicrobial peptide cathelicidin LL-37. (**a**) The core histone H2A contains a 'helix turn helix turn helix' central motif, named the histone fold, and an unstructured amino-terminal tail (PDB ID: 1AOI) (Luger et al. 1997). (**b**) The linker histone H1 contains a long C-terminal tail, a short N-terminal tail, and a central globular domain with a winged helix domain (PDB ID: 1GHC) (Cerf et al. 1994). (**c**) The antimicrobial peptide cathelicidin LL-37 is a linear peptide folded into an amphipathic α-helix (PDB ID: 2K6O) (Wang 2008)

of LPS (Kim et al. 2002). These histones are secreted from placenta epithelial cells into the amniotic fluid, contributing to fetal host defenses. Finally, in the Asian toad *Bufo gargarizans*, H2A is synthesized in excess of the amount required for DNA packaging, and unacetylated H2A accumulates within cytoplasmic secretory granules (Kim et al. 2000). Histones are also reported to localize to the plasma membrane, possibly for both signaling and targeted release (Watson et al. 1995).

Neutrophil extracellular traps (NETs) (Brinkmann 2004) are one of the best explored examples of histones playing a central role in combating bacterial infections. Neutrophils are the immune system's first line of defense against bacterial infections, and their prototypical function involves engulfing bacteria and other pathogens. The engulfed pathogens are subsequently killed through the fusion of the phagosome with antimicrobial, cytoplasmic granules. These granules contain an array of components that kill bacteria, including myeloperoxidase, defensins, lysozyme, proteinases (cathepsin G, elastase, and proteinase 3), bactericidal/permeability-increasing protein (BPI), NADPH oxidase, cathelicidin LL-37, lactoferrin (Segal 2005), and of course, the above-mentioned histones (Lominadze et al. 2005). However, neutrophils also have a less canonical, alternate killing pathway. The presence of virulent microorganisms (Delgado-Rizo et al. 2017), such as *Pseudomonas aeruginosa* (Dwyer et al. 2014; Floyd et al. 2016), *Escherichia coli* (Kambas et al. 2012; Yu et al. 2017), and *Staphylococcus aureus* (Pilsczek et al. 2010), stimulates a neutrophil immune response known as NETosis (Brinkmann 2004). During this process, histones are citrullinated by peptidylarginine deiminase 4 (PAD4), an enzyme essential for chromatin decondensation (Lewis et al. 2015). This enzyme converts arginine residues, which are charged, into neutral citrulline residues, resulting in a more open chromatin structure. The result is the formation of NETs, which are fibrous networks that contain cation-chelating mitochondrial and nuclear DNA and antimicrobial granular proteins (Brinkmann 2004; Keshari et al. 2012; Fuchs et

al. 2007; Papayannopoulos 2017; Brinkmann and Zychlinsky 2012; Yipp et al. 2012; Halverson et al. 2015). NETs kill and suppress the proliferation of microorganisms, though the mechanism of NET-mediated killing remains poorly understood (Papayannopoulos 2017). PAD4 knockout mice have increased susceptibility to bacterial infection due to an inability to form NETs; however, these neutrophils retain the ability to kill bacteria in other ways and mice exposed to septic conditions had comparable survival to wild-type mice (Li et al. 2010; Martinod et al. 2015).

Histones constitute a large fraction of the proteins in NETs (Brinkmann 2004). However, initially the role of histones in NETs was unclear, as histones might simply be remnant features of the neutrophils. Nonetheless, the co-localization of histones in the NET scaffold with the human antimicrobial peptide cathelicidin LL-37 (von Kockritz-Blickwede et al. 2008; Chow et al. 2010) and HNP alpha-defensins (Ganz 2003) suggests that histones could have a role as an antimicrobial agent here (Brinkmann and Zychlinsky 2007; Kawasaki and Iwamuro 2008). Importantly, antibodies against H2A and H2B eliminate NET-mediated killing of bacteria (Brinkmann 2004). Furthermore, purified H2A kill *S. flexneri*, *S. typhimurium*, and *S. aureus* bacterial cultures in 30 minutes with concentrations as low as 2 μg/mL (Brinkmann 2004). Combined, these findings suggest that histones likely to play an important anti-bacterial role.

7.3 Possible Side Effects of Histones and How to Modulate Them

The role of histone citrullination in NET antimicrobial activity is unclear. Antibacterial activity in antimicrobial peptides (AMPs) correlates with increasing arginine content (Cutrona et al. 2015), either by increasing permeabilization or improving translocation, depending on the mechanism of the AMP. PAD4-mediated citrullination of histones, which decreases the arginine content, may decrease the antimicrobial potency of histones (Li et al. 2010). PAD4 is tightly regulated, possibly to minimize the toxic effects of free histones in the host and to maximize antimicrobial activity, by controlling the potency of the histones within NETs (Neeli and Radic 2013). Given that NETs induce inflammation and are damaging to surrounding host tissue, there is a delicate balance that needs to be met in order to fight pathogen microbes without inducing high levels of damage to the host (Cheng and Palaniyar 2013).

Extracellular histone release, which can elicit toxic effects on pathogenic bacteria, can have negative side effects. Due to their ability to interact with biological membranes, extracellular histones can act as proinflammatory signals, triggering inflammatory responses and injury in the host. In contrast, AMPs are not known to serve as proinflammatory signals for the host. The presence of extracellular histones elicits the production of antibodies against histones and contributes to autoimmune and inflammatory responses in patients with systemic lupus erythematosus, neuropsychiatric lupus, and lupus nephritis (Sun et al. 2008). Histones have a pro-inflammatory role in several diseases, including sepsis, trauma, thrombosis, stroke, atherogenesis, and systemic lupus. Histones are suspected to be mediators of mortality in sepsis, contributing to endothelial dysfunction, organ failure, and death during sepsis (Xu et al. 2009). Extracellular histones are elevated following traumatic tissue injury and the ongoing rise of histone levels are predictive of mortality, suggesting the role of histones in the sterile inflammatory response following trauma may parallel the role of histones in sepsis (Kutcher et al. 2012). Elevated levels of circulating extracellular histones in trauma-associated lung injuries are associated with endothelial damage and coagulation activation (Abrams et al. 2013).

Extracellular histones contribute as a damage-associated molecular pattern (DAMP), inducing cytotoxicity and pro-inflammatory signaling through toll-like receptor (TLR) TLR2 and TLR4 (Xu et al. 2011). Extracellular histones promote thrombin generation, which triggers thrombosis (Semeraro et al. 2011). Histones bind to platelets, inducing calcium influx and platelet aggregation causing thrombocytopenia in mice within

minutes (Fuchs et al. 2011). Histones promote chemotaxis of human polymorphonuclear leukocytes, suggesting histones may modulate leukocyte activation (Nowak et al. 1990). Inflammation frequently causes cellular death, leading to the release of cellular components, such as chromatin components, potentially exacerbating the toxic effects of histones by causing the release of additional histones.

NETs and concentrations of H2A higher than 50 μg/mL induce the death of endothelial and lung epithelial cells (Saffarzadeh et al. 2012). While digestion of extracellular DNA decreases the ability of NETs to kill bacteria, DNA digestion does not have any effect on mediating cytotoxicity on epithelial and endothelial cells (Saffarzadeh et al. 2012). Thus, the controlled storage and release of histones upon bacterial infection appears critical. It is plausible that citrullination of histones decreases histone potency in NETs and provides a mechanism that balances antimicrobial activity and toxicity to the host.

In addition to playing an essential role in NET-mediated killing of microbes, histones have been shown to localize to cytoplasmic lipid droplets. Lipid droplets are lipid-rich organelles, found in all eukaryotic organisms, which dynamically regulate the storage and breakdown of lipids. Originally thought to serve solely as fat reservoirs, proteomic analyses have uncovered the presence various proteins, including histones (Cermelli et al. 2006). In early *Drosophila melanogaster* embryos, excess H2A, H2B, and H2Av histones, a variant of H2A, are recruited and bound to lipid droplets, perhaps as a means of temporary storage to avoid toxic effects introduced by free histones (Li et al. 2012). In the presence of bacterial lipopolysaccharide (LPS) or lipoteichoic acid (LTA), these lipid droplet-bound histones are released from the lipid droplets and kill bacteria *in vivo* (Anand et al. 2012). Histones bound to lipid droplets protect cells against bacteria without causing any of the harm normally associated with the presence of free histones. Purified *Drosophila* embryos lacking lipid droplet-bound histones also showed decreased survival when assaulted with bacterial species (Anand et al. 2012).

7.4 Biochemical Properties of Antimicrobial Peptides (AMPs)

Histones possess antimicrobial activity and play a critical role in the innate immune system. Histones share many biochemical similarities with AMPs, as summarized in Table 7.1. Like AMPs, histones are cationic, contain a high proportion of hydrophobic amino acids, and possess the ability to form alpha helices (Hancock and Lehrer 1998; Hancock and Sahl 2006). AMPs and individual histone proteins are comparable in size, averaging 18 kDa and 14 kDa respectively (Dürr et al. 2006; Chua et al. 2016). Additionally, both are present in NETs (Ganz 2003; Kawasaki and Iwamuro 2008). Here, we review the biochemical properties of AMPs and insights into their antimicrobial activity. However, unlike AMPs, far less is known about the antimicrobial and biochemical properties of histones.

In the first line of defense against pathogenic microbes, surface epithelial cells have a crucial role in mediating the host's innate immune response by secreting AMPs (Bals 2000; Agerberth et al. 1999; Bals et al. 1998). In addition to surface epithelial cells, these peptides are secreted by submucosal glands (Dajani et al. 2005; Chen and Fang 2004) and neutrophils (Wiesner and Vilcinskas 2010; Jann et al. 2009). AMPs are widely evolutionarily conserved and are found throughout all classes of life, including bacteria (Hassan et al. 2012), plants (Castro and Fontes 2005), fungi (Hegedüs and Marx 2013), insects (Lemaitre and Hoffmann 2007), aquatic species (Cole et al. 1997), birds (van Dijk et al. 2008), and mammals (Hancock and Diamond 2000; Selsted and Ouellette 2005; Zanetti 2004). AMPs exhibit activity against several classes of microorganisms, including bacteria (Hancock and Diamond 2000; Mahlapuu et al. 2016; Reddy et al. 2004; Marr et al. 2006), fungi (Hegedüs and Marx 2013; Cheng et al. 2012; De Lucca and Walsh 1999), viruses (Hsieh and Hartshorn 2016; Bastian and Schäfer 2001; Horne et al. 2005), protozoa (Torrent et al. 2012), and cancerous

Table 7.1 Comparison of the biochemical properties of histones and AMPs

Property	Histones	Histones				AMPs
	H1	H2A	H2B	H3	H4	
Molecular weight (kDa)	22 (Bäuerle et al. 2002)	14 (Haas et al. 1988)	14 (Haas et al. 1988)	15 (Haas et al. 1988)	11 (Haas et al. 1988)	18 (Dürr et al. 2006)
Charge	Positive due to abundance of lysine residues	Positive due to abundance of lysine residues		Positive, due to arginine residues		Positive, due to lysine and arginine residues
Structural motifs	Winged helix motif in the globular domain, short N-terminal tail, long C-terminal tail	Histone fold domain: three α-helices connected by two loops				α-helical, β-sheet, loop, or extended
Amino acid composition	High proportion of positively-charged amino acids and hydrophobic amino acids	High proportion of positively-charged amino acids and hydrophobic amino acids				High proportion of positively-charged amino acids and hydrophobic amino acids
Defining feature	Linker histone, stabilizing the chromatin fiber	Component of the histone octomer, which binds and condenses DNA				Associates with and permeabilizes membranes
Sequence diversity among species	Largely conserved, but less conserved than core histones	Largely conserved				Prominent sequence diversity

cells (Deslouches and Di 2017). In addition to their role as antimicrobial agents, AMPs direct multiple cellular processes in immune defense, including cytokine release, chemotaxis, antigen presentation, angiogenesis, and wound healing (Lai and Gallo 2009). These peptides have been proposed as alternative therapeutics due to their rapid-killing, high potency, and broad-spectrum of activity (Hancock and Sahl 2006).

AMPs tend to be small, typically less than 100 amino acids (Jenssen et al. 2006; Sang and Blecha 2008). AMPs are classified into broad groups based on secondary structure, including α-helical, β-sheet, loop, or extended (Bahar and Ren 2013). An example structure of an α-helical AMP, cathelicidin LL-37, is shown in Fig. 7.1. Most of these small peptides are cationic at physiological pH, stemming from the high proportion of the positively-charged amino acids arginine and lysine (Epand and Vogel 1999; Lehrer and Ganz 1999). Despite arginine and lysine having identical charges, arginine occurs more frequently in AMPs, indicating that guanidinium groups may be more beneficial for AMP activity than amine groups (Hristova and Wimley 2011). This may be attributed to the ability of arginine to form multiple electrostatic interactions and hydrogen bonds with lipid heads in the membrane, which may cause membrane deformation. AMP sequences also contain a high proportion of hydrophobic residues, lending to an amphipathic structure. Both the cationic and amphipathic characteristics of these AMPs allows for interactions with the anionic lipid bilayers of bacteria. Many AMPs are unstructured in free solution and fold upon insertion into a biological membrane (Yeaman 2003). The ability to associate with biological membranes is a defining feature of AMPs (Yeaman 2003; Pasupuleti et al. 2012).

The mechanism of antimicrobial action for many AMPs involves permeabilization or disruption of the microbial membrane; however, many AMPs also target DNA and protein synthesis, disrupt protein folding, or inhibit cell wall synthesis (Kumar et al. 2018; Scocchi et al. 2016; Le et al. 2017). A proposed global mechanism of action for this class of peptides is the Shai-Matsuzaki-Huang model of spontaneous translocation (Shai 1999; Shai 2002; Matsuzaki 1998; Huang 2000). The cationic and amphipathic properties of AMPs enable their binding to the surface of the bacterial membrane and inserting themselves, breaking lipid chain interactions and displacing cations that stabilize the membrane, such as Mg^{2+}. This alters membrane structure, causing membrane thinning and increasing membrane destabilization, in addition to increasing surface tension. At AMP concentrations above a threshold, the high level of surface tension causes permeabilization of the membrane by the formation of transient pores. This action enables additional peptides to enter the interior of the cell. If the AMP concentration is below that which will cause the membrane to fully collapse, overall membrane integrity is preserved. Virtually all AMPs, apart from insect apidaecin-type peptides, have high membrane affinity and induce a certain level of membrane perturbation (Casteels and Tempst 1994). An alternate mechanism for proline-rich groups of AMPs is to exploit the inner membrane protein SbmA to penetrate *E. coli* (Mattiuzzo et al. 2007).

Despite similarities in the cationic and amphipathic nature across AMPs, there is prominent sequence diversity, allowing for some AMPs to interact with intracellular targets or affect key cellular processes, either in addition to, or instead of, membrane permeabilization. Because of their strong positive charge, most AMPs permeabilize the membrane at concentrations above the minimum inhibitory concentration (MIC) *in vitro*, indicating that membrane permeabilization is a secondary effect of most AMPs (Patrzykat et al. 2002; Podda et al. 2006). Peptide concentrations well above the MIC or high peptide:lipid ratios can falsely indicate a membrane lytic mechanism and mask true intracellular effects. For instance, pleurocidin-derived AMPs inhibit RNA and protein synthesis at the MIC without affecting membrane integrity; however, at ten times the MIC, cells depolarize and membranes are disrupted (Patrzykat et al. 2002). Under conditions that support bacterial killing, human neutrophil peptide defensin [HNP]-1 penetrates the outer and inner membranes of *E. coli* (Lehrer et al. 1989). Upon penetration, bacterial synthesis of DNA, RNA, and protein stops. Inhibition of cy-

tokinesis has been seen with the alpha helical peptide cathelin-related AMP (CRAMP), the mouse ortholog of cathelicidin LL-37. CRAMP impairs *Salmonella typhimurium* cell division *in vitro* and in macrophage-phagocytized bacteria, resulting in long, filamentous structures (Rosenberger et al. 2004).

Mechanisms of cell death via AMPs can be elucidated by measuring the delay between cell death, measured by an inhibition of colony formation, and membrane permeability changes. AMPs that have a lytic mechanism of action have these two events occur rapidly and concurrently, whereas non-lytic mechanisms of cell death are characterized by a delay between cell death and changes in membrane permeability. Increases in permeability as a secondary effect after bacterial death has been observed with some classic antibiotics, including ceftazidime, ciprofloxacin, and gentamicin (Walberg et al. 1997; Wickens et al. 2000).Various intracellular AMP mechanisms of action have been studied, but the degree to which membrane permeabilization or intracellular mechanisms have a role in cell death are often not investigated. Given the negative charge of DNA and RNA, it is not surprising that positively-charged AMPs bind to nucleic acid polymers *in vitro*.

The similar biochemical properties between AMPs, such as cathelicidin LL-37, and histone proteins have led to the conclusion that the molecules serve redundant functions in their antimicrobial activities (Brinkmann and Zychlinsky 2012). Whether and AMPs have redundant or independent functions has not been fully explored.

7.5 The Role of Histones and Histone Fragments as Antimicrobial Agents

7.5.1 Full-Length Histones Are Antimicrobial

Full-length histones from a range of species have antimicrobial activity, including the rainbow trout, shrimp, and Atlantic salmon. Acetylated H2A is found in skin secretions of the rainbow trout *Oncorhynchus mykiss* (Fernandes et al. 2002). Reconstitution of H2A within the membrane perturbs the membrane, without forming ion channels, supporting a non-pore-forming mechanism of action. The core histone proteins, H2A, H2B, H3, and H4, are found in the blood cells of the invertebrate Pacific white shrimp (*Litopenaeus vannamei*) (Patat et al. 2004). These proteins have high sequence identity to the histones of other species, and the N-terminus of H2A have sequence identity to the antimicrobial histone peptides buforin I, parasin, and hopposin. Liver, intestine, and stomach extracts from healthy Atlantic salmon (*Salmo salar*) contain an antimicrobial protein identified as H1 (Richards et al. 2001).

Histones from *Gallus gallus* and mice also have antimicrobial activity. Sequences of bactericidal proteins from mice macrophages activated by gamma interferon have similarities to H1 and H2B histone sequences (Kawasaki et al. 2008). H2A, H2B.V, and an H2B C-terminal fragment identified in the liver extracts of White Leghorn hens (*Gallus gallus*) and histones from chicken erythrocytes have antimicrobial activity against Gram-negative and Gram-positive bacteria (Li et al. 2007). Additionally, histones from chicken erythrocytes bind to cell wall components, including lipopolysaccharide (LPS) and lipoteichoic acid (LTA) (Rose-Martel and Hincke 2014).

Numerous reports indicate antimicrobial activity of histones in humans. H1 and its fragments are present in human terminal ileal mucosal samples and the cytoplasm of villus epithelial cells and showed antimicrobial activity against *Salmonella typhimurium*. *In vitro* culturing of villus epithelial cells from the basement membrane releases antimicrobial H1 proteins while the cells undergo programmed cell death (Rose et al. 1998). A shotgun proteomics approach revealed the presence of core histones (H2A, H2B, H3, H4) and linker histones (H1) in human hair shafts and extracts of partially-purified histones kill *E. coli* in a radial diffusion assay (Adav et al. 2018). The antimicrobial action of sebocytes from the SEB-1 cell line against *S. aureus* has

been attributed to histone H4. Here, synergy between histones and free fatty acids in human sebum are responsible for the antimicrobial effects. As cells in the sebaceous gland secrete their cellular contents into the sebum through holocrine secretion, a secretion mode involving plasma membrane rupture and cellular death, sebocytes use histones as antimicrobial agents released as a sebum component. Analysis of the antimicrobial activity and polypeptide composition of meconium identified histones H2 and H4 (Kai-Larsen et al. 2007).

7.5.2 Histone-Derived Peptide Fragments Are also Antimicrobial

Peptides that have antimicrobial activity are formed from the N-terminus cleavage of full-length histones, although this cleavage is not known to occur in humans. These are considered to be AMPs and have been extensively observed in non-mammalian species. The synthesis of inactive proteins requiring processing to function properly is a common tactic used to prevent off-target harmful effects to the host. Classic examples in the antimicrobial realm are antimicrobial peptides generated from trypsin-mediated cleavage of lactoferrin and neutrophil elastase-mediated cleavage of thrombin (Kuwata et al. 1998; Papareddy et al. 2010). Endogenous proteases are implicated in the production of AMPs from lysine-rich histones. Following cleavage, AMP antimicrobial activity can be attributed to the amphipathic secondary structure with net positive charge, allowing for membrane binding, membrane permeabilization, and binding to nucleic acids (Hancock and Lehrer 1998). Here, we provide a summary of AMPs that have sequence similarity to the N-terminus of the different histones.

7.5.3 Histone H1 Homologs

AMPs with sequence similarity to H1 are present in Atlantic salmon, rainbow trout, and Coho salmon. In *Salmo salar*, the Atlantic salmon, a 30-residue N-terminally acetylated peptide derived from H1 is present in the skin mucus and has activity against both Gram-negative and Gram-positive bacteria. Isomerization of the proline peptide bond is crucial for activity, leading to increased structure, condensation, and rigidity of the peptide (Luders et al. 2005). A potent antimicrobial peptide in *O. mykiss* (Fernandes 2004) with sequence identity to the H1 induces destabilization of planar lipid bilayers. Blood and mucus antimicrobial fractions of Coho salmon (*Oncorhynchus kisutch*) have sequence identity with the N-terminus of H1. Synthetic peptides showed no antimicrobial effects, but showed synergy with the flounder peptide pleurocidin and lysozyme (Patrzykat et al. 2001).

7.5.4 Histone H2A and H2B Homologs

There are several known AMPs that have sequence similarity with histone H2A. Parasin I is a 19-amino acid antimicrobial peptide secreted into the epithelial mucosal layer by the catfish *Parasilurus asotus* in response to epidermal injury (Park et al. 1998a). The AMP shows high homology to the N-terminal region of H2A and is thought to be produced by cathepsin D-directed H2A proteolysis upon injury (Cho et al. 2002). The basic N-terminal residue is essential for membrane-binding, and the α-helical structure is necessary for membrane-permeabilizing activity (Koo et al. 2008).

Buforin I is a 39-amino acid AMP isolated from the Asian toad *Bufo bufo gargarizans*, composed of the N-terminal parasin and buforin II. Upon pepsin-mediated proteolysis of the Tyr^{39}-Ala (Cheng and Palaniyar 2013) H2A bond in the cytoplasm of gastric gland cells, buforin I is secreted into the gastric lumen where it adheres to the stomach mucosal surface and forms a protective antimicrobial coating (Kim et al. 2000). In contrast, unacetylated H2A is located in the cytoplasm of gastric gland cells, suggesting a portion of cytoplasmic unacetylated H2A is secreted into the lumen and undergoes pepsin processing,

while another portion of H2A is acetylated and targeted for nuclear translocation.

Buforin II (BF2) is a 21-amino acid peptide derived from endoproteinase Lys-C treatment of buforin I, which displays increased antimicrobial activity compared to buforin I and adopts a helix-hinge-helix structure in 50% trifluoroenthanol (Park et al. 1996; Yi et al. 1996). Both buforin I and buforin II share sequence identity to the N-terminus of H2A (Kim et al. 1996). Circular dichroism measurements of equipotent Trp-substituted peptides indicate that BF2 binds selectively to liposomes composed of acidic phospholipids and has weak membrane permeabilization activity when compared to magainin 2, a membrane-permeabilizing *Xenopus laevis* antimicrobial peptide (Kobayashi et al. 2000). Instead, BF2 is efficiently translocated across lipid bilayers, supporting an intracellular mechanism of bacterial death by nucleic acid binding. The Pro (Wang 2008) residue is structurally responsible for introducing a kink in the α helix and disturbing the helical structure (Kobayashi et al. 2004). To translocate the lipid bilayer, BF2 forms a toroidal pore that is destabilized by the electrostatic repulsion that accompanies five basic amino acids in close proximity, promoting translocation of the peptide across the bacterial cell membrane. In membranes, amidated BF2 adopts a poorly helical structure in membranes, mimicking the composition of *E. coli*, and binds to duplex DNA causing condensation (Lan et al. 2010).

The α-helical structure, which directs cell-penetration, has been shown to be critical in determining antimicrobial efficacy (Park et al. 2000). The helix-hinge-helix domain enables BF2 to enter bacterial cells without inducing membrane disruption, where the AMP binds to intracellular nucleic acids and inhibit cellular functioning (Park et al. 1998b). Although *in vitro* binding of BF2 to nucleic acid has been shown, it is unknown whether this interaction is directed or a result of opposite charged interactions. Further characterization of the nucleic acid binding property of BF2 indicates that the R^2 and R^{20} side chains of BF2 form interactions with DNA that are stronger than non-specific electrostatic interactions, and that the substitution of the basic residues with alanine decreases the antimicrobial activity of BF2 (Uyterhoeven et al. 2008).

Hipposin is a potent 51-residue antimicrobial peptide isolated from the skin mucus of Atlantic halibut *Hippoglossus hippoglossus L* (Birkemo et al. 2003). This AMP has 98% sequence similarity to the N-terminus of histone H2A from rainbow trout, and has sequence similarities to both parasin and BF2. The AMP was shown to kill bacteria through membrane permeabilization, as evidenced by increased propidium iodide fluorescence intracellularly following peptide exposure and localization of AlexaFluor conjugates around the cellular membrane (Bustillo et al. 2014). The localization of fluorescence around the cell membrane, with low fluorescence intracellularly, is similar to the fluorescence pattern depicted by parasin, another histone-derived peptide that causes permeabilization (Koo et al. 2008). The N-terminal parasin domain of hipposin is necessary for membrane permeabilization, as peptides lacking the parasin domain show translocation of the membrane, without permeabilization. The C-terminal domain of hipposin, HipC, is cell-penetrating, but shows no measurable antimicrobial activity.

A combination of molecular dynamics (MD) simulations and DNA binding affinity experiments provide support for BF2 forming specific interactions with DNA (Uyterhoeven et al. 2008). Additionally, through the use of BF2 variants, the affinity of the peptide for DNA has been correlated with increased antimicrobial activity. Additional MD simulations, along with electrostatic analysis and nucleic acid binding experiments, on buforin II and DesHDAP1, a designed histone-derived AMP thought to share a similar structure and mechanism of action with buforin II, support a sequence-independent method of AMP binding to DNA (Sim et al. 2017). Instead of peptide binding with sequence specificity, peptide-phosphate interactions are thought to be the predominant basis of AMP binding to DNA. As such, arginine residues are shown to have greater antimicrobial activity than lysine residues, possibly due to increased interactions with DNA; however, higher arginine composition could also influence AMP-membrane interactions.

7.5.5 H3 and H4 Homologs

No known natural fragments with similarity to H3 have been identified. Histogrannin, a slightly modified C-terminal 15 amino acid fragment showing similarities to the C-terminal end of H4 has been identified from bovine adrenal medulla (Lemaire et al. 1993). The fragment, which is synthesized from a separate mRNA variant, is an antagonist of N-methyl-D-aspartate (NMDA) receptor activity. Histogrannin has antimicrobial activity against Gram-negative and Gram-positive bacteria and is thought to function through inhibition of ATP-dependent DNA gyrase, a mechanism similar to quinolone antibiotics (Lemaire et al. 2008).

7.6 Insights into the Mechanism of Histone-Mediated Killing of Bacteria

The findings from histone-derived AMPs suggest that part of the antimicrobial activity of histones is achieved through membrane permeabilization, as depicted in Fig. 7.2. The linker histone H1 and four core histones from calf thymus bind LPS present on the outer membrane. All histones except H4 have affinities for LPS that are greater than that of the antibiotic polymyxin B (Augusto et al. 2003). The strong affinity of histones for phosphodiester bonds enables histone binding to DNA and facilitates proper chromatin structure formation. However, this affinity may extend to the phosphodiester bonds in phospholipids, facilitating the integration of histones into membranes. The strong positive charge of histones from *Plasmodium falciparum*, a unicellular protozoan parasite that causes malaria in humans, increases membrane permeability in human endothelial cells and induces IL-8 production at concentrations higher than 50 μg/mL (Gillrie et al. 2012). The negatively-charged glycoaminoglycans (GAGs) heparan sulfate and hyaluronan protect CHO cells from histone-induced cytotoxicity, supporting the notion that glycocalyx, the negatively-charged polysaccharide network that protects cells from bacteria, may further mitigate the effects of histones by preventing membrane insertion (Chaaban et al. 2015). The strong pos-

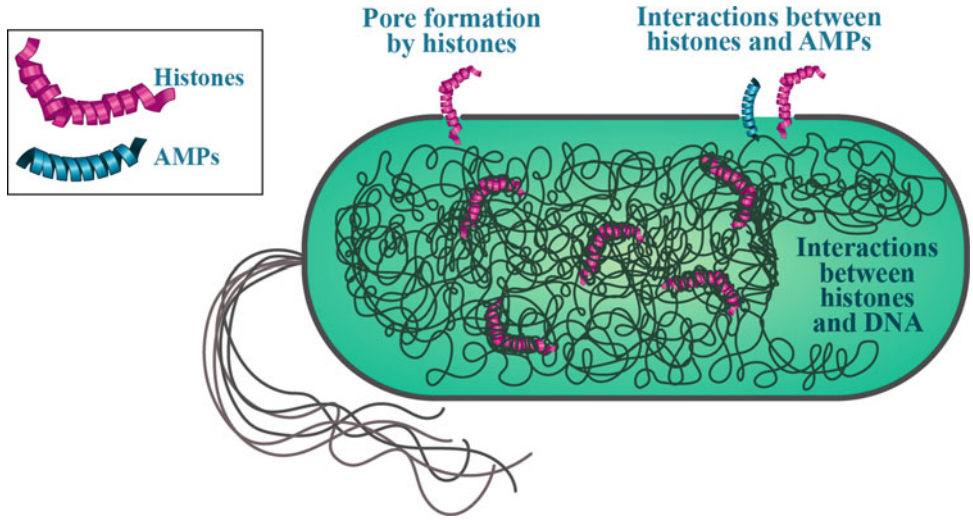

Fig. 7.2 Potential mechanisms of bacterial killing by histones. Histones have high affinity for LPS and histone-derived peptides induce membrane permeabilization. Full-length histones thus may bind to bacterial membranes, disrupting the membrane and forming pores. The high affinity of histones for phosphodiester bonds, which enables histones to bind and condense DNA, suggests that part of the antimicrobial activity of histones may involve interactions between histones and microbial DNA. Since histones alone show weak antimicrobial activity *in vivo*, the antimicrobial activity of histones may be dependent upon interactions with AMPs or other antimicrobial agents

itive charge of histones may induce permeability in membranes across of a broad range of organisms including bacteria. Divalent cations, such as Mg^{2+}, function as cationic bridges between adjacent phosphates on LPS. Histones may compete with divalent cations, compromising LPS cross-bridges, and destroying the outer membrane integrity.

Other work suggests that the antimicrobial mechanism of histones occurs following entry into the bacterium and that the target is cytoplasmic (Fig. 7.2). An active fragment of H2B from *R. schlegelli* is thought to be generated via digestion by the bacterial outer membrane protease T (OmpT) (Kawasaki et al. 2008). This fragment of H2B can penetrate the cell membrane of OmpT-expressing *E. coli*, but not *ompT*-deleted *E. coli*, accumulate in the cytoplasm, and inhibit cell function, presumably by binding to nucleic acids. In the absence of OmpT, H2B is unable to penetrate the membrane, and remains localized on the exterior of the bacteria (Kawasaki et al. 2008). Consistent with requirement for H2B translocation into the cell, the MIC values for H2B, H3, and H4 significantly increase in the absence of OmpT (Tagai et al. 2011). The antimicrobial effects observed at higher concentrations of histones may be due to the secondary effect of histones on increasing membrane permeation, and not the primary mechanism by which lysine-rich histones kill bacteria. In addition, lysine-rich (H1, H2A, H2B) and arginine-rich (H3, H4) histones likely kill bacteria using distinct mechanisms. While H2B penetrates *E. coli* membranes and enters the cytoplasmic space, H3 and H4 remain localized on the cell surface, causing membrane blebbing (Tagai et al. 2011).

7.7 Conclusion and Future Developments

Despite being originally proposed to function as antimicrobial agents (Miller et al. 1942; Hirsch 1958), and having an essential role in mammalian innate immune responses (Brinkmann 2004), little is known about how histones function as antimicrobial agents. Complicating matters is that studies on the antimicrobial activity of histones typically utilize low-ionic solutions and buffers that are not physiologically relevant (Brinkmann 2004; Anand et al. 2012; Cermelli et al. 2006; Hancock and Sahl 2006; Patat et al. 2004; Kawasaki et al. 2008; Luders et al. 2005; Park et al. 1998a; Birkemo et al. 2003; Tagai et al. 2011; Urban et al. 2009; Kahlenberg et al. 2013; Cho et al. 2009; Dorrington et al. 2011; Morita et al. 2013). In physiologically relevant conditions, histones are far less effective at killing bacteria (Anand et al. 2012; Hancock and Sahl 2006), and require high, unphysiological concentrations of histones (120 μg/mL) (Anand et al. 2012; Tagai et al. 2011; Morita et al. 2013). Furthermore, some studies use concentrations of histones well above the MIC (Tagai et al. 2011; Morita et al. 2013). As noted above, peptide concentrations in excess of the MIC may render bacteria susceptible to secondary mechanisms of histones through membrane permeabilization (Patrzykat et al. 2002; Podda et al. 2006).

It is plausible that since histones show weak antimicrobial activity *in vivo*, the antimicrobial activity of histones is dependent upon interactions with other immune system mechanisms or components (Fig. 7.2) (Elsbach et al. 1994). Synergy between antibacterial peptides released from activated neutrophils has been reported previously. In the absence of salt, defensins show antibacterial activity in a dose-dependent manner; however, antimicrobial activity is lost in the presence of salt (Nagaoka et al. 2000). Defensins exhibit synergy with cathelicidins in the killing of *E. coli* and *S. aureus* (Nagaoka et al. 2000). There have also been reports of histone H1 fragments having synergistic antimicrobial effects with lysozyme, lysozyme-containing extracts from *O. kisutch*, and pleurocidin against *Vibrio anguillarum* and *Aeromonas salmonicida* (Patrzykat et al. 2001). Future experiments will need to focus on mechanistic details of histones and will need to consider their role in the context of the immune system as a whole, not as a sole antimicrobial agent.

References

Abrams ST et al (2013) Circulating histones are mediators of trauma-associated lung injury. Am J Respir Crit Care Med 187:160–169

Adav SS et al (2018) Studies on the proteome of human hair – identification of histones and Deamidated keratins. Sci Rep 8:1599

Agerberth B et al (1999) Antibacterial components in Bronchoalveolar lavage fluid from healthy individuals and sarcoidosis patients. Am J Respir Crit Care Med 160:283–290

Allan J, Hartman PG, Crane-Robinson C, Aviles FX (1980) The structure of histone H1 and its location in chromatin. Nature 288:675–679

Anand P et al (2012) A novel role for lipid droplets in the organismal antibacterial response. elife 1:e00003

Augusto LA et al (2003) Histones: a novel class of lipopolysaccharide-binding molecules †. Biochemistry 42:3929–3938

Bahar A, Ren D (2013) Antimicrobial Peptides. Pharmaceuticals 6:1543–1575

Bals R (2000) Epithelial antimicrobial peptides in host defense against infection. Respir Res 1:5

Bals R, Wang X, Zasloff M, Wilson JM (1998) The peptide antibiotic LL-37/hCAP-18 is expressed in epithelia of the human lung where it has broad antimicrobial activity at the airway surface. Proc Natl Acad Sci U S A 95:9541–9546

Bastian A, Schäfer H (2001) Human alpha-defensin 1 (HNP-1) inhibits adenoviral infection in vitro. Regul Pept 101:157–161

Bäuerle M, Doenecke D, Albig W (2002) The requirement of H1 histones for a heterodimeric nuclear import receptor. J Biol Chem 277:32480–32489

Birkemo GA, Lüders T, Andersen Ø, Nes IF, Nissen-Meyer J (2003) Hipposin, a histone-derived antimicrobial peptide in Atlantic halibut (Hippoglossus hippoglossus L.). Biochim Biophys Acta Proteins Proteomics 1646:207–215

Brinkmann V (2004) Neutrophil extracellular traps kill Bacteria. Science 303:1532–1535

Brinkmann V, Zychlinsky A (2007) Beneficial suicide: why neutrophils die to make NETs. Nat Rev Microbiol 5:577–582

Brinkmann V, Zychlinsky A (2012) Neutrophil extracellular traps: is immunity the second function of chromatin? J Cell Biol 198:773–783

Bustillo ME et al (2014) Modular analysis of hipposin, a histone-derived antimicrobial peptide consisting of membrane translocating and membrane permeabilizing fragments. Biochim Biophys Acta Biomembr 1838:2228–2233

Casteels P, Tempst P (1994) Apidaecin-type peptide antibiotics function through a non-poreforming mechanism involving stereospecificity. Biochem Biophys Res Commun 199:339–345

Castro MS, Fontes W (2005) Plant defense and antimicrobial peptides. Protein Pept Lett 12:13–18

Cerf C et al (1994) Homo- and Heteronuclear two-dimensional NMR studies of the globular domain of histone H1: full assignment, tertiary structure, and comparison with the globular domain of histone H5. Biochemistry 33:11079–11086

Cermelli S, Guo Y, Gross SP, Welte MA (2006) The lipid-droplet proteome reveals that droplets are a protein-storage depot. Curr Biol 16:1783–1795

Chaaban H et al (2015) Inter- inhibitor protein and its associated glycosaminoglycans protect against histone-induced injury. Blood 125:2286–2296

Chen P-H, Fang S-Y (2004) The expression of human antimicrobial peptide LL-37 in the human nasal mucosa. Am J Rhinol 18:381–385

Cheng OZ, Palaniyar N (2013) NET balancing: a problem in inflammatory lung diseases. Front Immunol 4:1

Cheng S-C, Joosten LAB, Kullberg B-J, Netea MG (2012) Interplay between Candida albicans and the mammalian innate host defense. Infect Immun 80:1304–1313

Cho JH et al (2002) Cathepsin D produces antimicrobial peptide parasin I from histone H2A in the skin mucosa of fish. FASEB J 16:429–431

Cho JH, Sung BH, Kim SC (2009) Buforins: histone H2A-derived antimicrobial peptides from toad stomach. Biochim Biophys Acta Biomembr 1788:1564–1569

Chow OA et al (2010) Statins enhance formation of phagocyte extracellular traps. Cell Host Microbe 8:445–454

Chua EYD et al (2016) 3.9 Å structure of the nucleosome core particle determined by phase-plate cryo-EM. Nucleic Acids Res 44:8013–8019

Cole AM, Weis P, Diamond G (1997) Isolation and characterization of pleurocidin, an antimicrobial peptide in the skin secretions of winter flounder. J Biol Chem 272:12008–12013

Cutrona KJ, Kaufman BA, Figueroa DM, Elmore DE (2015) Role of arginine and lysine in the antimicrobial mechanism of histone-derived antimicrobial peptides. FEBS Lett 589:3915–3920

Dajani R et al (2005) Lysozyme secretion by submucosal glands protects the airway from bacterial infection. Am J Respir Cell Mol Biol 32:548–552

De Lucca AJ, Walsh TJ (1999) Antifungal peptides: novel therapeutic compounds against emerging pathogens. Antimicrob Agents Chemother 43:1–11

DeLange RJ, Smith EL (1971) Histones: structure and function. Annu Rev Biochem 40:279–314

Delgado-Rizo V et al (2017) Neutrophil extracellular traps and its implications in inflammation: an overview. Front Immunol 8:81

Deslouches B, Di YP (2017) Antimicrobial peptides with selective antitumor mechanisms: prospect for anticancer applications. Oncotarget 8:46635–46651

Dorrington T, Villamil L, Gómez-chiarri M (2011) Upregulation in response to infection and antibacterial activity of oyster histone H4. Fish Shellfish Immunol 30:94–101

Dürr UHN, Sudheendra US, Ramamoorthy A (2006) LL-37, the only human member of the cathelicidin fam-

ily of antimicrobial peptides. Biochim Biophys Acta Biomembr 1758:1408–1425
Dwyer M et al (2014) Cystic fibrosis sputum DNA has NETosis characteristics and neutrophil extracellular trap release is regulated by macrophage migration-inhibitory factor. J Innate Immun 6:765–779
Elsbach P, Weiss J, Levy O (1994) Integration of antimicrobial host defenses: role of the bactericidal/permeability-increasing protein. Trends Microbiol 2:324–328
Epand RM, Vogel HJ (1999) Diversity of antimicrobial peptides and their mechanisms of action. Biochim Biophys Acta 1462:11–28
Fernandes J (2004) Isolation and characterisation of oncorhyncin II, a histone H1-derived antimicrobial peptide from skin secretions of rainbow trout, *Oncorhynchus mykiss*. Dev Comp Immunol 28:127–138
Fernandes JMO, Kemp GD, Molle MG, Smith VJ (2002) Anti-microbial properties of histone H2A from skin secretions of rainbow trout, Oncorhynchus mykiss. Biochem J 368:611–620
Fleming A (1922) On a remarkable Bacteriolytic element found in tissues and secretions. Proc R Soc B Biol Sci 93:306–317
Fleming A (1980) Classics in infectious diseases: on the antibacterial action of cultures of a penicillium, with special reference to their use in the isolation of B. influenzae by Alexander Fleming, Reprinted from the British Journal of Experimental Pathology 10:226–236, 1929. Rev Infect Dis 2:129–139
Floyd M et al (2016) Swimming motility mediates the formation of neutrophil extracellular traps induced by flagellated Pseudomonas aeruginosa. PLoS Pathog 12:e1005987
Fuchs TA et al (2007) Novel cell death program leads to neutrophil extracellular traps. J Cell Biol 176:231–241
Fuchs TA, Bhandari AA, Wagner DD (2011) Histones induce rapid and profound thrombocytopenia in mice. Blood 118:3708–3714
Ganz T (2003) Defensins: antimicrobial peptides of innate immunity. Nat Rev Immunol 3:710–720
Gillrie MR et al (2012) Plasmodium falciparum histones induce endothelial Proinflammatory response and barrier dysfunction. Am J Pathol 180:1028–1039
Haas AL, Bright PM, Jackson VE (1988) Functional diversity among putative E2 isozymes in the mechanism of ubiquitin-histone ligation. J Biol Chem 263:13268–13275
Halverson TWR, Wilton M, Poon KKH, Petri B, Lewenza S (2015) DNA is an antimicrobial component of neutrophil extracellular traps. PLoS Pathog 11:e1004593
Hancock REW, Diamond G (2000) The role of cationic antimicrobial peptides in innate host defences. Trends Microbiol 8:402–410
Hancock REW, Lehrer R (1998) Cationic peptides: a new source of antibiotics. Trends Biotechnol 16:82–88
Hancock REW, Sahl H-G (2006) Antimicrobial and host-defense peptides as new anti-infective therapeutic strategies. Nat Biotechnol 24:1551–1557
Hassan M, Kjos M, Nes IF, Diep DB, Lotfipour F (2012) Natural antimicrobial peptides from bacteria: characteristics and potential applications to fight against antibiotic resistance. J Appl Microbiol 113:723–736
Hegedüs N, Marx F (2013) Antifungal proteins: more than antimicrobials? Fungal Biol Rev 26:132–145
Hirsch JG (1958) Bactericidal action of histone. J Exp Med 108:925–944
Horne WS et al (2005) Antiviral cyclic d,l-α-peptides: targeting a general biochemical pathway in virus infections. Bioorg Med Chem 13:5145–5153
Hristova K, Wimley WC (2011) A look at arginine in membranes. J Membr Biol 239:49–56
Hsieh I-N, Hartshorn K (2016) The role of antimicrobial peptides in influenza virus infection and their potential as antiviral and Immunomodulatory therapy. Pharmaceuticals 9:53
Huang HW (2000) Action of antimicrobial peptides: two-state model †. Biochemistry 39:8347–8352
Jann NJ et al (2009) Neutrophil antimicrobial defense against *Staphylococcus aureus* is mediated by phagolysosomal but not extracellular trap-associated cathelicidin. J Leukoc Biol 86:1159–1169
Jenssen H, Hamill P, Hancock REW (2006) Peptide Antimicrobial Agents. Clin Microbiol Rev 19:491–511
Kahlenberg JM, Carmona-Rivera C, Smith CK, Kaplan MJ (2013) Neutrophil extracellular trap-associated protein activation of the NLRP3 Inflammasome is enhanced in lupus macrophages. J Immunol 190:1217–1226
Kai-Larsen Y et al (2007) Antimicrobial components of the neonatal gut affected upon colonization. Pediatr Res 61:530–536
Kambas K et al (2012) Autophagy mediates the delivery of Thrombogenic tissue factor to neutrophil extracellular traps in human Sepsis. PLoS One 7:e45427
Kawasaki H, Iwamuro S (2008) Potential roles of histones in host defense as antimicrobial agents. Infect Disord Drug Targets 8:195–205
Kawasaki H, Koyama T, Conlon JM, Yamakura F, Iwamuro S (2008) Antimicrobial action of histone H2B in Escherichia coli: evidence for membrane translocation and DNA-binding of a histone H2B fragment after proteolytic cleavage by outer membrane proteinase T. Biochimie 90:1693–1702
Keshari RS et al (2012) Cytokines induced neutrophil extracellular traps formation: implication for the inflammatory disease condition. PLoS One 7:e48111
Kim HS, Park CB, Kim MS, Kim SC (1996) cDNA cloning and characterization of Buforin I, an antimicrobial peptide: a cleavage product of histone H2A. Biochem Biophys Res Commun 229:381–387
Kim HS et al (2000) Pepsin-mediated processing of the cytoplasmic histone H2A to strong antimicrobial peptide Buforin I. J Immunol 165:3268–3274
Kim HS et al (2002) Endotoxin-neutralizing antimicrobial proteins of the human placenta. J Immunol 168:2356–2364
Kobayashi S, Takeshima K, Park CB, Kim SC, Matsuzaki K (2000) Interactions of the novel antimicrobial peptide

Buforin 2 with lipid bilayers: Proline as a translocation promoting factor. Biochemistry 39:8648–8654
Kobayashi S et al (2004) Membrane translocation mechanism of the antimicrobial peptide Buforin 2. Biochemistry 43:15610–15616
Koo YS et al (2008) Structure–activity relations of parasin I, a histone H2A-derived antimicrobial peptide. Peptides 29:1102–1108
Kumar P, Kizhakkedathu J, Straus S (2018) Antimicrobial peptides: diversity, mechanism of action and strategies to improve the activity and biocompatibility in vivo. Biomol Ther 8:4
Kutcher ME et al (2012) Extracellular histone release in response to traumatic injury: implications for a compensatory role of activated protein C. J Trauma Acute Care Surg 73:1389–1394
Kuwata H, Yip T-T, Yip CL, Tomita M, Hutchens TW (1998) Bactericidal domain of Lactoferrin: detection, quantitation, and characterization of Lactoferricin in serum by SELDI affinity mass spectrometry. Biochem Biophys Res Commun 245:764–773
Lai Y, Gallo RL (2009) AMPed up immunity: how antimicrobial peptides have multiple roles in immune defense. Trends Immunol 30:131–141
Lan Y et al (2010) Structural contributions to the intracellular targeting strategies of antimicrobial peptides. Biochim Biophys Acta Biomembr 1798:1934–1943
Le C-F, Fang C-M, Sekaran SD (2017) Intracellular targeting mechanisms by antimicrobial peptides. Antimicrob Agents Chemother 61:e02340–e02316. https://doi.org/10.1128/aac/61/4/e02340-16.atom
Lehrer RI, Ganz T (1999) Antimicrobial peptides in mammalian and insect host defence. Curr Opin Immunol 11:23–27
Lehrer RI et al (1989) Interaction of human defensins with Escherichia coli. Mechanism of bactericidal activity. J Clin Investig 84:553–561
Lemaire S et al (1993) Isolation and characterization of histogranin, a natural peptide with NMDA receptor antagonist activity. Eur J Pharmacol 245:247–256
Lemaire S et al (2008) Antimicrobial effects of H4-(86-100), histogranin and related compounds–possible involvement of DNA gyrase. FEBS J 275:5286–5297
Lemaitre B, Hoffmann J (2007) The host defense of *Drosophila melanogaster*. Annu Rev Immunol 25:697–743
Lewis HD et al (2015) Inhibition of PAD4 activity is sufficient to disrupt mouse and human NET formation. Nat Chem Biol 11:189–191
Li G-H, Mine Y, Hincke MT, Nys Y (2007) Isolation and characterization of antimicrobial proteins and peptide from chicken liver. J Pept Sci 13:368–378
Li P et al (2010) PAD4 is essential for antibacterial innate immunity mediated by neutrophil extracellular traps. J Exp Med 207:1853–1862
Li Z et al (2012) Lipid droplets control the maternal histone supply of Drosophila embryos. Curr Biol 22:2104–2113
Lominadze G et al (2005) Proteomic analysis of human neutrophil granules. Mol Cell Proteomics 4:1503–1521
Luders T, Birkemo GA, Nissen-Meyer J, Andersen O, Nes IF (2005) Proline conformation-dependent antimicrobial activity of a Proline-rich histone H1 N-terminal peptide fragment isolated from the skin mucus of Atlantic Salmon. Antimicrob Agents Chemother 49:2399–2406
Luger K, Mäder AW, Richmond RK, Sargent DF, Richmond TJ (1997) Crystal structure of the nucleosome core particle at 2.8 Å resolution. Nature 389:251–260
Mahlapuu M, Håkansson J, Ringstad L, Björn C (2016) Antimicrobial peptides: an emerging category of therapeutic agents. Front Cell Infect Microbiol 6:194
Marr A, Gooderham W, Hancock R (2006) Antibacterial peptides for therapeutic use: obstacles and realistic outlook. Curr Opin Pharmacol 6:468–472
Martinod K et al (2015) PAD4-deficiency does not affect bacteremia in polymicrobial sepsis and ameliorates endotoxemic shock. Blood 125:1948–1956
Matsuzaki K (1998) Magainins as paradigm for the mode of action of pore forming polypeptides. Biochim Biophys Acta 1376:391–400
Mattiuzzo M et al (2007) Role of the Escherichia coli SbmA in the antimicrobial activity of proline-rich peptides. Mol Microbiol 66:151–163
Miller BF, Abrams R, Dorfman A, Klein M (1942) Antibacterial properties of protamine and histone. Science 96:428–430
Morita S, Tagai C, Shiraishi T, Miyaji K, Iwamuro S (2013) Differential mode of antimicrobial actions of arginine-rich and lysine-rich histones against gram-positive Staphylococcus aureus. Peptides 48:75–82
Nagaoka I, Hirota S, Yomogida S, Ohwada A, Hirata M (2000) Synergistic actions of antibacterial neutrophil defensins and cathelicidins. Inflamm Res 49:73–79
Neeli I, Radic M (2013) Opposition between PKC isoforms regulates histone deimination and neutrophil extracellular chromatin release. Front Immunol 4:38
Nowak D, Piasecka G, Hrabec E (1990) Chemotactic activity of histones for human polymorphonuclear leukocytes. Exp Pathol 40:111–116
Papareddy P et al (2010) Proteolysis of human thrombin generates novel host defense peptides. PLoS Pathog 6:e1000857
Papayannopoulos V (2017) Neutrophil extracellular traps in immunity and disease. Nat Rev Immunol 18:134–147
Park CB, Kim MS, Kim SC (1996) A novel antimicrobial peptide from Bufo bufo gargarizans. Biochem Biophys Res Commun 218:408–413
Park IY, Park CB, Kim MS, Kim SC (1998a) Parasin I, an antimicrobial peptide derived from histone H2A in the catfish, *Parasilurus asotus*. FEBS Lett 437:258–262
Park CB, Kim HS, Kim SC (1998b) Mechanism of action of the antimicrobial peptide Buforin II: Buforin II kills microorganisms by penetrating the cell membrane and inhibiting cellular functions. Biochem Biophys Res Commun 244:253–257
Park CB, Yi K-S, Matsuzaki K, Kim MS, Kim SC (2000) Structure-activity analysis of buforin II, a histone H2A-derived antimicrobial peptide: the proline hinge is responsible for the cell-penetrating ability of buforin II. Proc Natl Acad Sci 97:8245–8250

Pasupuleti M, Schmidtchen A, Malmsten M (2012) Antimicrobial peptides: key components of the innate immune system. Crit Rev Biotechnol 32:143–171

Patat SA et al (2004) Antimicrobial activity of histones from hemocytes of the Pacific white shrimp. Eur J Biochem 271:4825–4833

Patrzykat A, Zhang L, Mendoza V, Iwama GK, Hancock REW (2001) Synergy of histone-derived peptides of Coho Salmon with lysozyme and flounder Pleurocidin. Antimicrob Agents Chemother 45:1337–1342

Patrzykat A, Friedrich CL, Zhang L, Mendoza V, Hancock REW (2002) Sublethal concentrations of pleurocidin-derived antimicrobial peptides inhibit macromolecular synthesis in Escherichia coli. Antimicrob Agents Chemother 46:605–614

Pilsczek FH et al (2010) A novel mechanism of rapid nuclear neutrophil extracellular trap formation in response to Staphylococcus aureus. J Immunol 185:7413–7425

Podda E et al (2006) Dual mode of action of Bac7, a proline-rich antibacterial peptide. Biochim Biophys Acta 1760:1732–1740

Reddy KVR, Yedery RD, Aranha C (2004) Antimicrobial peptides: premises and promises. Int J Antimicrob Agents 24:536–547

Richards RC, O'Neil DB, Thibault P, Ewart KV (2001) Histone H1: an antimicrobial protein of Atlantic Salmon (Salmo salar). Biochem Biophys Res Commun 284:549–555

Rose FR et al (1998) Potential role of epithelial cell-derived histone H1 proteins in innate antimicrobial defense in the human gastrointestinal tract. Infect Immun 66:3255–3263

Rose-Martel M, Hincke MT (2014) Antimicrobial histones from chicken erythrocytes bind bacterial cell wall lipopolysaccharides and lipoteichoic acids. Int J Antimicrob Agents 44:470–472

Rosenberger CM, Gallo RL, Finlay BB (2004) Interplay between antibacterial effectors: a macrophage antimicrobial peptide impairs intracellular Salmonella replication. Proc Natl Acad Sci U S A 101:2422–2427

Saffarzadeh M et al (2012) Neutrophil extracellular traps directly induce epithelial and endothelial cell death: a predominant role of histones. PLoS One 7:e32366

Sang Y, Blecha F (2008) Antimicrobial peptides and bacteriocins: alternatives to traditional antibiotics. Anim Health Res Rev 9:227–235

Scocchi M, Mardirossian M, Runti G, Benincasa M (2016) Non-membrane Permeabilizing modes of action of antimicrobial peptides on Bacteria. Curr Top Med Chem 16:76–88

Segal AW (2005) How neutrophils kill microbes. Annu Rev Immunol 23:197–223

Selsted ME, Ouellette AJ (2005) Mammalian defensins in the antimicrobial immune response. Nat Immunol 6:551–557

Semeraro F et al (2011) Extracellular histones promote thrombin generation through platelet-dependent mechanisms: involvement of platelet TLR2 and TLR4. Blood 118:1952–1961

Shai Y (1999) Mechanism of the binding, insertion and destabilization of phospholipid bilayer membranes by alpha-helical antimicrobial and cell nonselective membrane-lytic peptides. Biochim Biophys Acta 1462:55–70

Shai Y (2002) Mode of action of membrane active antimicrobial peptides. Biopolymers 66:236–248

Sim S et al (2017) Investigating the nucleic acid interactions of histone-derived antimicrobial peptides. FEBS Lett 591:706–717

Sun X, Shi J, Han L, Su Y, Li Z (2008) Anti-histones antibodies in systemic lupus erythematosus: prevalence and frequency in neuropsychiatric lupus. J Clin Lab Anal 22:271–277

Tagai C, Morita S, Shiraishi T, Miyaji K, Iwamuro S (2011) Antimicrobial properties of arginine- and lysine-rich histones and involvement of bacterial outer membrane protease T in their differential mode of actions. Peptides 32:2003–2009

Torrent M, Pulido D, Rivas L, Andreu D (2012) Antimicrobial peptide action on parasites. Curr Drug Targets 13:1138–1147

Urban CF et al (2009) Neutrophil extracellular traps contain Calprotectin, a cytosolic protein complex involved in host defense against Candida albicans. PLoS Pathog 5:e1000639

Uyterhoeven ET, Butler CH, Ko D, Elmore DE (2008) Investigating the nucleic acid interactions and antimicrobial mechanism of buforin II. FEBS Lett 582:1715–1718

van Dijk A, Veldhuizen EJA, Haagsman HP (2008) Avian defensins. Vet Immunol Immunopathol 124:1–18

von Kockritz-Blickwede M et al (2008) Phagocytosis-independent antimicrobial activity of mast cells by means of extracellular trap formation. Blood 111:3070–3080

Walberg M, Gaustad P, Steen HB (1997) Rapid assessment of ceftazidime, ciprofloxacin, and gentamicin susceptibility in exponentially-growing E. coli cells by means of flow cytometry. Cytometry 27:169–178

Wang G (2008) Structures of human host defense cathelicidin LL-37 and its smallest antimicrobial peptide KR-12 in lipid micelles. J Biol Chem 283:32637–32643

Watson K et al (1995) Extra-nuclear location of histones in activated human peripheral blood lymphocytes and cultured T-cells. Biochem Pharmacol 50:299–309

Wickens HJ, Pinney RJ, Mason DJ, Gant VA (2000) Flow cytometric investigation of filamentation, membrane patency, and membrane potential in Escherichia coli following ciprofloxacin exposure. Antimicrob Agents Chemother 44:682–687

Wiesner J, Vilcinskas A (2010) Antimicrobial peptides: the ancient arm of the human immune system. Virulence 1:440–464

Xu J et al (2009) Extracellular histones are major mediators of death in sepsis. Nat Med 15:1318–1321

Xu J, Zhang X, Monestier M, Esmon NL, Esmon CT (2011) Extracellular histones are mediators of death through TLR2 and TLR4 in mouse fatal liver injury. J Immunol 187:2626–2631

Yeaman MR (2003) Mechanisms of antimicrobial peptide action and resistance. Pharmacol Rev 55:27–55

Yi G-S, Park CB, Kim SC, Cheong C (1996) Solution structure of an antimicrobial peptide buforin II. FEBS Lett 398:87–90

Yipp BG et al (2012) Infection-induced NETosis is a dynamic process involving neutrophil multitasking in vivo. Nat Med 18:1386–1393

Yu Y et al (2017) Characterization of early-phase neutrophil extracellular traps in urinary tract infections. PLoS Pathog 13:e1006151

Zanetti M (2004) Cathelicidins, multifunctional peptides of the innate immunity. J Leukoc Biol 75:39–48

Zhou B-R et al (2013) Structural insights into the histone H1-nucleosome complex. Proc Natl Acad Sci 110:19390–19395

Index

G. Duménil, S. van Teeffelen (eds.), *Physical Microbiology*, Advances in Experimental Medicine and Biology 1267, https://doi.org/10.1007/978-3-030-46886-6